On the nature of SERS from plasmonic nanostructures

James Tom Hugall

2 November 2012

University of Cambridge
Cavendish Laboratory
Selwyn College

A dissertation submitted for the degree of

Doctor of Philosophy

Cover art:

The hand image on the inside cover is a graphical representation of the top 200 most frequently used words in the thesis (ignoring the most common ones). The word size corresponds to the frequency of its use. The hand is a mask of the author's hand.

Supervisor:

Prof. Jeremy J. Baumberg

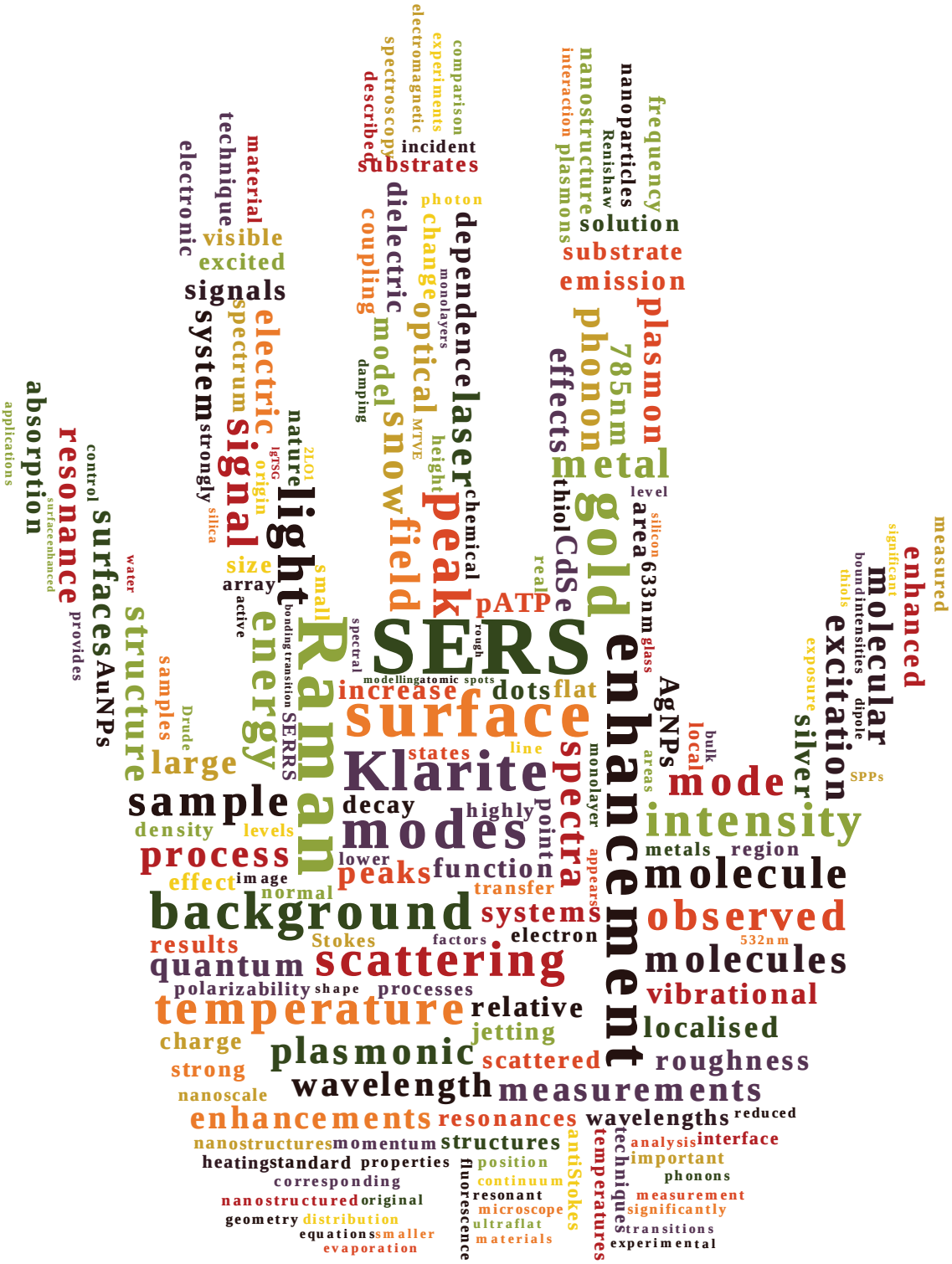
SERS
enhancement
surface
Raman
gold
plasmon
metal
phonon
peak
field
snow
model
coupling
dielectric
optical
dependence
laser
chemical
peaks
modes
Klarite
spectra
background
scattering
temperature
plasmonic
wavelength
measurements
enhancements
resonances
structures
molecule
molecules
observed
intensity
mode
excitation
molecular
enhanced
measured
silver
AgNPs
pATP
CdSe
thiol
effects
emission
solution
substrate
nanostructure
plasmons
nanoparticles
Renishaw
frequency
785nm
633nm
area
level
glass
silicon
bulk
local
areas
SPPs
exposure
thiols
boundintensities
dipole
significant
incident
substrates
described
spectroscopy
electromagnetic
experiments
comparison
photon
change
monolayers
height
MTVE
damping
rough
spectral
modellingatomic
spots
dots
flat
increase
line
monolayer
appears
point
highly
decay
lower
function
transfer
systems
electron
factors
Stokes
532nm
molecules
vibrational
localised
roughness
relative
jetting
scattered
charge
strong
nanoscale
polarizability
shape
processes
reduced
wavelengths
interface
analysis
important
phonons
measurement
significantly
transitions
experimental
temperatures
antiStokes
position
continuum
resonant
microscope
ultraflat
materials
fluorescence
nanostructures
momentum
heatingstandard
properties
corresponding
nanostructured
original
geometry
distribution
equations
smaller
evaporation
sample
process
structure
energy
signal
light
Raman
size
array
active
small
bonding
transition
SERRS
nature
2LO1
IgTSG
origin
silica
strongly
system
spectrum
electric
material
technique
visible
excited
signals
electronic
density
levels
effect
image
normal
results
quantum
large
samples
Drude
water
surfaces
AuNPs
provides
resonance
surfaceenhanced
absorption
control
applications

To my family, in memory of Mary Catterall.

Declaration

This thesis is the result of my own work and includes nothing which is the outcome of work done in collaboration except where indicated in the customary manner. The thesis has not previously been submitted in whole or part for a degree in any university and is within the word limit specified by the Degree Committee of the Faculty of Physics and Chemistry, University of Cambridge, UK.

_____

James Tom Hugall
2 November 2012

Abstract

On the nature of SERS from plasmonic nanostructures

The nature of surface-enhanced Raman scattering (SERS) on nanostructured surfaces is explored using both inorganic and organic-based systems and a variety of environmental perturbation mechanisms. Experimental optical characterisation systems are developed and existing systems extended to facilitate this exploration.

SERS of inorganic semiconducting quantum dots (QDs) is observed for the first time, paving the way for their use as spatially well-defined SERS markers. Tuning of the Raman excitation wavelength allows comparison between resonance and non-resonance QD SERS and identifies enhancement due to the plasmonic nanostructure.

A gentle mechano-chemical process (carbon dioxide snow jet) is used to rearrange adsorbed organic thiol monolayers on a gold plasmonic nanostructure. The necessity of nanoscale roughness to the large SERS enhancement on pit-like plasmonic nanostructures is shown and demonstrates a new method to boost SERS signals ($> 500\,\%$) on plasmonic nanostructures. A multiplexed time-varied exposure technique is developed to track this molecular movement over time and highlights the different origins of the SERS peak and its accompanying background continuum.

Using low-temperature cryogenics (down to 10 K) the SERS peak and background continuum intensity are shown to increase as the plasmonic metal damping reduces with temperature. Temperature dependent measurements of QD (resonance) SERS are shown to have strong wavelength dependence due to the excitonic transitions in QDs. Changes to the QD fluorescence at low temperature allows striking comparison between the Raman and fluorescence processes.

The role of charge transfer and electromagnetic enhancement in the SERS intensity of p-aminothiophenol (pATP) is investigated on nanostructured plasmonic surfaces coupled to metallic nanoparticles. The results support the importance of charge transfer effects to the SERS of pATP, and highlight the difference between those of electromagnetic origin. Addition of nanoparticles to the nanostructured surface was seen to enhance SERS signals by up to $100\times$.

James Tom Hugall

Acknowledgements

I would like to thank my supervisor, Jeremy, for giving me the opportunity to experiment in his labs and be a part of his group. He has been a continual source of inspiration and has provided a fantastic environment in which to work, bringing together many interesting minds with which to interact and great equipment with which to work. I welcome his fresh approach and non-conformity, which provides an environment where new ideas and approaches can thrive and challenge old reason.

I am also extremely grateful to the help and guidance of Dr. Sumeet Mahajan who helped shape this project and introduced me to the world of chemistry as well as delicious Indian cuisine amongst many other things. He has been responsible for fostering a SERS community in the Cavendish, which provided an excellent discussion forum and has also been a great sounding board throughout my PhD. I have enjoyed frequent discussions with him about almost anything!

I would like to thank Renishaw Diagnostics Ltd., for helping to fund this project and welcoming me so warmly into their labs in the summer of 2011 to conduct part of this research. Special thanks goes to my industrial supervisor Dr. David Eustace for looking after me up in Glasgow and for providing ideas, questions and a lot of Klarite samples throughout my PhD. Thanks also go to the EPSRC for co-funding this project.

The members of the ever-expanding NanoPhotonics group have been great to work with and made it a joy to come into the lab! I enjoyed the fluid-thinking and lengthy debates about the philosophical aspects of our work (what is a photon?) and life in general. A lot of fun was had in the 'fish bowl' and this saved me from complete insanity (or perhaps pushed me into it) towards the end of the writing process. I have learnt a lot from everyone and am looking forward to travelling the world to visit everyone in their natural habitats. Thanks to all the plasmonic boys – the ones who have been there throughout my time: Niraj Lal, Petros Farah, Max Bock (although not strictly plasmonics!), Kevin Savage, Bruno Soares and Fumin Huang; the new(er) ones who I have worked with: Richard Taylor, Christian Steuwe, Matthew Hawkeye and Daniel Sigle; and of course the older ones from before my time. Also thanks to Cornelius Grossman and Chris Coulson for the numerous office shenanigans and Lars Herrmann and Peter Cristofolini for striving to improve the antiquated Cambridge systems. A special mention also goes out to Gabriel Christmann and Silvia Vignolini for their wise musings. I also thank the many other newer members of NP for continuing the fantastic atmosphere of the group.

The NanoPhotonics winter school is a highlight of the year, and thanks to Jeremy and Prof. Ulli Steiner for continuing to take us to frozen mountainous environments – long may it continue! I would also like to thank members of Ulli's group with whom we collaborate strongly, especially Alex Finnemore for his infectious positivity and directness and also Stefan Guldin and Mathias Kolle.

Thanks to our fantastic technicians Anthony Barnett and Richard Hardy for creating a fun lab environment and putting up with us all and of course Angela Campbell for keeping the group running smoothly and Colin Edwards for keeping our server spinning and our internet connected.

Selwyn College has provided me with an ideal place to meet new people from all around the world doing all sorts of interesting things! I cannot think of a more friendly environment to spend my time at Cambridge. Thanks to Selwyn College Boat Club for providing me with a constant and excellent distraction from work, despite the freezing early mornings on the river and the sleepy afternoons in the office(!) Thanks also to all the members of Selwyn MCR who made life so enjoyable, a special mention go to the friends who have been there from start to finish: Campbell, Nick, Tamsin and Kian and of course Laurie for putting up with me.

Thanks to everyone who proof-read parts of this thesis: Matthew, Richard, Petros, Alex, Laurie and Richard Bowman.

Lastly, but by no means least, I would like to thank all my other friends (from Saffron Walden to Southampton) and my family for making life so enjoyable over the last four years, I am very privileged to know you all.

Physics helps us understand the world around us, but without people, there is nothing worth understanding.

Contents

List of Figures

Publications List

- Hugall JT, Baumberg JJ and Mahajan S. 'Surface-enhanced Raman spectroscopy of CdSe quantum dots on nanostructured plasmonic surfaces'. *Applied Physics Letters*, **95** 141111 (2009) DOI: 10.1063/1.3243982.

- Hugall JT, Baumberg JJ and Mahajan S. 'Disentangling the peak and background signals in surface-enhanced Raman scattering'. *Journal of Physical Chemistry C*, **116** 6184 (2012) DOI: 10.1021/jp3002977.

- Hugall JT, Finnemore AS, Baumberg JJ, Steiner U and Mahajan S. 'Solvent-resistant ultraflat gold using liquid glass'. *Langmuir*, **28** 1347 (2012) DOI: 10.1021/la204299h.

- Mahajan S, Lee TC, Biedermann F, Hugall JT, Baumberg JJ and Scherman O. 'Raman and SERS spectroscopy of cucurbit[n]urils'. *Physical Chemistry Chemical Physics*, **12** 10429 (2010) DOI: 10.1039/c0cp00071j.

- Speed JD, Johnson RP, Hugall JT, Lal NN, Bartlett PN, Baumberg JJ and Russell AE. 'SERS from molecules bridging the gap of particle-in-cavity structures'. *Chemical Communications (Cambridge, England)*, **47** 6335 (2011) DOI: 10.1039/c0cc05325b.

1. Introduction

Scattered light allows us to visualise the objects in the world around us. Light strikes objects and is scattered off them in all directions. This light can be collected by our eyes and focused to create an image of the objects from which it was scattered and thus create a picture of the world we live in.

Scattered light is also responsible for other physical phenomena such as the colour of the sky, blue in daylight, fading to red at sunset. [6] Most light scattering is elastic, with the light's energy conserved. This is called *Rayleigh scattering*. Light can also be inelastically scattered where a portion of energy is lost to or gained from the scattering object during the scattering event. This energy loss or gain is usually associated with vibrations in the scattering material. The scattered light shifts in energy depending on the vibration with which it has interacted, in a process known as *Raman scattering*. Raman scattered light from a molecule produces a unique energy spectrum of the different vibrations due to the chemical bonds within the molecule. This spectrum provides an optical 'fingerprint' of the molecule allowing its unique identification.

Molecules are formed when atoms come together and exchange or share electrons forming strong bonds between each other. The atoms, previously free to move around, are bound together restricting their freedom of movement. As in individual atoms, molecules can temporarily store energy by exciting these electrons into higher states or orbitals. Further to this, the restricted movement of the atoms in a molecule allows energy to be stored in vibrational or rotational motion of the molecule. The frequency of vibration or rotation depends on the molecular bond strengths and corresponds to the energy stored, since energy is directly proportional to frequency. These molecular energy storage mechanisms, principally electronic, vibrational and rotational, each store different magnitude amounts of energy and to a good approximation can be thought of as independent from each other. The total

energy of the molecule corresponds to the sum of the different components. Since $E_{electronic} > E_{vibrational} > E_{rotational}$, we can consider the molecule in terms of electronic energy levels which are sub-divided into vibrational levels, which are further subdivided into rotational levels as shown in Fig. 1.1a.

Molecular fingerprinting is an important technique for a wide range of scientific disciplines, including analytical chemistry, materials science, biochemistry and medicine. There are many ways to obtain such fingerprints. Mass spectrometry is a destructive technique and relies on breaking the molecule up into its constituent pieces and measuring the mass and relative abundances of these chunks to build a picture of the original molecule. By making use of different parts of the electromagnetic spectrum (Fig. 1.1b), we can directly or indirectly probe the molecules' various energy levels. Nuclear magnetic resonance spectroscopy probes the electronic environment of different protons within the molecule by measuring the change in energy levels via radio-frequency (RF) absorption caused by spin alignment when the molecule is placed in a magnetic field. Infra-red (IR) absorption spectroscopy directly excites the vibrational levels in the molecule using broadband low-energy light. The resulting absorption spectrum indicates the molecular vibrations excited in the molecule. Using microwave light we can also directly probe rotational states of the molecule.

Each technique for determining molecular properties has various advantages and disadvantages and different techniques are used dependent on the situation. IR spectroscopy, which directly probes the vibrational levels is limited since water cannot usually be used as a solvent as it itself absorbs a lot of IR radiation. Techniques such as mass-spectrometry and nuclear magnetic resonance spectroscopy require expensive and sometimes bulky machinery for accurate measurements. Consequently, there is a need for fast, simple and cheap processes, which would allow molecular fingerprinting to extend into new domains.

In contrast to the above techniques, Raman spectroscopy *indirectly* probes molecular vibrational levels. It is usually performed in the visible region of the spectrum, higher in energy than the vibrational levels being probed and normally below, or sometimes in resonance with, electronic transitions in the molecule as shown in Fig. 1.1a. It allows measurements to be made in water (since light at this frequency is not readily absorbed) and extensive sample preparation is not usually necessary. The basic equipment needed is more accessible than other techniques and spectroscopy can be performed in many situations not amenable to other techniques, including out-

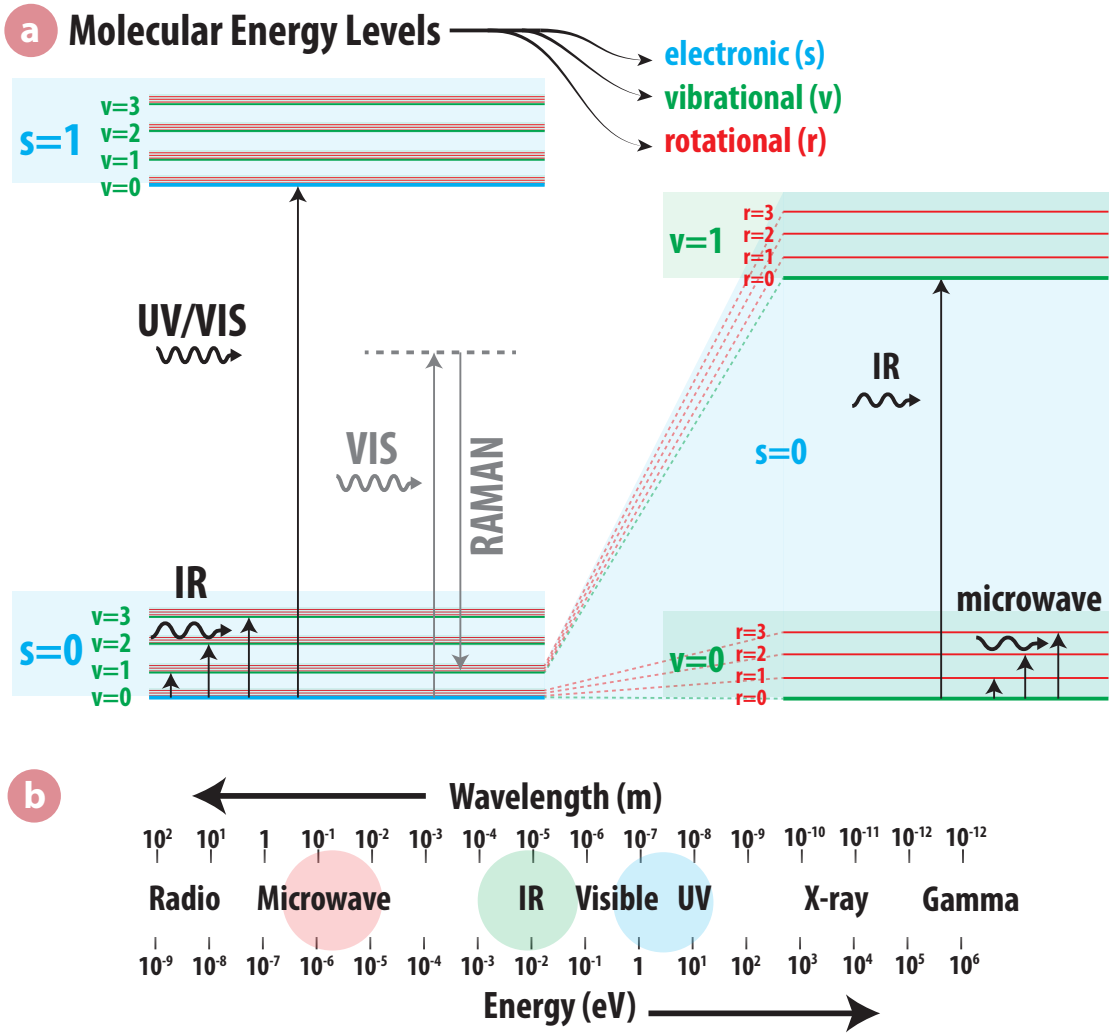

Figure 1.1.: (a) Molecular energy levels showing electronic, vibrational and rotational levels and direct excitation of levels using electromagnetic radiation. Indirect probing of vibrational levels using Raman scattering is also shown. (b) Electromagnetic energy spectrum indicating different spectral regions of interest for optical interrogation of molecules via absorption or emission.

of-the-lab or *in vivo* in a non-destructive manner. The major drawback of Raman spectroscopy, however, is that it is an inherently very weak process. For a typical molecule, for every billion photons shone on it, only about ten will undergo Raman scattering, the rest will be Rayleigh scattered. This compares very unfavourably to fluorescence, where in some quantum dots, better than one in every two photons absorbed is emitted as fluorescence.

Raman scattering can be enhanced by increasing the local electric field strength near the molecule. This can increase the intensity of both incoming and scattered light. On structured metallic surfaces or nanoparticles it is possible for light to become tethered to the surface due to plasmonic coupling. This trapped light produces large electric fields at the metal surface with an exponentially decaying nature. Molecules placed in this high local electric field experience a huge enhancement to their Raman scattering. This surface-enhanced Raman scattering (SERS) extends the field of Raman scattering to new possibilities, including high-sensitivity and even single molecule detection at high speed. [7, 8]

Despite the discovery of SERS nearly 40 years ago, the exact enhancement mechanisms of the process is unclear. This prohibits the ability to fully control it and thus maximise its usefulness. This has meant industrial and commercial adoption has been limited. In many systems repeatability remains a problem and it is still not generally possible to obtain a reliable correlation between SERS intensity and the number of molecules probed. Other issues remain unresolved, such as the origin of a broad background continuum signal accompanying the sharp SERS peaks observed in SERS spectra and the extent to which chemical enhancement effects play a role in the overall SERS enhancement compared to plasmonic-based electromagnetic effects.

Conquering these fundamentals of SERS will allow us the possibility of greater control and understanding of SERS spectra. It may even allow us to extract further information from the spectra and enable reliable detection of single molecules, leading to wide-scale adoption of SERS as an analytical technique. An ultimate use for SERS could be the rapid detection of trace biological molecules in a point-of-care scenario. One could imagine the extremely dilute biological matter contained within a human tear being analysed in seconds at home using this non-intrusive, low-cost technique (Fig. 1.2). This would allow instant diagnosis of a person's state of health with the potential to reveal any virus or bacteria present, completely revolutionising

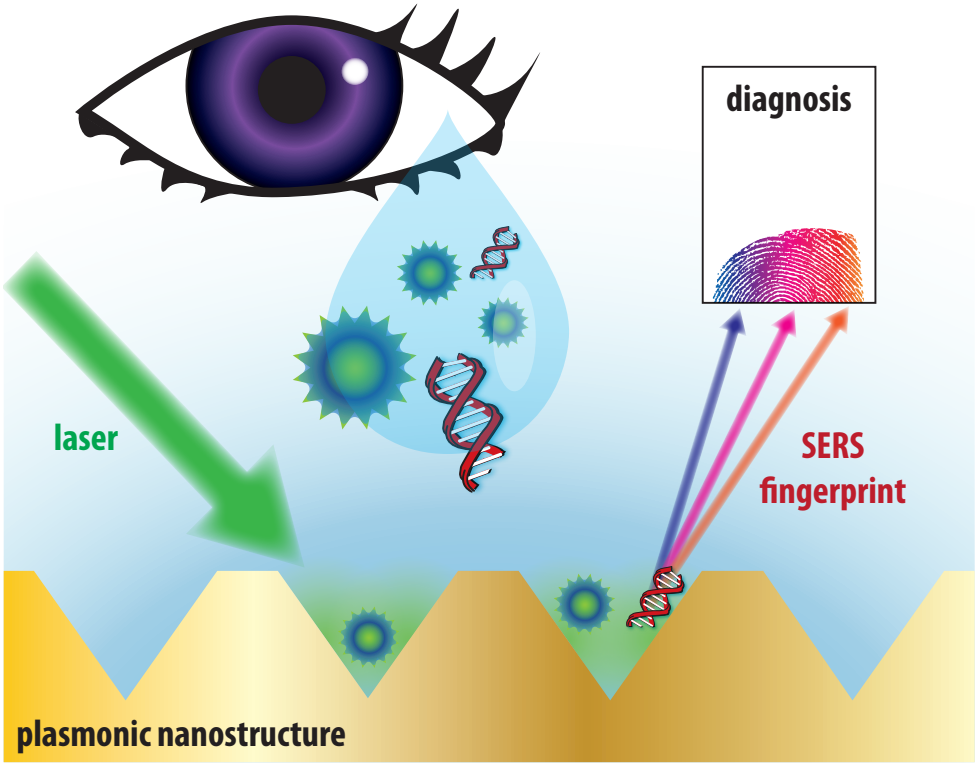

Figure 1.2.: A tear is harvested from a patient's eye onto a SERS-active plasmonic substrate. A laser incident on the substrate surface excites vibrations in the biological matter on the surface with the SERS scattered light leaving the surface in a range of frequencies corresponding to an 'optical fingerprint' of the molecule. This spectrum can be analysed to determine what biological matter, originating from the patient, was on the surface and provide a clinician with a series of test results to aide rapid diagnosis.

healthcare provision. The technical challenges to implement this, however, should not be underestimated. Biological systems are considerably more complicated than the ideal chemical systems studied here. Inside a human tear are many different biological molecules, and much else such as salt-water, producing extremely complicated SERS spectra. Not only must we determine how to control the SERS effect, but we must create systems capable of interpreting the large amounts of data generated. If we can overcome these challenges then SERS (or perhaps another enhanced Raman process) will progress as a very useful technique in the future.

1.1. Thesis structure

This thesis investigates the nature of the SERS enhancement on nanostructured SERS-active surfaces and focuses on an inverted pyramid geometry called 'Klarite'. Two prototype systems are used to study the SERS process in better detail:

Quantum dots: to study localised plasmons interacting with a well-defined local inorganic (non-degradable) nanostructure at points on a nanostructured surface.

Snow jet: to study interaction of molecular monolayers with localised plasmon resonances on surfaces perturbed using carbon dioxide crystals fired at the surface (snow jet).

Firstly the theoretical foundations of this area are explored in Chapter 2 before the principal experimental techniques used throughout this thesis are introduced in Chapter 3.

Chapter 4 gives a brief overview of SERS nanostructures in the literature and provides a current view to the enhancement mechanisms in Klarite complete with theoretical and optical characterisation.

The inorganic system is introduced in Chapter 5 where the SERS of semiconducting quantum dots is demonstrated. The effects on the SERS of a molecular monolayer due to changes in nanoscale surface morphology and molecular movement caused by a carbon dioxide snow jet is developed in Chapter 6. Differences between SERS peak and SERS background continuum signals are demonstrated on application of the snow jet.

In Chapter 7, low-temperatures (down to 10 K) are exploited on both quantum dot and molecular monolayer systems to further explore the nature of SERS enhancement in both cases.

The importance of the chemical charge-transfer effect of SERS is shown in Chapter 8, where molecular bridges are formed between plasmonic nanostructures and nanoparticles to give large enhancements to the SERS signal, plasmonic and otherwise.

Following this the main conclusions of this work are surmised and potential directions of future work are provided.

In Appendix A, a facile route to create near atomically flat gold is presented, which has proven useful in comparing SERS enhancement factors as well as facilitating imaging of quantum dots attached to gold surfaces in earlier chapters.

2. Theoretical foundations

Plasmonics extends the field of photonics into new and exciting areas. By coupling light to electron oscillations in certain metal surfaces, new control over light is possible. Light is three-dimensional in nature and difficult to confine to dimensions below the order of its wavelength (typically 0.5 µm for visible light). However, when coupled to electron oscillations (as plasmons) it can be transformed into a quasi two-dimensional state, where it becomes 'stuck' to a metal surface and acquires unique properties. Importantly this 'stuck' light is highly confined to the surface to dimensions much smaller than the wavelength of light. This means the electric field of the original light becomes tightly localized in space with light squashed into smaller spaces. Anything placed within this sub-diffraction-limit 'hot spot' experiences a much stronger electric field compared to being in normal light. Processes reliant on the electric field strength thus experience tremendous local enhancement.

This highly localized electric field is used to enhance sensing, such as Raman spectroscopy, where it can be used to detect single molecules. [7] Other uses have been envisaged, such as enhancing photovoltaics [9, 10] since the trapped light allows more efficient harvesting of solar energy. For some time, a Holy Grail of plasmonics has been to replace electronic microchips with a plasmonic equivalent. Such plasmonic microchips are purported to allow much faster processing and smaller chip size, whilst avoiding the problems associated with electronic resistive heating. [11, 12] However, unlike light in free-space, plasmon propagation is heavily damped due to the interaction with electrons in the metal and plasmons generally decay after travelling a few microns in the visible to around 100 µm in the near-IR spectral range. Whether this damping limitation can be overcome remains to be seen. [13, 14] If it is, the field of computing could be revolutionised. Even if it is not, other plasmonic applications which do not rely on long propagation lengths have the potential to revolutionise many areas of technology.

2.1. Surface plasmon polaritons

Before introducing surface plasmon polaritons (SPPs), we introduce the macroscopic form of Maxwell's equations from which everything in this section can be derived. The exact and full derivations can be found in much of the literature to which the reader is directed for a complete understanding. [15, 16, 17] By exploring Maxwell's equations we will discover the properties a material needs to support SPP modes: the sticking of light to a surface.

2.1.1. Maxwell's equations

Maxwell's equations encode the relationship between electric and magnetic fields and matter. They are used here to uncover the properties of an optical wave bound to a dielectric-metal interface as well as the optical properties of metals themselves.

Maxwell's equations appear in many forms but their macroscopic form (Eq. 2.1) is traditionally used to discover the electromagnetic properties of materials. This form aims to simplify the solutions of the equations by separating effects due to electrons closely bound to atoms in the material and electrons free to move around the material. This distinction is somewhat arbitrary depending on the material, [18] and here we adopt a commonly used method [19] distinguishing between charges ρ and currents $\mathbf{J}$ inside the material responding to the external charges ρ_{ext} and currents $\mathbf{J_{ext}}$ driving them. In this format they become,

$$\nabla \cdot \mathbf{D} = \rho_{ext} \qquad \text{Gauss's Law} \tag{2.1a}$$

$$\nabla \cdot \mathbf{B} = 0 \qquad \text{No magnetic monopoles} \tag{2.1b}$$

$$\nabla \times \mathbf{E} = -\frac{\partial \mathbf{B}}{\partial t} \qquad \text{Faraday's Law} \tag{2.1c}$$

$$\nabla \times \mathbf{H} = \mathbf{J_{ext}} + \frac{\partial \mathbf{D}}{\partial t} \qquad \text{Ampère-Maxwell Law} \tag{2.1d}$$

Two new vector fields are introduced in addition to the electric $\mathbf{E}$ and magnetic $\mathbf{B}$ fields: the electric field displacement vector $\mathbf{D}$ and the magnetic field vector $\mathbf{H}$. These are related to $\mathbf{E}$ and $\mathbf{B}$ via the polarization $\mathbf{P}$ and magnetization $\mathbf{M}$ of the

material by the constitutive (or material) equations,

$$\mathbf{D} = \epsilon_0 \mathbf{E} + \mathbf{P} \tag{2.2a}$$

$$\mathbf{B} = \mu_0 \mathbf{H} + \mathbf{M}. \tag{2.2b}$$

The polarization $\mathbf{P}$ and magnetization $\mathbf{M}$ are related to the induced charges and currents in the material respectively. We have also introduced the dielectric constant ϵ_0 (electric permittivity of free space) and the magnetic constant μ_0 (magnetic permeability) where $1/\sqrt{\mu_0 \epsilon_0} = c$, where c is the speed of light in vacuum.

Limiting ourselves to linear, isotropic materials we can further simplify the constitutive equations (Eq. 2.2a and Eq. 2.2b) using a frequency-dependent complex relative permittivity (also known as a relative dielectric function) ϵ_r and a complex relative permeability μ_r. Here we have generalised ϵ_r to depend on the frequency of the electric field ensuring validity for dispersive media. This generalisation can be shown to be valid in the spatially local limit given that λ is larger than other dimensions. [17]

$$\mathbf{D} = \epsilon_0 \epsilon_r(\omega) \mathbf{E} \tag{2.3a}$$

$$\mathbf{B} = \mu_0 \mu_r(\omega) \mathbf{H} \tag{2.3b}$$

Since we are only concerned with non-magnetic media where $\mu_r \approx 1$, we need not consider magnetic effects. The quantity of interest then becomes ϵ_r. This greatly simplifies Maxwell's equations and allows us to describe the response of a material to an electromagnetic wave, provided we know its dielectric function ϵ_r and the approximation of a linear and isotropic material are valid.

2.1.2. The dielectric function, ϵ_r

In the above we have introduced the concept of a dielectric function to encode the electromagnetic properties of a material. Here we attempt to illustrate the significance of this quantity and how it relates to other relevant quantities for describing material behaviour.

It is useful to compare the dielectric function to a quantity called the electric susceptibility χ_e via $\epsilon_r(\omega) = 1 + \chi_e(\omega)$. The susceptibility defines the polarization induced in a material upon application of an electric field through $\mathbf{P} = \epsilon_0 \chi_e \mathbf{E}$. The quantity χ_e is analogous to the polarizability of a molecule $\hat{\alpha}$ which relates the local electric field to the induced dipole moment in a molecule as will be seen later in our discussion on Raman scattering.

In wave optics it is often more intuitive to describe optical effects using a material's complex refractive index $\tilde{n}$ instead of the dielectric function. Since $\tilde{n} = \sqrt{\epsilon_r \mu_r}$ we can derive the following relations:

$$\epsilon_r' = n^2 - \kappa^2 \tag{2.4a}$$

$$\epsilon_r'' = 2n\kappa \tag{2.4b}$$

$$n^2 = \frac{\epsilon_r'}{2} + \frac{1}{2}\sqrt{\epsilon_r'^2 + \epsilon_r''^2} \tag{2.4c}$$

$$\kappa = \frac{\epsilon_r''}{2n} \tag{2.4d}$$

where $\tilde{n} = n + i\kappa$ and $\epsilon_r = \epsilon_r' + i\epsilon_r''$.

In a metal where free electrons dominate the response to applied fields, it is customary to characterise it by its conductivity σ. In the low-frequency electrostatic regime the conductivity is a material-dependent, frequency-independent constant σ_{DC}. At optical frequencies the conductivity becomes highly frequency dependent $\sigma(\omega)$ and can no longer be considered constant.

The internal current density is related to the electric field and conductivity via Ohm's law:

$$\mathbf{J} = \sigma \mathbf{E}. \tag{2.5}$$

Since charge conservation requires the rate of change in internal charge density to be accounted for by the flow of internal current,

$$\nabla \cdot \mathbf{J} + \frac{\partial \rho}{\partial t} = 0, \tag{2.6}$$

and since the internal charge density is related to the material's polarization via $\nabla \cdot \mathbf{P} = -\rho$, we require:

$$\mathbf{J} = \frac{\partial \mathbf{P}}{\partial t}. \tag{2.7}$$

Combining Eq. 2.7 with the constitutive equations (Eq. 2.2) we find the relationship between the conductivity and dielectric function, [17]

$$\epsilon_r(\omega) = 1 + \frac{i\sigma(\omega)}{\epsilon_0 \omega}. \tag{2.8}$$

This formulation will prove useful in Chapter 7 for determining the temperature dependence of the dielectric function.

2.1.3. Drude-Lorentz model of metals

The Drude-Lorentz model describes a metal as a spatially fixed background of positive ions (representing atomic nuclei and bound electrons) amongst a sea of free and mobile electrons (see Fig. 2.1). The various effects of lattice potentials and electron-electron interactions are approximated and encoded in an effective electron mass m^* and a damping term γ in the equation of motion describing the electrons.

An electron in free-space under the influence of an external and oscillatory electromagnetic field $\mathbf{E} = \mathbf{E_0} e^{-i\omega t}$ will experience a force proportional to the electric field and its charge $-e$. Including the damping term we can write the equation of motion for such an electron as,

$$m^* \ddot{\mathbf{x}} + m^* \gamma \dot{\mathbf{x}} = -e\mathbf{E}. \tag{2.9}$$

The solution to Eq. 2.9 is oscillatory in nature with $\mathbf{x} = \mathbf{x_0} e^{-i\omega t}$, where the frequency is the same as that of the driving field. If we solve Eq. 2.9 and consider an electron

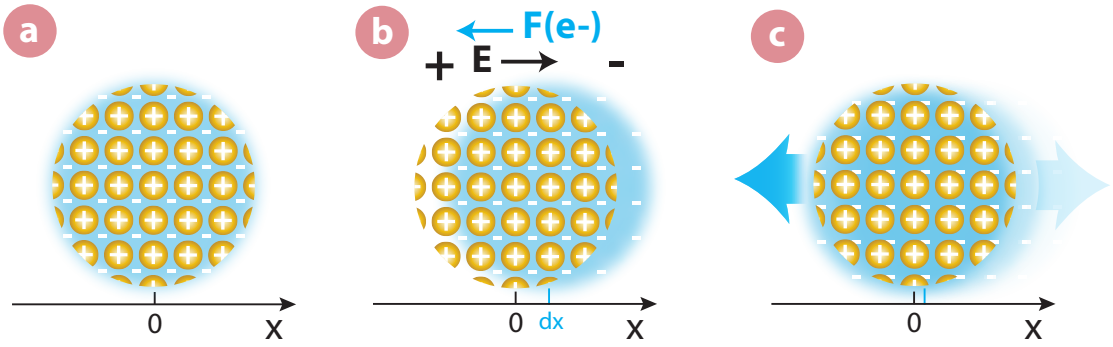

Figure 2.1.: Drude model of a metal: **(a)** The metal is simplified to a fixed positive background (corresponding to atomic nuclei and bound electrons) with a mobile negatively charged electron cloud. **(b)** The EM field causes displacement (dx) of the electron cloud relative to the background. **(c)** The electron cloud oscillates around the electrons equilibrium position.

density n, the free electrons' contribution to the material's polarization $\mathbf{P}$ becomes:

$$\mathbf{P} = -ne\mathbf{x} = -\frac{ne^2}{m^*(\omega^2 + i\gamma\omega)}\mathbf{E} \tag{2.10}$$

Using this result for the polarization and comparing with Eq. 2.3a gives us the electric permittivity of a Drude metal,

$$\epsilon_r(\omega) = 1 - \frac{ne^2}{\epsilon_0 m^*(\omega^2 + i\gamma\omega)} = 1 - \frac{\omega_p^2}{\omega^2 + i\gamma\omega}, \tag{2.11}$$

where we have introduced the metal's plasma frequency $\omega_p^2 = \dfrac{ne^2}{\epsilon_0 m^*}$.

Depending on the frequency of the electric field, we can explore the different responses of the Drude metal:

1. $\omega > \omega_p$: Above the plasma frequency the real part of the dielectric function ϵ_r' is increasingly positive, and the imaginary part ϵ_r'' is increasingly small. The metal here behaves like a dielectric, and is transparent in this region. The incoming field is oscillating too fast for the electrons to respond.

2. $\omega < \omega_p$: Just below the plasma frequency, ϵ_r' is negative, but the damping corresponding to ϵ_r'' is still small. This is a region of interest in plasmonics.
3. $\omega << \omega_p$: Far below the plasma frequency, ϵ_r' becomes increasingly negative, but importantly the damping $\epsilon_r'' > \epsilon_r'$. This means that the metal becomes strongly absorbing but highly reflective in this regime.

As we will see, real metals do not behave exactly like Drude metals, and there are strong perturbations from this model especially in the noble metals used in visible-wavelength plasmonics.

2.1.3.1. Extending the Drude model

This Drude derived dielectric function provides a useful model for the EM response of metals. However, for noble metals, including gold and silver (which are important metals in plasmonics) the actual response varies significantly from the predicted Drude theory at certain photon energies. This is due to the excitation of interband transitions in the metal, which can directly absorb the photons. In gold, these transitions occur for energies greater than 2 eV. This gives gold its golden colour as the blue-green part of the spectrum is absorbed and only red-yellow light is reflected. These transitions limit the range of excitation of surface plasmons. Additionally, the noble metals have nearly full d-bands which significantly affects the polarization of the material, and the initial term '1' in Eq. 2.11 must be replaced with ϵ_∞ to account for this, giving,

$$\epsilon_r(\omega) = \epsilon_\infty - \frac{\omega_p^2}{\omega^2 + i\gamma\omega}. \tag{2.12}$$

Fig. 2.2a shows the calculated dielectric function for gold based on a best-fit Drude model, where the parameters in Eq. 2.12 have been fitted to the commonly used experimental data from Johnson and Christy [20]. For low energies the model fits the experimental data well, but as we enter the region of interband transitions (>2 eV) the Drude model is unable to effectively model the data. Fig. 2.2b shows the equivalent data but in terms of the refractive index.

The Drude theory can be extended to model interband transitions as Lorentz-like oscillators to provide a more accurate model of the dielectric function at higher

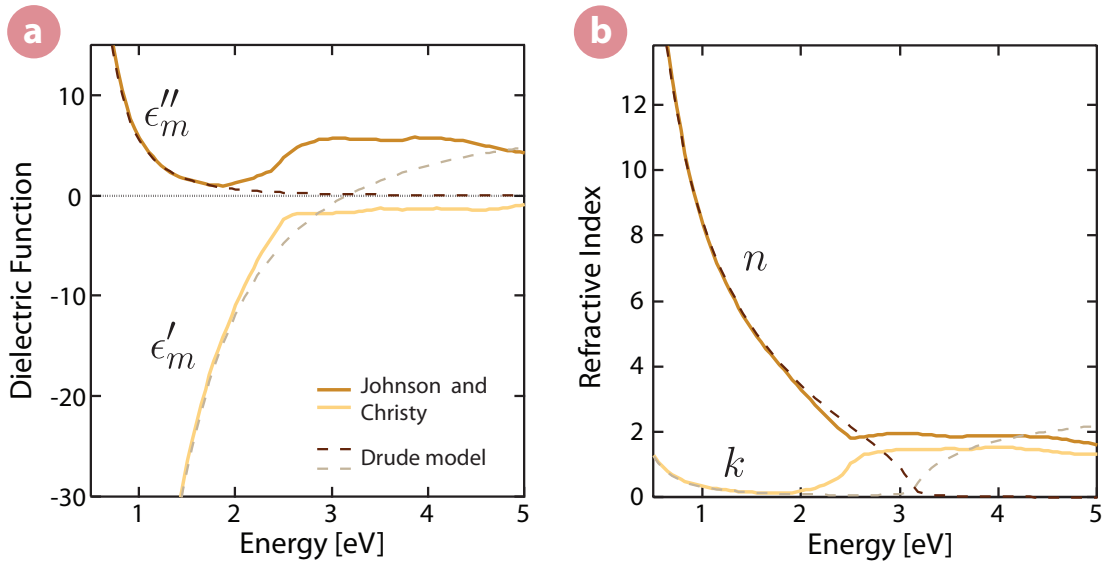

Figure 2.2.: **(a)** Real ϵ'_m and Imaginary ϵ''_m components of the complex dielectric function for gold. **(b)** Real n and imaginary k components of the complex refractive index for gold. Solid lines show experimentally derived data (Johnson and Christy [20]) and dashed lines indicate a best-fit Drude model plotted using Eq. 2.12 with $\epsilon_\infty = 8\,\text{eV}$, $\omega_p = 8.9\,\text{eV}$ and $\gamma = 0.07\,\text{eV}$

.

visible frequencies and can be adapted to better reproduce experimentally observed data.

In the next section, we show the properties of a metal's dielectric function which are necessary to create SPPs at a metal-air interface.

2.1.4. Bound surface modes

To uncover the properties of SPPs, we solve Maxwell's equations (Eq. 2.1) at the boundary between two materials. We will see later that for SPPs to exist one of these materials must be dielectric (ϵ_d) and the other metallic (ϵ_m). Using Eq. 2.1c and Eq. 2.1d and restricting the problem to one-dimension with a wave propagating in the x-direction and the interface normal in the z-direction we arrive at the solutions for an SPP at an interface. For TE (s-polarized) light no modes exist (since there is no component of electric field out-of-plane or in the direction of

propagation) but for TM (p-polarized) light the solutions are:

$$\mathbf{H}(\mathbf{x})|_{z>0} = (\ 0,\quad A,\quad 0\ )e^{(ik_x x - k_z^d z)} \tag{2.13a}$$

$$\mathbf{E}(\mathbf{x})|_{z>0} = -A\frac{c}{i\omega\epsilon_d}(\ k_z^d,\quad 0,\quad ik_x)e^{(ik_x x - k_z^d z)} \tag{2.13b}$$

$$\mathbf{H}(\mathbf{x})|_{z<0} = (\ 0,\quad B,\quad 0\ )e^{(ik_x x + k_z^m z)} \tag{2.13c}$$

$$\mathbf{E}(\mathbf{x})|_{z<0} = -B\frac{c}{i\omega\epsilon_m}(-k_z^m,\ 0,\quad ik_x)e^{(ik_x x + k_z^m z)}. \tag{2.13d}$$

These solutions describe propagating waves travelling in the x-direction with in-plane momentum[1] proportional to k_x and bound to the interface (Fig. 2.3), where the common time-dependent $[e^{-i\omega t}]$ has been left out and A and B are constants. k_z^m represents momentum normal to the surface into the metal and k_z^d momentum normal to the surface and into the dielectric. The solutions decay exponentially away from the interface in the $\pm z$-directions indicating their bound evanescent nature. We define the evanescent decay length into the dielectric and the metal as,

$$\delta_z^{m,d} = \frac{1}{|k_z^{m,d}|}. \tag{2.14}$$

EM boundary conditions dictate that D_z and E_x must be continuous across the interface. Applying these conditions in conjunction with the continuity of their derivatives (Helmholtz conditions) at $z = 0$, we find the constants A and B in Eq. 2.13 are equal to each other and that,

$$\frac{k_z^d}{k_z^m} = -\frac{\epsilon_d}{\epsilon_m}. \tag{2.15}$$

For k_z^d and k_z^m to describe a propagating wave bound to the interface, they must be real and positive. Given that the dielectric material has $\mathrm{Re}\{\epsilon_d\} > 0$, Eq. 2.15 is satisfied only for $\mathrm{Re}\{\epsilon_m\} < 0$, indicating these solutions exist at the interface

[1] Momentum p is proportional to wavevector k via $p = \hbar k$, although throughout this thesis, k is frequently referred to as momentum

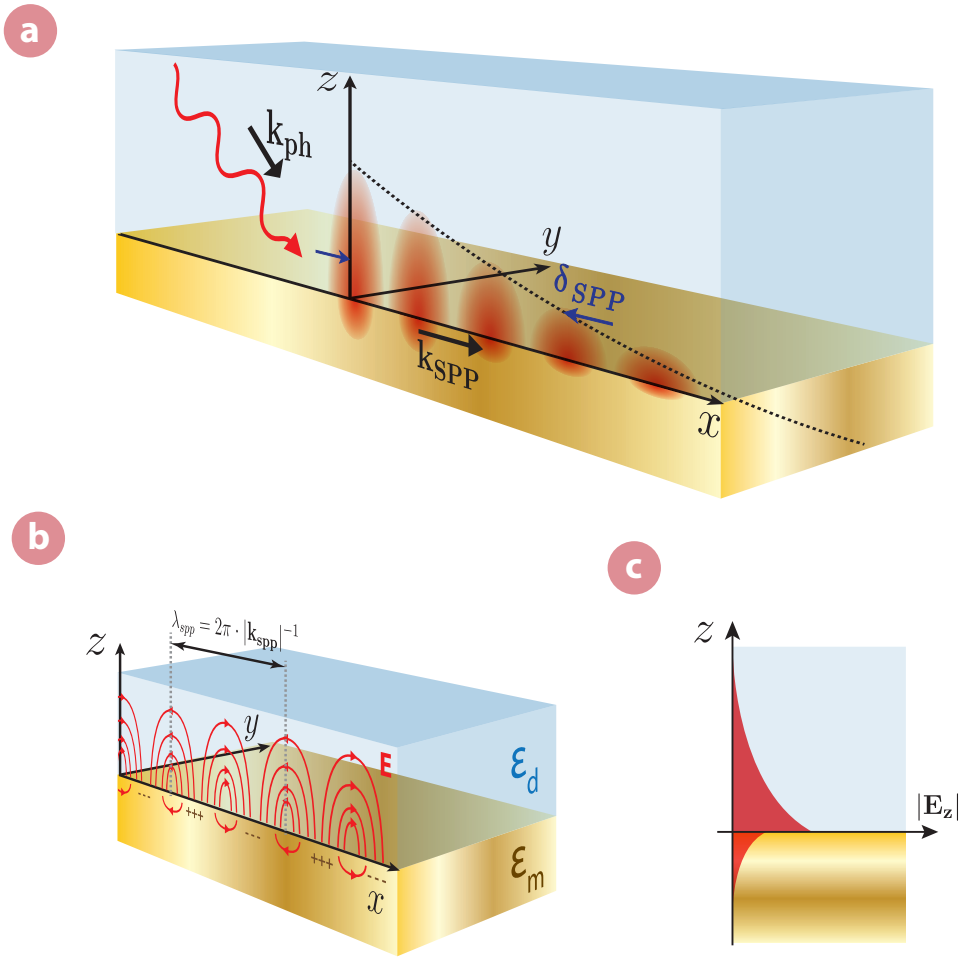

Figure 2.3.: **(a)** Excitation of propagating SPP in the x-direction on a metal surface with a TM polarized EM wave with wavevector $\mathbf{k_0}$. The plasmon's electric field strength decays as it propagates over a characteristic length scale δ_{SPP}. **(b)** Electric field character of surface plasmon indicating charge distribution in the metal surface and relation to surface plasmon wavelength λ_{SPP} **(c)** Electric field strength perpendicular to the interface showing evanescent binding of the surface plasmon to the interface.

between a dielectric and a metal for frequencies below the plasma frequency ω_p. In an actual metal, interband transitions cause the real part of the dielectric function to stay negative even past the plasmon frequency, however the modes still cannot exist here as the light is absorbed by the transitions.

Solving the wave equations (remembering the Helmholtz wave equation $\nabla^2\mathbf{E} + k_0^2\epsilon_r\mathbf{E} = 0$) and using Eq. 2.13b and Eq. 2.13d leads us to the following identities:

$$(k_z^{d,m})^2 = k_x^2 - \left[\frac{\omega}{c}\right]^2 \epsilon_{d,m}. \tag{2.16}$$

These can be combined with Eq. 2.15 to give the SPP dispersion relation:

$$k_{spp} = k_x = \frac{\omega}{c}\sqrt{\frac{\epsilon_d\epsilon_m}{\epsilon_d + \epsilon_m}}. \tag{2.17}$$

Plotting this dispersion relation (Fig. 2.4a) provides insight into the nature of the SPP mode. The SPP momentum is always greater than light in free-space. At lower energies the SPP momentum approaches that of free-light and the mode is more light-like, whilst at higher energies (but below the plasmon energy) it becomes quasi-static and behaves like a localized plasmon oscillation at the surface.

2.1.5. Exciting surface plasmons

For a given energy, SPPs always have a larger momentum than light in free-space (Fig. 2.4). Photons, therefore, need to gain extra momentum before they can excite SPPs. There are three principle ways this can be achieved: prism coupling; grating coupling or scatter coupling. Many existing SPR sensing approaches rely on prism coupling in either the Kretschmann and Raether or Otto configurations. These allow an increase of momentum parallel to the surface as shown in Fig. 2.5. Here the higher refractive index of the glass effectively slows light down and increases the momentum parallel to the surface,

$$k_{SPP} = k_{\shortparallel} = \frac{\omega}{c}\sqrt{\epsilon_{prism}}\,\sin\theta. \tag{2.18}$$

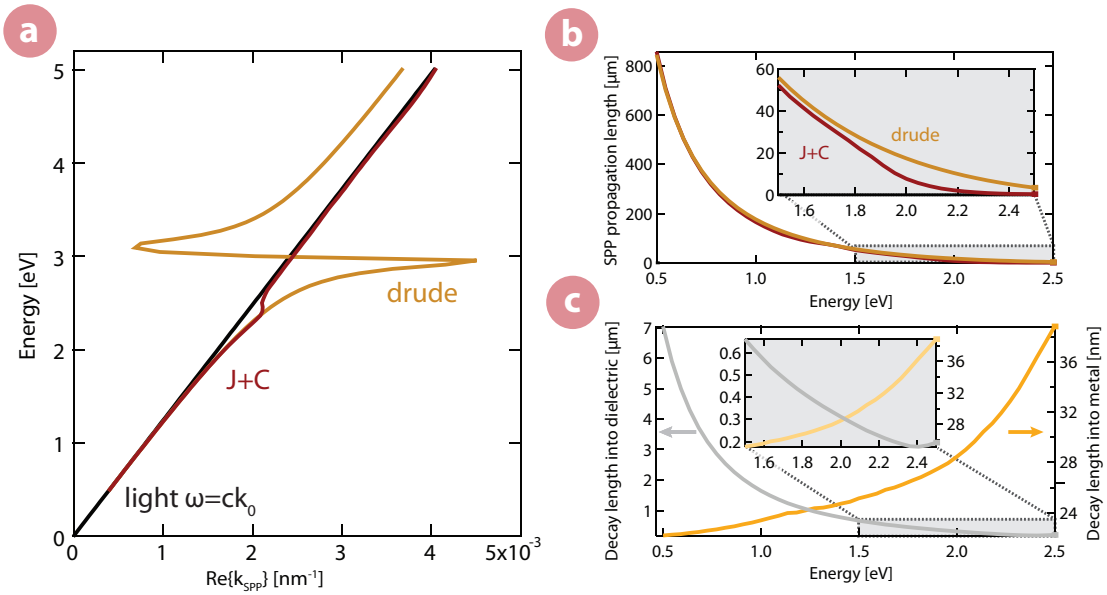

Figure 2.4.: Nature of an SPP at a gold-air interface. **(a)** Dispersion relation for SPPs with energy against real part of their wavevector, calculated using the dielectric function for gold based on a damped Drude model (Drude) and experimentally derived data from Johnson and Christy [20] (J+C). Also shown is the dispersion for light in a vacuum (black line). **(b)** Propagation length δ_{SPP} of an SPP as a function of incident photon energy. **(c)** Decay length of the SPP normal to the interface into the gold and air.

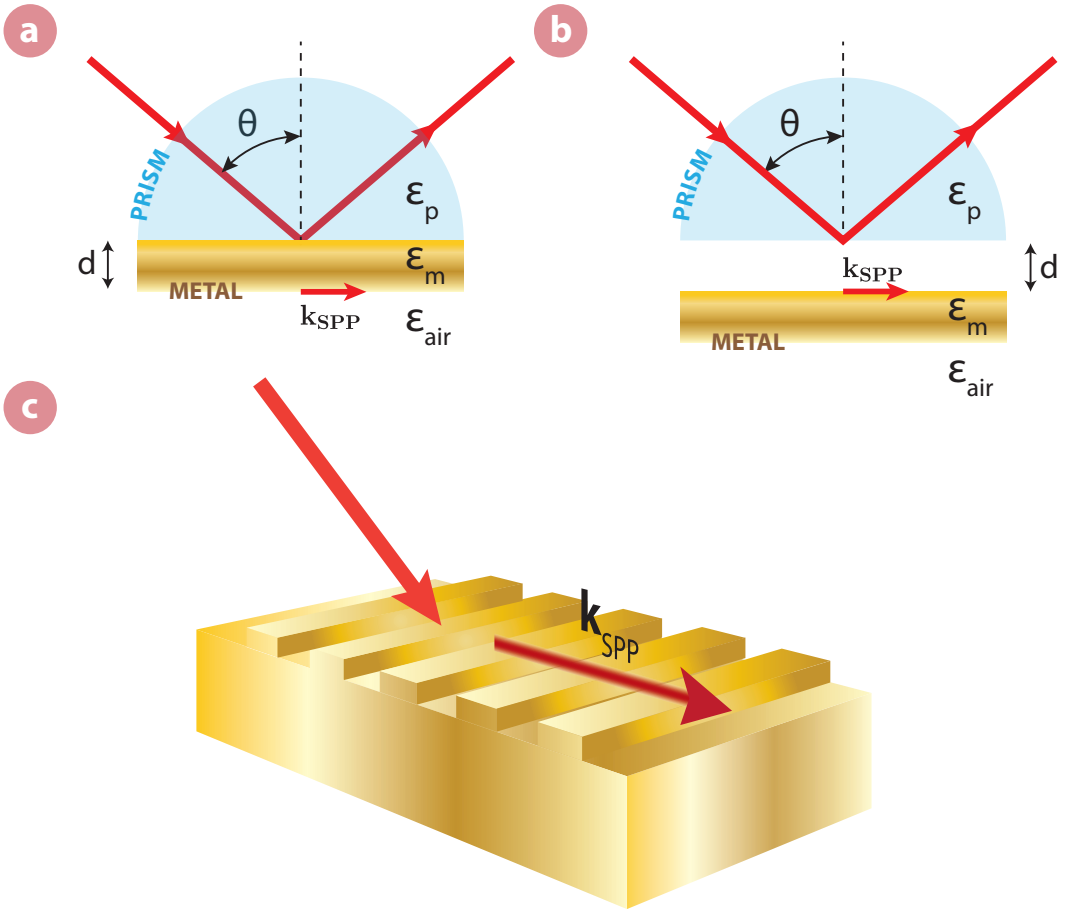

Figure 2.5.: Three coupling mechanisms for optically exciting SPP. Prism coupling using attenuated total internal reflection **(a)** Kretschmann and Raether, where a thin metal film is deposited onto a prism. **(b)** Otto configuration, where the prism is separated from the metal surface by a small distance. In both these configurations, the light is totally internally reflected by the prism creating an evanescent wave normal to the reflection surface of the prism. This allows coupling to the SPPs. **(c)** Grating coupling, where the increase in momentum is provided by scattering from the grooves dependent on the pitch Δ: $k = k_0 \pm \frac{2\pi}{\Delta}$

As well as prism coupling, extra momentum can be provided in other ways such as through a diffraction grating (Fig. 2.5) or even scattering off rough surfaces. [15]

2.1.6. Localized plasmons

The SPPs described above are known as propagating SPPs. In certain geometries, it is possible to excite spatially localized SPPs.

If we break up a metal surface so that it is no longer a continuous block it is possible to change the way it interacts with light. As the metal pieces decrease in size, becoming smaller than the wavelength of light, light interacts not only with the surface but with the whole structure (Fig. 2.6). The charge in the structure oscillates in one or more modes determined by its geometry and size. The charge is confined to the object and therefore the excited plasmons modes are spatially localized. [21]

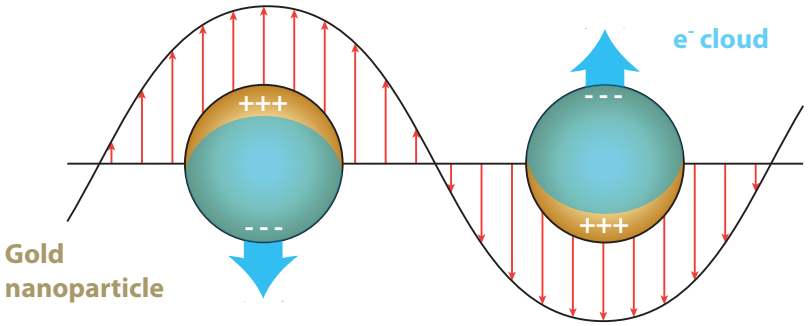

Figure 2.6.: Localized plasmon resonance induced in gold nanoparticle at resonant frequency with an incoming EM wave.

The effect is dramatic. A flat sheet of gold reflects and looks like the metallic mirror we would expect. If the mirror is taken and smashed, it forms many pieces each looking like smaller metallic mirrors. If, however, we grind the shards into sufficiently small pieces, they will lose their golden colour and form other colours. This technique was known in medieval times, where ground gold was used to form the bright red colour in stained glass windows.

In spherically symmetric structures, these resonances can be solved analytically using a solution to Maxwell's equations called Mie theory.

Since the resonances are localized, they usefully provide areas of high electric field intensity that remain in one place. This allows efficient coupling of energy into a nearby system, such as a molecule, which is the basis of SERS.

Another type of localized plasmon resonance can occur on larger structured surfaces. These are analogous to standing wave modes, such as those on a guitar string. Here a surface plasmon becomes trapped reflecting off the edges of surface features. By designing appropriately shaped dishes or pits, localized plasmons modes of different frequencies can be trapped to a metal surface.

By structuring surfaces on the nanoscale it is possible to create an environment supporting a variety of plasmonic resonances, both localized and propagating. By careful design, the surface can be tuned to give plasmon resonances at different frequencies and positions within the structure. This will be discussed further in Chapter 4 with respect to the Klarite nanostructure used in this thesis.

2.2. Raman scattering

Raman scattering was discovered in 1928 by Chandrasekhara Venkata Raman and Kariamanickam Srinivasa Krishnan [22] for which Raman received the Nobel Prize for Physics in 1930. Raman searched for an equivalent of x-ray Compton scattering in visible light. He believed there should exist two types of scattering: that from the normal interaction of light with atoms and molecules; and another from the interaction of light with their 'fluctuations from the normal state'. By tightly focusing a beam of sunlight onto various liquids and using a pair of filters, he was able to observe this predicted second type of scattering at different frequencies from the incident light. Due to the extreme relative weakness of the secondary scattered light and its polarized nature he was able to rule out fluorescence and so had discovered what is now known as Raman scattered light.

Raman scattering provides a tool to explore the lower energy excited states of molecules and atomic lattices; the atomic motional displacements: vibrational, rotational and translational excitations. Their energy is usually much less (meV) than the electronic excited states (eV) and can be thought of (to first order) as a perturbation to the electronic state.

2.2.1. Light-molecule interaction

Light can interact with a molecule in various ways. These can be thought of as direct (absorption) and indirect (scattering) events. Light (generally ultra-violet/visible) can be directly absorbed by a molecule via promotion of an electron into a higher electronic energy level. Alternatively, lower energy (infra-red) light can excite vibrational states within an electronic level. After a molecule has absorbed a photon it is in a more unstable state and there are various decay channels it can use to return to its original state. These channels can be a combination of non-radiative or radiative

decays. The relaxation time depends on the lifetime of the various states, which depend on the decay paths available for the excited molecule and the probability of taking particular paths. Absorption and subsequent emission of light is therefore a multi-step process.

Light is also *scattered* by molecules. Here the light is not absorbed by the molecule, but its direction and energy can be altered. Depending on the interaction with the molecule, light is either scattered elastically, where the energy remains the same, or inelastically, where the energy is altered. Elastic scattering is referred to as Rayleigh scattering and is the most common type of scattering. In inelastic scattering a photon interacting with a molecule gains or loses energy. The most common type of inelastic scattering in molecules is Raman scattering. The energy lost from the incoming photon is taken by the molecule promoting it to an excited vibrational state. This is called Stokes Raman scattering. When the incoming photon gains energy, a molecule already in an excited vibrational state relaxes down to a lower energy state. This is called anti-Stokes Raman scattering. The Raman and fluorescence processes are depicted in Fig. 2.7.

Analysis of the scattered light provides us with information about the vibrational states of molecules. The amount a molecule interacts with the light can be condensed into a scattering cross-section σ_{sca} corresponding to the effective area of interaction a molecule 'occupies' in relation to a scattering event. The smaller the cross-section the less likely a scattering event will occur. The cross-section relates the outgoing intensity of a scattering process to the incident light intensity density,

$$I_{sca} = \sigma_{scat} S_{in}. \tag{2.19}$$

The scattering cross-section can be split into multiple cross-sections corresponding to elastic and inelastic scattering contributions.

2.2.2. Raman scattering cross-section and selection rules

Like other scattering events Raman scattering has an associated scattering cross-section. In this case the cross-section depends on the vibrational mode excited or destroyed; $\sigma_R(\omega_{vib})$.

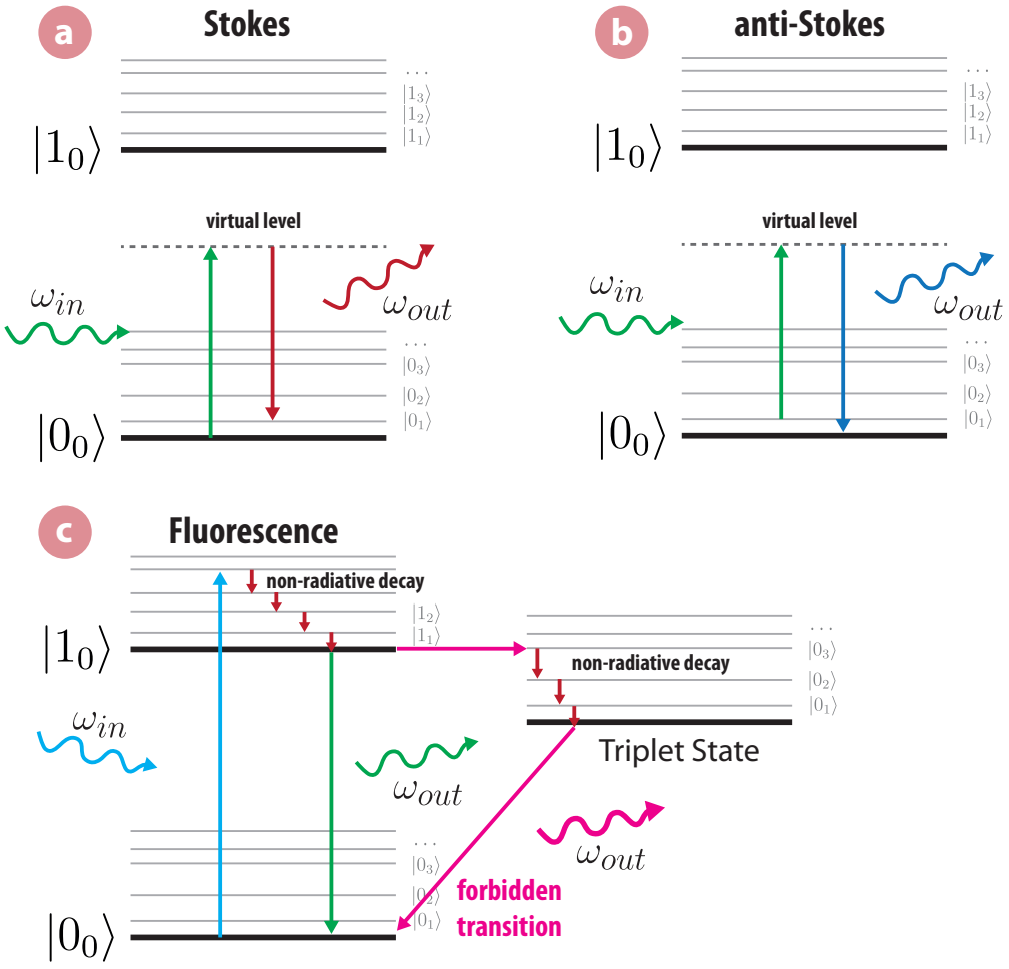

Figure 2.7.: Jablonski diagrams showing (a) Stokes Raman scattering, (b) Anti-Stokes Raman scattering and (c) Fluorescence in a molecule.

The selection rules for Raman scattering are determined by the ability of a vibrational mode to polarize the molecule. Specifically, a mode is Raman-active if the internal displacement of atoms caused by the vibration creates a change in the polarizability of the molecule.

In the presence of an oscillatory electric field,

$$\mathbf{E_i}(\omega_{in}) = \mathbf{E_0}\cos(\omega_{in}t), \tag{2.20}$$

such as that caused by light, a molecule becomes polarized inducing a dipole moment $\mathbf{p}$:

$$\mathbf{p}(\omega_{in}) = \hat{\alpha}\mathbf{E_i}(\omega_{in}). \tag{2.21}$$

Here we have introduced $\hat{\alpha}$, the linear optical polarizability of the molecule. The polarizability varies for different molecular orientations with respect to the incident field. Therefore $\hat{\alpha}$ is in general a second-rank tensor defining how easy it is to polarize the molecule along different directions relative to the polarization of the incoming field.

Molecular vibrational movements can be conveniently analysed by transforming the atomic positions into simplified normal co-ordinates. These co-ordinates correspond to the amplitude of molecular displacement along an orthonormal basis relative to a particular normal mode (k) of the molecule. The polarizability can then be re-cast with respect to these co-ordinates $\hat{\alpha}(Q_k)$.

Each normal mode oscillates at a particular frequency ω_k so that at any time,

$$Q_k = Q_{k0}cos(\omega_k t + \phi), \tag{2.22}$$

where ϕ represents an arbitrary phase factor.

The polarizability of a vibrating molecule can be expanded in terms of the normal co-ordinates using a Taylor expansion, which to first-order (valid for many molecules

[23]) gives:

$$\hat{\alpha} = \hat{\alpha_0} + \sum_k \left.\frac{\partial \hat{\alpha}}{\partial Q_k}\right|_0 Q_k, \tag{2.23}$$

where ∂Q is the displacement of the molecules due to the vibrational mode from their equilibrium position $Q_{k=0}$, Q_k is the molecular displacement and α_0 is the polarizability at equilibrium.

For a particular vibrational mode, we can write a polarizability tensor,

$$\hat{\alpha}_k = \hat{\alpha}_{0k} + \left.\frac{\partial \hat{\alpha}}{\partial Q_k}\right|_0 Q_k. \tag{2.24}$$

Combining Eq. 2.21 and Eq. 2.24 and adding in the time-dependence of the vibration Eq. 2.22 and the frequency dependence of the electric field Eq. 2.20 we get:

$$\mathbf{p}_k = \hat{\alpha}_0 \mathbf{E_0} cos(\omega_{in} t) + \frac{\partial \hat{\alpha}}{\partial Q_k} \frac{\mathbf{E_0} Q_{k0}}{2} [cos[(\omega_{in} + \omega_k)t + \phi] + cos[(\omega_{in} - \omega_k)t + \phi]]. \tag{2.25}$$

Equation 2.25 shows the appearance of the Stokes ($\omega_{in} - \omega_k$) and anti-Stokes ($\omega_{in} + \omega_k$) shifted frequency components of the dipole, as well as the Rayleigh contribution. From this equation we can define a new tensor called the Raman polarizability, [24]

$$\hat{\alpha}_k^R = \frac{\partial \hat{\alpha}}{\partial Q_k} \frac{Q_{k0}}{2}. \tag{2.26}$$

For a particular vibrational mode to be Raman active it therefore must have a non-zero Raman polarizability, i.e. $\hat{\alpha}_k^R \neq 0$.

We can visualise the polarizability of a molecule by plotting $1/\sqrt{\hat{\alpha}}$ in all directions. (This is by convention since $1/\sqrt{(\hat{\alpha})}$ is proportional to the electric field needed to polarize the molecule. [18]) The resulting picture is called a polarizability ellipsoid and by plotting the ellipsoid at the extremes of a particular vibrational mode we can

determine whether a vibrational mode is Raman active or not. If the polarizability ellipsoid changes size, shape or orientation then the mode is Raman active but only if the derivative of the polarizability as it passes through the equilibrium position is non-zero. Fig. 2.8 shows the vibrational modes of CO_2 with their polarizability ellipsoids.

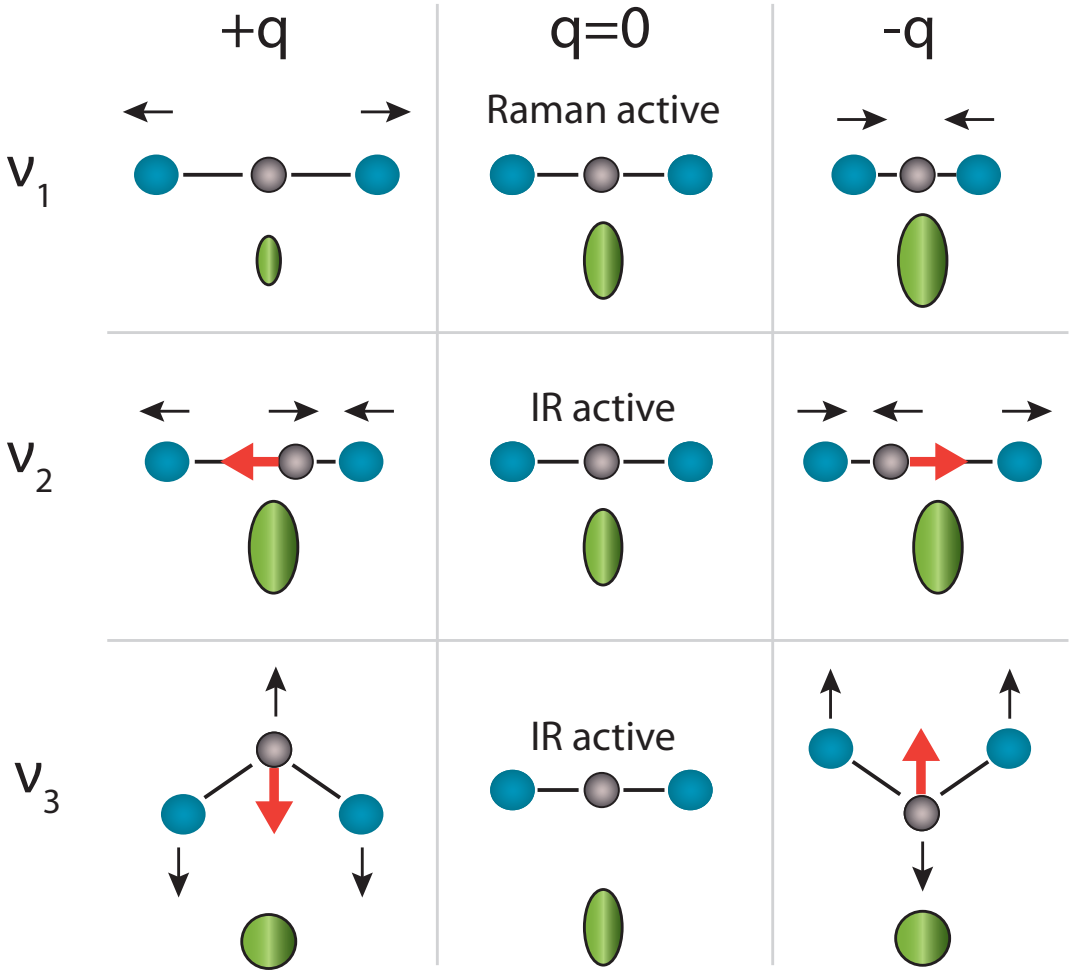

Figure 2.8.: Normal vibrational modes of CO_2 as a function of atomic displacement, pictured at equilibrium ($q = 0$) and both extremes ($\pm q$) of vibration, where q is the atomic displacement. Atomic movement indicated with black arrows. Polarizability ellipsoids are pictured underneath in green. ν_1 is the only Raman active mode as the polarizability ellipsoid changes with atomic displacement and changes non-symmetrically about the equilibrium. Also pictured is the dipole moment of the molecule (orange arrow) which must change for a molecular vibration to be IR active, hence ν_2 and ν_3 are IR active. ν_3 is doubly degenerate as it also has an out-of-plane equivalent vibration to the in-plane one shown.

2.2.3. Anti-Stokes and Stokes

We have used a classical picture to derive the key principles of Raman scattering. This is valid for most cases and certainly in the understanding that we will use in this thesis. However, there is a key problem with this description when predicting the relative intensities of Stokes and anti-Stokes modes. From Eq. 2.25 it would appear that these are equal in amplitude. Experimentally, this is not the case and the anti-Stokes scattering is generally much lower in magnitude than the Stokes scattering.

We can explain this discrepancy by considering the occupation of vibrational levels in a molecule, which follow the Boltzmann thermal distribution function,

$$F_{Boltzmann}(\omega_{vib}, T) \propto \exp\left[\frac{-\hbar\omega_{vib}}{k_b T}\right], \tag{2.27}$$

where k_bT is the thermal energy of the system and $\hbar\omega_{vib}$ is the energy corresponding to the vibrational frequency ω_{vib}.

In practice, most molecules are in the ground-state at room temperature, with an exponentially decaying probability of being in higher vibrational states. Since anti-Stokes scattering relies on a molecule initially existing in an excited state, it is much less probable than Stokes scattering, where the molecule is initially in the ground state. As Stokes Raman is much stronger than anti-Stokes in most cases, Stokes Raman is more frequently used to characterise molecules.

Heating the molecule, however, increases the population of higher vibrational states and thus increases the magnitude of the anti-Stokes scattering. Comparing the magnitude of Stokes to anti-Stokes can therefore provide information on the local temperature of the system. Cooling the molecule to very low temperatures can all but remove anti-Stokes scattering.

2.2.4. Extensions to Raman scattering

A specific case of Raman scattering which can result in far larger scattering cross-sections is called resonance Raman scattering. Here the incident radiation excites the molecule to a virtual level coinciding with an electronic transition in the molecule,

resonantly enhancing the Raman process and leading to much stronger Raman signals.

There are an array of alternative Raman techniques such as coherent anti-Stokes Raman scattering (CARS) and stimulated Raman scattering (SRS) which rely on pumping on resonance with a transitions to stimulate the process.

There are also hyper-Raman processes which rely on higher order changes to the polarizability (above we only considered first order). These processes are non-linear and rely on high laser intensities to become significant.

2.3. Surface-enhanced Raman scattering

The key problem with Raman scattering is its relatively weak scattering cross-section compared to fluorescence, resulting in a low probability of an incident photon being Raman scattered. For typical SERS molecules the Raman scattering cross-section is $10^{-29}\,\mathrm{cm}^2\,\mathrm{molecule}^{-1}$, far weaker than typical fluorescence cross-sections of $10^{-16}\,\mathrm{cm}^2\,\mathrm{molecule}^{-1}$. [25] In 1974, Fleischmann et al. [26] reported anomalously large Raman scattering from a monolayer of pyridine on the surface of a roughened silver electrode. It was not until 1977 that Albrecht and Creighton, [27] and Jeanmaire and Van Duyne [28] independently discovered the significance of the data presented by Fleischmann. They saw an enhancement in the Raman signal $\sim 10^5$ far greater than could be explained by an increase in the surface area due to electrochemical roughening. This breakthrough was of significant interest to the scientific community and spawned a great deal of research which continues to this day.

The enhancement found on SERS substrates is primarily electromagnetic in origin. Light is coupled into localized surface plasmon modes which provide an enhanced local field $|\mathbf{E_{loc}}(\omega_0)|$ many times larger in magnitude compared to the incident field $|\mathbf{E_{inc}}|$. The field therefore induces a Raman dipole in the molecule which is enhanced by a factor $|\mathbf{E_{loc}}(\omega_\mathbf{0})|/|\mathbf{E_{inc}}|$ (Fig. 2.9). Since the intensity of light emitted by a dipole is proportional to the square of the dipole, the radiation is enhanced by a factor,

$$g_{in} = \frac{|\mathbf{E_{loc}}(\omega_\mathbf{0})|^2}{|\mathbf{E_{inc}}|^2}, \tag{2.28}$$

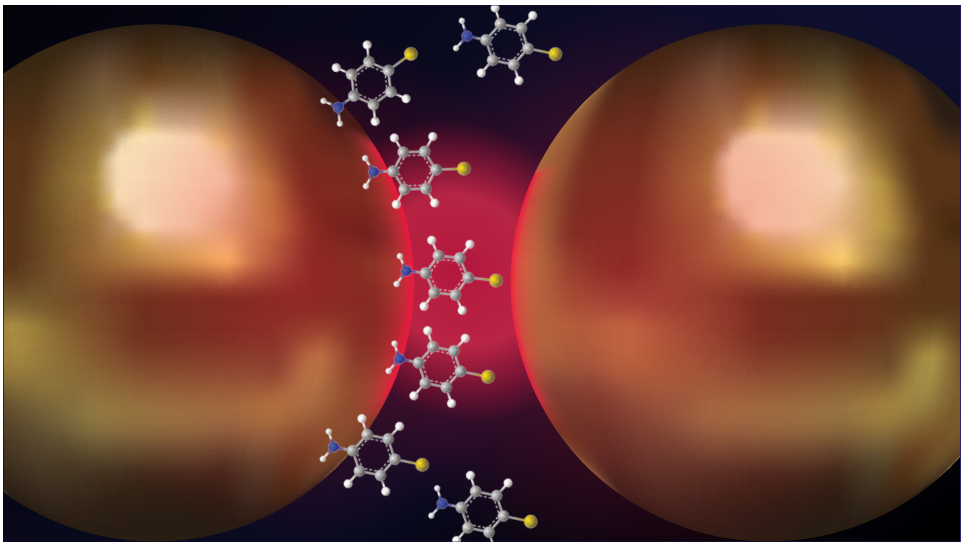

Figure 2.9.: The electric field between two metal nanoparticles can be massively enhanced due to the formation of localized plasmon resonances in the nanometer sized-gap. Placing molecules in this localized field can cause massive enhancement to their Raman scattered light, leading to SERS.

due to this local field enhancement. As well as enhancing light-coupling into the molecular Raman dipole, there is a further enhancement g_{out} as the local field environment and geometry affects how the dipole can radiate. This effect can be thought of as enhancing the radiated light. The exact mechanism behind this outward coupling enhancement is quite involved. Intuitively, since it is based on the same physical origin (local EM field enhancement) one would not be surprised by a similar dependence to the inward coupling enhancement. Indeed in most cases $g_{out} \approx g_{in}$ and further treatment of this subject is not necessary in the context of this thesis. Combining these two enhancement factors, results in an important formula relating the total SERS enhancement factor G to the local electric field:

$$G = g_{in}g_{out} = \frac{|\mathbf{E_{loc}}(\omega_\mathbf{0})|^2}{|\mathbf{E_{inc}}|^2}\frac{|\mathbf{E_{loc}}(\omega_\pm)|^2}{|\mathbf{E_{inc}}|^2}. \tag{2.29}$$

As has been emphasised in the above equation, it is important to remember that the incoming and outgoing radiation are of different frequencies $\omega_\pm = \omega_0 \pm \omega_{vib}$, and so have different enhancement factors. In practice, for small Raman shifts this difference is negligible and the above formula is simplified:

$$G = \frac{|\mathbf{E_{loc}}(\omega_\mathbf{0})|^4}{|\mathbf{E_{inc}}|^4}. \tag{2.30}$$

This gives us the famous E^4 SERS enhancement approximation and explains why even seemingly modest EM field localisation can lead to huge Raman signal enhancements. The approximation is also powerful in relating the enhancement found in plasmonic nanostructures to their modelled electric field behaviour. However, over-reliance on this approximation can hamper precise understanding of the enhancement mechanism in specific cases, and should be treated as a rough guide to attainable enhancements.

2.3.1. Chemical enhancement

The electromagnetic (EM) enhancement, with its E^4 dependence, does not explain the whole picture of SERS enhancement. There are further enhancements which have been grouped under the umbrella term 'chemical (CM) enhancement'.[2] This

[2]In the literature, the chemical enhancement is variously referred to as CE or CM

term refers to any enhancement caused by the adsorbate's chemical interaction with the substrate and the surrounding environment. In general, studies find a limit of CM enhancement of about 10^2 but in some cases this limit is understated and the value can be significantly higher. [29] It is therefore important to take this effect into account when interpreting experimental results in a new or unknown substrate-adsorbate system.

The CM enhancement can be divided into its principle causes: adsorbate-substrate chemical bonding, resonance surface complex formation and photon-induced charge transfer (CT), with the latter being of most importance. [30] To a good approximation [31] the CT enhancement is highly vibrational level dependent, whilst the EM enhancement is not. The two enhancements are multiplicatively linked [31],

$$G_{total}(vibration) = G_{EM} \cdot G_{CT}(vibration). \tag{2.31}$$

For a molecule attached to a metal surface charge transfer can occur, with either an electron passing from the highest-occupied molecular orbital (HOMO) level in the molecule to the Fermi level in the metal, or an electron in the metal transferring to the molecule (see Fig. 2.10). [31, 32, 33, 34] This effectively alters the electronic distribution of states in the molecule and can shift the system from a pure SERS case to a resonant SERS case, where the coupled metal molecule system allows an electronic excitation within the molecule as explained in Fig. 2.10. The Raman process is then enhanced in a similar way to standard resonance Raman, where here the electronic transition is brought into a metal-mediated resonance with the incident photon.

A model by Lombardi et al. [35, 36] explains CT between the metal and molecule as an extension to the quantum mechanical picture of SERS. The molecular states become coupled to those in the metal through Herzberg-Teller vibronic coupling with two possible cases identified: CT involving charge transfer from metal-to-molecule and vice versa. A new resonant SERS transition pathway is created which borrows intensity from an allowed electronic transition within the molecule.

As well as CT effects, the bonding interaction between the metal and the molecule can lead to changes in the occupation of lone electron pairs and an altering of the electron cloud surrounding the molecule. This leads to different Raman mode

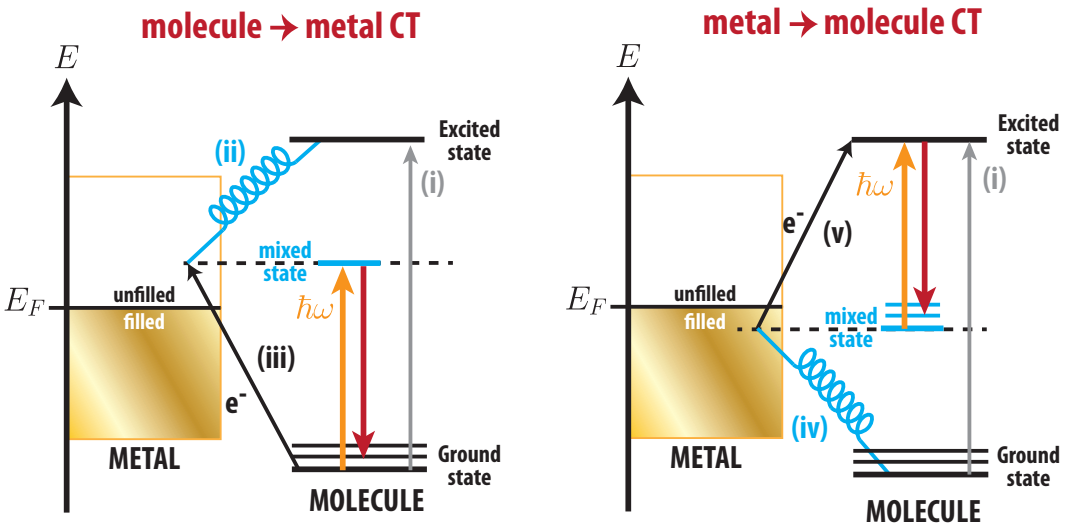

Figure 2.10.: Charge transfer based on Herzberg-Teller vibronic coupling of metal and molecule states. [35] **(a)** molecule-to-metal CT and **(b)** metal-to-molecule CT. In molecule-to-metal, unoccupied states in the metal are coupled to the unoccupied states in the molecule via vibronic coupling (ii). A CT transition, with an electron excited from the molecule to the metal (iii) is then possible with intensity borrowed from an allowed transition in the molecule (i). From a Raman point-of-view, we can imagine the vibronic coupling creates a new mixed state to which the incident Raman photon can resonantly interact with. A previously non-resonant Raman process thus can become resonant. In the metal-to-molecule case, the filled metal states and occupied molecular ground states couple together vibronically (iv). A resonant Raman transition can then occur, with an electron promoted from the metal to the excited molecule state (v), again borrowing intensity from the allowed molecular transition (i).

intensity distributions compared to normal Raman as certain modes are suppressed and others enhanced. The bonding can also affect the vibrational positions of the modes which are dependent on the local environment and chemical structure.

The chemical effects effectively alter the polarizability tensor of the adsorbed molecule due to its proximity and bonding to the interface.

Although neither strictly CE or EM related, the polarizability tensor is orientation dependent. In liquid Raman this orientation effect is averaged out. However, in SERS where aligned monolayers and even single molecules are important, such averaging is not possible. The molecular orientation (relative to the electric field) can strongly vary the radiated intensity distribution of the Raman mode and can even seem to activate or deactivate certain Raman modes. Depending on orientation the vibrational frequency of the modes may also be altered as they interact with their environment.

The chemical enhancement varies strongly from system-to-system and should not be forgotten when considering particular systems such as those in Chapter 8.

2.4. Conclusion

We have introduced the basic theory necessary to understand the origin of plasmonics and Raman scattering and how combining the two can lead to large enhancements with a principal $\mathbf{E^4}$ dependence. We have taken a quasi-classical approach throughout this chapter which remains valid in most situations and provides the best intuition to the processes involved. There are many subtleties to Raman scattering and SERS in particular, a detailed overview of which has been published by Le Ru and Etchegoin. [24] SERS remains a very active area of research, with much still to be understood.

3. Experimental methods

A range of techniques have been used to fabricate, prepare and characterise the samples used in this thesis. Many of the techniques such as atomic-force microscopy (AFM) and scanning-electron microscopy (SEM) are now standard tools when working in domains with dimensions smaller than the wavelength of light. In addition to Raman scattering measurements, optical characterisation and computational modelling were initially used to define the plasmonic response of the surfaces. Here we introduce the optical spectroscopic techniques used and developed in this thesis and some of the tools established for data analysis and computational modelling.

3.1. Optical spectroscopy

Spectroscopy allows us to discover properties of a material by shining light at it and looking at what comes out. Careful analysis of the light that is absorbed, scattered or reflected allows us to probe the finer structure of the material, not merely the shape and overall colour we can see with our eyes. In doing so we can deduce certain properties of the material smaller than we can see without even touching it.

A suitable analogy might be as follows:

> On receiving a gift-wrapped present, there is generally an insatiable desire to discover what is inside the box without unwrapping the gift. This inevitably results in the box being shaken (sometimes at the detriment of the gift inside!). This shaking inputs energy into the gift (via vibrations) and then our ears are used to listen to the sounds produced. From this we learn a little more about what is in the box, with surprising accuracy! This is a primitive form of spectroscopy.

Here we use a white light source with a continuous broadband spectrum to probe our plasmonic nanostructures. The reflected, transmitted or scattered light is collected

and fed to a spectrometer which allows us to visualise the light as a distribution of energies with different intensities; a spectrum.

3.1.1. Angle-resolved spectroscopy: the goniometer

The angle at which light hits a surface changes how it interacts with that surface. As well as energy, light carries momentum and by adjusting the angle we change the component of the light's momentum parallel and perpendicular to the surface. This changes the light's interaction with features on the surface. Measuring the reflected light as a function of energy (inversely proportional to wavelength) and angle (related to the momentum in a certain direction) allows us to extract a dispersion diagram for light interacting with the surface, representing the relationship between energy and momentum. Analysing these dispersion plots allows us to track different optical modes excited on our structure and determine their nature. We perform this angle-resolved spectroscopy in a custom built goniometer as seen in Fig. 3.1.

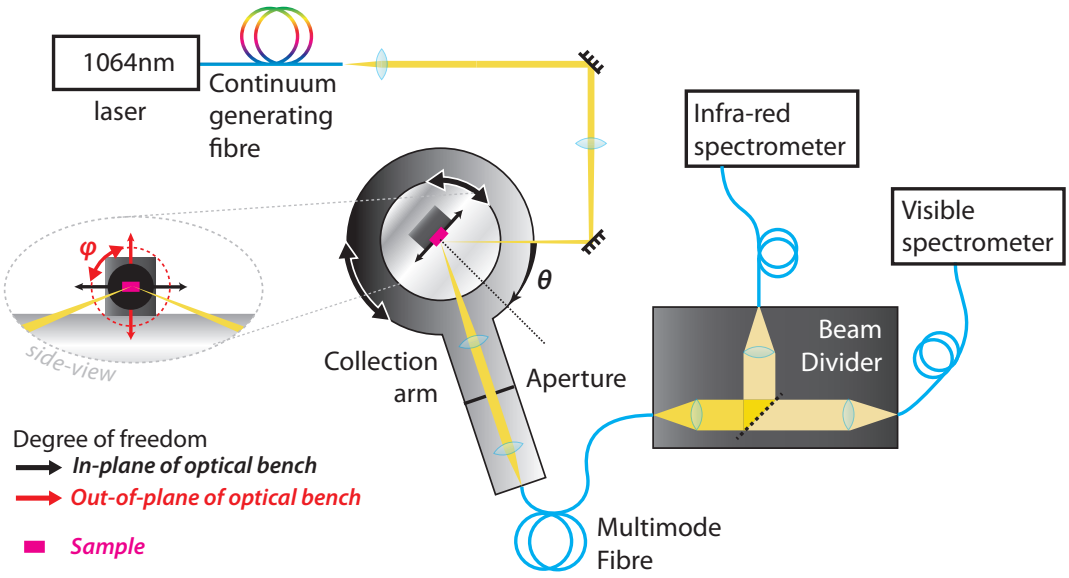

Figure 3.1.: Goniometer allows automatic angularly-resolved reflectivity measurements to be recorded over a large wavelength range for multiple sample points and incident angles.

Using a goniometer originally developed by previous group members but upgraded here to improve signal quality and reliability (Fig. 3.1), we track reflected light from our structured surfaces. The light source is a passively mode-locked,

pulsed $\lambda = 1064\,\text{nm}$, microchip laser (JDS Uniphase) focused into a holey photonic crystal fibre (Blaze Photonics). Through accumulative non-linear effects over the length of the fibre, a broadband continuous spectrum from 480-1500 nm of high intensity is created out the other end of the fibre. This resulting intense white-light source can be attenuated as required via neutral density filters placed in the beam path. The light source is collimated and focused onto the sample through a 10 cm focal length lens giving an average power of 0.1 mW and a spot-size of $0.2\,\text{mm}^2$. The beam arrives slightly off normal incidence from the sample ($\approx 3\,^\circ$) due to the difficulty in illuminating and collecting from the same angle.

Two rotation stages (Sigma-Koki) rotate the sample relative to the incident light (θ) and a collection arm collects specularly reflected light (at 2θ). The collection arm collects, collimates and focuses the light into a 200 µm diameter broadband optical fibre positioned at the image plane. The diameter of the fibre determines the collection region on the sample. Since the optics on the collection arm demagnify the image $0.5\times$ onto the fibre end, the sampling region on the surface is twice the size of the fibre-diameter.

This fibre passes the collected light into a cage-mounted beam-splitter system. The light emerges from the fibre and is expanded and collimated to a diameter of 25 mm. A 50/50 polka-dot beamsplitter ensures wavelength independent broadband splitting of the beam with minimal diffractive effects. The light from the beamsplitter is then focused into two fibres (Ocean Optics) one leading to a visible spectrometer (Ocean Optics QE65000) and the other to a near-infra-red spectrometer (Ocean Optics NIRQuest 512).

A further rotation stage behind the sample allows the sample to be in the sample plane (ϕ) and two linear translation stages allow the sample to be moved vertically and horizontally to allow different areas of the sample to be probed. All these stages have been fully automated and are controlled via software written in Igor Pro (Wavemetrics Inc.), which also handles display and recording of the spectra. This allows an angular-spectral map, illuminating the sample's dispersion information, to be recorded for various positions on a sample without human intervention. Before an automated scan can start the system is aligned using further manual translation stages (not pictured in Fig. 3.1 for clarity) and a series of pinholes to ensure the focused beam is aligned with the centre of rotation of the stages. Before a sample is scanned, a reference scan is performed with a gold or silver mirror to which the

sample scan is normalised. Silver has broadly frequency-independent reflection in the visible range and gold allows us to compare our gold structured samples to a flat gold surface to observe any differences.

3.1.2. Micro-spectroscopy

Micro-spectroscopy allows us to combine standard optical spectroscopy with the spatial accuracy and control of a visible microscope. A reflection-based köhler-illuminated Olympus BX51 microscope is adapted (Fig. 3.2) to incorporate a multi-mode optical fibre to collect reflected light. This fibre is positioned in the image plane of the sample and therefore collects light from a specific position on the sample, which is illuminated using the microscope's broadband halogen light source. Compared to the goniometer, the microscope has a much better spatial resolution, allowing small areas of the sample, close to the Rayleigh resolution limit, to be analysed in detail. This comes, however, at the loss of angular-resolution. The range of angles illuminated is determined by the numerical aperture (NA) of the objective and the microscope's aperture stop. In general, the objective illuminates a large range of angles centred around 0° incidence and so the reflectivity spectra are optically integrated over this angular range. This results in a loss of the dispersion information.

This technique is useful since it is far quicker than goniometer measurements and provides information about the spatial uniformity of the sample. Since the localised plasmon modes are not angularly-dependent, this is a reasonable method for interrogating them.

3.2. Raman spectroscopy

The main technique used in this thesis is Raman spectroscopy with the key elements of this technique illustrated in Fig. 3.3. A monochromatic laser illuminates the sample normal to the surface, creating Raman and Rayleigh scattered light. The scattered light is collected and passes through a filter to remove the Rayleigh scattered and non-scattered incident laser light. The filtered light is spectrally dispersed in a spectrometer and a Raman scattering spectrum recorded. A Raman spectrum is usually presented with respect to a shift in energy away from the incident laser's

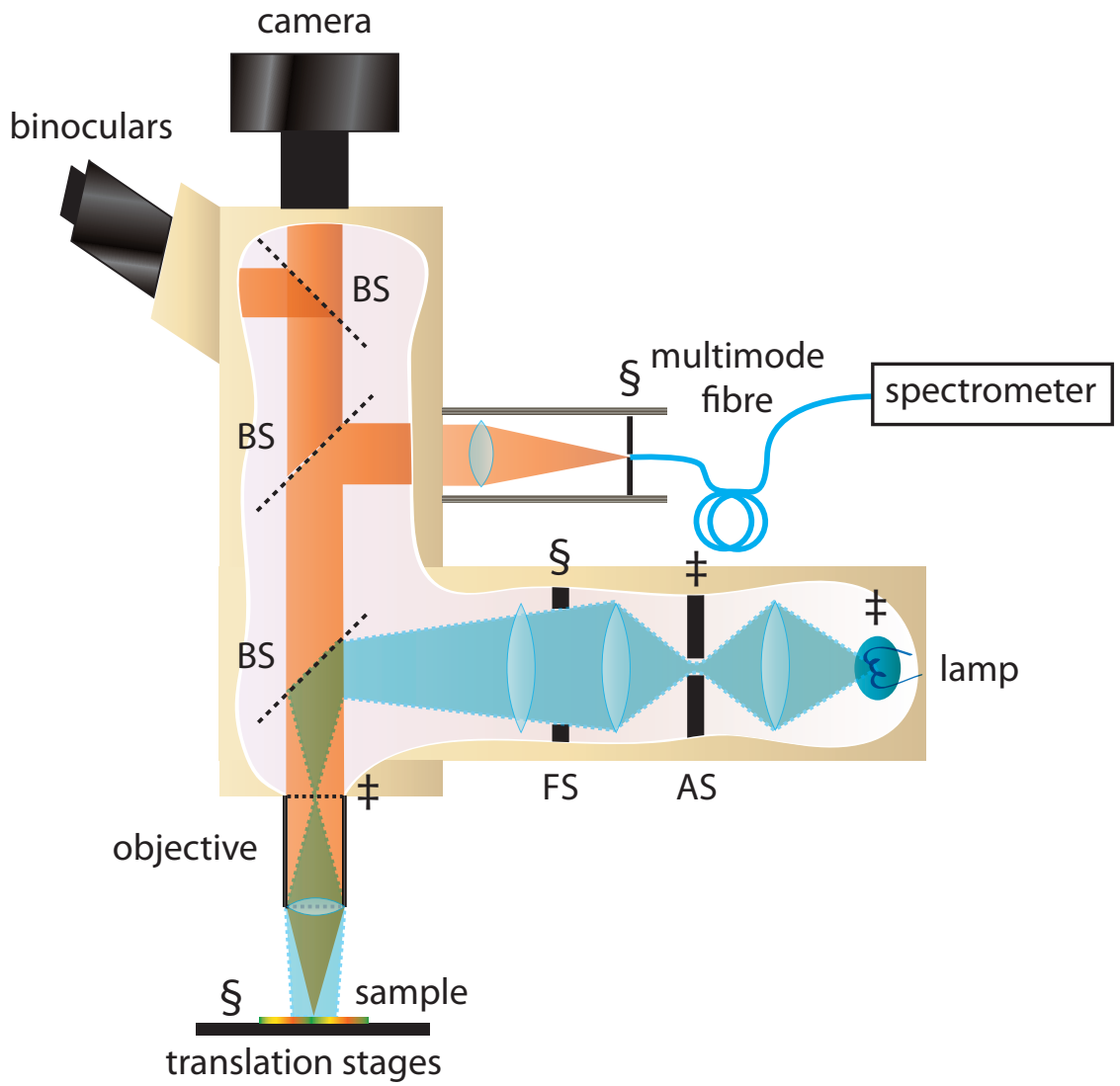

Figure 3.2.: BX51 microscope showing illumination and collection paths as per Köhler-illumination ensuring lamp and sample image planes are at opposite foci. § indicates the sample's real conjugate image planes and ‡ indicates the lamp's real conjugate image planes. The optical-fibre is placed in the sample's image plane and translating it in this plane corresponds to collection of light from different positions on the sample. The aperture stop (AS) can be closed to limit the range of angles incident on the sample, and the focal stop (FS) can be closed to restrict the area of the sample illuminated.

energy. Raman shifts are usually presented in units of the spectroscopic wavenumber (cm^{-1}), where the spectroscopic wavenumber is defined as $\nu = \lambda^{-1}$. These shifts, therefore, are proportional to the energy of the vibrational levels in the system as shown in Sec. 2.2. For reference, $1000\,cm^{-1} \approx 124\,meV$.

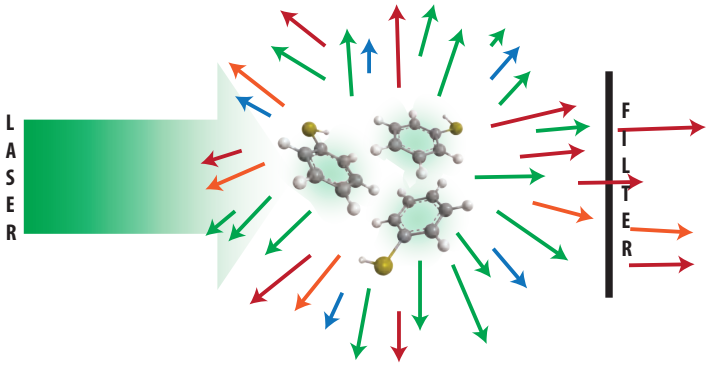

Figure 3.3.: Basic principle of Raman spectroscopy. Molecules are excited via a monochromatic laser source. This creates Rayleigh and Raman scattered light. A filter is used to block the Rayleigh scattered light, leaving the Raman scattered light to pass through and be recorded by a spectrometer.

The filter used can either be an edge or notch filter. The edge filters allow light of lower energy than the laser wavelength to pass through. This allows transmission of Stokes scattered Raman light only with the Rayleigh and anti-Stokes Raman scattered light blocked out. This is the most common set-up for Raman. If the anti-Stokes scattered light is also required, it is possible to use a notch filter. This filter blocks the area of the spectrum only around the laser wavelength, allowing light of lower and higher energy to pass through. Edge filters are generally used if anti-Stokes spectral information is not required, as they allow the filter to cut-off closer to the laser line.

3.2.1. SE1000: a desktop Raman machine

The SE1000 (Renishaw Diagnostics Ltd.) is a table-top Raman system equipped with a 185 mW 785 nm CW laser. The Raman spectrometer (shown in Fig. 3.4a) consists of a Raman probe (BWTek), which both excites the sample and collects the Raman scattered light through an objective attached to a dual-purpose optical fibre. The sample is placed on a stage which is controlled by three stepper motors

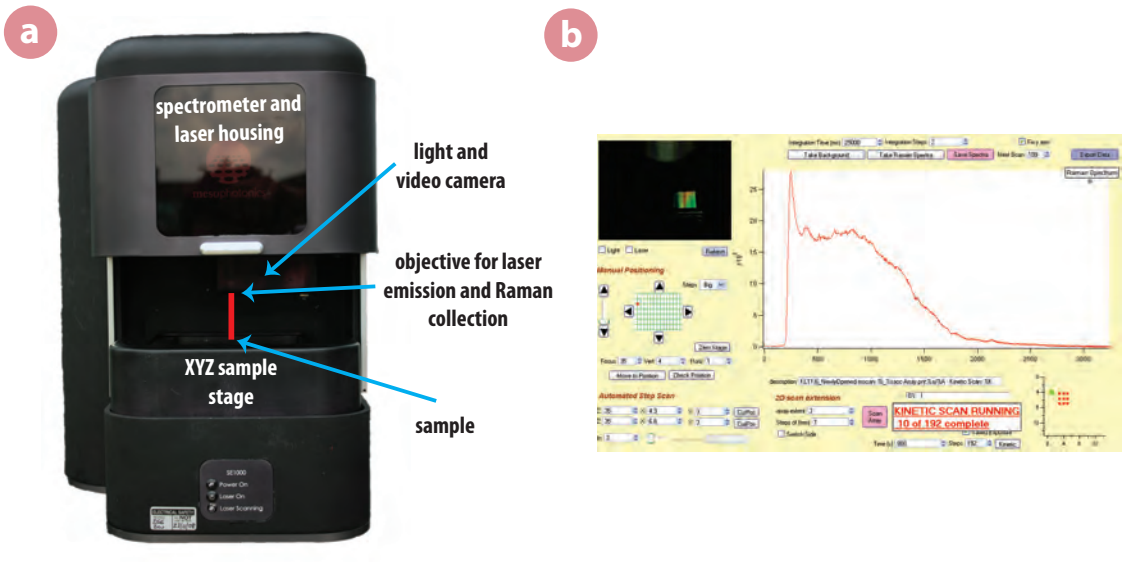

Figure 3.4.: (a) Enhanced photograph of SE1000 Raman device indicating sample position and 785 nm laser illumination. (b) Screenshot showing the SE1000 user interface.

in the XYZ directions. The whole system is enclosed in a small coffee-machine sized box complete with a video camera and LED lighting. This allows the user to watch the laser position on the sample.

The SE1000 has a large spot-size (diameter 120 µm) and focussing is performed using a step-wise control of the z-stage to maximise the Raman signal. A control interface was written using `C++` and Igor Pro to provide full control of the system in a unified graphical interface (Fig. 3.4b). The software has many features including the ability to allow arrays of points to be scanned around the sample as well as time-dependent measurements such as the multiplexed time-varied exposure procedure (discussed in Sec. 3.2.1.1).

3.2.1.1. Multiplexed Time-Varied Exposure Raman Measurements

The multiplexed time-varied exposure (MTVE) technique provides the ability to distinguish between different time-dependent and time-independent processes affecting the SERS signal. In Chapter 6 this allows us to distinguish time-effects and effects caused by heating under laser illumination. It also allows us to track the different dependence of different parts of the SERS spectrum, such as the peak intensity compared to the accompanying SERS background intensity.

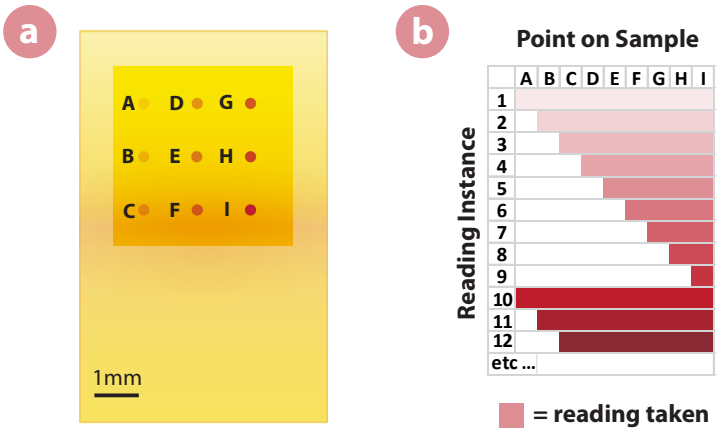

Figure 3.5.: Multiplexed Time-Varied Exposure Raman Measurements (a) Klarite sample indicating 9 exposure regions on the Klarite active area. Intensity of red dot indicates relative total exposure time of the different points. (b) Table indicating which spots are exposed and measured in each subsequent reading instance. Intensity of red colour indicates the amount of exposure time for a point at a particular reading instance.

In essence, an array of points is measured periodically over the course of an experiment. However, in each period of measurement not all the points in the array are always measured. At the end of the experiment, this results in an array of points, where each point has been measured a different number of times. Each point in the array is measured only a fraction of the total time of one point in the array, which is measured every period. This results in a series of points with periodic Raman spectra taken at regular intervals, that over the course of the experiment have had different lengths of exposure to the laser.

In the implementation used in Chapter 6, an array of nine well-spaced points is chosen on the Klarite sample. The array is scanned using a computer-controlled XY translation stage. The sample (mounted on a microscope slide) is locked into position using a built-in sample clamp on the stage to ensure the same points are measured before and after chemical/mechanical processing. The points illuminated may differ slightly due to stage repeatability ($\sim 1\,\mu m$); however this effect is found to be minimal due to the large spot-size of the SE1000 system. A Raman spectrum is recorded at each point in the array with a 10 s integration time (two acquisitions). This forms the first reading. After a period of time ($t = 15$ mins here) a further set of measurements of the point array is taken, this time at every point in the array except one, in this case, point A. Over these two sets of readings, point A will therefore have

had less total exposure to the laser compared to all the other points. On subsequent measurement sets, one less point is measured each time, until only one point in the array (point I) is measured (this happens on the ninth measurement set here). On the next measurement set, the whole process repeats and all the points are measured again. This procedure continues until the end of the experiment. As implemented here, this means point H has been exposed 89 % of the time point I was (which was exposed every time), point G was exposed 78 % of the time point I was, and so forth. The same total time has elapsed for all the points, so time-only dependent effects are the same for all points, but each point has experienced different lengths of laser exposure. The resulting large and complex datasets are analysed using JDAP (see Sec. 3.5).

3.2.2. Renishaw inVia

The majority of Raman spectra in this thesis were recorded using a Renishaw inVia Raman microscope equipped with 532 nm, 633 nm, and 785 nm wavelength excitation lasers. Some spectra were also recorded on a Renishaw RM1000 system which preceded the inVia and was equipped with a 514.5 nm Argon-ion laser as well as 633 nm and 785 nm lasers. The inVia offers far greater control, resolution, sensitivity and flexibility over the simplified SE1000 Raman set-up.

A simplified schematic of the inVia is shown in Fig. 3.6. All the elements (except the sample and objective output) are contained within a light-tight box to prevent stray light entering the system. The sample can be imaged using the built-in white-light source and camera. The objectives can be selected to determine the focused spot-size of the lasers and magnification of the sample down to the diffraction limit.

The system is highly automated. Laser power is controlled by neutral density (ND) filters and the bottom left and right mirrors (Fig. 3.6) allow the beam path to be adjusted to align the laser on the sample. Polarisers can be placed within the beam path to alter the incident polarization and a line shaper (cylindrical lens) can be inserted to facilitate the streamline mapping facility (explained below). The filter wheel contains edge filters for each of the lasers and these can be changed to notch filters as necessary. The filter optics allow the incident beam to be directed to the microscope, whilst the scattered return beam is directed to the spectrometer. The filtered light is focused through a slit which helps determine the resolution of the

system. The diffraction grating spatially separates the different wavelengths of light which are then detected at different locations on the thermoelectric-cooled CCD.

The standard scan is called a static scan. Here all the elements remain fixed in position. The CCD records the spectrum of light falling on it, with each pixel a different wavenumber. The range of wavenumbers that can be detected at once depends on the laser wavelength used, the grating line density, the focussing optics and the physical width of the CCD.

As well as standard static scans, the system is able to perform extended scans allowing spectra over a large range of wavenumbers to be recorded. This works by rotating the diffraction grating during the measurement to change the wavelengths of light falling on the CCD.

Streamline mapping can be used to create Raman maps of the surface. Here a line laser is used to illuminate a line on the sample. The different positions are then mapped onto different locations on the CCD. This means one dimension of the CCD maps location within the line, and the other one maps the spectra. This makes good use of the 2D CCD and allows for fast scanning compared to point-by-point.

All-in-all the Renishaw inVia provides a highly flexible Raman system, which has been used in various ways throughout this thesis. We have also been able to extend it to take low temperature Raman measurements using a cryostat system (Sec. 3.2.2.1).

3.2.2.1. Cryogenic Raman Measurements

An Oxford Instruments Microstat® He (liquid helium cryostat) allows low-temperature Raman and SERS measurements to be made. The normal microscope stage on the Renishaw inVia is removed and replaced with a custom-built cryostat holder with XYZ translation ability (Fig. 3.7a). The Microstat has a quartz window allowing optical access to the sample attached to the cold finger (Fig. 3.7b). Quartz is chosen since it has little Raman scattering in the spectral region of interest for the molecules we study. The liquid-helium cryostat enables the sample to be probed at a range of temperatures down to 4.2 K (and even below) as controlled by a temperature controller (ITC 503, Oxford Instruments). The change in temperature alters the thermal population of molecules as well as the dielectric properties of the SERS substrate. Before each run, the sample is carefully attached to the cold finger using a silver paste (Electrodag 1415 M, Acheson Colloiden B.V., The Netherlands).

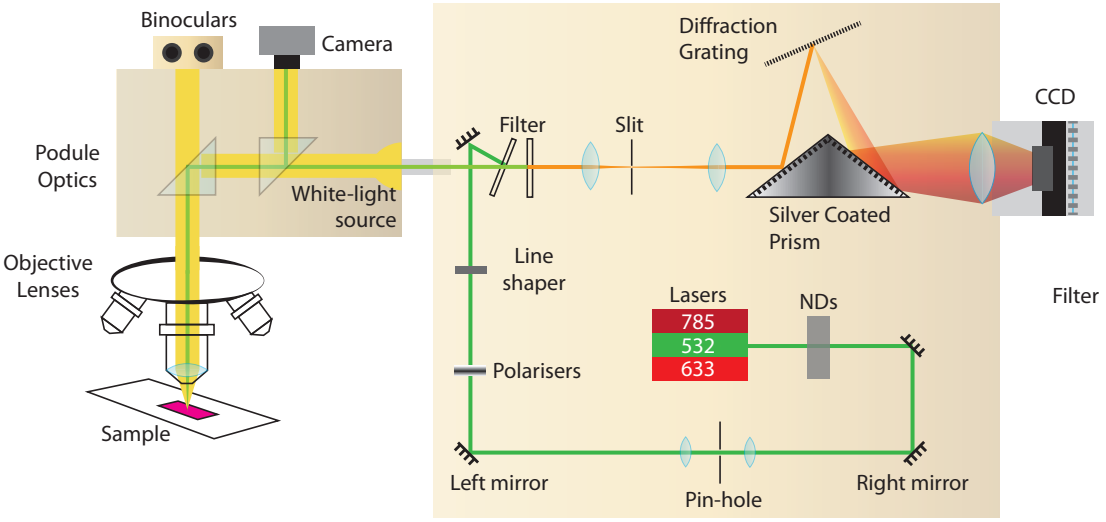

Figure 3.6.: Simplified Renishaw inVia Raman microscope schematic. To the left is the microscope section with the podule linked to a video camera, binoculars and the objective wheel. To the top-right is the spectrometer section, and bottom right is the alignment optics for the incident lasers.

The cryostat is then pumped-down over a few hours using a turbo-molecular pump backed by a rotary pump to obtain a high vacuum with a pressure at the pump below 10^{-5} mbar. This ensures the low temperatures can be sustained evenly across the sample. Sufficient time is also given to allow any solvents left in the silver past to out-gas and be removed. The cryostat is then sealed and removed from the turbo pump (to reduce vibration during measurements). The cryostat is connected into the Raman microscope and to the helium transfer tube and pump. Liquid helium is pumped around the cold finger (attached to the sample) and a temperature controller automatically adjusts a heater to maintain the cold finger at the specified temperature. Due to the more restrictive geometry it is necessary to use a long-working distance lens to focus the laser onto the sample within the cryostat. For most of the measurements we used a $\times 5$ objective with a 0.12 numerical aperture, which collects light over a $11.5\,^{\circ}$ full-angular range and has a 14 mm working distance. To prevent condensation on the quartz window, it is necessary to blow dry nitrogen air onto the window to lower the humidity when the temperature of the cryostat is above 50 K.

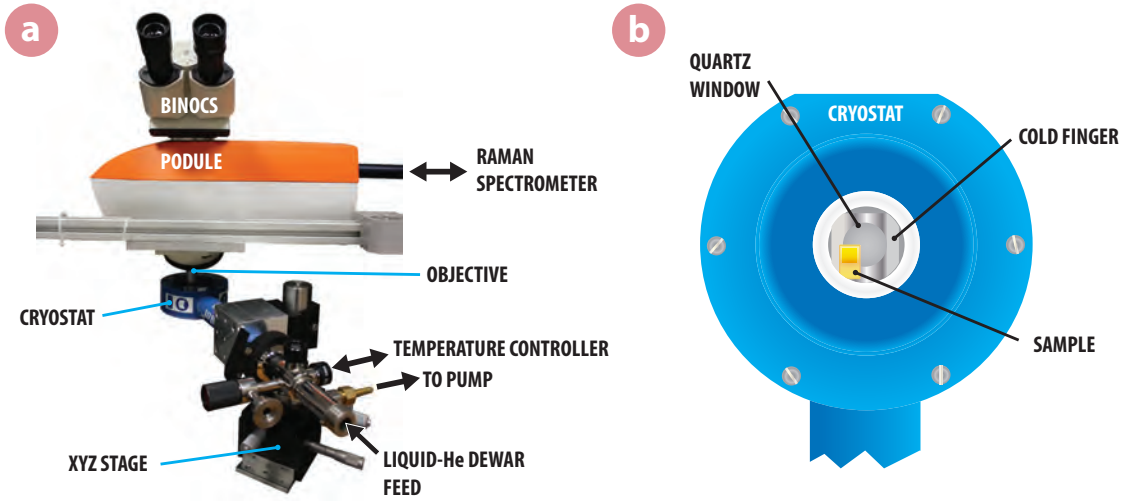

Figure 3.7.: (a) Photograph of the microscope section of the Renishaw inVia Raman spectrometer. The cryostat is shown replacing the normal translation stages attached to custom-built holder. For clarity the cryostat is shown disconnected from electronic leads to the temperature controller and the helium transfer tube and pump return. (b) Top-down schematic of the cryostat end, showing a Klarite sample attached to the cold finger visible through a quartz window.

3.3. Computational modelling

Despite the simplicity and elegance of Maxwell's equations, in many real situations they cannot be analytically solved. To help understand the nature of light in all-but-the-simplest nanostructures, we must resort to computational modelling.

There are many flavours of modelling techniques available. The most popular include finite difference time domain (FDTD) and the direct dipole approximation (DDA). There are a plethora of commercial and research-based programs available. The accuracy, speed and ability of the software programs vary considerably and high costs are generally involved with the high-end commercial solutions. Care must be taken when choosing the method to solve a particular system as each technique makes different assumptions. For example, DDA breaks the 3D environment into a matrix of dipole elements depending on the local dielectric function. The electric field can then be found by systematically solving Maxwell's equations for each dipole and its neighbours. This works well for small structures such as short nanoparticle systems but ignores the effects of higher order multipoles which become increasingly important as the size of the structure increases and the gaps between them decrease.

Boundary element method (BEM) techniques are another modelling technique,

which like FDTD, follow the time-evolution of a particular frequency. BEM is computationally less expensive compared to FDTD as it only requires the boundaries to be discretized, rather than the whole interior of the structure, reducing the dimensionality of the solution. In some cases the computation can be further simplified due to symmetry in the structure. F. J. Javier García de Abajo has developed a fast BEM code which applies to objects with axial-symmetry: boundary element method for axial symmetry (BEMAX). [37, 38] This code was originally designed for enclosed surfaces such as nanoparticles. To use it for open surface structures, the intended local structure has to be placed within a larger 'virtual' structure which allows definition of material regions but without supporting surface charges or currents. For the most part this generates realistic results, although it is necessary to ensure the structure is large enough to prevent erroneous leakage of light through the virtual structure. Previous studies have confirmed the validity of this approach for similar dish-like nanovoid structures. [39] The Klarite nanostructure (described in Chapter 4) which is based on an array of inverted square-based pyramids can be modelled with BEMAX. In the simulations shown in Chapter 4 we approximate a single pit from the Klarite nanostructure as a cone to be able to use such an axially symmetric method. (Fig. 3.8).

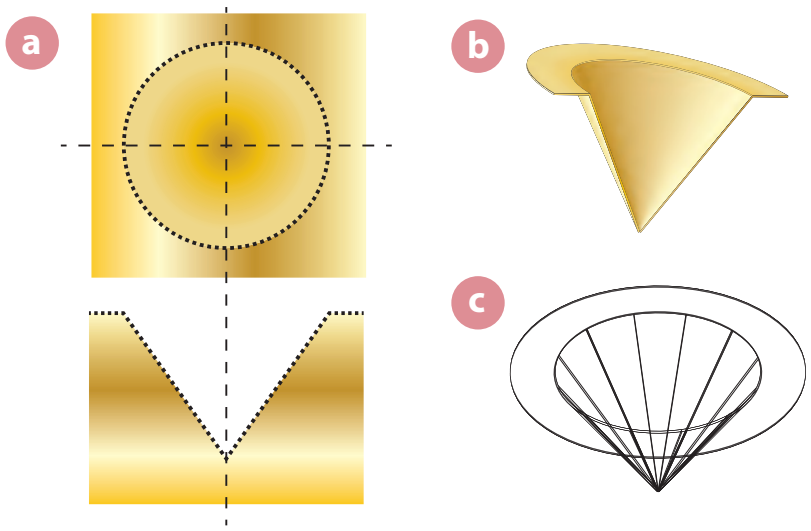

Figure 3.8.: Centro-symmetric modelling shape of Klarite used as approximation in BEMAX modelling. **(a)** Plan and cross-section views. **(b)** 3D rendered cross-section **(c)** Wireframe view of inverted cone-structure.

3.4. Self-assembled monolayers

Studying the principles of SERS requires robust, well-defined analytes. Self-assembled monolayers (SAMs) form from organic molecules which interact with a surface to spontaneously create well-defined monolayers. [40, 41, 42] These well-studied monolayers generally provide a reliable system with close-packed domains of similarly orientated molecules. SAM molecules are formed of three components: a surface group that bonds to the surface; a functional group to allow further interaction with other systems and a tail to join the two groups together and provide rigidity.

In this work we use a class of molecules called thiols (also known as mercaptans) which have a $-$SH end group, which allows binding to the surface through the sulphur atom. The thiol group has a particularly strong affinity to gold and is thus very useful in work involving plasmonics. Their strong affinity means they quickly form close-packed monolayers on gold and also displace many species which may already be present on the surface. This high affinity also means they are stable under various external conditions such as different solvents or changes in temperature. When the thiol adsorbs on the surface it forms a thiolate-gold complex, with a high bond energy of $\sim 44\,\mathrm{kcal\,mol^{-1}}$ ($\sim 184\,\mathrm{kJ\,mol^{-1}}$). [43] This compares to C$-$C bonds which have roughly double the bond energy. [44] Another advantage of thiol-based SAMs is their ease-of-preparation. Many thiols dissolve readily in ethanol forming an ethanolic thiol solution. To form a SAM, gold substrates are placed in an ethanolic solution (typically $1-10\,\mathrm{mM}$ thiol concentration) for a minimum of 3-4 hours. The longer the sample is left in solution the better the quality of the SAM. [45] The thiols continue to adsorb onto the surface until they reach saturation. As more thiols are added the system becomes more organised and depending on the molecule and the binding site, they tend to align at an acute angle away from the normal to the surface. The nature of the close-packing is determined by the van der Waals forces between the molecular groups.

With alkanethiols the exact packing and orientation depends on the length of the chain (with longer chains giving better packing), time in solution and orientation of the gold. For gold with a [111] oriented surface, a tight packing overlayer is possible with arrangement $(\sqrt{3} \times \sqrt{3})\mathrm{R}\,30\,^{\circ}$, where R signifies rotation has been shown in many studies. [45] This arrangement corresponds to sulphur atoms positioned at the centre of three gold atoms such that there is one sulphur atom per three gold atoms.

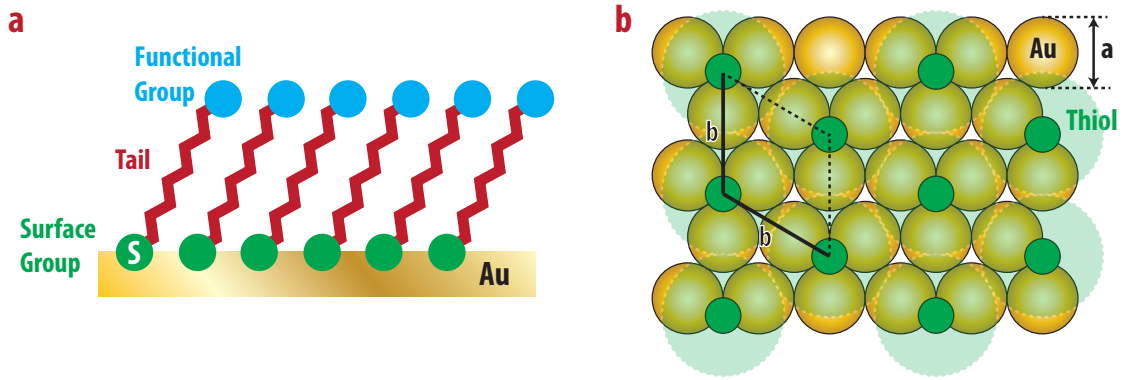

Figure 3.9.: (a) Alkanethiol SAM on gold. (b) Optimum packing density of thiol of Au[111] surface with $\left(\sqrt{3} \times \sqrt{3}\right)\mathrm{R}\,30\,^{\circ}$ arrangement of thiol molecules. With gold lattice constant $\mathrm{a} = 2.88\,\text{Å}$ and $\mathrm{b} = \sqrt{3} \cdot a$.

This means that the density of thiol molecules is a third of that of gold atoms. Given that the gold lattice constant $\mathrm{a} = 2.88\,\text{Å}$, this gives an optimal molecular packing density of $\sim 1.2 \times 10^{9}\,\text{molecules}\cdot\text{m}^{-2}$.

Whilst alkanethiols are historically the most studied thiol-SAM system and produce very tightly packed monolayers, many other molecules such as benzenethiol or carboxylic acids have also shown similar ability to form SAMs. The exact packing tends to not be so well-defined or as organised as in the alkanethiol case. Benzenethiol forms less-densely packed monolayers than alkanethiols or benzenethiol derivatives with alkane chains between the thiol and the phenyl group. [46, 47] Thiols with carboxylic groups can also form SAMs with some double layer areas. [48] Despite this, SAMs of benzenethiol have been widely used in SERS experiments due to their high Raman cross-section, whilst still forming reasonable SAMs.

The use of thiols can be extended beyond simple conformal coatings. By using nanoimprint lithography, thiols can be used like an ink and selectively stamped onto regions of interest on a nanostructure. Atomic force microscopes have also been used to remove thiols from certain regions of a metal analogous to scraping them off the surface. A good overview of some of these techniques is provided by Gooding et al. [49] and an extensive review of SAMs is given by Love et al. [45] The versatility and flexibility, yet robustness, of thiols makes them very useful systems for many areas of nanotechnology.

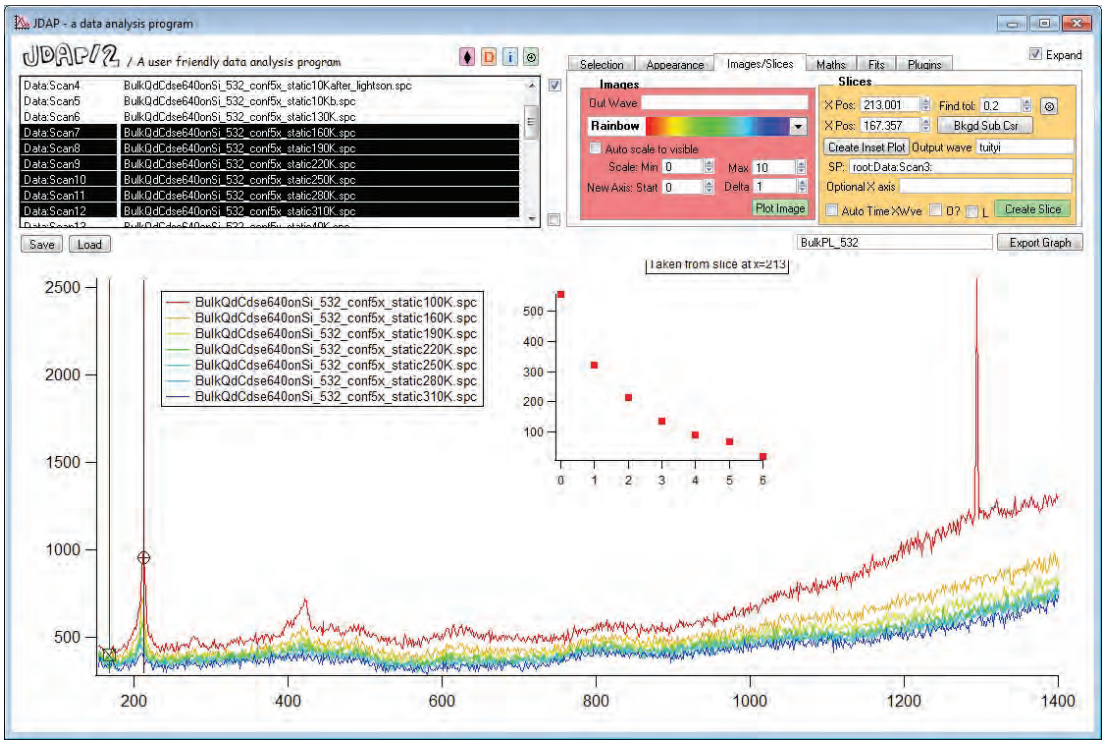

Figure 3.10.: A typical screenshot of the JDAP data analysis program showing the peak height extraction feature on a set of SERS spectra.

3.5. Data analysis

The majority of data analysis was completed in Igor Pro using custom analysis functions. An interactive analysis environment, *JDAP*, was developed to quickly deal with the spectra produced from the Raman spectrometers and other optical rigs in the lab. It provides a graphical interface (see Fig. 3.10) to deal with both small and large datasets. It allows extraction of peak heights and background intensities and facilitates the complicated analysis of the MTVE (Sec. 3.2.1.1) data. The code for *JDAP* is extensive and has been used throughout the labs and adapted to the needs of other experiments to provide quick and simple analysis routines, as was used, for example by Farah et al. [50]

As well as Igor Pro, some Raman data was analysed in the Renishaw WiRE 3.1 software with its flexible peak fitting software, allowing many of the results found in Chapter 7.

4. Plasmonic nanostructures for SERS

4.1. SERS-active nanostructures

Plasmonic nanostructures for SERS can broadly be split into four types: roughened surfaces, nanoparticles, nanostructured surfaces and combinations of the above (Fig. 4.1).

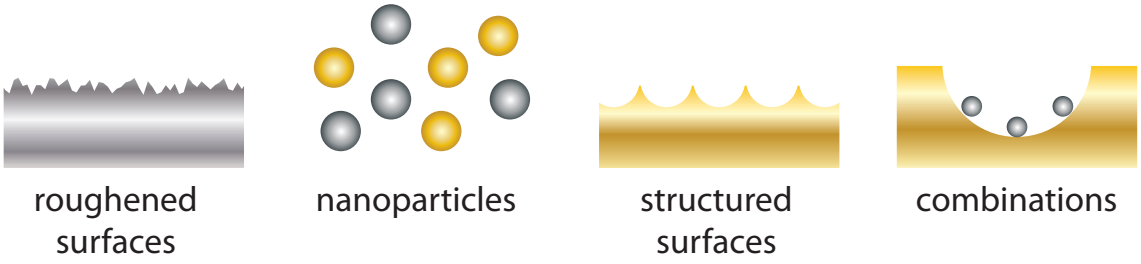

Figure 4.1.: Types of SERS-enhancing plasmonic structures.

Early research into SERS centred on its discovery on Ag-roughened electrode surfaces. [26] Electrochemical roughening was explored as a way to SERS-activate a silver metal surface allowing coupling to surface plasmon modes on the surface. [51] This was soon extended to other noble metal surfaces including Au and Cu, [52] which also showed plasmonic activity. Later Ag vapour-deposited metal films were used to explore the SERS effect [53, 54] and a variety of other deposition techniques were also used. The exact role of surface roughness in the SERS enhancement was still unclear and this eventually led to the use of self-assembled monolayers of metal colloids. [55] These were used to simulate roughness in a controlled way, which was a first step towards creating well-ordered SERS substrates.

As roughened surfaces continued to be explored to understand the fundamentals of

the SERS effect, metal nanoparticle suspensions began showing potential for much larger SERS enhancement than their surface-roughened alternatives. These relied on localised plasmon excitation on Ag and Au nanoparticles. It was also found that forcing these nanoparticles to aggregate could lead to huge SERS signals. A breakthrough came in 1997 when colloidal-based SERS gave enhancements to a degree large enough to detect single molecules. [7, 8] Colloidal systems are still intensely studied with many groups trying to achieve higher and higher SERS enhancement factors. A good brief review of this area is provided by Schwartzberg and Zhang. [56]

There are widely different values given for SERS enhancement factors for different systems in the literature and this is not helped by the lack of a fully standardised method of calculation. This has made such systems hard to compare. The recently accepted view is that the enhancement over Raman should be calculated relative to the number of molecules excited in the scattering area/volume,[24]

$$G_{SERS} = \frac{I_{SERS}/N_{Surf}}{I_{Raman}/N_{Vol}} \tag{4.1}$$

where I_{SERS} is the intensity of the SERS signal, N_{Surf} the number of adsorbed molecules in the scattering volume, I_{Raman} the Raman intensity of the equivalent species in bulk and N_{Vol} the number of molecules in the bulk scattering volume. Of course, even with this there remains difficulty in calculating the scattering volumes and whether active and non-active regions of the scatterer are included.

Apart from the difficulty in comparing Raman efficiency from system to system, a major problem of colloidal systems is the large degree of irreproducibility from measurement to measurement. The enhancement depends strongly on the size and shape of the nanoparticles, the size of aggregates formed, the exact size of the gap between colloids, and the molecular binding site amongst other factors. These factors have proven experimentally very hard to control.

A new class of structures emerged with the aim of greater reproducibility. This was spurred by recent advances in both top-down and bottom-up nanofabrication techniques. E-beam and focused-ion-beam (FIB) milling allowed structures such as arrays of well defined nanoparticles [57] and inverted structures such as nanohole arrays. [58] These techniques, however, are very time consuming and costly to fabricate large-scale devices.

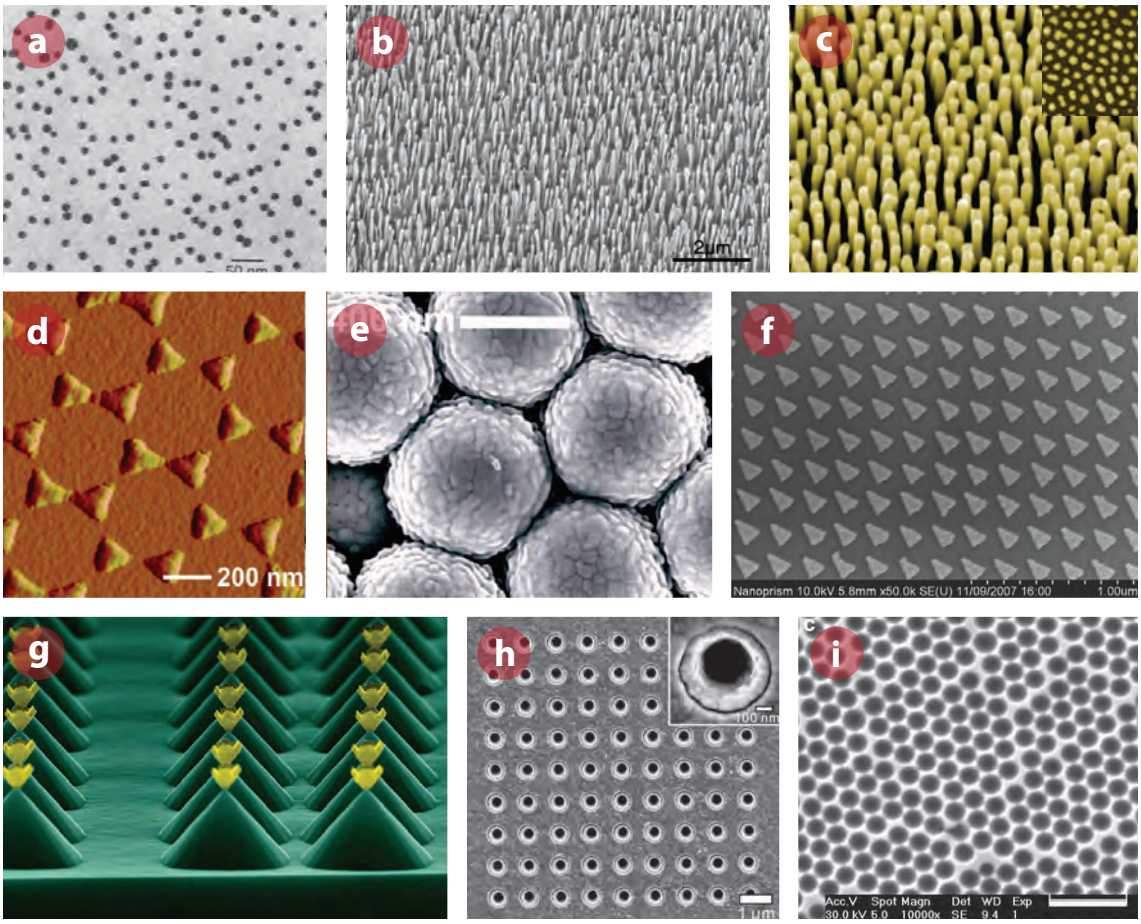

Figure 4.2.: Various attempts at ordered nanostructures **(a)** (sub) monolayer of 12 nm gold nanoparticles ligand-bound to silica coated TEM grid via silane. [55] **(b)** E-beam evaporated oblique angle deposited array of 1µm long silver nanorods. [59] **(c)** Gold nanorods grown through porous anodized aluminium oxide template. [60]. **(d)** Silver nanotriangle array formed from nanosphere lithography. [61] **(e)** Silver film on nanosphere (AgFON) structure. [61] **(f)** Silver nanopyramid array (period=200 nm) formed using nanoimprint lithography and angled-evaporation. [62] **(g)** Au nanopyramids on top of larger silicon pyramid structure part-way through a process to embed Au nanopyramids in PDMS matrix. [63]. **(h)** Nanohole array with 500 nm diameter. Holes are surrounded by very small sub-10 nm nanogap. [64] **(i)** Nanovoid surface using 600 nm PS and 460 nm of electrochemically grown gold. [65] All images taken from the references cited with copyright belong to the respective publishers.

More recent substrates have made use of self-assembled structures and nanotemplating, providing scalable structures with good reproducibility. Polystyrene (PS) spheres, commercially available in nanoscale-sizes, have been widely used to act as templates. This is due to their ease of deposition into self-assembled hexagonally packed crystal structures. Haynes et al. [66, 61] use this as a mask to form well-ordered hexagonal arrays of nanotriangles via metal evaporation or sputtering and subsequent dissolving of the PS. They call this nanosphere lithography (NSL) and it has shown enhancements of up to 10^8.

Abdelsalam et al. [65] used PS colloids as a template to electrochemically grow gold around them. Dissolving the spheres resulted in nanovoid structures: a large array of nanoscale gold dishes. These gold dishes have been shown to give reproducible enhancements via excitation of localised plasmons within each dish, similar to those observed in the Klarite nanostructure introduced later in this chapter (Sec. 4.2). [67, 68]. Dieringer et al. [69] used a self-assembled layer of PS and then coated them with metal to give modulated SERS-active metal surface called metal-film on nanospheres (MFONs).

As well as polystyrene spheres, other nanostructures have been tried as templates to grow metals electrochemically. Anodized nanoporous aluminium oxide (AAO) [60] has been used to grow periodic arrays of nanowires. Like many SERS structures, however, the uniformity of SERS signal has not been sufficiently examined or validated across the sample.

Some top-down approaches have also yielded results with fast fabrication. Angle evaporation has led to formation of well-defined nanorods [70] and optical lithography has been able to produce well-defined ($\sim 10\,\%$ variation - estimated from SEMs, but not shown) nanogaps. [64] Combinations of such approaches have also been used, such as that of Cui et al., [62] who use a mixture of wet-etching into silicon with nanoimprint lithography to create a polymer pyramid array. This is then subjected to angle-evaporated metal deposition before being plasma etched to leave behind a well-defined array of nanoprisms, giving reproducibility of less than $20\,\%$ in SERS across the sample. Henzie et al. [63] have also tried to create reproducible arrays of metal nanoparticles suspended in a poly[dimethyl siloxane] (PDMS) matrix.

These are just a handful of the many types of SERS substrate being created. They all have a trade-off between their maximum SERS intensity and SERS reproducibility but also between the ease of manufacture and quality of the resulting nanostructure.

Brown et al. [71] have provided a good review of nanostructures for SERS and the trade-offs involved with the different systems, illuminating the complexity involved in creating well-defined nanostructured surfaces with long range order versus the ease of creating metal nanoparticle based systems. There are many extensive reviews on SERS nanostructures in the literature. [72, 73, 74]

Many possible applications for SERS require quantitative data which is reliably comparable from measurement to measurement. It is important to keep this in mind as new SERS substrates emerge. Any successful substrate must show SERS reproducibility across the sample, and from sample-to-sample, as well as strong SERS enhancements.

In very recent years, there has been a resurgence in nanoparticle SERS studies. It is clear that the spacing between the particles is key to the SERS enhancement seen. Unfortunately, the enhancement varies strongly with gap size. Small changes in the gap size cause large changes in SERS signal. Recently Taylor et al. [75] have shown good control over the gap-size using rigid macrocyclic molecules fixing the gap between nanoparticles at 0.9 nm, which could present a promising new future for controlled aggregated nanoparticles SERS with the potential for large enhancements and reproducibility.

Li et al. [76] have shown they can achieve reproducible enhancements using their shell-isolated nanoparticle-enhanced Raman spectroscopy (SHINERS). These are silica coated gold nanoparticles. The silica coating allows a pre-defined distance to be set between analyte and the gold particle surface. This also means that charge transfer effects between the gold and the particle can be removed. The silica also acts as a highly compatible system with biological and water based systems as well as in a whole range of solvents.

Separating out charge transfer effects from plasmonic effects is necessary to ensure reproducibility between molecular systems. In the future, creation of new SERS substrates needs to take this seriously into account if SERS is to greatly impact the quantitative sciences. A study of metal oxide nanoparticles on flat gold surfaces [77] has also been able to show SERS enhancement but without charge transfer effects.

It is worth noting that other non-plasmonic based substrates have been demonstrated for SERS. These are generally based on chemical effects and the enhancements have been far more limited to those on metallic systems. Quagliano et al. [78] demonstrated a couple orders of magnitude enhancement for pyridine absorbed on

to InAs/GaAs quantum dots. A similar effect has been observed for CdTe [79] and CdS [80] systems. Graphene has also shown similar enhancements and has been suggested as an ideal system to separate out chemical effects from plasmonic ones, since it does not support plasmons in the visible range. [81] SERS on non-plasmonic substrates is in the early stages of study and it is not clear whether it will prove fruitful in the long term, however coupling these systems with plasmonic ones could produce interesting hybrid systems with potential for large enhancements, which also aid the understanding of the origin of SERS. [82]

4.2. Klarite

Klarite® is a commercially-available SERS substrate, manufactured by Renishaw Diagnostics Ltd., Glasgow, UK. Klarite is a nanostructured gold surface consisting of a square-array of inverted pyramidal pits, which enable the trapping of light inside them to create large local EM-field amplitudes to enhance the Raman process.

The light trapped by these structures is wavelength dependent and has been shown to be simply tuned by adjusting the pit geometry. [83] In commercially-available Klarite, the pits are spaced on a 2 µm square pitch and the sides of the square pyramid base are 1.5 µm each (Fig. 4.3). This allows the resonances of Klarite to be tuned to near two commonly used Raman excitations at 785 nm and 633 nm (Fig. 4.4).

Klarite does not boast the extreme SERS enhancement factors quoted in some of the research literature, but still has an enhancement factor on the order of 10^6. [84] Despite this, its strength lies in reliability and reproducibility of the SERS enhancement around the sample and from one sample to the next. The precise and reproducible nature of the Klarite fabrication process ensures the reliability of the substrates. SERS signals collected around the substrate generally fall within 10 % of each other.

This reliability has led to an increasing amount of use of the substrate both in academia and industry. The research spans many areas of SERS detection. Detection of disease-causing bacteria such as Bacillus endospores [85] has been shown by the US Navy with discrimination between 5 different types and single-spore sensitivity possible. [86] DNA sequence analysis using SERRS (Surface-Enhanced Resonant Raman Scattering) [87, 88] and detection of low concentrations of squaraine dyes as unique reporters for SERRS multiplexing. [89] Stokes et al. [90] combined SERS

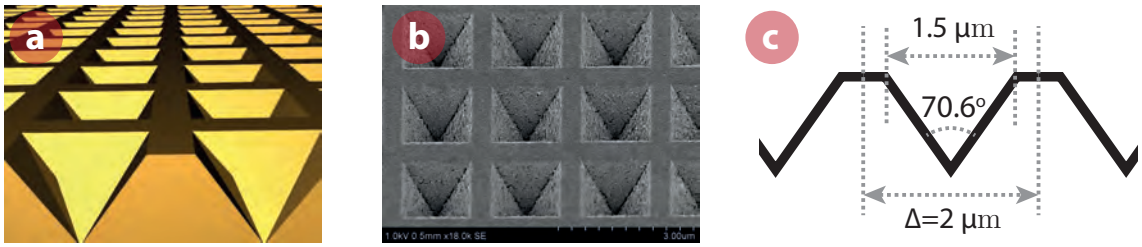

Figure 4.3.: **(a)** Klarite nanostructure - a square-array of inverted square-base pyramidal pits **(b)** SEM of the structure **(c)** Cross-section of Klarite nanostructure indicating important geometric dimensions.

using Klarite with dip-pen nanolithography to enable DNA-based SERRS pixel arrays. Detection and characterization of the toxic melamine molecule [91, 92] has been possible in various foods and solutions. Lin et al. [92] showed that it is possible to use SERS on Klarite to obtain sufficiently useful quantitative results for the amount of melamine present. Fan et al. [93] have shown that rapid detection and discrimination of food and water-borne viruses is possible. Trace-level detection of explosive materials have been shown for 2,4,6-trinitrotoluene (TNT) and nitroglycerine (NG) [94, 95]. Molecular imprinted polymers (MIPs) have shown promise at adapting the physical binding site specificity available on Klarite not only to detect TNT [94] but also the uptake of β-blocking drug propranolol. [96, 97] Corrigan et al. [98] have shown the possibility to use SERS with Klarite in the pharmaceutical industry to verify purification and cleaning of drugs such as nelarabine, with the potential to speed up this process. Finally Klarite has also been used to demonstrate surface-enhanced coherent anti-Stokes Raman scattering (SECARS), [99] extending the substrates use beyond traditional SERS techniques. As well as this, more recently Klarite is increasingly used as a standard of comparison for potential new SERS substrates [100, 101, 102, 103] where reproducibility as well as high enhancement factors are necessary.

4.2.1. Fabrication

Klarite is created in a three-stage process:

1. A square array mask of micron-sized features is formed using optical or e-beam lithography onto a (100) oriented silicon wafer. The holes are aligned along the [110] direction.

2. An anisotropic KOH-etch [104] is then performed, which etches the silicon preferentially along the {111} atomic planes. This forms a square-array of square pyramids with atomically smooth surfaces.

3. The structure is sputter-coated or evaporated with a thick layer ($\sim 200 - 300\,\text{nm}$) of a suitable metal, generally gold, to create a plasmonically active surface.

These processes have been well documented before [105, 84] and further refinement of the proprietary manufacturing process has since been made by Renishaw Diagnostics especially to ensure uniformity of application of the gold coating and sample-sample reproducibility.

4.2.2. Local field enhancement

The inverted pyramid structure has been extensively studied in our group by Perney et al. [84, 83] Localised EM-modes excited on Klarite can be tuned by changing the size or geometry of the pit. Changing the pitch (distance between pits) does not significantly affect the position of the resonances. This indicates that diffraction effects of the structure are not key to the excitation of these modes. The localised modes have previously been modelled as trapped surface plasmon polariton modes akin to standing waves on a string. In this model the tip of the pyramidal pit allows wave propagation, whilst the top surface edges reflect. This model matched well to finite-difference time-domain (FDTD) modelling on a two-dimensional groove structure performed at the time. [84] The model predicts the experimentally observed existence of a discrete set of modes dependent on wavelength. Inverted pyramid structures can therefore be tuned to have a plasmon resonance where it is spectrally required (as long as it is lower in energy than the plasmon frequency). This makes the structure desirable for SERS applications. They compared the gold-coated structure with bare silicon where they did not find evidence of the same modes, highlighting the plasmonic nature of the modes.

The nature of the localised optical modes inside the pit have recently been modelled by Vernon et al. [106] and Mechler et al. [107] Vernon models the pits using a computationally intensive 3D-FDTD which they compare to an equivalent 2D model. This aims to improve upon the 2D-groove FDTD performed by Perney. They find similar modes to those observed by Perney on a silicon structure with a 300 nm gold

coating, however the 2D model they use shows the field is completely localised to the tip, which does not agree with Perney's standing wave model. In the 3D case the electric field is pushed away from the tip, presumed to be due to the proximity of repelling like-charges caused by the four surfaces coming together. They also compare the gold-coated silicon structure to one coated with a perfect electrical conductor (PEC), with an infinite plasmon frequency which is thus unable to sustain surface plasmons. Remarkably, they appear to find only a 5 % reduction in the electric field on the pit sides compared to the case with gold. They say that this reduction is within their modelling errors ($\sim 5\,\%$). Unfortunately, they do not provide a figure showing the electric field distribution in the PEC case, making exact comparison to other models difficult. They therefore conclude that the enhancement must be diffractive in origin and not plasmonic, since a plasmonic material is not necessary to achieve the same electric field enhancement.

Mechler takes an analytical approach to the problem based on Neerhoff-Mur formalism. [107] This approach is limited to a 2D case and they calculate the electric field-distribution inside a V-groove structure with a 90 ° apex (a quasi-2D projection of Klarite). Here they also use a PEC which will not sustain plasmons and model it as an aperture in a thin PEC (1 µm thick) sheet with one opening infinitesimally small (the tip) and the other 2 µm wide. Mechler obtains markedly different electric field distributions to Vernon's 2D case. They claim that near-field diffraction can cause charge redistribution on the metal surface which causes the local field enhancement at the surface. The result appears to more closely matched to Vernon's 3D case. Despite some ambiguity surrounding the precise electric field amplitudes, they believe that a SERS enhancement of $\sim 10^4$ can be achieved in a V-groove structure without taking into account the effect of surface plasmons. Unfortunately, direct comparison is difficult since they did not model at 785 nm. They also acknowledge that on top of the near-field diffractive effects they would expect to see an effect of plasmons on top of this resonant diffractive effect, which leads to the higher enhancements of SERS seen experimentally.

Using the boundary element method, BEMAX, described in Chapter 3, we add to these interpretations of the electric field distribution, by modelling a conical approximation to the Klarite structure. We obtain absorption resonances around 630 nm, 750 nm and 1000 nm which match well with those observed experimentally. The near-field intensity distribution is shown for these three wavelengths in Fig. 4.4. The distribution of these modes agrees strongly with the square based gold-coated

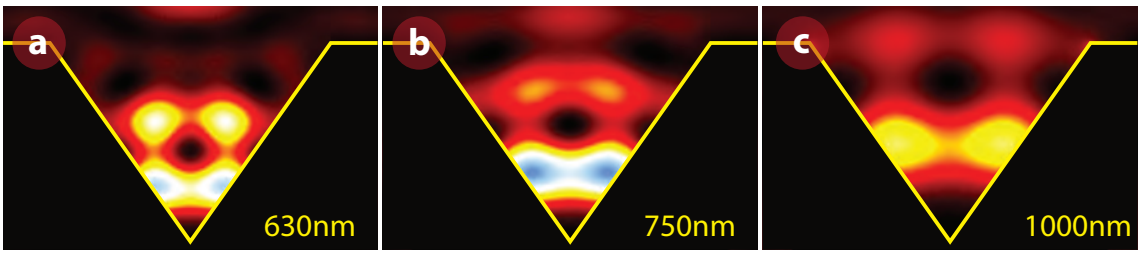

Figure 4.4.: Klarite resonant plasmon modes showing near-field intensity (E^2) distribution for **(a)** 630 nm, **(b)** 750 nm and **(c)** 1000 nm modes.

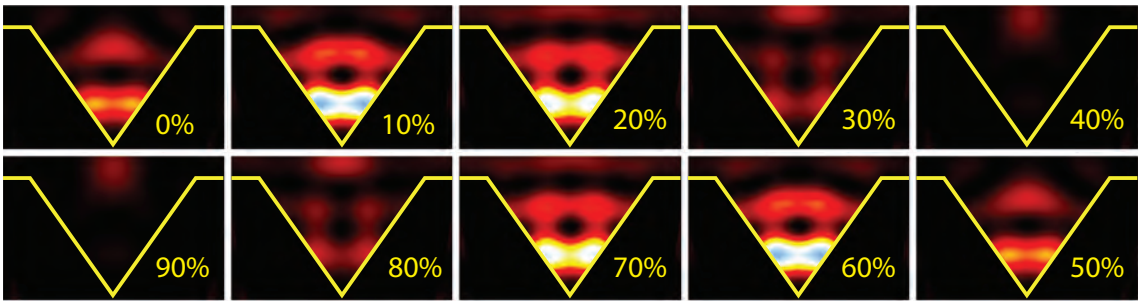

Figure 4.5.: Evolution of the 750 nm Klarite plasmon mode through one optical cycle showing electric-field amplitude. Snapshots at percentage through full 2π optical cycle in clockwise direction.

inverted pyramid modelled by Vernon et al. [106] in their full-3D FDTD calculations, although the exact wavelength dependence is slightly different probably due to the subtly increased geometry size used by Vernon. We see that the absorption modes are strongly localised towards the bottom of the pit and to its sides, although they avoid the apex. This differs from the FDTD modelling of Vernon [106] and Perney [84] for V-grooves, where the field is concentrated at the apex. Perney's wavelength model again does not appear to match well to the observed field distributions.

Using the calculated electric field amplitude vectors, we can recreate the electric field magnitude progression over an optical cycle. For the 785 nm mode (Fig. 4.5) we see that the electric field is spatially localised to the lower half of the pit edges and remains fixed in the same place throughout the cycle. This fixed location and strong field intensity enables the large Raman enhancements seen. It must also be noted that the strong enhancements only come from certain areas of the pit. Analysis of the near-field distribution close to the surface, reveals an approximate mode area on the surface of 1 % relative to the total area. In the case of a monolayer coverage of a molecule on Klarite, only some of the molecules (in the hot spots) will experience

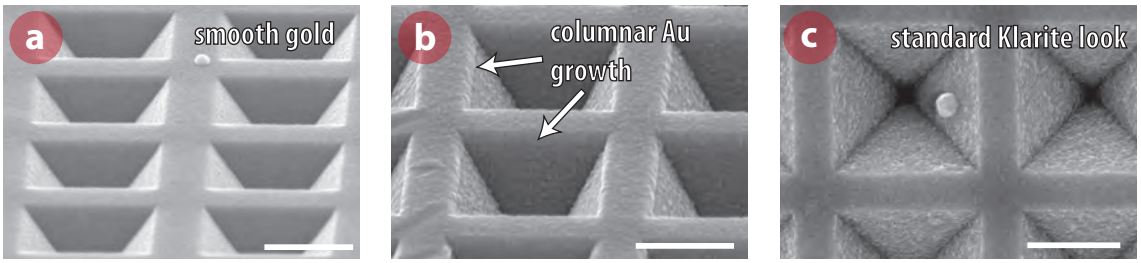

Figure 4.6.: Scanning electron micrographs indicating some of the possible Klarite evaporation results. (a) smooth gold surface (b) columnar growth on rim (c) standard Klarite. SEMs courtesy of Renishaw Diagnostics Ltd.

the higher EM-fields.

4.2.3. Importance of nanoscale morphology

The Klarite structure bridges two distinct size regimes. The main aperture (a 1.5 µm-sided square) is on the order of twice the wavelength of the incident light captured. Going into the pyramid, the size becomes smaller than the wavelength of light approaching the nanoscale regime as we approach the apex. Bridging two size regimes makes it conceptually harder to pin-down the origin of the absorption resonances experimentally observed: plasmonic or near-field diffractive. Not only this, but all the models ignore another important factor: the surface roughness. Although the etched silicon surface provides an atomically smooth platform, the gold coating applied on top has nanoscale roughness due to its evaporated or sputtered application. It is very difficult and computationally intensive to model this random nanoscale roughness in the mesoscale inverted pyramid containing structure. It is clear from experiments, however, that roughness has an important part to play in the enhancement factors observed.

By changing the angle of evaporation of gold onto the Klarite and the rate of evaporation, Renishaw Diagnostics have created slightly different Klarite structures with differing smoothness (Fig. 4.6). This leads to subtle changes in the pyramid aperture morphology as well as the surface roughness as is commonly seen in thermal deposition studies. [108] Compared to standard Klarite, the different angular evaporated structures gave varying degrees of Raman enhancement from a benzenethiol monolayer, with some giving average enhancements of 3 x that of standard Klarite and showing signs of columnar growth on the Klarite edge (Fig. 4.6a), whereas the

smoothest ones (Fig. 4.6a) give enhancements of less than 10 % compared to normal Klarite (Fig. 4.6c).

Using an angle-resolved goniometer and an adapted microscope as described in Chapter 3 it is possible to track the optical absorption modes which exist on some of these structure. (Fig. 4.7). On the Klarite structure we see strong-localised modes (flat) towards 0 ° corresponding to the main absorption resonances. Interestingly, these do seem to change significantly between samples, despite only slight changes in overall pit geometry between the differently evaporated samples. We can also see that the largest Raman intensity does not correspond to the pits where the absorption is in resonance with the Raman excitation or emission wavelengths. This indicates that the enhancement depends not only on the resonances within these large structures, but perhaps also the highly localised fields within the pit structure resulting from surface roughness. Clearly this is dwarfed in our far-field measurements by the main Klarite structure's absorbance as we do not see evidence for this in the reflectivity maps, but they could be responsible for the disparity in the SERS signals observed.

We will see in Chapter 6 how nanoscale roughness plays an important role in the SERS enhancements seen. This has also been studied and controlled in other similar sized structures. [109]

A plausible model for the enhancement seen in Klarite could involve both the meso- and nano-scale features. Light is first trapped into the pyramid pits via near-field diffraction or large-scale plasmonic resonances, here it couples with rough features on the gold surface creating further smaller and highly localised hot spots in an antenna-like effect. These small localised hot spots are then responsible for the large Raman enhancements seen.

4.2.4. Solving the enhancement mechanism

Questions still remain, such as why the enhancement is so reproducible across the substrate if it results from random roughness features? There is clearly more work to be done to ascertain the exact origin of the SERS enhancement in the Klarite structure. Given attempts to model Klarite are still not in complete agreement, adding roughness into this picture further complicates matters. An experimental approach appears best suited to understand the enhancement. Some future experi-

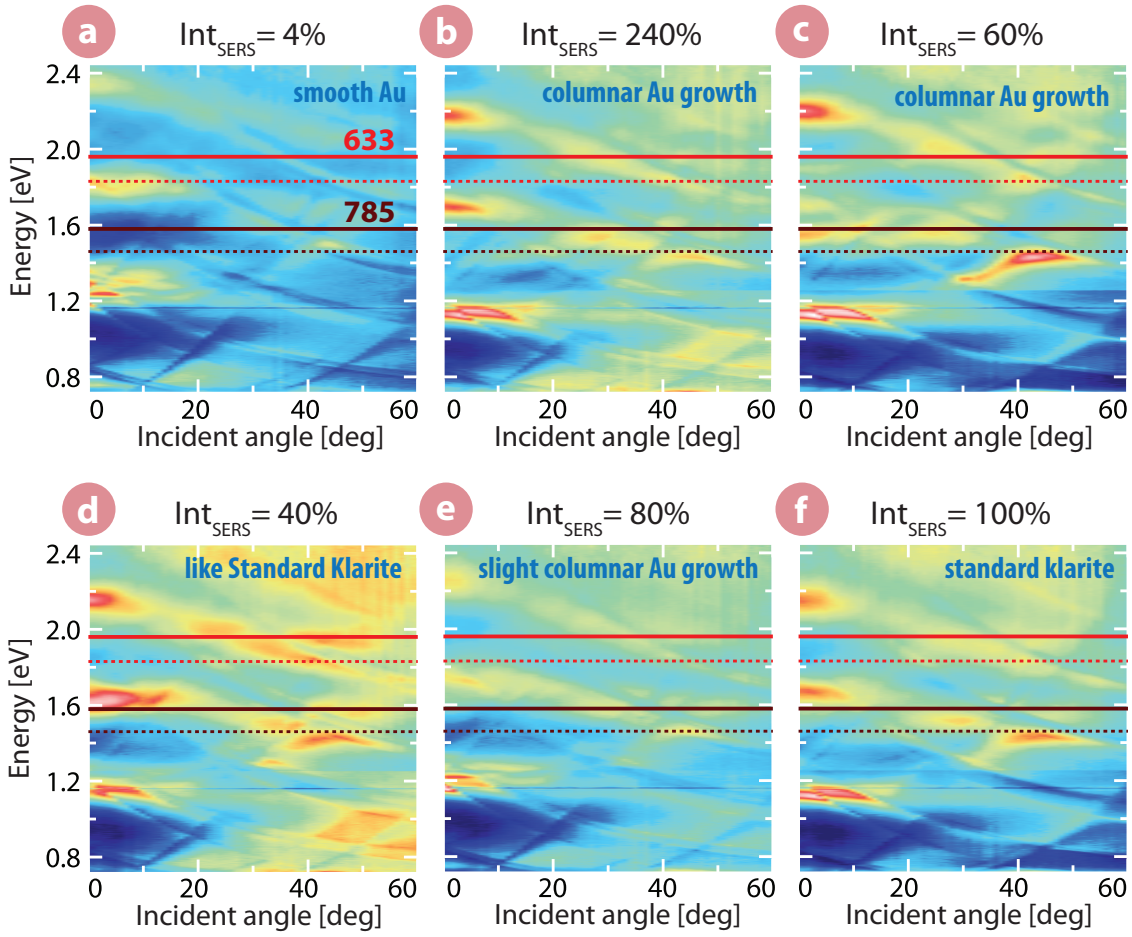

Figure 4.7.: Angle-resolved goniometer dispersion plots for differently angle-evaporated Klarite structures. Int$_{SERS}$ gives the relative SERS intensity compared to standard Klarite at $\lambda_{ex} = 785\,\text{nm}$. Horizontal axis related to in-plane momentum via $k_x = k_0 \sin\theta$. Overlaid is the 633 nm and 785 nm excitation laser positions in bright red and dark red respectively along with the energy position of $1000\,\text{cm}^{-1}$ (dashed lines) corresponding to the approximate emission location of the Stokes ring-breathing benzenethiol line. Colour indicates log(reflectance) from dark blue (-2) indicating reflective areas red/white (0) indicating absorptive areas. (a-e) variously angle-evaporated Klarite samples causing change in the surface roughness and definition of the pit aperture. (f) standard Klarite sample for comparison.

mental tracks are highlighted in Chapter 9.

4.3. Conclusion

Despite the fact that the exact mechanism of the SERS enhancement in the Klarite nanostructure is still under investigation, it is clear that it has proved an increasingly useful SERS substrate with large enhancements and excellent reproducibility. Recently other companies have attempted to launch SERS substrates but have been let down by a lack of robustness and repeatability compared to Klarite. The Klarite structure is thus a useful one to study some of the subtleties of the SERS effect such as its temperature dependence and background continuum which we will investigate later in this thesis. We have suggested further experiments in Chapter 9 which should help pin-down the enhancements observed in Klarite. Full understanding of the enhancement mechanism should allow improvements to future SERS structures and potentially far higher enhancements.

Research into new SERS substrates or enhancement systems remains very active. As our ability to control nanoscale objects improves, it seems likely that much greater enhancing structures will be possible in the future which maintain the reproducibility seen in Klarite. When this happens, SERS will be able to launch into proper analytical applications and could be a disruptive technology across a huge range of industries.

5. Quantum dot SERS

In this chapter we use a well-defined local inorganic (non-degradable) nanostructure and study its interaction with localised plasmons on the Klarite and nanovoid nanostructured surfaces. Further to this, quantum dots (QDs), with photon absorption and emission resonances in the visible region of the electromagnetic spectrum allow us to probe both resonance and non-resonance Raman scattering using common Raman laser excitation wavelengths in the visible region.

Semiconductor QDs are of interest for many applications due to their narrow photoluminescence (PL) lines, high quantum yield, and broadband absorption spectra. [110, 111] Most sensing and imaging applications currently use PL [112, 111] due to its greater sensitivity compared with other spectroscopic techniques such as Raman scattering. For PL, QDs possess many attractive features over standard molecular dye markers including their broad excitation spectral region, resistance to photobleaching, low photo- and chemical degradation, and size-tunability of their narrow emission peak. [112] Although the use of QDs as fluorophore labels has been well studied, [113] their use as Raman spectroscopy labels has yet to be realized.

Surface-enhanced Raman scattering boosts low Raman signals in molecules, and, with surface-enhanced resonance Raman scattering (SERRS), the enhancements can be further increased by several orders of magnitude when exciting at an electronic resonance of the chromophore. [114] Thus SE(R)RS (SERS or SERRS) can be more sensitive than fluorescence with the added advantage of detection specificity and multiplexability. [115] These enhancements are due to the intense local electric fields caused by exciting surface plasmons at metal surfaces as has been shown in Chapter 4. [116]

Besides QDs acting as (bio)-chemical markers, the ability to detect (sub)-monolayer concentrations of QDs through SERS can be useful for monitoring QD devices in real time, for instance measuring the QD temperature or tunnelling-induced phonon emission in photovoltaic or QD LED devices. In this chapter the SE(R)RS of CdSe

QDs on nanostructured gold surfaces is described.

5.1. Quantum dots

5.1.1. Quantum confinement

Semiconductors have an energy band gap between their valence and conduction bands caused by the periodic crystalline lattice. This allows an excited electron in the conduction band to radiate energy proportional to the band gap size via emitting a photon. This is photoluminescence and is similar to that which occurs in-between the electronic states in molecules.

In a semiconductor, an electron can be promoted from the valence to the conduction band. This leaves an electronic hole in the valence band and the two charge carriers interact via a coulombic interaction. The distance between the electron and the hole is called the exciton Bohr radius.

As the size of a semiconducting structure is reduced to nanometre-scale dimensions, the spatial confinement can alter its properties significantly. This happens as the characteristic dimensions approach and decrease past the size of the exciton Bohr radius. This new boundary restriction leads to quantum confinement of the system, effectively restricting the degrees of freedom in all spatial dimensions. This confinement means that instead of continuous bands of energy-momentum states, only discrete energy-momentum states exist. As the nanocrystal is further reduced in size below the exciton Bohr radius, the quantum confinement increases and the number of states further reduces. This leads to a system with purely discrete energy levels, leading to highly confined quantum dots, sometimes called 'artificial atoms'.

As the confinement increases, the reduction and quantization of states leads to an increasing energy gap between the lowest unoccupied energy level and the highest occupied energy level (see Fig. 5.1). This changes the photoluminescence observed. In bulk CdSe the bandgap is 1.74 eV, putting it into the visible optical range in the far red of the spectrum. As a nanocrystal, the band gap can be controlled via its size over the entire visible spectrum.

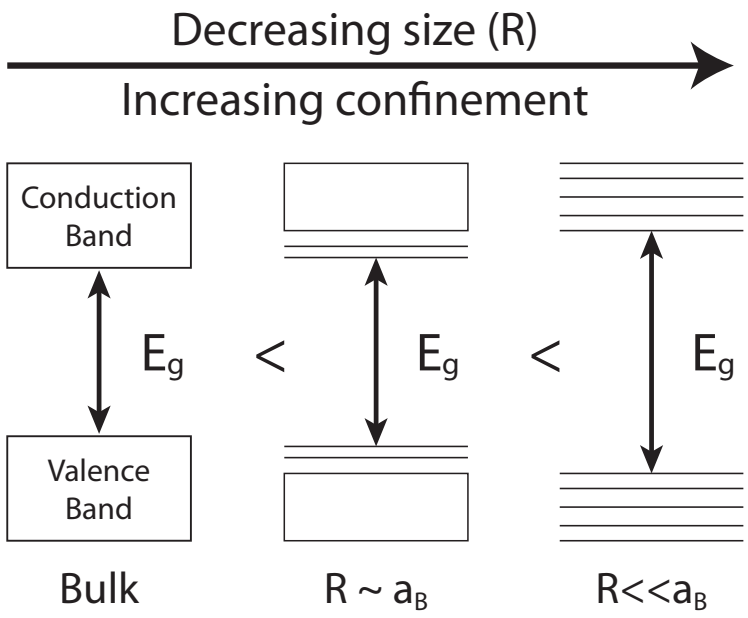

Figure 5.1.: Simplified energy structure of semiconductor as it becomes a quantum dot. **(left)** bulk material **(middle)** poorly confined quantum dot **(right)** tightly confined quantum dot. Bandgap energy increases (blue-shifts) as the quantum dot radius shrinks.

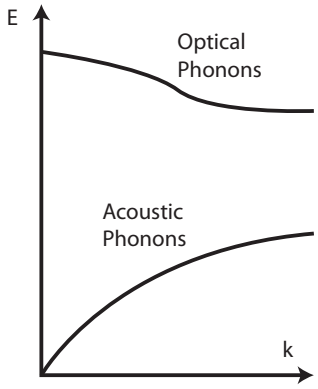

Figure 5.2.: Characteristic optical and acoustic phonon dispersion relations for a diatomic system.

5.2. Raman of inorganic materials

Raman scattering has long been used as a method to investigate crystalline semiconductors. Instead of exciting molecular vibrational modes (discussed in Chapter 2), vibrational phonon modes in the crystal lattice can be excited. Lattice phonons can be split into two types: acoustic and optical. Acoustic phonons are of much lower energy than optical phonons (see Fig. 5.2). When a photon is inelastically scattered by an acoustic phonon, it is called Brillouin scattering, and when it is scattered by optical phonons it is called Raman scattering. In a standard experimental Raman set-up, it is not possible to see the Brillouin scattering as the low energy modes lie too close to the laser line and are thus cut-off by the filters. Optical phonons, of energy close to molecular Raman modes, can be detected.

The Raman scattering process is a two-photon process (one-in and one-out). The momentum of light ($p_{photon} = \hbar k = \frac{h}{\lambda}$) is much smaller than the phonon lattice momentum ($p_{lattice} = \frac{h}{a}$), where a is the lattice spacing. This means that only phonons with $p \approx 0$ can be excited during the Raman process in bulk materials so as to conserve momentum. However, in nanocrystals this selection rule gets relaxed. As the phonon mode becomes more localised in real space, due to size confinement, uncertainty in momentum is allowed. This means a broader range of phonon modes can be excited, leading to a broader line-width. They also red-shift and become asymmetrically broadened on the low-energy side due to the dispersion of optical phonons.

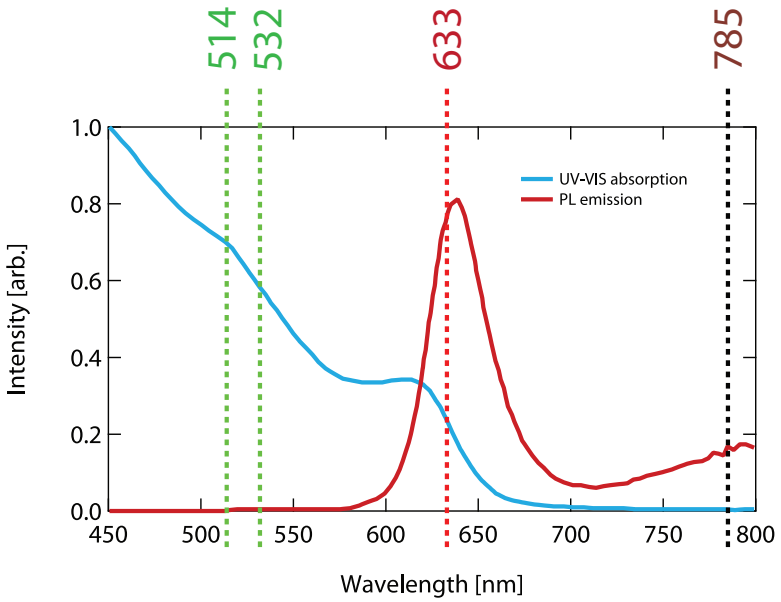

Figure 5.3.: PL emission and UV-VIS absorption of 640 nm emission CdSe quantum dots. Overlaid are the Raman excitation wavelengths used in this thesis illustrating the possibility of excitation on and off quantum dot resonances. [117]

5.2.1. Resonance Raman scattering

A system with defined electronic transitions, such as a quantum dot, has the potential to undergo resonance Raman scattering. Here the normal Raman scattering is greatly enhanced when the incident radiation is resonant with an electronic transition. Some semiconducting quantum dots have important electronic transitions in the visible range, leading to the absorption and emission of photons. This makes them perfect candidates for resonance Raman scattering. By varying the incident laser wavelength we can probe the quantum dot on absorption, emission or off-resonance.

5.3. Method

In this chapter CdSe/ZnS core/shell QDs (Nanocotechnologies Ltd.) with 6 nm diameter and an emission peak centred at 640 nm were attached to nanostructured gold surfaces. Two well-characterised plasmonic substrates were used: Klarite

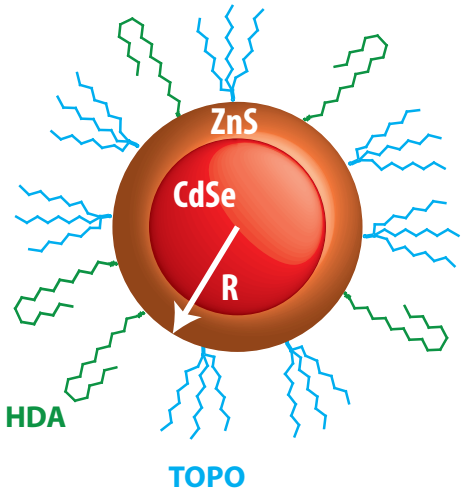

Figure 5.4.: CdSe/ZnS core/shell quantum dot with organic ligand stabilization. TOPO = trioctylphosphine oxide and HDA = hexadecylamine. Not to scale.

(Chapter 4) and graded nanovoids, [118] comprised of hexagonal arrays of truncated spherical voids of controllable thickness (Fig. 5.10a). The QDs are capped with hexadecylamine (HDA) and trioctylphosphine oxide (TOPO) which act as binding and stabilizing agents (see Fig. 5.4). Using standard thiol chemistry (as described in Sec. 3.4) a self-assembled monolayer of 3-mercaptopropionic acid (MPA) was adsorbed on the gold surfaces. The thiol displaces other species adsorbed on the surfaces and ensures sub-monolayer coverage of quantum dots due to only weak hydrophobic interactions with the QDs. The modified surfaces were then placed overnight in a 1 mg/ml solution of QDs in toluene to allow the QDs to bind to the surface. They were then rinsed to remove excess QDs. Using AFM we quantify the coverage as $\sim$1000 QDs/μm^2 (see Fig. 5.6) using the template-striped gold (TSG) technique described in Appendix A.

Successful attachment of QDs on the Klarite surface is confirmed by the large fluorescence emission profile observed on excitation at $\lambda_{ex} = 633$ nm (Fig. 5.7), when compared to the Klarite surface coated with 3-MPA alone.

Both the Klarite nanostructure and 'flat' gold (which has nanoscale roughness caused by the deposition process) were used to record SERS spectra. Raman spectra of bulk QDs were acquired for comparison by drying a concentrated (50 mg/ml) solution into an opaque agglomerate. Measurements were taken at three excitation wavelengths: $\lambda_{ex} = 785$ nm, 633 nm and 514 nm using a Renishaw RM1000 spectroscope (as de-

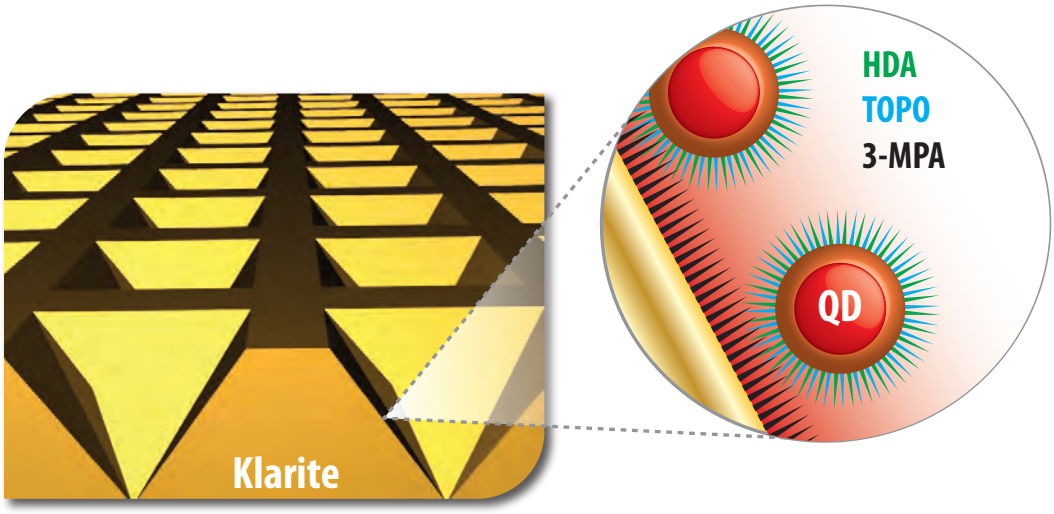

Figure 5.5.: Thiol-attachment of QDs on the Klarite nanostructured surface. HDA=hexadecyalmine, TOPO=trioctylphosphine oxide, 3-MPA=3-mercaptopropionic acid

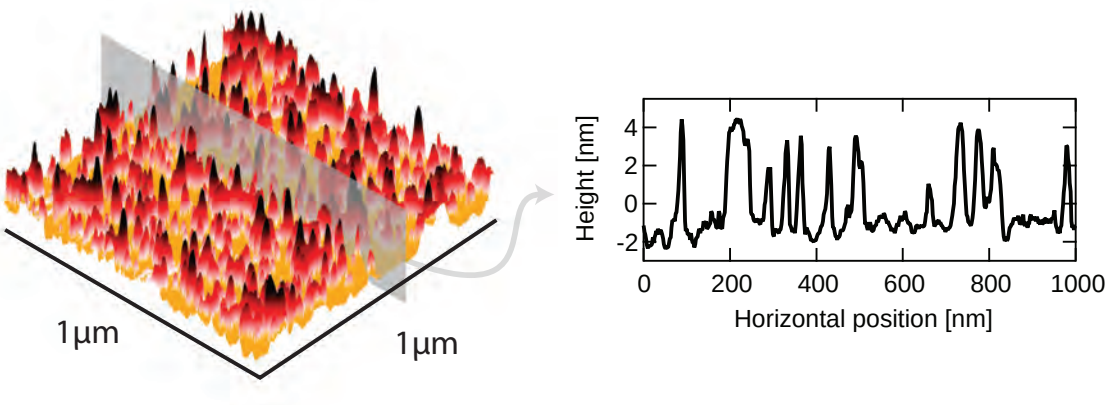

Figure 5.6.: AFM image of quantum dots on top of a flat template-stripped gold (see Appendix A) coated with a 3-MPA SAM. Cross-section profile extracted from the AFM image as shown.

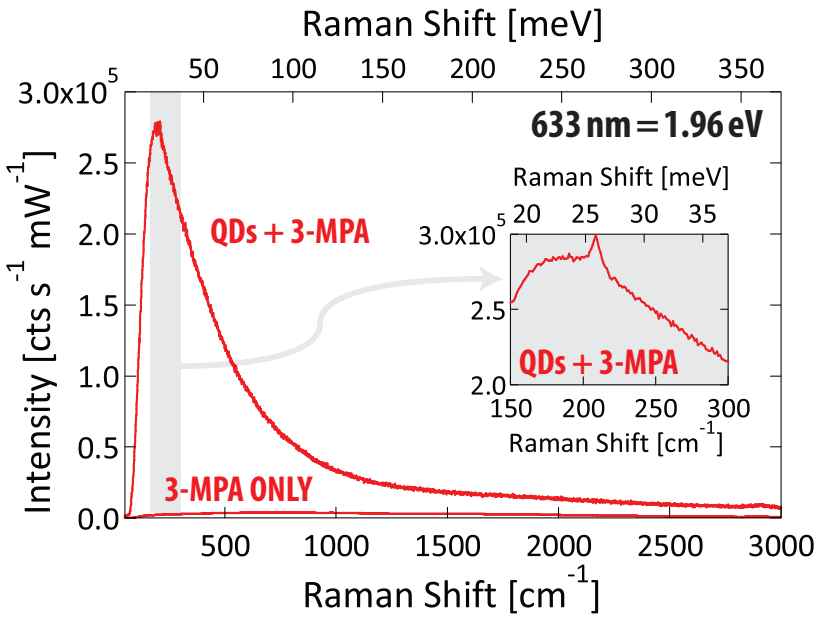

Figure 5.7.: SE(R)RS spectra from the Klarite surface with MPA thiol only and on addition of QDs. Inset shows SERRS phonon peak at 208 cm^{-1}.

scribed in Chapter 3. This allows comparison of SERS on and off resonance with the QD absorption and emission transitions as well as the plasmonic resonances of the Klarite structure.

5.4. Results and discussion

The QD SERS spectra on Klarite nanostructures and on flat gold, with the corresponding Raman spectra of bulk aggregated QDs, are shown in Fig. 5.8. [1] On Klarite at all three laser wavelengths, a SERS peak at 208 cm^{-1} is present. This peak corresponds to the longitudinal optical phonon mode LO(1) of CdSe. [120, 121, 122] Also observed is the two-phonon mode, 2LO(1). The SERS enhancement of these phonon modes varies strongly with the laser excitation wavelength, being more than 100× stronger at 633 nm [note y-scale in Fig. 5.8(a-c)].

We see no evidence of a ZnS phonon from the ZnS shell. Since the bandgap of ZnS is greater than CdSe and just outside the visible range (for bulk wurtzite-phase ZnS it is 3.91 eV), there can be no RRS at the excitation wavelengths used here. This means we are unlikely to see a ZnS phonon peak compared to the resonantly probed CdSe

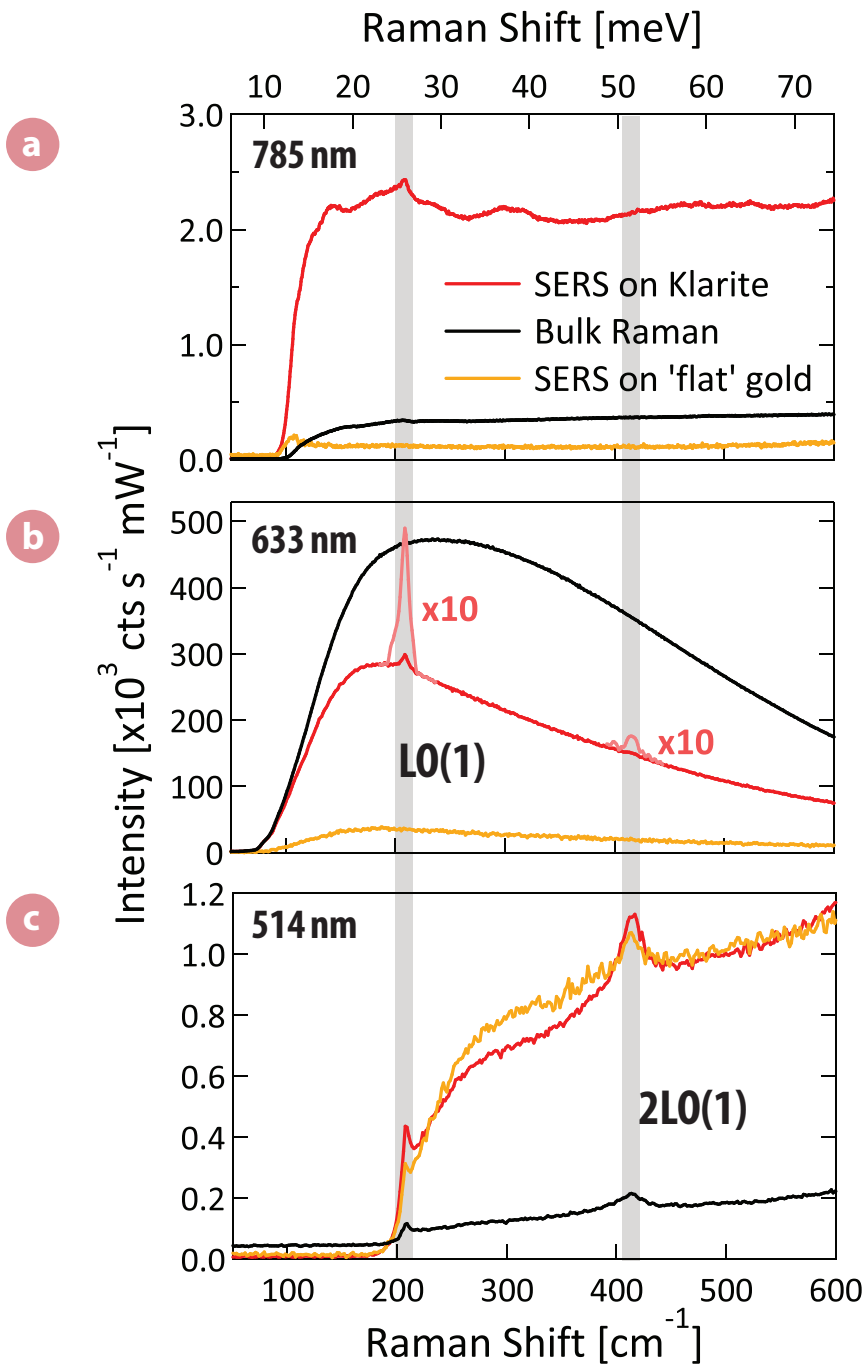

Figure 5.8.: QD SERS spectra from Klarite and flat gold substrates, using laser excitation wavelengths (a) off-resonance at 785 nm, (b) on emission resonance at 633 nm, and (c) within the absorption resonance at 514 nm. Raman spectra of bulk aggregated QDs are also shown. For 633 nm, the region of the spectrum near the LO phonon modes is overlaid at 10× the actual intensity. The peak at 35 meV in (a) comes from the MPA. [119]

phonons. Further to this, using non-QD resonant 785 nm excitation, the phonon peak for ZnS is still not observed. Due to the relatively low amount of ZnS shell coating relative to the CdSe core, we expect the intensity of any ZnS phonon peak to be far less than those for CdSe. Others have observed the ZnS phonon peak [122] at 350 cm^{-1} but at intensities equal and less than the 2LO(1) CdSe peak. Since we do not observe this peak at 785 nm it is not surprising we see no evidence of a ZnS peak.

At 785 nm [Fig. 5.8a], the SERS on Klarite displays more peaks than at other laser wavelengths. In the low frequency region shown, although the principal CdSe LO(1) mode dominates (128±5 counts s^{-1} mW^{-1}), peaks corresponding to SERS of HDA, MPA and other adsorbed species are also observed. [119] At this wavelength we are outside of the absorption resonance of the quantum dots and observe no quantum dot PL. No SERS is seen on 'flat' gold as expected from the absence of localised plasmon modes. SERS at 785 nm of both molecules and quantum dots is enhanced by the substrate due to the localised plasmon resonances of the Klarite nanostructure (see Chapter 4). At this wavelength, Raman of the bulk aggregated QDs (with $\sim 10^3$ times more QDs in the laser focal volume) shows a weak CdSe LO(1) peak (10±5 counts s^{-1} mW^{-1}), whilst other peaks are absent. This weak peak in the bulk allows us to calculate an approximate SERS enhancement factor (as per Eq. 4.1) of $\sim 10^4$. A better comparison would be to that on the flat gold, as this removes possible changes in the aggregated case due to QD-QD interaction, however this was not possible due to the LO(1) peak not being visible at this excitation wavelength on flat gold.

The mode area of the 785 nm Klarite plasmon resonance at the gold surface (see Chapter 4) is around 1 % of the total Klarite surface area. To calculate the average signal from each QD we use the QD density calculated above, and assume a diffraction limited spotsize, which for the ×20 objective used here is 2.4 μm^2 for $\lambda_{ex} = 785$ nm. This means that at $\lambda_{ex} = 785$ nm we get ~ 5 counts QD^{-1} s^{-1} mW^{-1} for the LO(1) mode.

Closer inspection of the LO(1) peak reveals a non-symmetric line-shape with a double peak structure with a low-frequency shoulder. The low-frequency shoulder can be assigned to optical surface phonons at an energy slightly lower than the longitudinal optical phonon in CdSe. [121, 122, 123, 124, 120] Surface phonons result from the small dimensions of the QD and the boundary conditions imposed by the

surface.

At 633 nm [Fig. 5.8b], the laser is on resonance with the QD absorption (principally the lowest $1S_{3/2}$-$1S_e$ transition [125]) *and* QD emission as well as a localised plasmon resonance of the Klarite nanostructure. An intense background from PL of the QDs is observed which dwarfs the molecular Raman peaks seen at 785 nm. While Raman of bulk QDs and on 'flat' gold show no LO phonon Raman peaks, the QD SERRS signal on Klarite shows a strong LO(1) ($17.8\pm0.6 \times 10^3$ counts s^{-1} mW^{-1}) peak and a corresponding 2LO(1) harmonic ($2.6\pm0.3 \times 10^3$ counts s^{-1} mW^{-1}). Although PL/fluorescence is also enhanced by the plasmonic nanostructure, the metal surface facilitates heavy quenching of the PL. This does not affect the much faster SERS process due to the quasi-instantaneous Raman transition.

The SERS peak at 633 nm is $\sim 10^2$ times the SERS signal at 785 nm. This figure even includes a scaling factor to allow more accurate comparison to 785 nm due to the ω^4 dependence of Raman scattering, common with other forms of dipole radiation. [126] Therefore the resonance contribution to the SERRS signal at 633 nm is at least 10^2 times the SERS enhancement alone. Since the plasmonic mode is weaker at 633 nm than 785 nm, the resonance component is likely to be greater. This is supported by the fact that unlike at 785 nm, we cannot see the phonon SERS signal at all in the bulk Raman, despite the large peaks observed on the Klarite surface.

At 514 nm [Fig. 5.8c], the laser is no longer in resonance with QD emission and the absorption resonances shifts to a higher energy QD absorption transition (potentially the $3S_{1/2}$-$1S_e$ transition [127]). The LO(1) peak is clearly visible in the SERS spectra on Klarite although is prematurely cut-off by the Raman notch filter. The 2LO(1) harmonic is now observed very strongly. This appears to have amplitude double the LO(1) phonon line, although we attribute this primarily to suppression of the LO(1) peak by the notch filter cut-off as confirmed by later experiments in Chapter 7. The 2LO(1) peak is 210 ± 5 counts s^{-1} mW^{-1}. This mode is also clearly visible in the bulk Raman (43 ± 1 counts s^{-1} mW^{-1}) giving a SERS enhancement factor of $\sim 5 \times 10^3$. Given the ω^4-dependence of SERS, this should be reduced by a factor of 5.4 when comparing to the enhancement at 785 nm. This results in a plasmon assisted SERS enhancement an order of magnitude below that observed at 785 nm. This is surprisingly high since we are now no longer on a localised plasmon resonance of the Klarite nanostructure. In distinct contrast to the other wavelengths, these results are similarly found for the SERS on 'flat' gold with the 2LO(1) peak only half that

observed on the Klarite structure.

Light at 514 nm is absorbed directly within the QD and so ingoing and outgoing RRS is responsible for the large bulk QD Raman signals observed. This RRS dwarfs the peaks from other adsorbed species (similar to SERRS at 633 nm). The absence of any localised plasmon resonance on Klarite at this wavelength explains the similarity between the SERS signals on Klarite and 'flat' gold. We believe the SERS enhancement at 514 nm may be caused by the excitation of propagating SPPs from weak random roughness of the surface – at 514 nm these SPPs will be more closely confined to the surface than at longer λ. Generally SERS on gold at this wavelength is very weak, however, which is at odds with what is observed here. This could indicate that in fact what is observed is predominately RRS, with little plasmonic enhancement. This explains the similarity in intensity between the 'flat' and Klarite samples. However, based on this, we would expect much larger bulk signals. This could be due to the difference in exciting the QDs on a gold surface, and in an aggregated form. To understand this further studying the enhancement to QDs in a dielectric matrix, or in a dilute layer on a non-metallic substrate, is desirable.

5.4.1. Core only quantum dots

Colloidal quantum dots are typically constructed in a core/shell arrangement. The optically active core is surrounded by a semiconductor of higher bandgap energy. In this case CdSe cores have been surrounded by ZnS shells. The shell protects the core from environmental degradation such as oxidation and improves the quantum yield of photoluminescence by passivating the CdSe core surface and removing non-radiative decay sites. [128] Exciting CdSe core-only QDs, of the same PL emission wavelength as the CdSe/ZnS QDs above, we can compare the difference between core/shell and core-only QDs (see Fig. 5.9).

As well as the principal longitudinal optical phonon of CdSe LO(1) and its first harmonic 2LO(1), a new phonon peak around 274 cm^{-1} is observed. This peak is associated with the LO phonon mode of Cadmium Sulphide [129] (CdS) [LO(2)] a by-product of the QD manufacturing process. Nanoco Technologies find a 3 % wt S/Se in their CdSe cores, some of which could be in the form Cd-S as this is a component of the original fabrication precursor. [130] The ratio of CdSe LO(1) to CdS LO(2) appears similar but greater than that seen in a monolayer coverage of ZnS on a CdSe core, [129] suggesting a significant but sub-monolayer coverage which

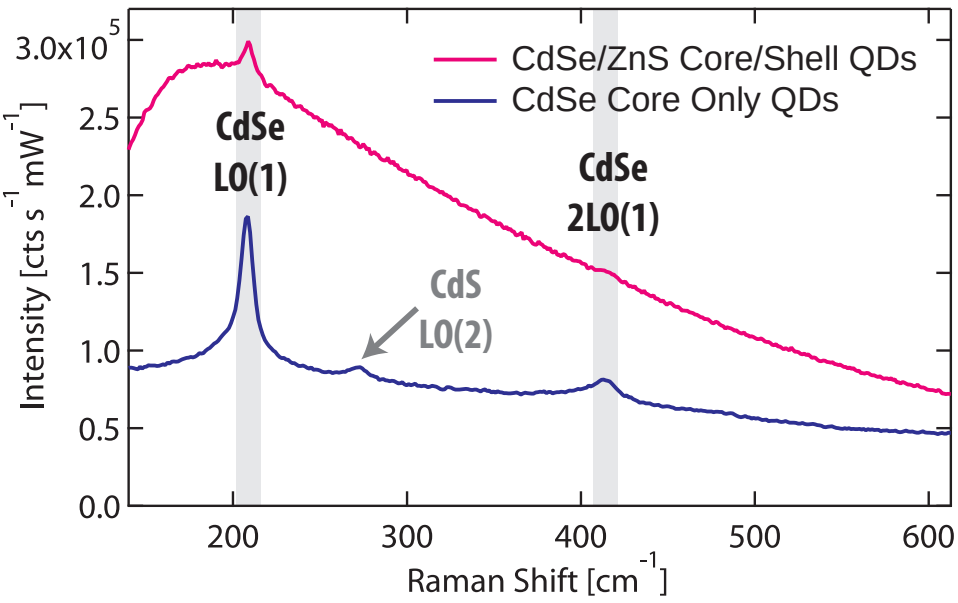

Figure 5.9.: SERRS spectra of CdSe (core-only) and CdSe/ZnS (core/shell) QDs excited at $\lambda_{ex} = 633\,\text{nm}$.

correlates with the suggested weight of sulphur present. This peak was not seen in the core/shell case, probably since the ZnS shell coating displaced sulphur surface defect states on the core surface. [122] It is also clear that the PL is reduced in the CdSe-only case compared to the core/shell case and the Raman peaks are enhanced.

5.4.2. SERS on nanovoid structure

The previous data demonstrate the SE(R)RS of QDs and its tunability with excitation wavelength. To demonstrate the dependence of QD SERRS on plasmonic resonances we use a graded nanovoid sample (Fig. 5.10a), fabricated in-house by Dr. Sumeet Mahajan. Nanovoids are fabricated by electroplating through a monolayer of self-assembled spheres, which are subsequently removed to give an array of interconnected voids. By retracting the template from the electrodeposition solution at various intervals, different thicknesses can be deposited on the same sample resulting in a graded substrate. [118] Plasmons on nanovoid surfaces are well characterised and tune with the void depth [68, 131].

A graded gold nanovoid substrate templated with 600 nm diameter spheres, which possesses plasmon resonances around 2 eV, was fully mapped using reflectance mea-

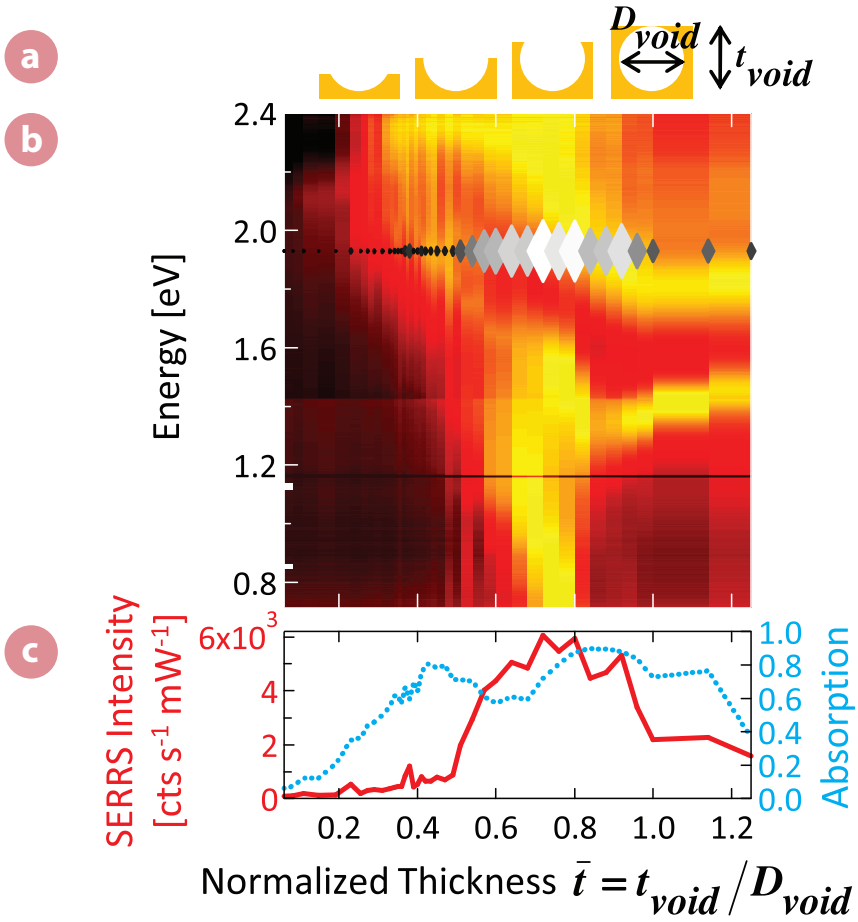

Figure 5.10.: (a) Nanovoid geometry versus thickness. (b) Image: Reflectance versus thickness (normalised to the void diameter) for graded nanovoid sample, yellow indicates low reflectivity (plasmon resonant absorption). Image overlaid with SERRS amplitude (as marker size) of the CdSe LO(1) mode excited at 633 nm. (c) Sample absorption (dashed) at the Stokes Raman energy (1.93 eV) and SERRS amplitude (line), versus normalised thickness.

surements (Fig. 5.10b) on the angle-resolved goniometer described in Chapter 3. After QDs were attached to the surface, SERRS measurements were carried out using 633 nm laser excitation, at regular spaced intervals across the sample (corresponding to different normalised thicknesses). This allows comparison of the plasmon resonances with the SERRS enhancement.

The background-subtracted peak height of the CdSe LO(1) mode is plotted over the reflectivity data revealing how the SERS enhancement of the LO(1) mode increases as it comes into resonance with the localised plasmon modes of the void indicated by absorption dips in the reflectivity. This proves the importance of localised plasmons for SERRS enhancements and supports results seen previously for molecular SERS on nanovoids. [68, 114]

5.5. Conclusions

These results demonstrate that SE(R)RS is an appropriate tool to directly measure phonon excitations in QDs, giving signals of $\sim 5\,\text{photons}\,\text{QD}^{-1}\,\text{s}^{-1}\,\text{mW}^{-1}$ which can be further optimised. Phonons in CdSe/ZnS QDs are clearly observed at three different wavelengths which give different enhancements due to the relative tuning of emission, absorption and plasmonic spectra on two different plasmon-enhanced gold nanostructured surfaces. This first study paves the way for use of QDs as SE(R)RS markers.

6. Disentangling the peak and background Raman signals

In this chapter we use well-defined thiol SAMs to probe the nature of the localised plasmon resonances on the Klarite nanostructure and the importance of nanoscale roughness. By changing the local density of the SAM and sequestering molecules inside surface hotspots, we find large increases in the SERS signals. These changes are shown to decay back to normal levels over time as the molecules diffuse back out of the hot spots. Here, we use a low-energy mechano-chemical process (conventionally termed a 'snow jet' process) to perturb molecules on a SERS substrate, and track the dynamics of the different contributions to the SERS enhancement. This allows identification of components which arise from changes in molecular distribution and from surface morphology.

There are many factors which affect the measured SERS enhancement on plasmonic nanostructures; the most important of these depends on the localized plasmonic resonances on the structure. Our nanostructures have localized plasmon resonances tethered to specific positions within the structure defined by its geometry. [83, 68] The plasmonic areas give the principal EM part of the SERS enhancement to molecules adsorbed in those regions. In addition to this, the metal surface roughness, at atomic and greater length scales, has been shown to alter the CE effect [132, 133, 134] as well as aiding coupling of light into the plasmonic modes. The orientation of molecules on the surface affects their Raman selection rules and therefore the relative peak intensity since the Raman polarizability tensor is modified. Laser heating of the sample has also been shown to affect molecular orientation and the Raman polarizability tensor. [135]

6.1. SERS background

As well as the complex EM and CE enhancements introduced in Chapter 2, SERS signals are accompanied by an underlying broad continuum, the 'background'. The background has proved to be one of the most enduring elements of SERS remaining to be understood. It has received relatively little attention in recent years by the SERS community, with many ignoring it completely. It is generally assumed to occur due to coupling between the well-defined energy levels in the molecular system and the broad electronic continuum of energy states in the metal (though many groups attribute it to 'surface contamination'). There are many competing theories as to the exact mechanism causing this background, most of which emerged towards the end of the 1970s [136, 137, 138, 139, 34] and have been reviewed by Furtak and Reyes. [140] A more promising model based on coupling between the molecule and its image dipole in the metal substrate has recently been discussed and developed by our group. [141] On top of this limited progress, none of the models have attempted to predict how the background differs with substrate geometry and therefore none have been successful at accurately emulating real SERS spectra. Understanding the real nature of the background and how to control it is critical to extending SERS to quantitative analysis and providing further enhanced signals for advanced diagnostic and analytical applications.

6.2. Snow jet

The snow jet process (Fig. 6.2) is a commonly used cleaning procedure in nanofabrication, which removes organics and particulates from a surface by firing CO_2 microcrystals at it. A combination of the excellent solvent properties of CO_2, its low temperature and the momentum imparted by the crystals facilitates the cleaning. [142] Until now, the process has been used purely as a cleaning technique, principally on flat silicon surfaces where it has widespread industrial use in the silicon electronics industry. Here, we extend and study its use for cleaning nanostructured SERS substrates and as a tool for inducing transient perturbations to the SERS process allowing us to track short-term changes to the strength of the SERS signal and background. Furthermore, during SERS measurements both temporary and permanent changes to the system can occur due to the laser irradiation involved. This can cause transient changes to the substrate including local heating, annealing, changes

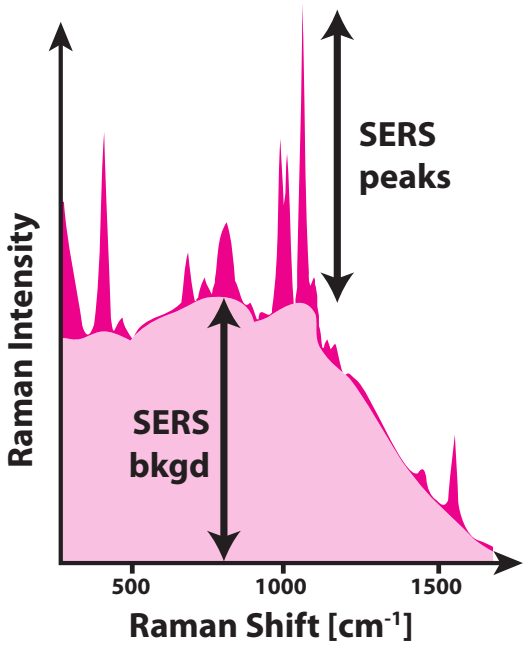

Figure 6.1.: SERS spectra consist of a series of peaks corresponding to the Raman active molecular vibration modes (SERS peaks) which are accompanied by a broad background continuum (SERS bkgd). In this case the molecule is benzenethiol.

in molecular orientation, photodamage to the molecules or their desorption from the surface.

We study the effect of the snow jet process on the transient response of the SERS peaks and the background. We use the multiplexed time-varied exposure (MTVE) procedure (Sec. 3.2.1.1) to study the time and laser heating effects on SERS. The study of the decay of snow-jet-induced transient processes coupled with the MTVE measurements helps to distinguish the effects of laser heating from those which are a function of time (such as relaxation processes) on the SERS substrate. Using this we disentangle the contributions to the peak and accompanying background in the SERS process. Our work points to differing origins of the peak and background signals in SERS and highlights the additional dependence of the SERS background on the local morphology.

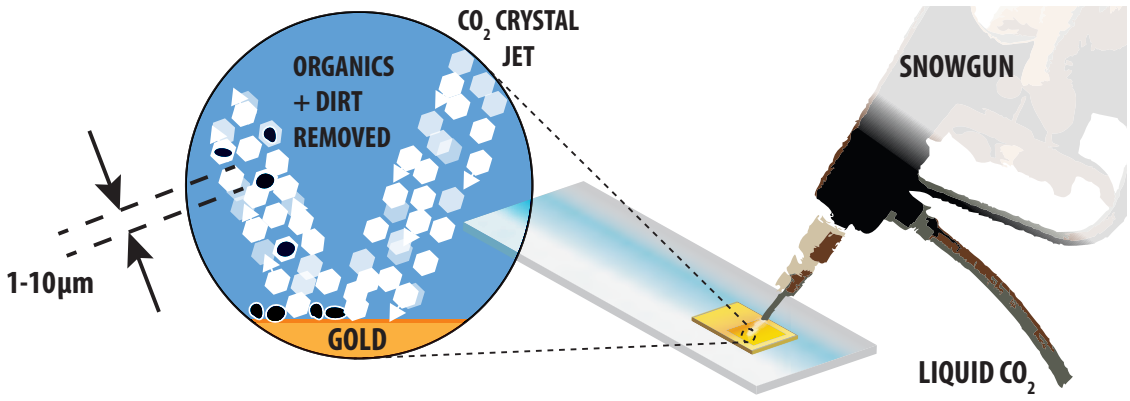

Figure 6.2.: The snow jet process removes dirt and organic materials from the gold surface via blasting with a stream of carbon dioxide microcrystals.

6.3. Experimental section

6.3.1. Substrate preparation

The SERS substrates used were Klarite as introduced in Chapter 4. SAMs of benzenethiol (BTh) were formed on Klarite by placing the new, clean substrates into 10 mM ethanolic solution for at least a few hours before being removed and washed thoroughly with ethanol to remove any excess thiol. This is a well-documented technique used throughout this thesis for forming SAMs as described in Sec. 3.4. [45]

6.3.2. Snow jet experiments

The samples were snow jetted with solid carbon dioxide crystals using a snow jet unit manufactured by Applied Surface Technologies (the only vendor). The samples (mounted on a microscope slide) were vacuum clamped to a hot plate, with the sample surface reaching a temperature of T= 100 °C just prior to snow jetting to reduce ice build-up during the process. This momentary uniform heating causes a small decrease in the average SERS peak intensities as can be seen in the non-snow jetted areas in the Raman mapping data discussed in Sec. 6.4.2. As described later, this further supports the conclusions drawn in this study that despite this decrease, snow jetting results in massive improvements in signal. The samples were snow jetted for a period of two minutes with the jet continuously moving around the active area of the sample.

6.3.3. Raman measurements

The SE1000 Raman system equipped with a 185 mW 785 nm laser was used for the SERS measurements. Raman spectra were taken with 10 s integration times and two acquisitions. The laser has a large spot-size of 120 µm. The average power density in this case is 1.6 kW/cm^2, which is at least a few orders of magnitude less than those typically used in SERS measurements ($\sim$ MW/cm^2). Most importantly, there was no significant evidence in the SERS spectra of laser damage to the thiol when compared to control experiments with a more focused laser which resulted in burning and decomposition of the thiol as indicated by a reduction of the thiol peak intensities and the growth of a peak at 980 cm^{-1} corresponding to the oxidation of the sulphur head group. [143] To further minimize the impact of any desorption effect, the points were pre-exposed to the laser illumination to energetically remove any loosely bound thiols, which reduced the signal to a stable point before MTVE measurements were made. In-house software was developed in Igor Pro (Wavemetrics Inc.) to control the instrument and record spectra in array and time-resolved SERS measurements. The MTVE technique (described in Sec. 3.2.1.1) was used to distinguish between time-dependent and laser heating dependent relaxation processes. The MTVE technique was performed both before and after the sample had been snow jetted to observe the transient behaviour of the SERS signals over several days.

6.3.4. Raman mapping measurements

Raman mapping measurements were performed using the inVia microscope (Sec. 3.2.2) using a $\times$5 objective. A Klarite sample was coated with a BTh SAM as previously described. A 'Raman map' was recorded over a large area of the sample (0.4 mm $\times$ 4 mm) using the 785 nm line laser and the streamline acquisition mode (Sec. 3.2.2). The laser power was reduced to such an extent as to not alter the signal of BTh on repeated measurements of the same area. The total acquisition time was 1 hour and 4247 spectral points were recorded. A restricted area of the sample was then snow jetted for two minutes (as in MTVE experiments) and a comparative SERS map was recorded afterwards of the same area.

6.4. Results and discussion

6.4.1. Removal of non-thiol organics

A Klarite sample coated with a BTh SAM was left in ambient atmosphere over a period of a few days, during which it became weakly contaminated with other organics as identified in the SERS spectra in Fig. 6.3a. After the sample was snow jetted the non-BTh peaks disappear from the SERS spectra (Fig. 6.3b) indicating removal of organics which had been adsorbed into the BTh SAM. [2] The contaminants, with low bonding affinity to gold are removed by dissolution in the CO_2 crystals impinging on the surface, while the BTh, with its high binding affinity to gold, remains attached to the surface. The snow jet process is thus able to clean the surface of unwanted organics while leaving target molecules unharmed, which supports existing studies that show the snow jet process can remove non-bound organics. [144, 145] Fig. 6.3 also shows evidence of new SERS peaks appearing at $1269\,\mathrm{cm}^{-1}$ and $1460\,\mathrm{cm}^{-1}$ after snow jetting. These modes can be assigned to the **3**(b_2) bending and **19b**(b_2) stretching lines of BTh, and indicate a reorientation of the BTh molecules on the surface, since, based on the Raman selection rules, these modes should be enhanced for molecules lying flatter on the surface. [146, 147, 36]

In Fig. 6.3 we also observe relative peak intensity changes between the spectra before and after snow jetting. This is especially evident in the benzene ring modes between $999\,\mathrm{cm}^{-1}$ and $1074\,\mathrm{cm}^{-1}$ (*). The ratio of the $999/1074\,\mathrm{cm}^{-1}$peaks changes from 0.6 before snow jetting to 1.1 after snow jetting. This clearly indicates a change in the BTh polarizability tensor and is suggestive of a re-orientation or phase-change of the SAM. Over the course of the experiment, this relative peak height did not revert to its original position but remained constant, indicating a permanent change and is therefore not linked to the subsequent decay in SERS signals. This reorientation could be linked to the removal of non-bound organics, as these do not return over the time-scales explored here as evidenced by the lack of re-appearance of non-BTh peaks in the post-snow jet SERS spectra.

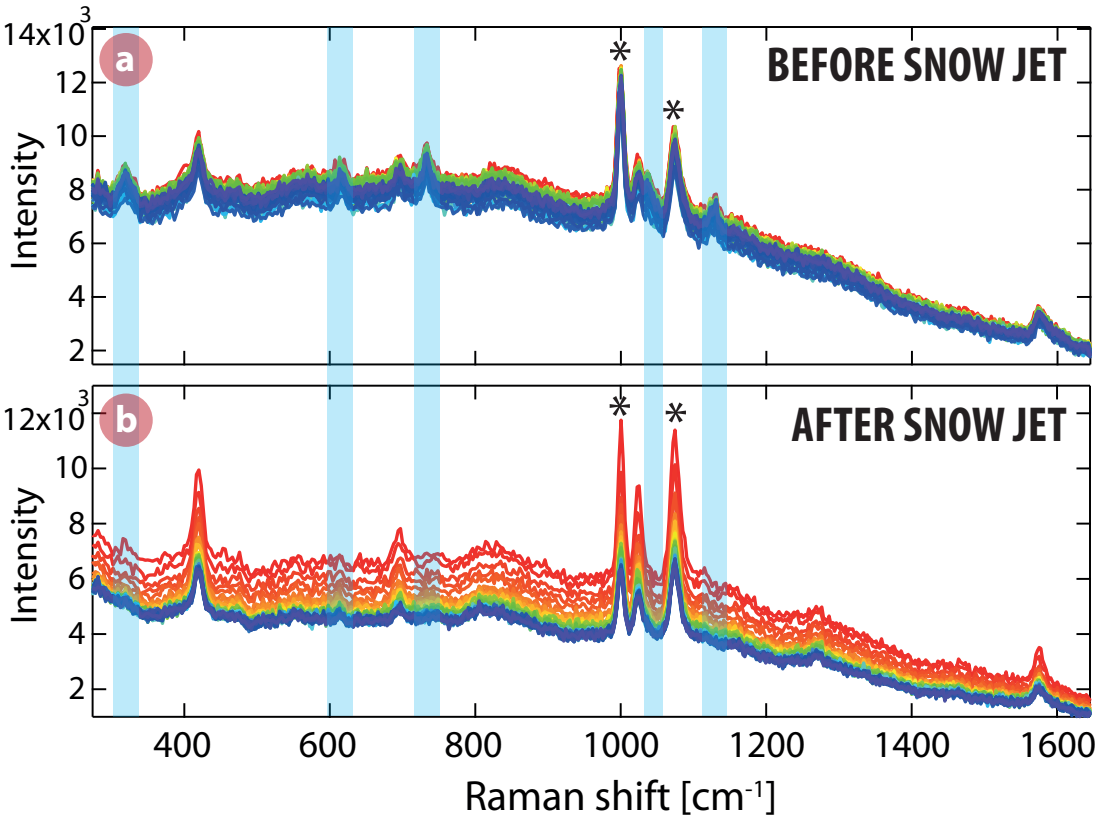

Figure 6.3.: Fingerprint region of the SERS spectra of a BTh monolayer on Klarite **(a)** before and **(b)** and after snow jetting. Each spectra is recorded after 15 min intervals with time progressing from red to blue using the acquisition parameters specified in Sec. 6.3.3. After snow jetting the timer is reset and measurements continue on the same position on the sample as before. Presence of non-BTh peaks (before snow jetting) indicated with blue shaded boxes. Distinct changes to relative peak heights are highlighted with asterisks (*).

6.4.2. SERS peak and background signal before and after snow jet perturbation

The peak height (defined as the absolute intensity minus the background) of the different vibrational modes of BTh is the same for all measurement points before snow jetting (within a variation of <15 %). The peak height for the 1074 cm^{-1} BTh ring-breathing mode is plotted in Fig. 6.4. Background heights (taken from a spectral position near each peak) before snow jetting vary slightly more in absolute intensity (±20% of mean) for the different sample points, and unlike the peak height drop off over initial MTVE measurements before snow jetting (by around 5 %). This indicates that the background is much more sensitive than the peak to the surface environment and spectral acquisition conditions.

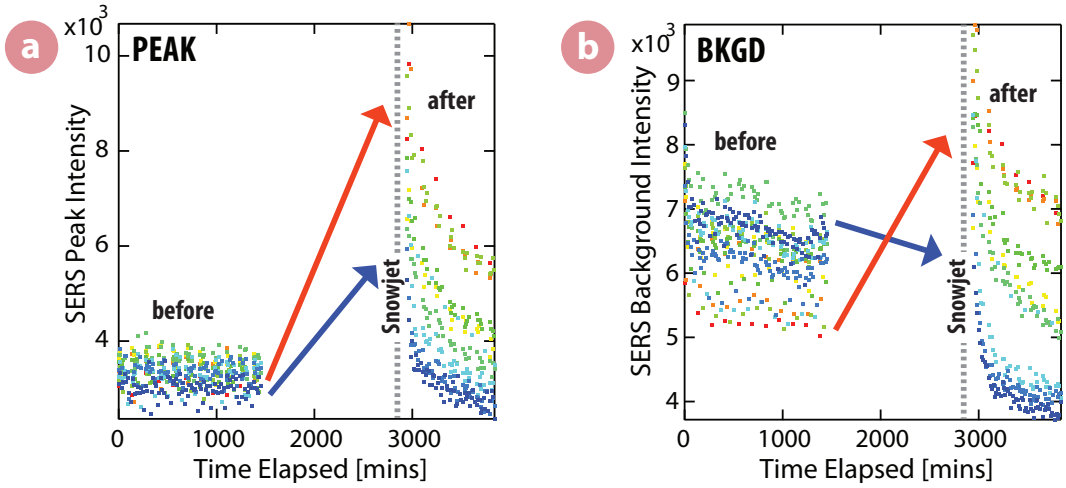

Figure 6.4.: 1074 cm^{-1} BTh **(a)** peak intensity only and **(b)** the background intensity before and after snow jetting Klarite nanostructure. Points on sample represented by colour from the least measured Point A (red) to most measured Point I (dark blue).

After snow jetting, the intensity of the 1074 cm^{-1} BTh SERS peak increased across all points on the sample, but by differing amounts depending on the measurement point. This was similar for all the other BTh peaks (not shown). In contrast the background intensity after snow jetting either increased or decreased depending on the position on the sample. This was also consistent for all other positions on the background. That the increase in peak intensity is not always accompanied by an increase in background intensity clearly indicates that the two are decoupled from each other and suggests different origins to the signal change.

6.4.2.1. Raman mapping

The Raman maps of the Klarite sample before and after snow jetting support the data obtained via the MTVE experiments. The areas of the sample that had not experienced the snow jet showed a slight decrease in the average peak intensities (see Sec. 6.3.2) while the snow jetted area displays a clear enhancement over the non-snow jetted areas of the sample as shown in Fig. 6.5. The snow jetted area produced an enhancement of BTh peaks up to 15 times.

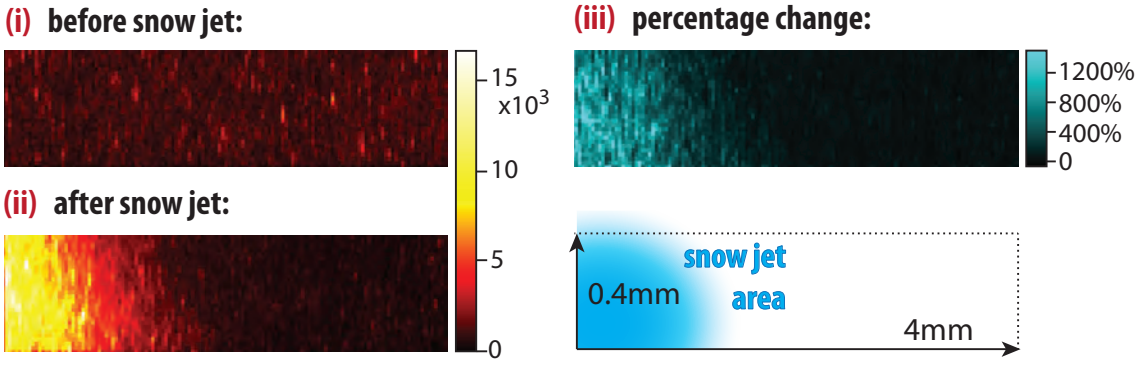

Figure 6.5.: Integrated intensity maps of the 999 cm^{-1} BTh ring-mode peak **(i)** before and **(ii)** after snow jetting a restricted area of the sample as indicated in the diagram. Percentage increase in integrated intensity after snow jetting is shown in **(iii)**. The increase in the snow jetted area is up to $> 1500\,\%$.

6.4.3. Signal decay after snow jetting using MTVE

After snow jetting, both the SERS peak and background signal begin to decay away from their new levels as seen in Fig. 6.4 and Fig. 6.6. The decay occurs both as a function of exposure (via laser heating) and as a function of time elapsed after snow jetting. The peak signal drops back to its original level after snow jetting, suggesting that the number of thiol molecules attached to the surface has not changed significantly and that they return to a similar state to that before snow jetting. The background signal also decays but not necessarily back to the position it started at before snow jetting. Using the MTVE method discussed above, we can gain insight into the dominant processes causing these decays. Fig. 6.6a shows the decay of the 1074 cm^{-1} BTh breathing mode (other peaks follow similar decay trends) and (b) & (c) show a nearby background point not associated with any vibration mode of the molecule (1107 cm^{-1}) plotted against both the number of measurements made (proportional

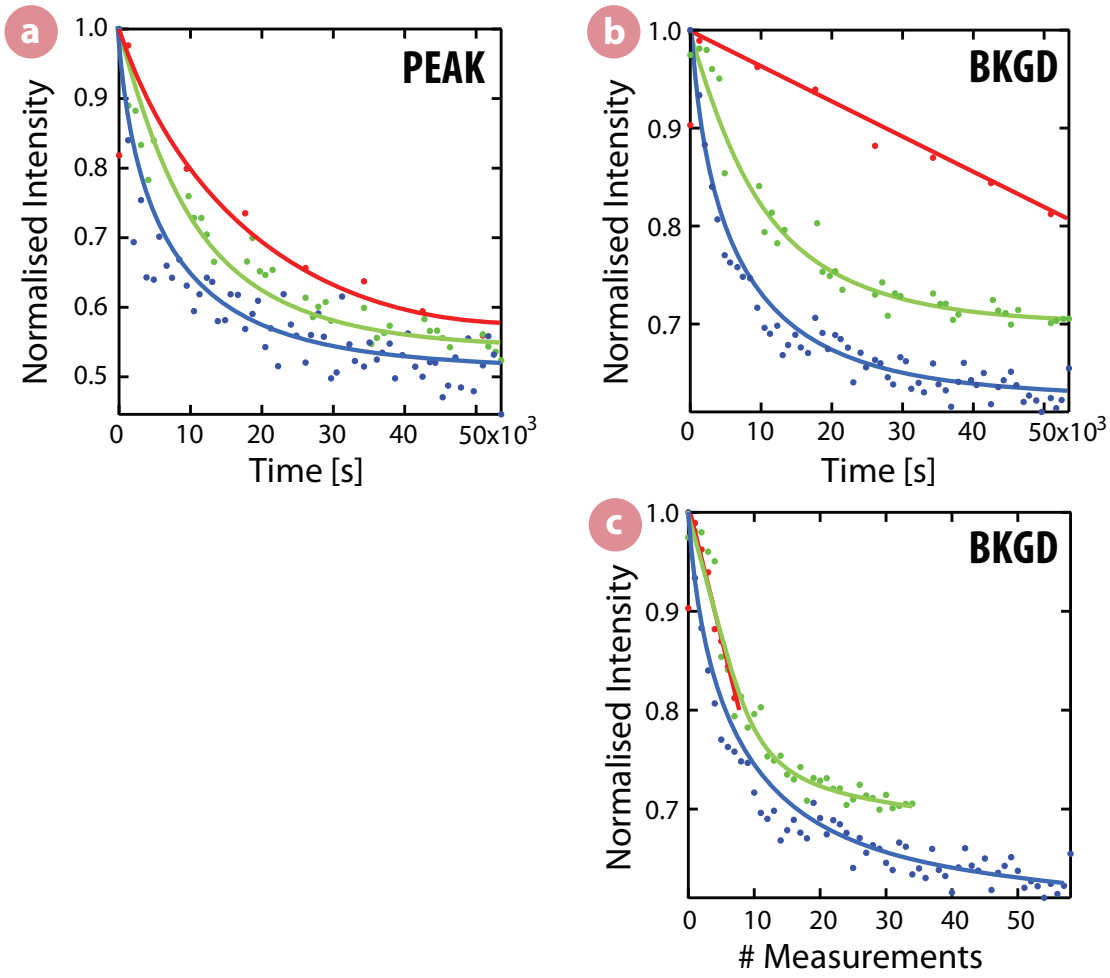

Figure 6.6.: **(a)** SERS peak height of the BTh ring-breathing mode at 1074 cm^{-1} (background subtracted using the intensity at 1107 cm^{-1}) versus total time elapsed. **(b)** Intensity of the SERS background at 1107 cm^{-1} versus total time elapsed and **(c)** versus number of measurements taken. Three different MTVE sample points are shown. Traces coloured as in Fig. 6.4 with red (point A, least measured), green (point E, mid-number of measurements) and blue (point I, most measured). All lines are guides to the eye.

to laser exposure time on the sample) and real time expired. The intensity has been normalized to the initial measurements of each point, to allow better comparison of trace shapes. It is immediately evident that the peak height and background signals decay at different rates, with the background especially affected by the number of measurements. Comparing decay shapes shows that the peak height decay process is principally dependent on real time expired, whereas the background signal has a more significant component related to the number of measurements taken. This reinforces the differing origins of changes to the background and peak signals, both of which are modified by the snow jet: one decays principally over time, while the other decays mainly as a function of laser exposure. To identify the natural decay of the system irrespective of measurement artefacts, we fit an exponential to the intensity versus time decays of the SERS peak and background signals. Due to the mixed nature of the decay, exponentials will not provide a precise decay profile, but they satisfactorily track the relative total decay times. Plotting these decay times as a function of fractional measurement frequency (where the maximum frequency of 1.0 corresponds to Point I which is measured every time, and 0.0 corresponds to a hypothetical point which cannot be measured) and extrapolating, gives an estimate for the natural decay time of the system without laser measurement (Fig. 6.7). This shows that the natural (non-heat related) decay time is around 7.0±2.8 hours for the peak signal and 9.3±2.8 hours for the background signal. This suggests the same origin for both the peak and background natural decay times.

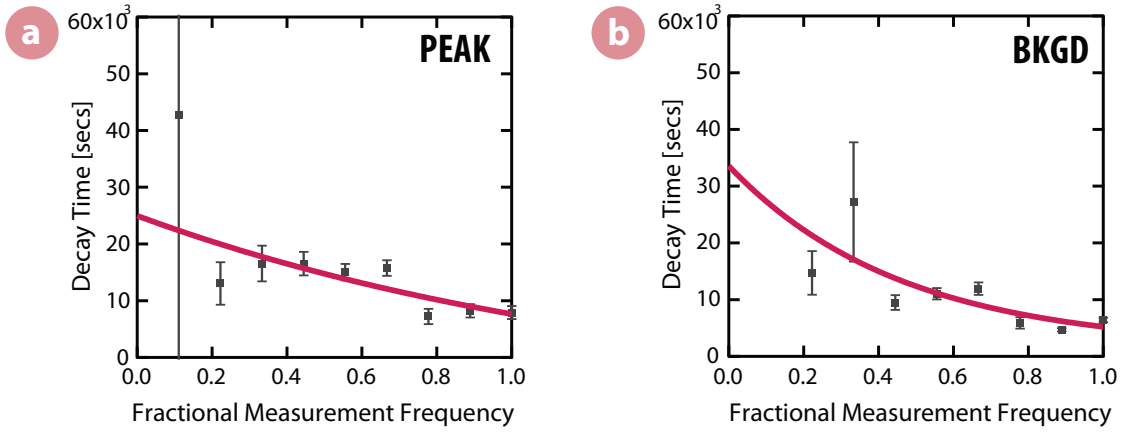

Figure 6.7.: Extracted decay times for all points plotted against fractional measurement frequency (defined in text). The y-axis intercept of the extrapolated fit provides an estimate for the decay time of a hypothetical non-measured point on the sample. **(a)** Peak decay times and **(b)** Background decay times.

6.4.4. Discussion and analysis

Snow jetting the SERS active substrate, as well as removing loosely bound hydrocarbons from the surface, significantly boosts the SERS signal obtained from the strongly bound thiol by on average 250 % for the 1074 cm^{-1} line across the entire sample (Fig. 6.4). This is similar (or even more) for all the other SERS peaks (not shown), with enhancements of up to 500 % found for certain peaks and regions.

The action of snow jetting affects the SERS peak of the molecule and the background signal in dissimilar ways pointing to the different origins of these processes. The molecular SERS peak signal is always boosted in intensity after snow jetting, before decaying away over time ($>$ 12 hours) towards its original value. However the background signal intensity varies differently depending on position on the sample with some points showing an increase after snow jet and some showing a decrease. Irrespective of the level of background signal after snow jet, the signal then decays, with a key component due to laser exposure, and does not return to its original level, unlike the peak signal.

The snow jet process imparts momentum locally to the Klarite surface and the organics held on it and this can cause the molecules to change orientation and position over very small scales. One proposal is that molecules are pushed deeper into nanocrevices that exist between the gold clusters formed during the evaporation process (as depicted in Fig. 6.8 and Fig. 6.10). Since the radii of curvature of these nanocrevices is much smaller than the wavelength of light, we expect localized field enhancements in these regions as previously identified and modelled in nanoscale grating grooves and crevices between nanoscale silver cylinders. [148, 149] The work of Van Duyne and co-workers, also highlight the significance of surface roughness to the SERS enhancement in their work on metal film over silica nanosphere (MFON) surfaces. [150, 151] Molecular diffusion of thiols is well known on gold surfaces, [152, 153] hence we propose that the SERS peak signals rise transiently due to concentration of molecules in these nanocrevices and then over time the molecules diffuse across the surface back to their original lower energy configuration, with the signal returning to its initial value as a consequence. This restorative diffusion process has been observed before in thiol monolayers on similar time scales to that observed here. [154, 152] Such 2D molecular migration has not so far been tracked in real time as here, and gives new insight into their motion on the nanoscale, and how this can be externally affected.

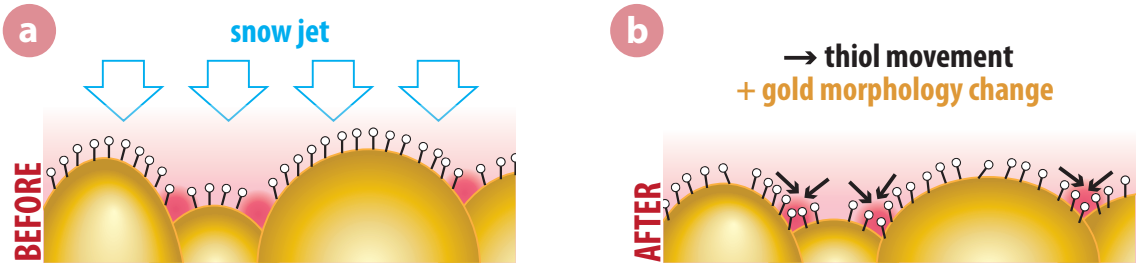

Figure 6.8.: BTh molecules (not to scale) on an evaporated gold surface showing location of nanocrevices with enhanced EM fields **(left)** before and **(right)** after snow jetting. BTh molecules are pushed into the crevices by the snow jet process and also re-orient. The gold surface itself is also modified by the snow jet process.

On a perfectly flat gold surface, a SAM monolayer can form as shown in Sec. 3.4. The packing is maximised if left for sufficient time and the thiol molecules well-aligned and uniformly distributed. In most situations, this ideal case is just an approximation. The roughness and changes in crystallinity of the surface cause defects in the coating. With thiols orienting in various directions and the overall packing density decreased relative to the perfect case. This leaves room for a change in density and packing efficiency when subjected to external conditions such as the snow jet and subsequent molecular diffusion. We can model the crack sequestration theory as the cause of the enhancement after snow jetting by an increase in the density of thiols in the crack hotspot areas. We estimate the density of cracks relative to the total area by considering the roughness as a collection of nanoparticles with radius R = 30 nm in a hexagonal array but packed together, thus increasing the active hot spot area. This equates to a relative area of $\sim 1.0 \pm 0.5\,\%$. We also restrict the increase in density of the hot spot area to not exceed three times that of the original density. We provide an estimate for the enhancement in the gaps to be 1000 times that of the surrounding area. Using this simple model we see in Fig. 6.9a that we nearly achieve the enhancement factors experimentally observed. Increasing the enhancement factor substantially does not yield significant changes, as the original signal from the hotspots is also amplified. The change in density is the important factor here. We note that due to the small size of the nanogaps, it is possible that some of the nanogaps do not have particles in their active region before snowjet, but do after. We thus include a factor which effectively turns off or on a percentage of the hotspots before snowjetting, but due to later occupation are then activated after snow jet. Using a factor of 10 % hot spots activated before snow jet we obtain the

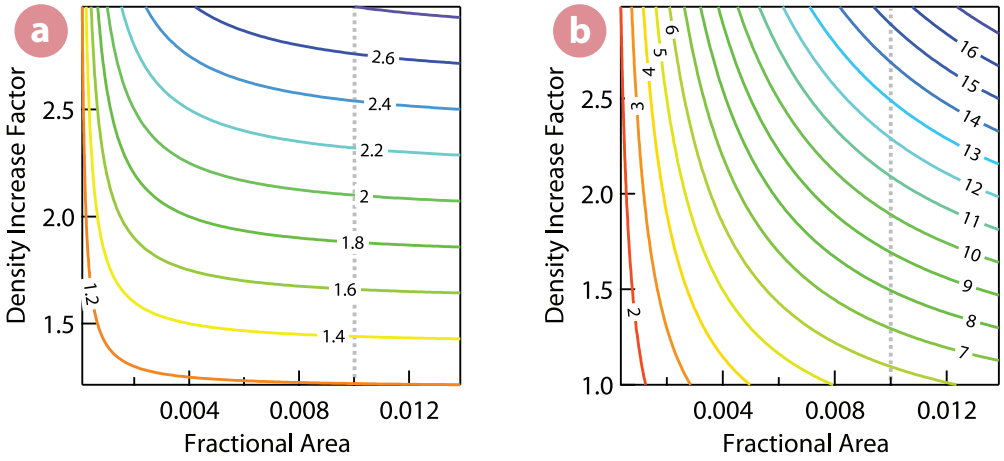

Figure 6.9.: Enhancement of SERS signal after snow jet predicted using model described in text. Estimated density of roughness cracks indicated at 1 % with dashed line. **(a)** Model based on simple increase in density of thiol in cracks after snow jetting and **(b)** adapted model to include percentage of occupied gaps before snowjetting (10 %) compared to those after snow-jetting.

results shown in Fig. 6.9b. This shows a stark increase in the predicted enhancement factors closer to the high ones sometimes seen in the experiments, even for modest changes in density. This simple model shows that even with relatively modest hot spot enhancements the sequestering of molecules into roughness cracks by snow jet may explain the increase enhancement seen in SERS signals.

Along with molecules being pushed into nanocrevices, molecular reorientation takes place as evident by changes in the SERS peak intensity ratios. Much slower decays of the peak intensity are due to slight air-mediated degradation of the SAM over time as evidenced by the re-emergence of the 614 cm^{-1} peak after snow jetting corresponding to an S=O stretching mode. We do not, however, see the peak at 980 cm^{-1} attributed to oxidation observed during our control laser heating experiments (Sec. 6.3.3) and postulate that this could be due to differences in oxidation state of the thiol group in the two cases.

Background signals are also enhanced by high local electric fields. [141, 155] Hence the instantaneous changes in the background are also related to the concentration effect of snow jet moving molecules into nanocrevices. To explain the longer term effects we note that the background is much more sensitive to nanoscale surface geometry than the SERS peaks. This is seen in the different relative SERS:background contributions from nanoparticle versus nanostructured surfaces, and from the greater

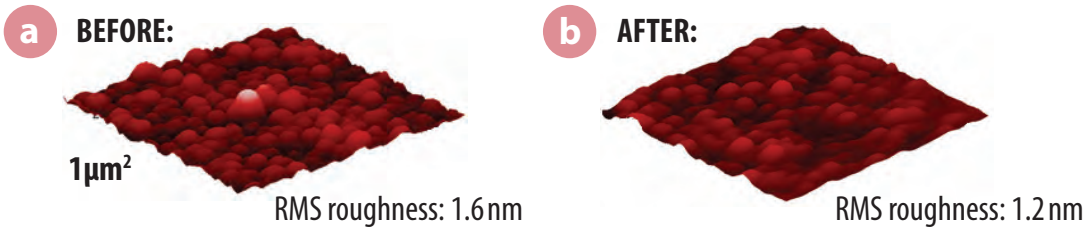

Figure 6.10.: AFM scans of the gold Klarite surface **(a)** before and **(b)** after snow jetting, showing 25 % reduction in RMS roughness after snow jetting.

variability of the background at different locations on such samples. We thus believe that the snow jet process produces nanoscale changes to the gold structure, morphology or roughness, which causes changes in the background signal that either increases or decreases depending on the competitive effects of local enhancement and surface roughness. AFM measurements before and after snow jetting indicate a slight large-scale smoothing of the surface, with the root-mean-square (RMS) roughness being reduced by 25 % as shown in Fig. 6.10. This appears to have both permanent (as the background does not return to its original value) and transient effects (since the background does decay after snow jetting).

Since the background signal is linked with molecular locations (as observation of the background requires molecules, [141]) one component of the dynamics should follow that of the peak, which is indeed observed. In addition, the background signal decays as a function of laser exposure. We suggest that the laser causes local heating of the sample which can affect the fine structure of gold via an accelerated annealing process. The SERS peaks are not significantly affected by the number of measurements (laser heating) and have a decay pathway (after snow jet perturbation) as proposed by the model in Fig. 6.8, however, in contrast, the background depends on local morphology and surface roughness and hence, its decay is dependent on annealing processes, which are likely to be accelerated by laser heating.

6.5. Conclusion

Understanding the background is essential to establish SERS as a mainstream technique for developing quantitative applications. This study [2] highlights the different origins of the SERS background compared to those of the SERS peak signal. Using a soft mechano-chemical process to perturb the surface of a standard SERS substrate

we subsequently track changes to the peak and background as a result of heating and time using a newly-developed MTVE technique. This allows us to identify different contributions to the peak and background signals with differing decay channels. The background signal is strongly dependent on laser heating and the data supports our hypothesis that the background signal is linked to gold morphology or crystallinity, which changes on laser heating and after snow jet. The peak signal appears to be much less dependent on laser heating, showing a distinct decay channel after snow jetting, dependent on time. Using a simple roughness sequestration model, we believe increases to peak signal after snow jetting can be explained by movement of molecules into nanoscale SERS active hotspots, and the subsequent decrease of the SERS peak signal is explained by surface transport of the thiol back to an equilibrium position. The two differing dependencies of the peak and background signal allow us to identify the possibility of reducing the SERS background signal at the same time as increasing the SERS peak signal, desirable for many applications. The results obtained cannot entirely be explained by current SERS theories and thus highlight the need for more in-depth studies of the SERS background based on the geometry of SERS substrates. This work paves the way for new studies into the SERS background and new methods for temporarily perturbing SERS substrates to increase the peak to background signal to noise. It also finally shows, that SERS substrates *can* be cleaned using a cheap and ubiquitous semi-conductor cleaning technique.

7. Temperature dependence of SERS

In this chapter we study the temperature dependence of the SERS signal and corresponding SERS background signal over a large temperature range from $10 - 300\,\mathrm{K}$. In addition to this, we measure SERS spectra using multiple Raman excitation wavelengths on the well-characterised Klarite SERS substrate to separate the different contributing effects to both the background and SERS peak signals.

The importance of the thermal occupation of molecular vibrational levels on the ratio of intensity of anti-Stokes and Stokes Raman scattering was seen in Chapter 2. In SERS the temperature effects become further complicated. As well as the effect of temperature on the molecule or inorganic system, the metal surface, which is defined by its dielectric function, also varies with temperature. This impacts the SERS signal and the SERS background through changes to the plasmon's damping.

As before, we use a self-assembled monolayer (SAM) of benzenethiol (a common SERS marker) or a sub-monolayer of CdSe based quantum dots (QDs) adsorbed onto the SERS structure to study the temperature dependence of SERS using Raman excitation wavelengths $\lambda_{ex} = 532\,\mathrm{nm}$, $633\,\mathrm{nm}$ and $785\,\mathrm{nm}$. We also compared these monolayers on Klarite with the same QDs aggregated on a silicon substrate. This enables us to compare the effect of the SERS to non-surface enhanced QD Raman scattering.

We first look at the case of an organic molecule, benzenethiol, which has been previously studied and then compare to the case with a robust inorganic system, QDs.

7.1. Temperature dependence of SERS

The Stokes Raman intensity remains broadly temperature independent due to the high occupation of the ground state relative to other states over a wide temperature

range. This is in contrast to the strong temperature dependence of the anti-Stokes Raman intensity due to the normally low occupation of excited vibrational states, which varies strongly with thermal occupation. Some systems have Raman polarizability cross-sections which are also temperature dependent leading to temperature dependence in the Raman intensity to the Stokes spectrum as well as the anti-Stokes. This is the case for crystalline solids such as the QDs we consider here. Most molecular systems exhibit negligible changes to their Raman cross-sections over wide temperature ranges.

In SERS, the plasmonic enhancement mechanism depends strongly on the metal as seen in Chapter 2. The conductivity of the metal relates to a change in the dielectric function of the material which determines the nature of localised surface plasmons on the surface. Since the enhancement seen is SERS is directly linked to the localised electric field caused by the plasmon (Chapter 2), changes in the metal dielectric function cause changes to the SERS enhancement. There may also be other temperature-dependent behaviour due to annealing and morphological changes, and absorption and desorption of molecules from the surface.

7.1.1. Temperature dependence of gold

As temperature decreases, a metal's conductivity increases. This is due to a decrease in electron-phonon scattering, as the thermal population of phonons decreases. This relates to a change to the dielectric properties of the gold through the damping term γ in Eq. 2.11. We can split the dielectric function's real (ϵ') and imaginary (ϵ'') components found using the Drude model (Eq. 2.11) as:

$$\epsilon' = 1 - \frac{\omega_p^2}{\omega^2 + \gamma^2} \tag{7.1a}$$

$$\epsilon'' = \frac{\gamma\omega_p^2}{\omega(\omega^2 + \gamma^2)} \tag{7.1b}$$

Assuming $\gamma \ll \omega$ then these equations can be reduced to:

$$\epsilon' = 1 - \frac{\omega_p^2}{\omega^2} \tag{7.2a}$$

$$\epsilon'' = \frac{\gamma\omega_p^2}{\omega^3} \tag{7.2b}$$

The damping term γ is therefore critical to the imaginary part ϵ'' of the dielectric function, but has minimal effect on the real part ϵ'. To appreciate the temperature dependence of the imaginary part of the dielectric function, we examine the temperature dependence of $\gamma(T)$.

The damping $\gamma(T)$ is related to the DC resistivity (inverse of conductivity) of the metal via: [156, 17]

$$\gamma(T) = \epsilon_0\omega_p^2\rho_{DC}(T). \tag{7.3}$$

Eq. 7.3 predicts that the metal's damping $\gamma(T)$ tends to zero as the temperature approaches zero. In this model we have only considered electron-phonon scattering (which dominates DC resistivity) and neglected other damping processes which become important at lower temperatures when considering damping at optical frequencies. The most important of these processes is the spontaneous emission of a phonon by a photon-excited electron; also known as phonon-assisted intraband transitions. [157] This is a temperature independent process and can be accounted for as an offset γ_0 added to the damping in Eq. 7.3. Following the work of McKay et al. [157], the overall damping is related to the fractional absorptivity $A(T)$ of the metal via the Mott-Zener formula, $A(T) = 2\gamma(T)/\omega_p$, where ω_p is the metal's plasma frequency. Since we require γ to have both time-dependent and time-independent terms, so must the absorptivity, such that $A(T) = A_0 + A'(T)$, where $A(T)$ tends to A_0 at $T = 0\,\mathrm{K}$. The damping at optical frequencies thus becomes,

$$\gamma(T) = \epsilon_0\omega_p^2\rho_{DC}(T) + \frac{\omega_p A_0}{2}. \tag{7.4}$$

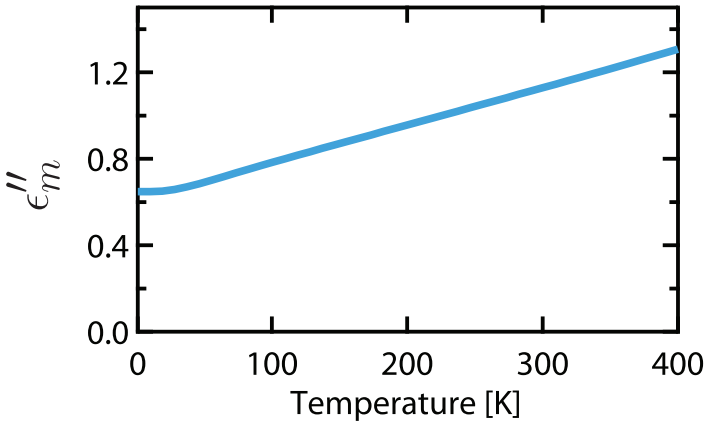

Figure 7.1.: Temperature dependence of the imaginary part of the complex dielectric function of gold (ϵ''_m) for excitation at wavelength $\lambda = 785\,\text{nm}$. The figure was plotted using Eq. 2.12 and parameters $\epsilon_\infty = 8\,\text{eV}$, $\omega_p = 8.9\,\text{eV}$. The temperature-dependent damping γ was calculated using Eq. 7.4, with experimentally calculated values for the DC resistivity of gold [159] and a zero-temperature absorptivity of $A_0 = 0.0072$ [157].

The absorptivity at 4.2 K ($\approx A_0$) has been measured for silver using excitation at $\lambda = 785\,\text{nm}$ to be 0.007 [158]. This value is similar for that of gold, which has separately been found at 0 K to be between 0.0045 and 0.0072. [157]

Using the Drude model from Chapter 2, where we fitted to the experimental data using $\epsilon_\infty = 8\,\text{eV}$, $\omega_p = 8.9\,\text{eV}$ and using the temperature-dependent DC resistivity of gold [159] and a value for the 0 K absorptivity $A_0 = 0.0072$, we can plot the approximate expected temperature dependence of ϵ'' (Fig. 7.1).

The imaginary part of the metal's dielectric function affects the properties of the surface plasmons through the dispersion relation (Eq. 2.17 seen in Chapter 2). For the case of air ($\epsilon_d = 1$) and with $|\epsilon'_m| >> |\epsilon''_m|$, as is the case for plasmonic metals, the imaginary component of the SPP's momentum becomes, [160, 161]

$$k''_x \simeq k_0 \frac{\epsilon''_m}{(\epsilon'_m)^2}. \tag{7.5}$$

This determines the damping of the surface plasmon, where the reciprocal of this also gives the propagation length of the plasmon. The lower the damping, the higher the propagation length, and the longer the plasmonic lifetime. Thus we predict higher quality-factor plasmon modes in the pit, which strengthen the resonant electromag-

netic enhancement.

7.2. Benzenethiol on Klarite

As has been used elsewhere in this thesis, a SAM of BTh was formed on the Klarite nanostructure as described in Sec. 3.4. After rinsing to remove excess BTh from the surface, the sample was set-up in the cryostat as described in Sec. 3.2.2.1. The temperature inside the cryostat was reduced to 10 K. Raman measurements were taken on the Renishaw inVia (Sec. 3.2.2) as the temperature was increased in increments of 30 K back to room temperature (290 K). At each step the temperature was allowed to stabilise ($\approx$ 15 mins) before measurements were taken at different positions on the sample. After a complete cycle, further measurements were taken at 10 K to see if there was any hysteresis. Measurements were recorded at several isolated positions on the sample surface and showed good concordance. Raman measurements were made with a $\times 5$ long working distance objective using the 785 nm excitation laser. Stokes Raman measurements were made between 0 cm^{-1} and 3500 cm^{-1} using the extended scan mode, edge filters and a 1200 lines mm^{-1} grating. The exposure time was 15 s and the laser power was $\approx$ 20 mW after the objective. Minimal effect of laser damage was observed with these parameters as tested by repeat measurements at a single spot giving a repeatable SERS spectrum.

7.2.1. Results

As the temperature was increased from 10 K, clear spectral changes were observed. Most notably a large background 'hump' in the spectra (Fig. 7.2) reduced in intensity as the temperature increased to 140 K, beyond which it showed minimal change in intensity. After the cycle had completed at 290 K, the temperature was reduced back down to 10 K. Interestingly, the spectrum recorded after the return to 10 K did not return to the line shape at the initial 10 K reading, with the background hump no longer present.

This irreversible change could be due to an annealing-like process or a thiol phase change, affecting this portion of the background signal. It could also be the result of surface contamination in the sample preparation process. The sample is attached to the cryostat finger using a commercial conductive silver paste (Electrodag 1415 M,

Acheson Colloiden B.V., The Netherlands). The paste contains various solvents, including ketones and alcohols, which evaporate on application. There could however be some residual solvent that transfers to the sample surface in the cryostat. Further to this, there is the possibility of contamination from water monolayers from the atmosphere, which are very difficult to remove under these vacuum conditions (10^{-5} mbar). These contaminants could be responsible for the background hump observed in Fig. 7.2, although it is unclear why the spectral shape remains broadly featureless. After a cooling and heating cycle the hump is removed, which could be a result of removal of the weakly attached water or solvents by evaporation under the vacuum condition. Since the hump was not uniformly observed throughout experiments, this seems a reasonable explanation.

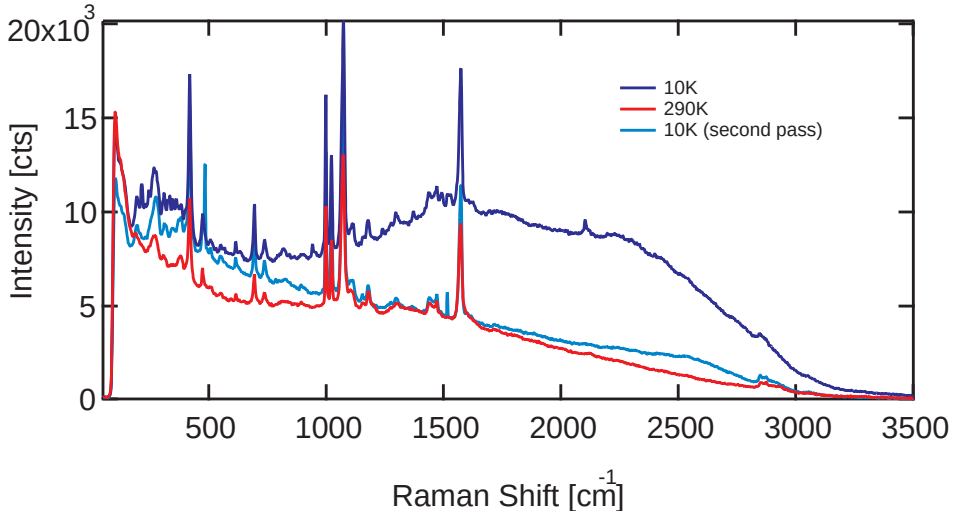

Figure 7.2.: SERS spectra of BTh on Klarite at 10 K and 290 K. Second pass 10 K indicates the spectra after returning to 10 K after a complete temperature cycle. This highlights a non-reversible change to some parts of the background signal in the region from 1000 cm^{-1} to 3000 cm^{-1}. Spectra were taken from a larger dataset as described in Sec. 7.2 at $\lambda_{ex} = 785$ nm using an extended scan with total exposure time of 15 s. In between the first 10 K and 290 K spectra shown here is a series of spectra (not shown) at intermediate temperature steps of 30 K. The second pass 10 K spectra was directly returned to after reaching 290 K.

In addition to this large change to the SERS background, there also appears to be a more subtle and reversible change to the peak signals and the background signal outside the 'hump' area. Extracting the peak intensities we see that the intensity doubles at 10 K compared to that at 290 K and attains a maximum intensity at the higher temperature of 50 K (Fig. 7.3a,b). Moreover, there is also a similar

change in intensity to the background signal. Taking the ratio of the peak intensity to a nearby background intensity, we can see for the $420\,\mathrm{cm}^{-1}$ mode (background: $394\,\mathrm{cm}^{-1}$), outside of the hump area, both the peak and background signal decrease with increasing temperature but the peak intensity becomes weaker relative to the background intensity. For a mode on the edge of the hump area, $999\,\mathrm{cm}^{-1}$ (background: $973\,\mathrm{cm}^{-1}$), we see that this is not the case and the peak to background ratio appears to remain constant.

7.2.2. Discussion on the temperature dependence of molecular SERS

The increase in SERS intensity at low temperatures, follows a similar trend to that which has been observed previously on rough silver films. [162, 163] In Fig. 7.3 we plot $1/(\epsilon'')^2$, scaled to best fit the data as a zeroth order model of the temperature-dependent Raman intensity. This provides a good fit for the mid temperature range (60 K to 180 K) but deviates at both high ($> 180\,\mathrm{K}$) and low ($< 50\,\mathrm{K}$) temperatures. At low temperatures the value of ϵ'' becomes sensitive to the value of the damping offset we chose in Sec. 7.1.1. Experimentally determining this value or more generally the low temperature ($< 50\,\mathrm{K}$) dielectric properties of gold could provide a better fit than using the simplified temperature-dependent Drude model used here. At high temperatures ($> 180\,\mathrm{K}$) the experimental data diverges from the theory. This high temperature behaviour was not observed by Pang et al. [162] and was not consistently observed in our repeat experiments. We are unclear on its origin, but it could potentially be related to phase changes in the thiol monolayer as have been observed in alkanethiol experiments, where below 200 K the changes become frozen-in. [164, 165] The model we have plotted, relating changes in SERS intensity to $1/(\epsilon'')^2$, is also highly simplified and we would not expect an exact fit to the experimental data. Creating a more sophisticated model is difficult due to the nature of the plasmonic modes in the Klarite structure with interplay between the larger pit modes (Chapter 4) and roughness hot spots (Chapter 6) on the surface. It is unclear how the combined effect of these factors will vary with temperature. To a good approximation, however, we see that the SERS peak intensity increases as the metal damping decreases as expected.

The background continuum intensity appears to change with a similar trend to the SERS peaks, however the ratio of the peak and background can change with temper-

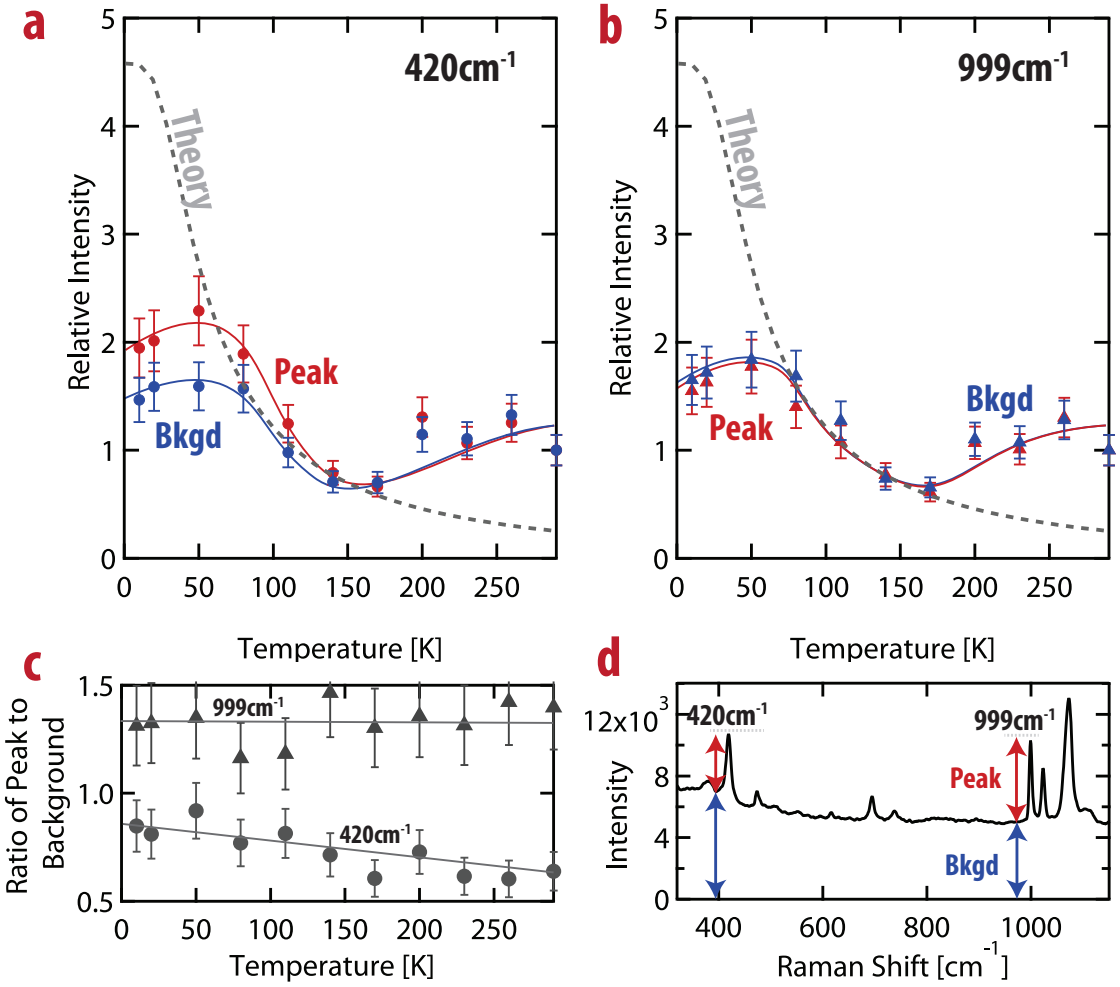

Figure 7.3.: Extracted peak heights for two BTh modes and nearby background continuum point **(a)** 420 cm^{-1} mode with background height at 394 cm^{-1}, **(b)** 999 cm^{-1} mode with background height at 973 cm^{-1}. Both peaks have been normalised to their intensity at 290 K. Red and blue lines are guides to the eye. The 'Theory' line plots $1/(\epsilon'')^2$ and has been scaled to best fit the data. **(c)** Ratio of peak to background height for the two modes as a function of temperature with triangle markers belonging to 999 cm^{-1} and circles to 420 cm^{-1}. **(d)** BTh spectra indicating the mode and background height used to extract the data. Original SERS spectra were taken using $\lambda_{ex} = 785$ nm on BTh SAM-coated Klarite as described in Sec. 7.2

ature depending on the vibrational mode excited. What is also clear from Fig. 7.2 is that at low temperatures, some spectral areas of the background have increased in intensity, whereas others have decreased in intensity. This is in contrast to peak height, which always increases at lower temperatures. The large hump observed in Fig. 7.2, which disappears after a low-to-high temperature sweep, suggests an annealing-like process in the thiol monolayer or the metal, which has a large effect on the so-called 'hump' spectral region of the background continuum. This suggests multiple origins to the background continuum as suggested in Chapter 6, with some which do not affect the peak intensity. The large changes to the background 'hump' region are not consistent across all samples and further research is needed to discover its true origin.

7.3. Temperature dependence of Raman and SERS of quantum dots

As shown in Chapter 5, the SERS of QDs is highly dependent on the frequency of excitation due to their excitonic absorption and emission resonances. This is in addition to the strong wavelength-dependence of the Klarite nanostructure. CdSe quantum dots with 640 nm emission were attached to the Klarite surface using the attachment protocol from Chapter 5. Comparison was made to aggregated quantum dots, by repeated drop-casting and evaporation of a concentrated (5 mg/ml) colloidal QD solution onto silicon to form a thick layer of quantum dots. Samples were placed into the cryostat as described in Sec. 3.2.2.1 and Raman measurements were taken at 532 nm, 633 nm and 785 nm using the extended scan mode of the Renishaw inVia (Sec. 3.2.2). Raman grating was chosen to best match laser excitation wavelength (2400 lines/mm for 532 nm, 1800 lines/mm for 633 nm and 1200 lines/mm for 785 nm) and laser power and exposure time was adjusted to obtain a decent signal without damage to the sample. Anti-Stokes spectra were collected at the same time as Stokes spectra using a notch filter.

7.3.1. Results and discussion

Due to their striking wavelength-dependence, the results are split into three sections based on their excitation wavelength.

7.3.1.1. Excitation at $\lambda_{ex} = 532\,\text{nm}$

In this configuration, we have:

- No localized Klarite plasmon resonances
- QD absorption resonances

At 532 nm the quantum dot Raman scattering is best described as RRS. At room temperature, the result is similar to that seen at 514 nm excitation in Chapter 5. As well as the principal longitudinal optical phonon of CdSe [LO(1)] accompanied by a lower frequency shoulder caused by an optical surface phonon[121] (Fig. 7.4) a phonon peak around $274\,\text{cm}^{-1}$ is observed, corresponding to the CdS LO(2) phonon mode observed at 633 nm excitation for the CdSe core-only dots in Chapter 5.

As the temperature is decreased the phonon peaks blue-shift in energy (Fig. 7.5 a). This is expected due to the contraction of the crystalline lattice forcing a shorter optical phonon wavelength. The LO(1) and 2LO(1) shift in a similar manner. The shift matches that observed previously by Tanaka et al. [166] for CdSe quantum dots in a germanate glass matrix and Dzhagan et al. [167] for CdSe quantum dots in a gelatin matrix. The SO(1) [123] peak is harder to track due to the large error in fitting the peak, but appears to blue-shift as expected. The phonon Raman bands also narrow as the temperature is reduced (Fig. 7.5 c). This has also been observed for the LO(1) mode in Raman scattering of CdSe quantum dots by Kusch et al. [168] who attribute the change to the temperature dependence of contributions from optical phonon decay into low energy phonons. [169] The intensity of the phonon Raman bands increase as the temperature decreases. Kusch et al. [168] and Tanaka et al. [166] observe this increase with decreasing temperature, with the intensity of the CdSe LO(1) mode at 5 K roughly double that at 310 K. Here, we see a larger increase (Fig. 7.5) with the 10 K LO(1) intensity being approximately 6.5× that at 310 K. Some of this increase may be explained by the temperature dependence of SERS, which, as seen in Sec. 7.2.2, also increase with decreasing temperature.

At room temperature we are able to see higher harmonics, or multi-phonon excitations of the LO(1) phonon mode. As the temperature decreases the harmonics become increasingly visible as their intensity increases. These harmonics, labelled nLO(1), are multi-phonon excitation processes, where n stands for the number of LO(1) phonons excited. Also visible are combinatorial phonon excitations of both CdSe and CdS. These are labelled nLO(1)+LO(2). Scattering events involving two

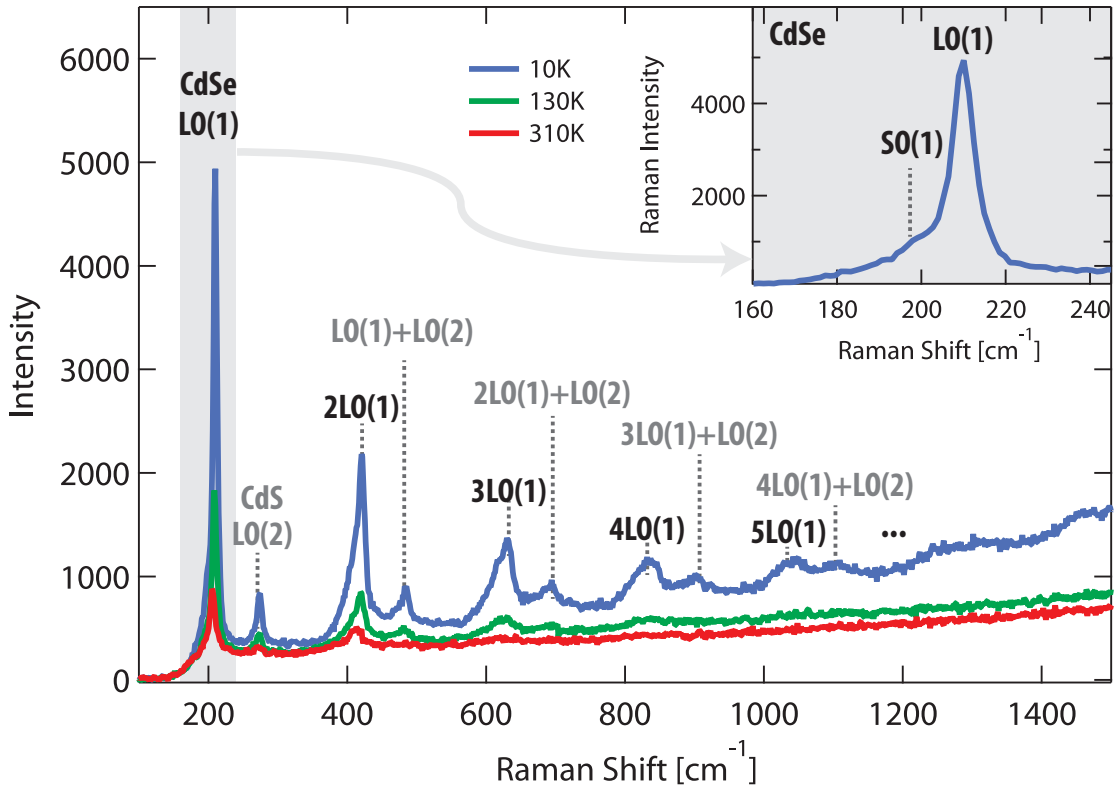

Figure 7.4.: Stokes SERS of CdSe QDs at three temperatures (10 K, 130 K and 310 K) with $\lambda_{ex} = 532$ nm of QDs on the Klarite nanostructure. Laser power was 1 mW with an exposure time of 10 s per spectra. CdSe LO(1) modes and their harmonics nLO(1) are shown. The CdS LO(2) mode is also shown and combinations of this with the LO(1) harmonics labelled [nLO+LO(2)]. Detail of the CdSe LO(1) mode (inset) showing the low-energy shoulder due to optical surface phonons SO(1).

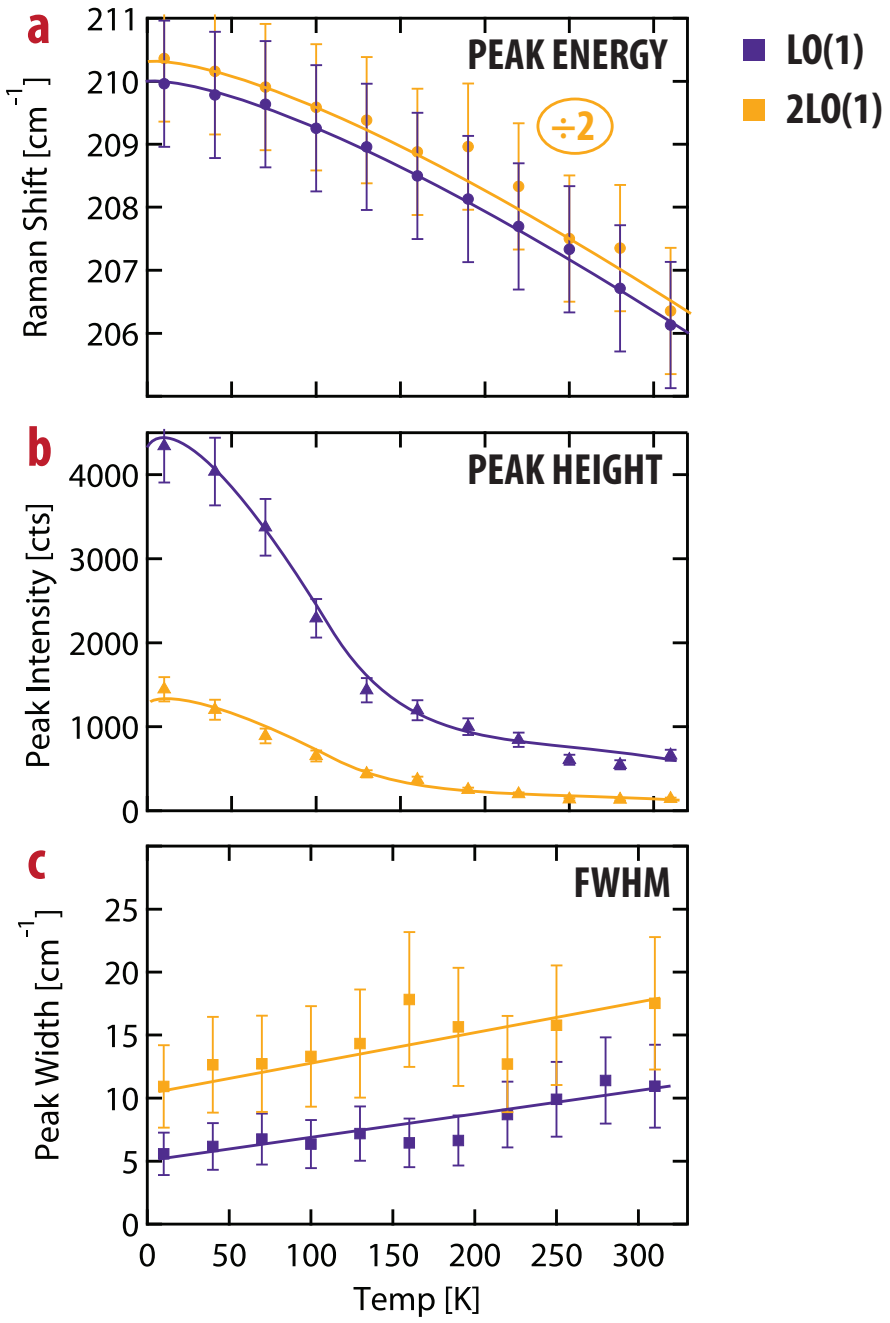

Figure 7.5.: Temperature-dependent SERS of QDs at $\lambda_{ex} = 532\,\text{nm}$ showing LO(1) and 2LO(1) CdSe phonon mode as extracted from spectra recorded over 10 s with a laser power of 1 mW, a subset of the raw spectra are shown in Fig. 7.4. **(a)** peak energy positions (2LO energy divided by two), **(b)** peak heights (intensities) and **(c)** peak full-width at half maximums (FWHM).

or more LO(2) phonons with LO(1) phonons are not observed.

For the case of aggregated QDs on silicon a similar spectrum to the sub monolayer on Klarite is observed, with multiple harmonics visible, although not to the same extent as seen at low temperatures on Klarite. The LO(1) and 2LO(1) peak widths are comparable to the on-Klarite case and the LO(1) to 2LO(1) ratio of peak heights shows the same temperature dependence. This increases linearly with temperature as has been seen before by Alivisatos et al. [170] and Klein et al. [120]. Here the ratio at 310 K is approximately 1.5× larger than at 10 K. This means at high temperatures there is decreased electron-phonon coupling, resulting in the relative intensity decrease of the LO phonon Raman harmonics.

7.3.1.2. Excitation at $\lambda_{ex} = 633$ nm

In this configuration we have:

- A Klarite localized plasmon resonance
- On QD absorption and emission resonance

At $\lambda_{ex} = 633$ nm we are pumping close to the QD PL emission (640 nm) and on the edge of the QD absorption. The Raman spectra is therefore dominated by the PL signal (Fig. 7.6). At room temperature the LO(1) Raman mode is visible as well as the next two harmonics. The LO(2) mode is also visible. There are noticeably fewer harmonics compared to the 532 nm case.

As the temperature is decreased the LO(1) and 2LO(1) peak heights stay constant until the temperature drops below 100 K, after which they start to increase (see Fig. 7.7). Below 100 K the PL spectral shape changes significantly for the Stokes Raman scattering. The Raman phonon modes appear superimposed on broader modes (≈10 x FWHM) close to the energy position as the Raman LO phonon modes (Fig. 7.8). Furthermore, there also appears to be an additional broad mode accompanying each LO(1), labelled '??' in Fig. 7.8. The broad peaks accompanying each LO(1) harmonic overlap and this combined with the LO(1) and weak LO(2) makes an accurate peak fit harder. In the measurements the notch filter used to block the laser power (at 0 cm^{-1}), prohibits accurate fitting of the primary LO(1) mode due to signal cut-off. LO(1) peak heights were instead extracted by subtraction of maximum intensity from a nearby background position.

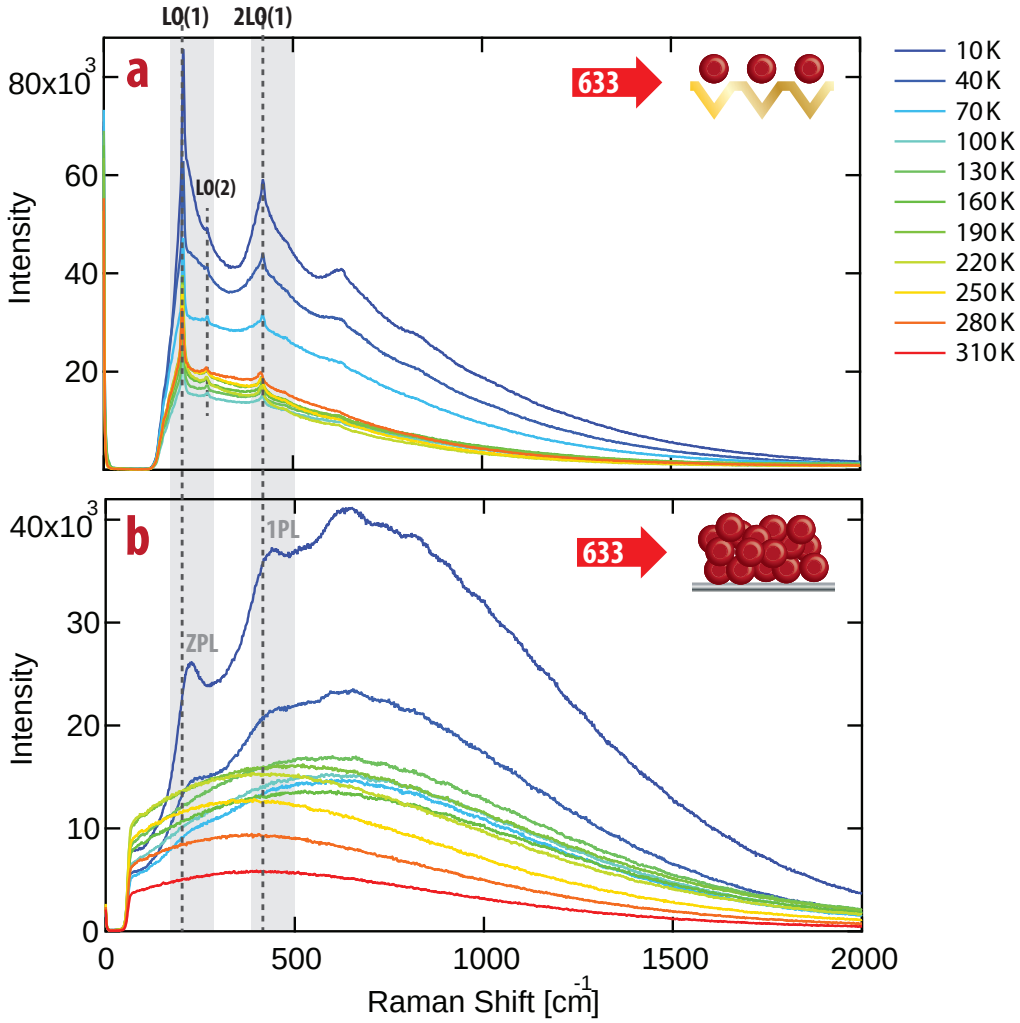

Figure 7.6.: (a) Stokes SERS spectra of CdSe QDs on Klarite as a function of temperature with $\lambda_{ex} = 633\,\text{nm}$. Each spectra has a 10 s exposure time using a laser power of 0.3 mW. First two CdSe Raman modes highlighted LO(1) and 2LO(1) and CdS mode highlighted LO(2). Broader PL phonon replica modes highlighted in grey and labelled ZPL and 1PL. (b) Equivalent Raman spectra for aggregated QDs, showing PL phonon replica modes but no Raman modes. Aggregated QD spectra collected using same exposure conditions as the SERS spectra.

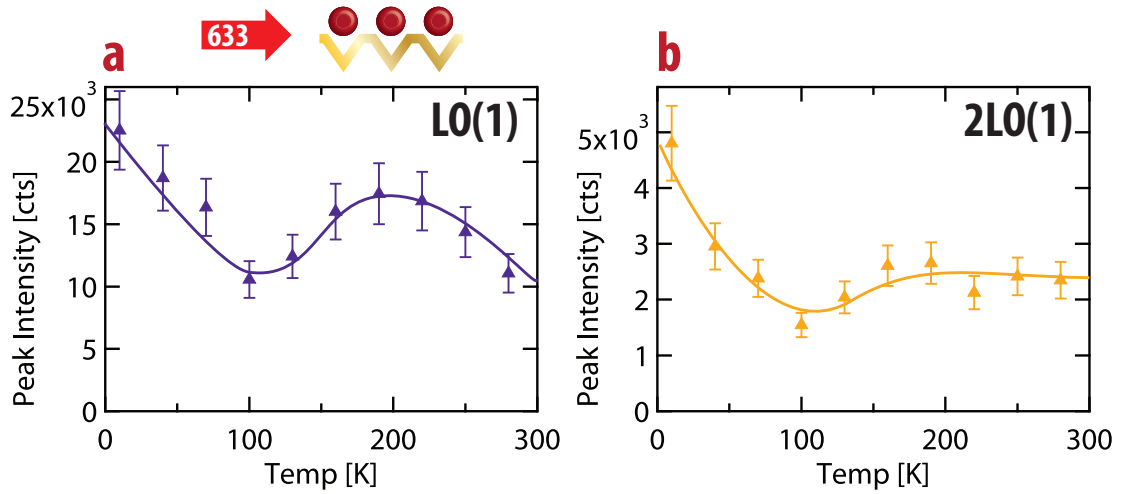

Figure 7.7.: **(a)** Extracted LO(1) and **(b)** 2LO(1) peak heights (intensities) from temperature-dependent SERS of QDs on Klarite at $\lambda_{ex} = 633\,\text{nm}$. Raw spectra shown in Fig. 7.6.

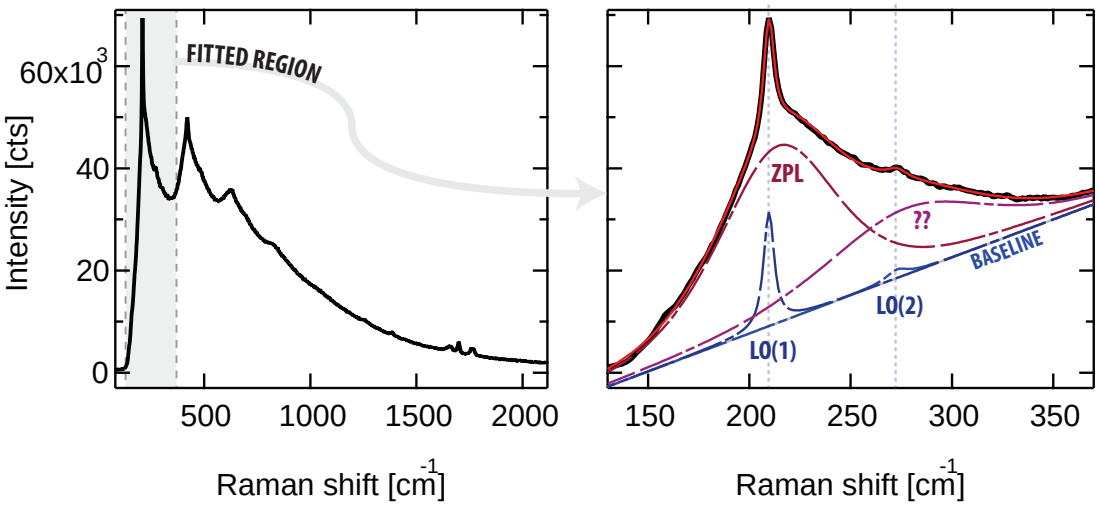

Figure 7.8.: **(left)** 10 K SERS spectra of CdSe QDs on Klarite at $\lambda_{ex} = 633\,\text{nm}$, showing expanded fitted region **(right)**. Limited spectral area (surrounding LO(1) Raman peak) fitted with Lorentzian for sharp Raman phonon peaks: CdSe LO(1) and CdS LO(2) and a broader Gaussian peak for the PL phonon replica peak (ZPL). Peaks are plotted against a linear offset baseline to account for PL from phonon replicas outside the fitted region. A further Gaussian peak labelled '??' was needed to provide a good fit and may also be accounted for by PL outside the fitted region.

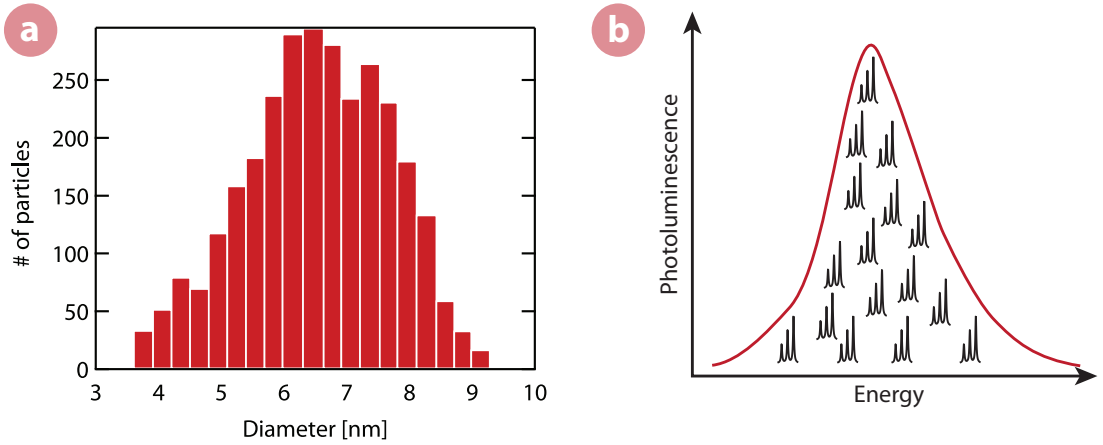

Figure 7.9.: (a) Typical size-distribution of the Nanoco CdSe QDs used in these experiments. The range of sizes (polydispersity) is responsible for inhomogeneous broadening of the absorption and emission spectra. [130] (b) Schematic of ensemble QD PL emission (red), highlighting the contribution of individual QD's PL emission phonon replica progressions (black) to the overall emission spectra. [171]

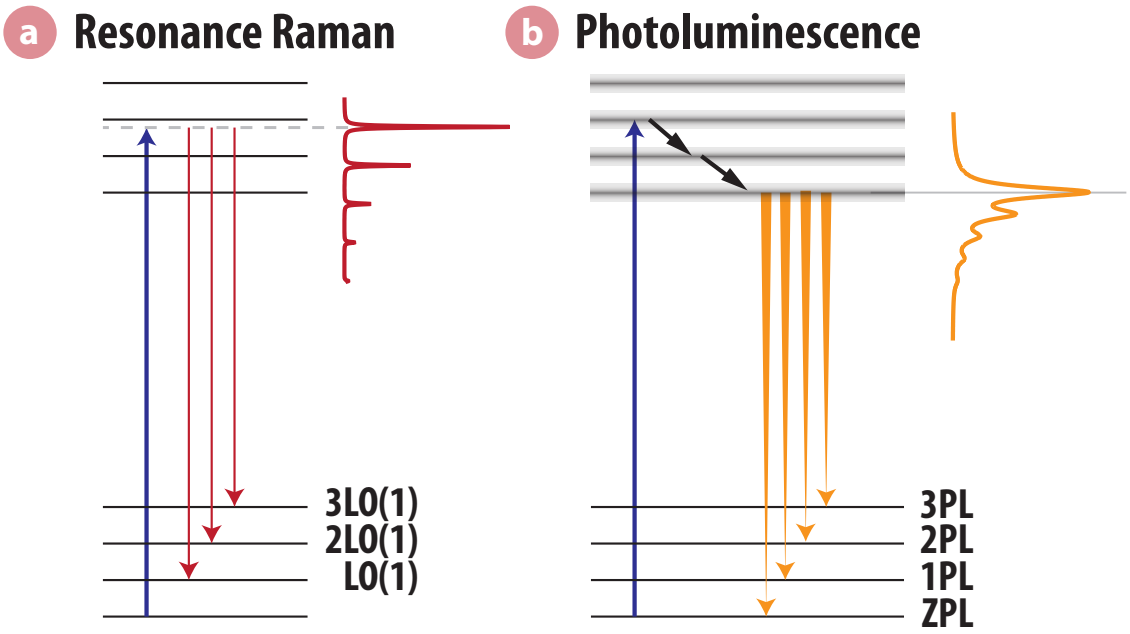

Figure 7.10.: Comparison between the origin of (a) sharp resonance Raman phonon peaks and (b) broader PL phonon replica peaks. Dashed line represents the virtual resonant energy level involved in the Raman scattering event. In the PL case the QD is excited to a real excited state resulting in homogeneous broadening of the emission linewidth due to dephasing of the excited state.

At room temperature the PL spectra of colloidal QDs appears as a broad distribution of energies centred around a peak emission wavelength; $\lambda = 640\,\text{nm}$ for the CdSe QDs used here. The large spectral width of the emission is a result of inhomogeneous broadening due to the strong QD size-dependence of the bandgap energy and the distribution of QD sizes present in the colloidal system (Fig. 7.9). The PL of a single QD is itself composed of multiple peaks due to phonon coupling in the crystal lattice on emission of a photon. This results in a PL phonon progression, similar to that observed in the Raman case. Importantly, it differs from the Raman case in three key ways: (1) The phonon energy shifts are relative to the QD bandgap emission rather than the laser excitation wavelength in Raman, (2) The peaks are broader than in the Raman scattered case due to homogeneous broadening, (3) The peaks are inhomogeneously broadened by the QD polydispersity.

Resonant Raman scattering is a very fast process (quasi-instantaneous) since the incoming photon is not absorbed and re-emitted by the QD, but interacts resonantly with the transition. In PL, however, the incoming photon is absorbed into the QD exciting an electronic transition. The excited state has a finite lifetime and will undergo non-radiative decay before returning to the ground electronic state by emitting a photon. During the time it is excited, dephasing of the state occurs through various mechanisms due to phonon coupling, defect and interface scattering and carrier-carrier scattering. This results in homogeneous broadening of the observed PL peaks as illustrated in Fig. 7.10. [127] Further to this the peaks are inhomogeneously broadened due to the QD size distribution and the strong size dependence of the bandgap energy.

As the temperature is lowered there is reduction in strength of the broadening mechanisms. The thermal occupation of acoustic phonon states decreases with temperature thus reducing the homogeneous broadening of the PL peaks. Pumping at 633 nm, we are on the edge of the lowest excitonic absorption resonance, so that only the largest QDs with lower band gap energies are excited. This reduces the inhomogeneous broadening and is known as fluorescence line narrowing (FLN). [172, 173, 174] As the temperature decreases the bandgap in the quantum dot increases in energy shifting the absorption region to higher energies. This results in even larger QDs no longer being in resonance with the excitation laser energy and the inhomogeneous broadening is further decreased (Fig. 7.11). The inhomogeneously broadened PL spectra observed at room temperature thus become a progression of broad but resolved PL phonon replicas at low temperatures, due to the reduction in homoge-

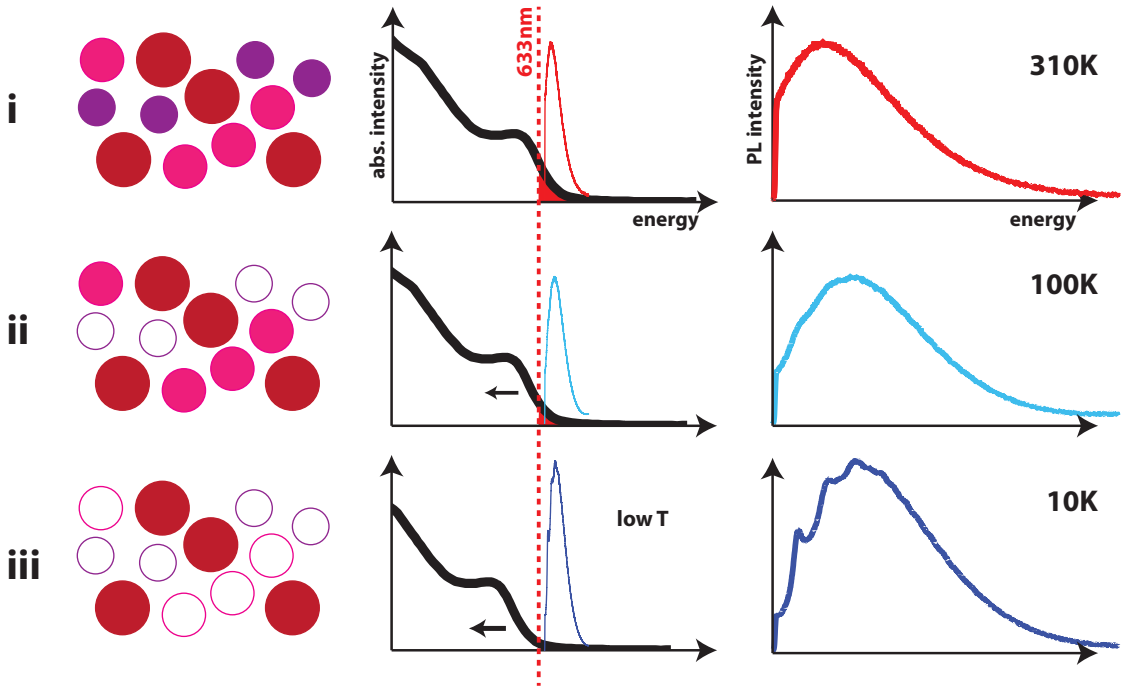

Figure 7.11.: Low-temperature induced fluorescence line narrowing. On room temperature excitation **(i)** slightly to the red-side of the absorption resonance, most of the quantum dots are excited. As the temperature cools **(ii)** the absorption resonance of the QDs blue-shifts. Due to the inhomogeneous size-distribution of dots, this means that the smallest dots with the largest excitation band gap can no longer be excited and switch-off. On further cooling **(iii)** the absorption continues to blue-shift and fewer QDs are excited. Since now far fewer larger dots are excited, the fluorescence spectrum of the ensemble loses its inhomogeneously broadened character and specific PL phonon replica modes can be resolved.

neous and inhomogeneous broadening mechanisms.

In the aggregated QDs on silicon case, at room temperature we see a characteristic QD PL spectra. There is no evidence of any Raman scattered phonon modes. As the temperature is decreased the overall PL blue-shifts in frequency as expected due to the semiconductor's increasing bandgap energy. However, below 100 K, the shape of the PL changes to a LO-phonon replica progression as a result of the reduced broadening. Since the QD PL emission centre at low temperatures is almost the same as the excitation laser wavelength, the PL LO-phonon progression occurs at almost the same position as we would expect to see the LO-Raman modes.

The combination of the broad PL LO-phonon replicas and the sharp Raman LO-phonon modes mostly explains the unique spectral shape observed at low temperatures with $\lambda_{ex} = 633\,\text{nm}$. However, there still appears to remain a contribution to the spectral shape by another broad peak, which appears to be situated close to the energy of the nLO(1)+LO(2) combination modes. This is not observed in the aggregate QD spectra and it is most likely an artefact of the linear background subtraction used, although we cannot rule out another unaccounted source.

7.3.1.3. Excitation at $\lambda_{ex} = 785\,\text{nm}$

In this configuration we have:

- a localized Klarite plasmon resonance
- no QD excitonic resonances

At 785 nm the SERS spectra is significantly different from that at 532 nm and 633 nm (Fig. 7.12a). The background shape is similar to that observed for molecular SERS at this wavelength on the Klarite nanostructure. At this wavelength the Raman scattering is far from the QD absorption and emission lines. As a consequence, there is no enhancement from resonance Raman scattering, and the spectra are not swamped by PL signal. Indeed, at this wavelength we see, as in Chapter 5, evidence of molecular SERS as well as the LO(1) mode of the QD.

The LO(1) peak heights are hard to fit in the 785 nm case due to their low intensity relative to the noise. A rough extraction is shown in Fig. 7.12c. It seems that qualitatively there is a similar temperature dependence of the peak intensity (Fig. 7.12b) to that of benzenethiol (Fig. 7.3). This is despite the actual peak intensity at 10 K being less than at 310 K, which is probably explained by the large errors. This suggests

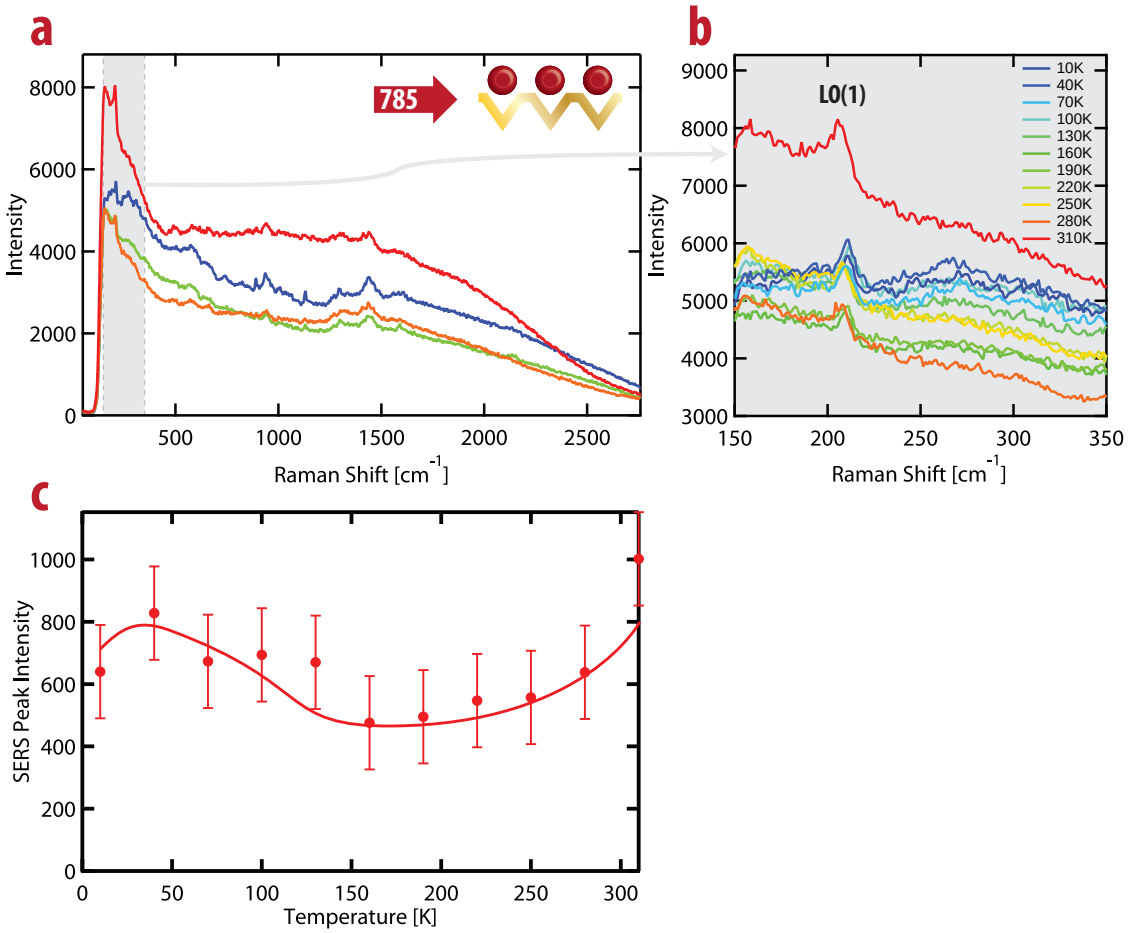

Figure 7.12.: (a) SERS spectra of CdSe QDs on Klarite at $\lambda_{ex} = 785\,\text{nm}$ with an exposure time of 10 s and a laser power of 20 mW. Four spectra are plotted across a large temperature range from 10 K to 310 K. (b) Zoomed in area around CdSe LO(1) phonon mode showing the full range of temperatures measured. (c) Extracted peak height (intensity) of LO(1) phonon mode as a function of temperature.

that at the other wavelengths, the strong temperature dependence seen is largely due to excitonic resonance effects rather than surface-enhancement Raman scattering, whereas here it more closely matched to a molecular SERS effect.

A comparison with the aggregated QDs was not possible, since at 785 nm there was no signal attributable to any Raman modes visible at any temperature. This is understandable since there is no enhancement mechanism available to enhance these weak Raman signals.

7.3.1.4. Anti-Stokes

For the anti-Stokes Raman scattering using 532 nm excitation it is only possible to see the LO(1) mode and no harmonics. The background signal in this region is also absent since this spectral region lies outside the PL tail of QD emission. The LO(1) intensity is far less than for Stokes-scattered light (as is usually expected) and decreases to zero as the temperature is reduced, emptying the thermally occupied vibrational levels. The lack of visibility of the harmonics on the anti-Stokes side could be explained by the relatively low intensities and the reduced possibility of a multi-phonon excited state spatially co-existing.

Comparing the ratio of the Stokes and anti-Stokes LO(1) intensities we see that the ratio follows the normal intensity ratio expected due to population of thermal states.

In the anti-Stokes spectra at $\lambda_{ex} = 633\,\text{nm}$ (Fig. 7.13), we see the LO(1) mode and at high temperatures we can also see the 2LO(1) harmonic, which we did not see at 532 nm excitation and the LO(2) CdS mode. It is not clear why we see the LO(2) mode here and not at 532 nm where we would equally expect to see it. As the temperature reduces all these modes disappear as the thermal occupation of vibrational states decreases, consistent with the Maxwell-Boltzmann dependence. However, for the $\lambda_{ex} = 633\,\text{nm}$ case, for temperatures $> 200\,\text{K}$, the experimentally observed LO(1) phonon height decreases, where it is expected to continue increasing as the thermal occupation of phonon states continues to rise (see Fig. 7.13).

7.4. Conclusion

In this section we have looked at the temperature-dependent properties of SERS of a molecular system (BTh) and an inorganic system (QDs). In the molecular system

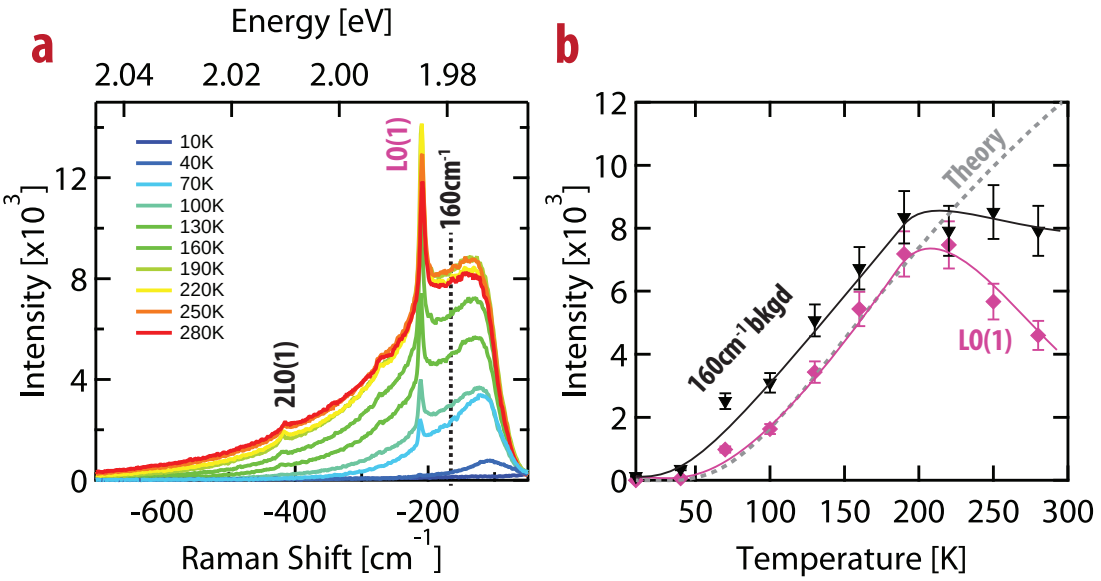

Figure 7.13.: (a) Temperature dependence of anti-Stokes SERS of CdSe QDs on Klarite at $\lambda_{ex} = 633\,\text{nm}$. LO(1) phonon modes are labelled. (b) Extracted anti-Stokes LO(1) phonon height of (a) as a function of temperature shown alongside extracted intensity of background ($160\,\text{cm}^{-1}$). Maxwell-Boltzmann fit (Theory) is plotted as a dashed line alongside the experimental data.

the temperature-dependent properties agreed strongly with those seen previously in the literature. The temperature dependence of the SERS background continuum again highlighted similarities and differences in its origin compared to that of SERS peaks. It showed some strong features which we attribute to annealing and more gradually varying features of similar origin to the SERS peaks. It emphasises the importance of pinpointing the various origins of the SERS background so that it can be effectively controlled.

In the QD case, we saw very strongly wavelength dependent effects we attribute to resonance Raman scattering via interaction with the excitonic transitions. At 785 nm the case most resembles the molecular SERS, although the signals were too weak in this case to effectively extract a temperature dependence. Temperature dependent effects were dominated in the 633 nm case by the QD PL signal and we observed FLN in this case, leading to intriguing spectral shapes at low temperature. At 532 nm, again the background was dominated by a fluorescence tail and very strong phonon harmonic modes were observed.

8. Hybrid Klarite–nanoparticle molecular junctions

The relatively modest SERS enhancement factor given by the Klarite structure precludes its use in high-sensitivity applications where the detection of ultra-low concentrations (towards single molecule) of analyte is necessary. Increasing the SERS enhancement is desirable to further the use of Klarite. Here we study how the addition of plasmonic nanoparticles (NPs) to the Klarite surface can lead to enhancement ($\sim 100\times$) of the SERS signal over the case of bare Klarite. Using both gold and silver NPs, in addition to EM effects, we also gain insight into the influence of potential chemical enhancement using an analyte molecule, p-aminothiophenol (pATP), which has previously been shown to be sensitive to charge transfer effects.

Gold and silver NPs can harbour localised surface plasmons (Sec. 2.1.6) causing localisation of electric field around them. If two such NPs are placed close together (closer than the NP diameter) the induced plasmon modes can couple to each other in this near-field zone. This leads to huge electric field enhancement in the interparticle-gap between them. The enhancement of the electric field in this gap is strongly distance dependent. [175, 176, 177] If a molecule is placed in the interparticle-gap region a huge SERS enhancement can thus be observed, which correspondingly is strongly gap distance-dependent. [178, 179] These 'gap' plasmons are the principal enhancement mechanism in aggregated colloidal NPs and are responsible for the large observed SERS enhancements in such systems. [180] They are also responsible for highly variable and irreproducible hot spots with high SERS enhancements due to the difficulty in experimentally controlling gap size.

NPs situated close to gold films have also shown localised electric fields in the region between the particle and the film. This is caused by coupling between the localised plasmon resonance on the particle and the surface plasmon polariton on the

metal film. [181] The field enhancement, which is highly dependent on the particle-film spacing has been used to demonstrate reproducible SERRS signals from dye-molecules placed within the gap. [182] Recently, Huang and Speed et al. [177, 5] have demonstrated electric field enhancements in the gap between silver NPs molecularly bound to a nanovoid plasmonic substrate. They observed enhancements up to 90 % stronger than those found in equivalent NP-dimers. They attributed this to coupling between the localised plasmon on the NP and those of the nanovoid structure. As well as these new gap plasmon modes, they also found that addition of NPs enhanced coupling into the existing plasmonic modes of the void, acting like an antenna.

In this chapter we create a large increase, ~ 100 times. to the SERS enhancement found on the Klarite nanostructure by using a molecular bridge to attach NPs of gold (AuNPs) and silver (AgNPs) nanometre distances away from the Klarite surface (Fig. 8.1). The molecular bridge acts both as a NP binding agent and an analyte molecule positioned in the enhanced field, from which SERS signals are collected. As well as enhancement due to electric field localisation, we also see evidence, in the case of AgNPs, of charge-transfer driven SERS enhancement or photo-induced formation of 4,4'-dimercaptoaminobenzene (DMAB). We explore the wavelength dependence of these hybrid plasmonic systems and compare to the case of a NP on a rough gold surface.

8.1. Methods

Here we form a SAM of a para-aminothiophenol (pATP), known elsewhere as 4-mercaptoaniline (4-MA) or 4-aminobenzenthiol (4-ABT), on the gold Klarite structure using standard thiol chemistry as described in Sec. 3.4. The pATP bonds to the gold through the thiol linker, leaving the amine group, on the opposite side of the phenol ring, pointing away from the surface. After a SAM has formed, the substrate is removed from solution and rinsed in ethanol before being placed straight into a dilute aqueous gold or silver colloid solution.

To form NPs, gold and silver colloidal solutions were made in-house by Dr. Graeme McNay (Renishaw Diagnostics Ltd.), using a standard citrate-based methodology based on the adapted method by Grabar et al. [183] for AuNPs and the Lee and Meisel [184] method for AgNPs. TEM images (taken with the help of J. J. Rickard, Cavendish Laboratory) confirmed the AgNPs had a mean diameter of 30 ± 6 nm

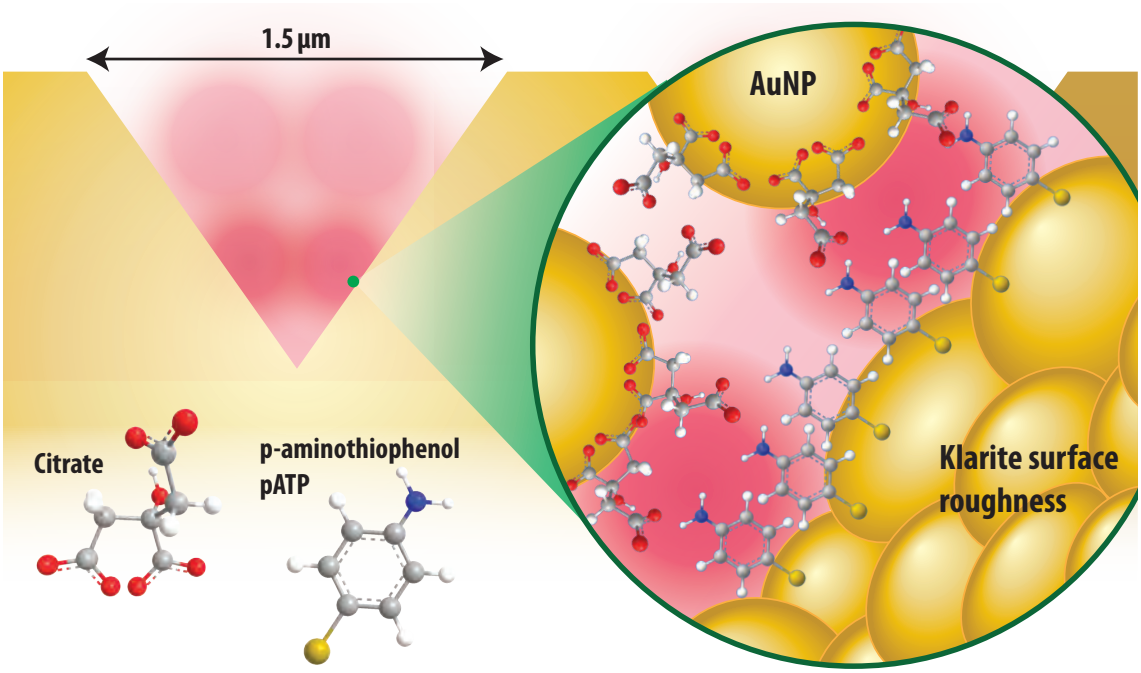

Figure 8.1.: Klarite nanostructure showing localised optical modes in the micron-sized structure and expanded view showing possible AuNP interaction with Klarite nanostructure via citrate and pATP molecular bridge. Highly localised electric field hotspots between NP and Klarite surface are pictured in red in the expanded view. [Not to scale]

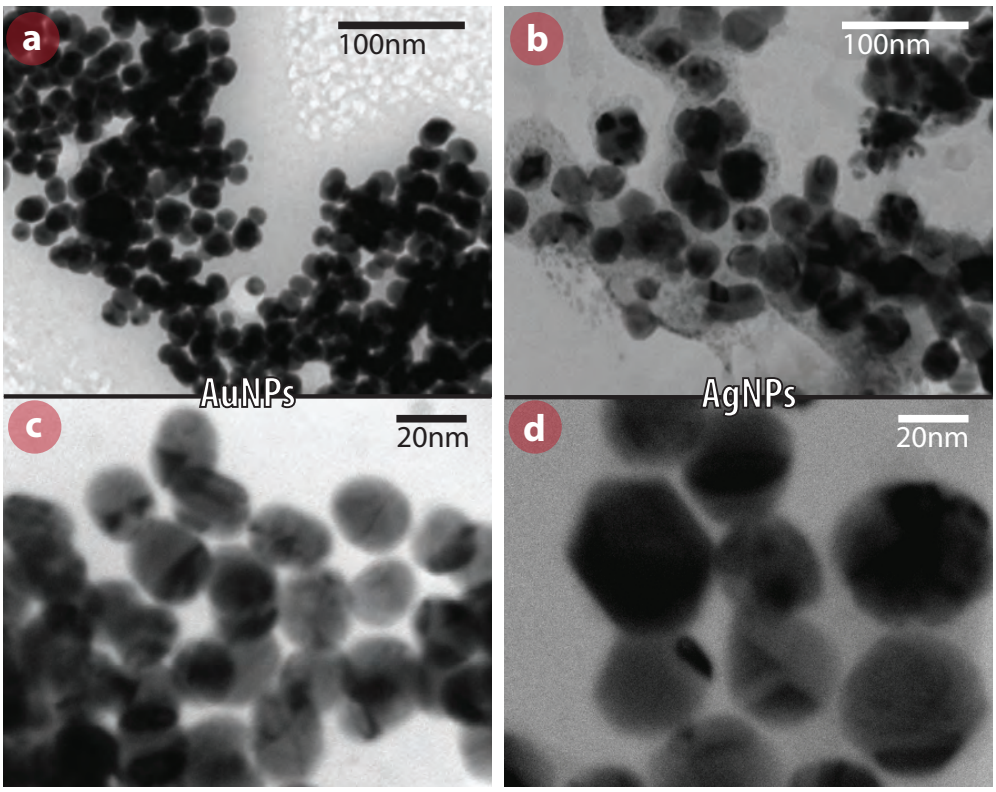

Figure 8.2.: Transmission electron micrographs of a selection of the NPs used in this study: **(a, c)** Gold (Au) and **(b, d)** Silver (Ag). Contrasting sections of NPs indicate differing crystal domain orientation.

with the AuNPs smaller at 19 ± 2 nm (Fig. 8.2). The AuNPs showed greater size homogeneity and less faceting than the AgNPs. The citrate used in the NP production method stops further growth of the NPs and acts as a capping and stabilising agent.

The citrate-capped AuNPs and AgNPs can interact with the dangling amine group on pATP, causing the NPs to be held close to the Klarite surface. It is also possible that the amine can displace the citrate and bond directly to the metallic NP, especially in the AgNP case as evidenced by the strong change in relative SERS peak heights.

Given the small size of the NPs and the Klarite geometry and surface roughness, it is difficult to image the NPs on the Klarite structure to confirm their presence. High-resolution SEM images (Hitachi S-5500 In-Lens FE SEM) of the pATP coated structure where taken with and without NP attachment (Fig. 8.3), but there is little evidence of the NPs. A similar study to this one has recently been performed by Scholes et al. [185] They found very sparse coverage using dilute drops of NP solution.

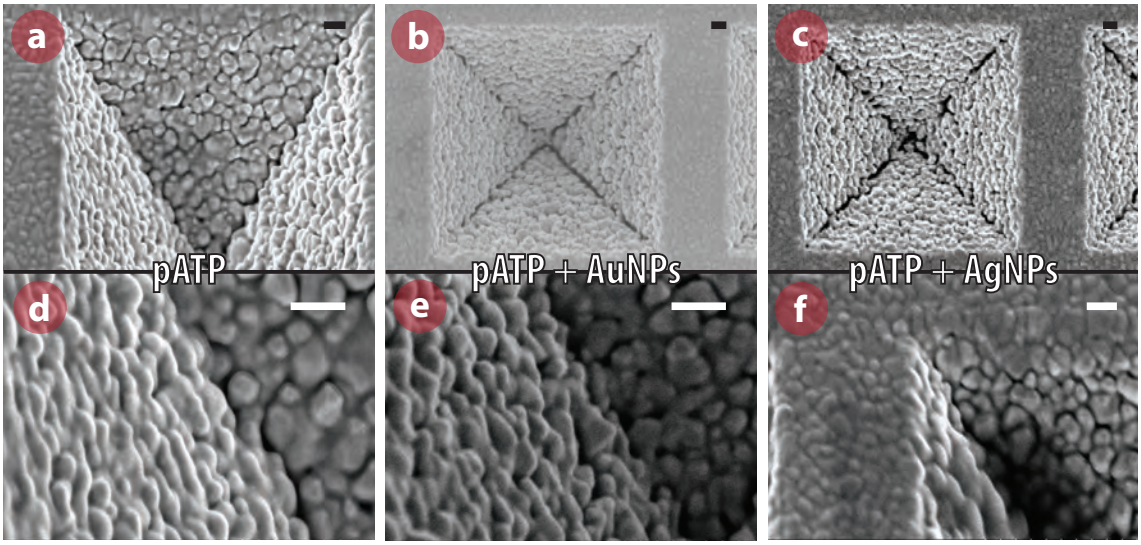

Figure 8.3.: High-Resolution SEMs of Klarite nanostructures after **(a, d)** pATP monolayer coating **(b, e)** pATP monolayer and AuNPs **(c, f)** pATP monolayer and AgNPs. Scale bars 100 nm.

Using a similar high resolution SEM they were able to observe small features they attributed to NPs. We do see similar small structures in our SEMs, although we only speculate that these are NPs. At the most, it confirms we have a very sparse coverage of dots on the structure. Instead we confirm attachment by the changes in peak height observed in the SERS spectra.

Raman measurements were taken using a Renishaw inVia Raman microscope (Sec. 3.2.2) at 532 nm, 633 nm and 785 nm using a $\times 20$ objective. All spectra have been normalised to the laser intensity measured leaving the objective using a wavelength calibrated LaserCheck (Coherent, Inc.) meter.

8.2. Results

SERS signals were observed across all wavelengths for a pATP monolayer on Klarite. Addition of AuNPs or AgNPs enhanced the SERS signals on Klarite at all three Raman excitation wavelengths due to charge-transfer enhancement as well as enhanced coupling into Klarite plasmonic modes. The largest increase in SERS signal was observed for $\lambda_{ex} = 785$ nm excitation, where modes were enhanced by around 2500 % for AuNPs and around 1000 % for AgNPs. The exact enhancement depended on the Raman excitation wavelength and the particular vibrational mode. There were

	Au	**Ag**	**$AgNO_3$**
Klarite	- λ-dependent (follows Klarite plasmon modes) - all vibrational modes enhanced	- λ-independent - b_2 vibrational modes strongly enhanced	- SERS is equivalent to AgNP-case
Flat Gold	- no SERS observed	- λ-independent - SERS with strong b_2 vibrational modes	- No SERS observed (small signal at 532 nm)

Table 8.1.: Tabular summary of key results of SERS enhancement after addition of AuNPs, AgNPs and $AgNO_3$ to the Klarite nanostructure and the flat gold surface.

clear differences in the SERS spectra between the enhancements caused by AgNPs compared to that of AuNPs (Fig. 8.4), with different vibrational modes being enhanced in each case. In the AgNP case we saw enhancement which has previously been attributed to charge transfer, which we also see on comparison to the addition of $AgNO_3$ instead of AgNPs. A summary of the key observations in this chapter are shown in Tab. 8.1.

Throughout this chapter, we assign vibrational modes based on those used by Osawa et al. [33] using notation developed under the assumption of $C_{2\nu}$ symmetry of the phenol group developed by Wilson. [186] The two main symmetry groups (a_1) and (b_2) will be frequently discussed. For reference, the main peaks have been labelled in Fig. 8.5. In Fig. 8.5 the $\lambda_{ex} = 785\,\text{nm}$ spectra are background subtracted with intensity normalised to the **7a** peak. Here it is clear to see that in the AgNP case, significant enhancement of the b_2 peaks occurs relative to the a_1 peaks, whilst in the AuNP case, the enhancement appears equivalent for all modes seen in the pATP spectra. The relative enhancements over the pATP on Klarite without NPs at each wavelength are shown in Fig. 8.6. Below we discuss the AuNP and AgNP case in more detail for each wavelength.

8.2.1. Gold nanoparticles on Klarite

At excitation wavelength $\lambda_{ex} = 785\,\text{nm}$ (Fig. 8.4a and normalised in Fig. 8.6): The addition of AuNPs, to form a Klarite-pATP-AuNP bridge, resulted in a large ($\approx 25\times$) increase in the SERS intensity across all visible vibrational modes (principally the a_1 symmetry modes) in the pATP-Klarite spectra. New modes also

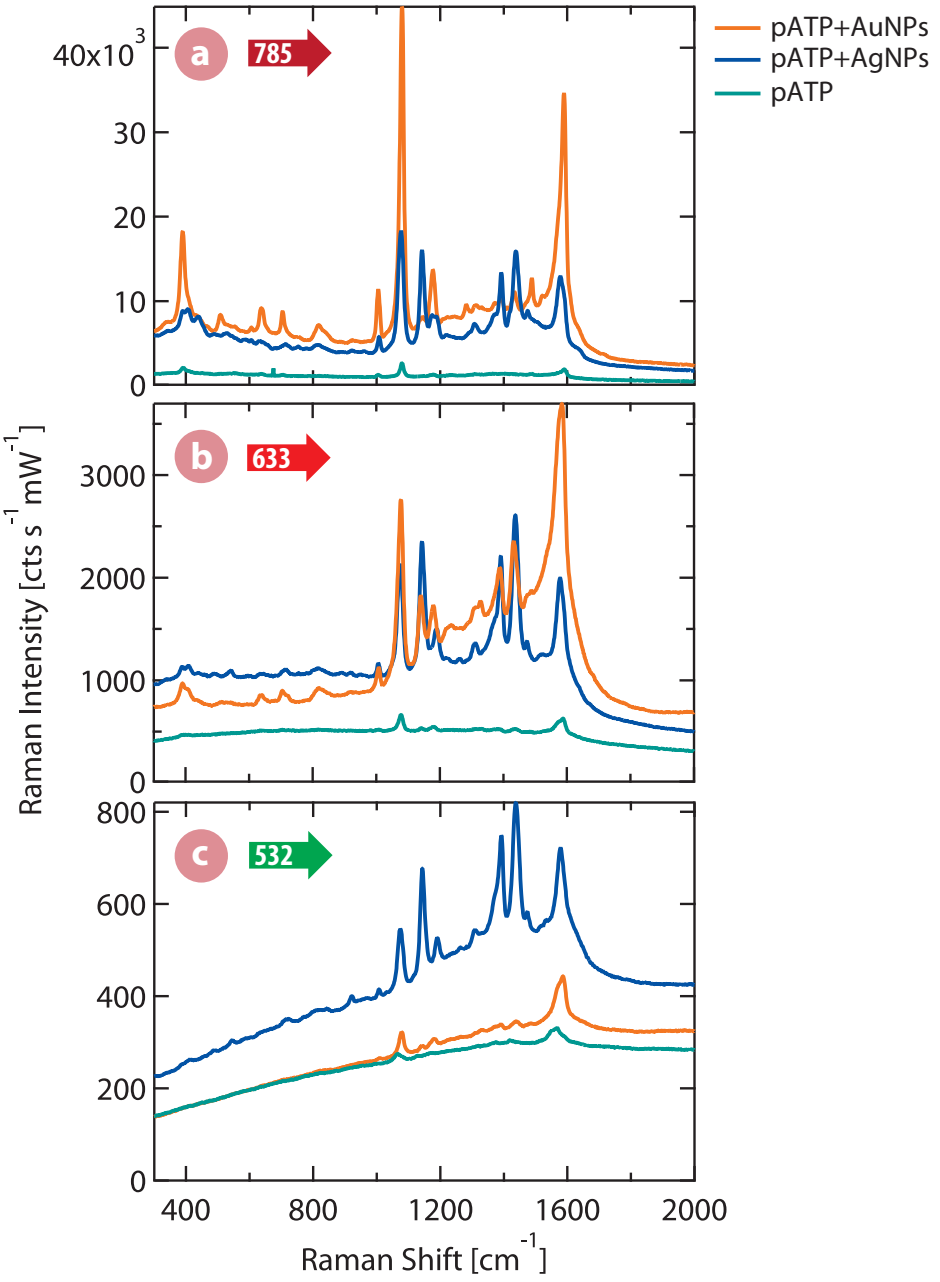

Figure 8.4.: SERS measurements of pATP on Klarite (turquoise) and with addition of AuNPs (orange) or AgNPs (blue). Different figures show response to differing Raman excitation wavelengths at **(a)** 785 nm, **(b)** 633 nm and **(c)** 532 nm. Strong dependence of vibrational mode enhancement and NP metal was observed. Raman intensity has been normalised to laser power.

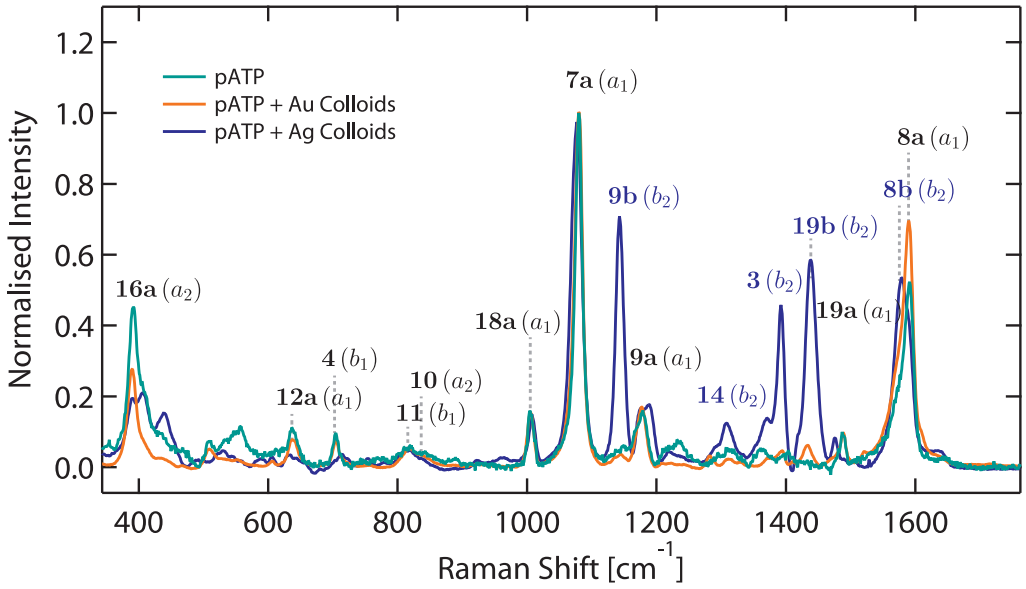

Figure 8.5.: SERS measurements of Klarite-pATP only and with addition of AgNP or AuNPs at $\lambda_{ex} = 785\,\text{nm}$ as in Fig. 8.4a but background removed using a cubic spline and intensity normalised to the height of the **7a** (a_1) peak. Peaks labelled according to symmetry-group assignments given by Osawa et al. [33]. b_2-labels are highlighted in dark blue.

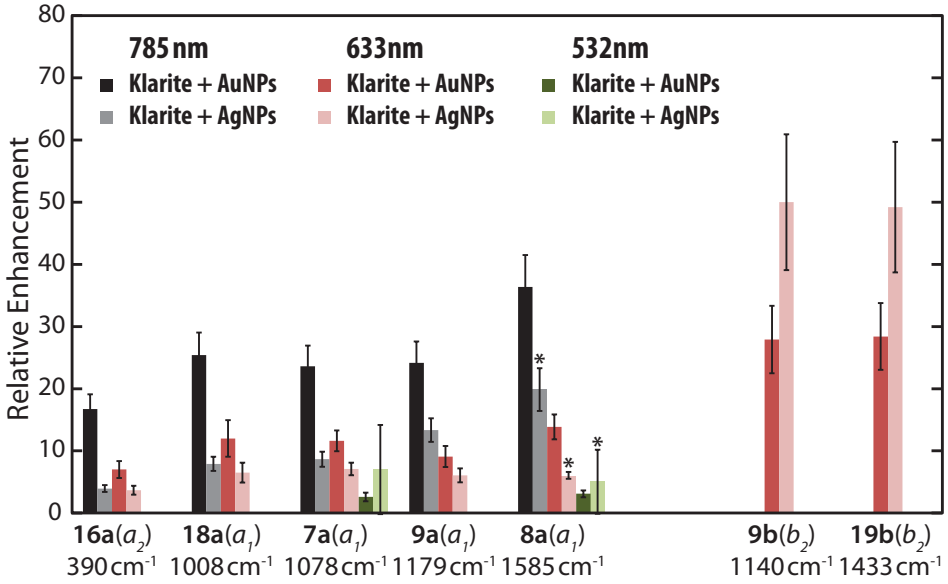

Figure 8.6.: Relative increase in SERS intensity for different pATP SERS peaks on addition of AuNPs or AgNPs. Enhancement is relative to SERS on Klarite without NPs for each corresponding wavelength. For the **8a** peak, in the AgNP cases (labelled '*') the peak is shifted in wavelength such that it corresponds to the **8b** (b_2), but for a comparison enhancement is calculated with respect to the **8a** peak.

emerged, such as 1144 cm^{-1} [**9b** (b_2)] and 1434 cm^{-1} [**19b** (b_2)]. Given the relative low intensity of these emerging b_2-type modes and the size of the enhancement observed on the previously visible modes, these new modes are unresolvable from the noise in the original Klarite-pATP only spectra. The observation is therefore consistent with equal enhancement of all SERS modes on addition of AuNPs.

At $\lambda_{ex} = 633$ nm (Fig. 8.4b): The Klarite-pATP only spectrum at 633 nm is broadly similar to that at 785 nm. The overall background continuum signal appears quite different however, showing signs of a broad fluorescence-like signature. The peak to peak intensity ratios are also roughly the same, but there is a noticeable presence of b_2 symmetry modes, which could not be seen at 785 nm, but are barely visible in (Fig. 8.4b). On addition of AuNPs, the SERS spectra is enhanced. The enhancement of the a_1 modes is more modest than at 785 nm at around 10 ×. However, the b_2 modes are even more strongly enhanced than at 785 nm by 30 ×. This in contrast with what was observed at 785 nm with AuNPs. The **19b** peak is 15 % of the intensity of the **7a** peak with Klarite-pATP only, rising to 40 % after addition of AuNPs (compared to just 4 % in the 785 nm case).

At $\lambda_{ex} = 532$ nm (Fig. 8.4c): The Klarite-pATP Raman spectrum at 532 nm is poor and rides above a large fluorescence-like background, only the **8a** and **7a** peaks are clearly visible. On addition of AuNPs the enhancement of these two modes is minimal at around 3 ×. We do see the emergence of other low intensity modes including the **9a** and **9b**, but it is not possible to calculate the enhancement due to the lack of modes in the pATP on Klarite only spectra.

8.2.2. Silver nanoparticles on Klarite

The addition of AgNPs instead of AuNPs presents a different story. At $\lambda_{ex} = 785$ nm, for most of the a_1 modes we see an enhancement of around 10 × after the addition of AgNPs (Klarite-pATP-AgNPs). However, we now see a much larger enhancement of the b_2 modes which become enhanced to match the intensity of the a_1 modes, changing significantly from the original Klarite-pATP spectra (Fig. 8.6). With AuNPs the **19b** and **9b** peaks are around 5 % of the **7a** peak intensity. With AgNPs they are 77 % and 62 % respectively. This means in the AgNP case the enhancement seen is highly dependent on the vibrational mode, with the b_2 modes being preferentially enhanced.

In the 633 nm Klarite-pATP-AgNP case, the general mode enhancement is more modest compared to the AuNP case (as in the 785 nm for AgNPs) except again for the b_2 modes which show a very strong enhancement of $50\times$ compared to the Klarite-pATP only case, making the **19b** and **9b** peaks around 110 % of the **7a** after NP addition. In the 532 nm AgNP case, we again see a huge enhancement of the b_2 modes including **9b** and **19b** which are $20\times$ and $35\times$ enhanced over the Klarite-pATP only intensities. We also see enhancement of the a_1 modes by a more modest $\approx 5\times$. Here the b_2 modes again dominate the spectrum over the a_1 modes, with the **9b** and **19b** 180 % the intensity of the **7a** mode.

From these measurements it is clear that there are differing enhancement processes occurring after addition of Au and Ag NPs and there also appears to be wavelength dependence to the measurements. Comparing the relative enhancements (Fig. 8.6), the increase in enhancement after addition of AuNPs seems to be strongly wavelength dependent, while the AgNP case seems broadly wavelength independent. Proper comparison with the enhancement at $\lambda_{ex} = 532$ nm is not possible due to the very low intensity of initial modes.

8.2.3. Gold and silver nanoparticles on rough flat surface

Previous studies have shown that AgNPs and AuNPs on gold surfaces can give SERS enhancements by the coupling of plasmon modes on the NP and the surface. By using a rough gold surface (of same roughness as in the Klarite pit) we can compare the SERS enhancement given by the NPs alone on rough gold to those in the Klarite structure. For pATP alone on the rough surface we do not see a SERS signal at any excitation wavelength (see Fig. 8.7a). On addition of AuNPs to the surface the signal does not appear to change significantly. This suggests that any plasmonic enhancement here is not strong enough to see SERS modes. Due to the small diameter ($\approx$19 nm) of the NPs, we expect dimer modes to be relatively weak and simulations by Dr. Fumin Huang show it would be situated around $\lambda = 590$ nm (for a nm gap). Since we do not have any existing cavity mode (unlike in the Klarite case) we do not expect enhancement at other wavelengths. On addition of AgNPs, however, a well-defined SERS spectra appears at all excitation wavelengths (see Fig. 8.7b). The shape of the spectra is broadly similar for all wavelengths and similar to those seen on the Klarite structure. For the AgNPs, any plasmonic resonance will be blue-shifted compared to that of the Au, and we would expect a dimer mode to be situated near

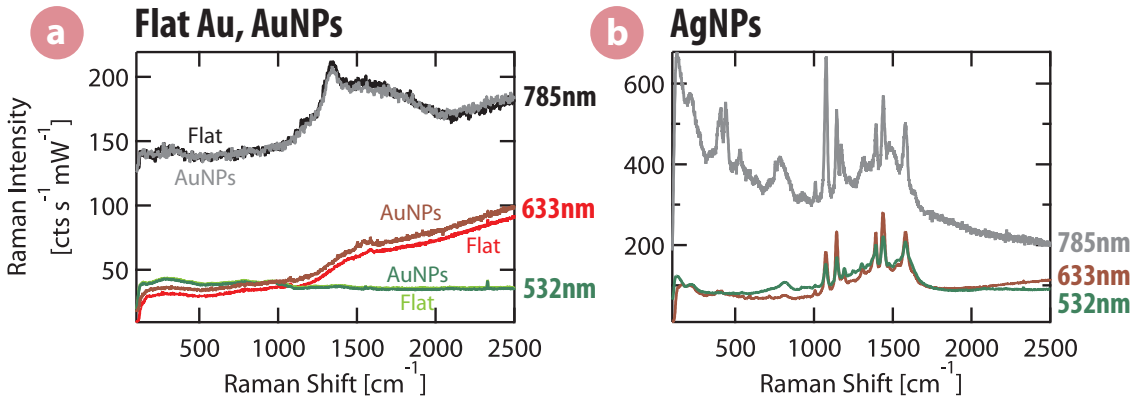

Figure 8.7.: Raman/SERS measurements on flat gold (with same nanoscale roughness as Klarite) at various excitation Raman wavelengths (785 nm, 633 nm and 532 nm) of pATP **(a)** On its own and with AuNPs showing no Raman signal and **(b)** with AgNPs showing SERS enhancement.

$\lambda = 430$ nm, which is far away from the excitation wavelengths we are using. This strongly suggests that the enhancement seen for AgNPs must be a chemical change or charge-transfer effect.

8.2.4. Silver nitrate as a substitute for AgNPs

To try to separate out the possible effects of charge transfer from electromagnetic SERS enhancement we use silver nitrate ($AgNO_3$) solution. After forming a pATP SAM we put the Klarite and rough flat gold into 0.1 mM $AgNO_3$ solution. Looking at the SERS spectra on the rough flat gold, we see that, unlike for the AgNPs, at 785 nm there is no enhancement in signal from the original pATP SAM (Fig. 8.8). At 532 nm there is some difference as we can see the appearance of very small peaks associated with pATP, indicating an enhancement of these modes. On the Klarite structure, there is a large enhancement of the modes, almost identical to that created with AgNPs, except the **7a** and **8a** modes are not as enhanced as the other modes at 785 nm excitation.

8.3. Discussion

There is a large debate as to the relative contributions of the EM and CT enhancements seen in SERS. PATP is a molecule of significant interest for plasmonic systems

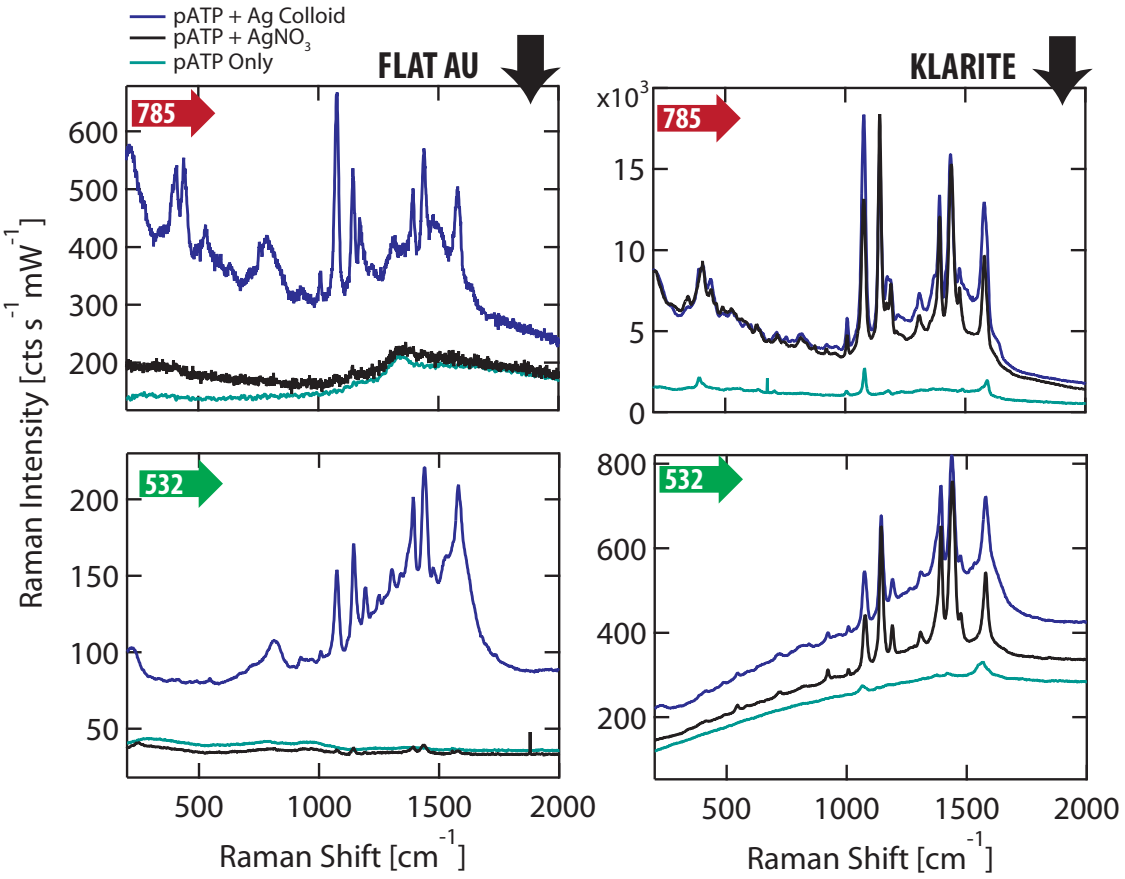

Figure 8.8.: SERS measurements on **(left)** flat gold and **(right)** Klarite with a pATP SAM on its own, with addition of AgNPs or after soaking in silver nitrate solution ($AgNO_3$). Raman excitation at **(top)** $\lambda_{ex} = 785\,\text{nm}$ and **(bottom)** $\lambda_{ex} = 532\,\text{nm}$

due to its thiol and amine groups that allow interaction and binding to noble metals on both sides of the molecule. Systems with pATP and AuNPs or AgNPs have been extensively studied. [187, 188, 189] It is widely believed that the b_2 modes can be strongly charge-transfer enhanced, whilst the a_1 modes appear less affected. [190, 29]. There is currently a large debate in the scientific community between the origin of the b_2 modes seen in SERS of pATP. Some groups contest that these modes are not CT enhanced pATP modes but are due to 4,4'-dimercaptoaminobenzene (DMAB) which is formed from the photo-induced bonding of pATP molecules on silver. [189, 191, 192]. The problem arises since the SERS and Raman modes of pATP are quite different with the former appearing very similar to those for DMAB. [193] All pATP derivatives appear to share the b_2 symmetric modes. A recent paper has given convincing evidence supporting the CT nature of the b_2 modes with a careful comparison of pATP and DMAB. [194] However, a more convincing study has very recently been performed by Huang et al. [195] In this study they provide a thorough overview of the field before providing systematic experimental and theoretical evidence supporting the idea that the b_2 modes are indeed from the formation of DMAB and not from charge-transfer effects.

Broadly speaking, there could be two charge-transfer situations occurring. The pATP preferentially bonds to the gold and the sulphur group is electron donating. Here we can expect a charge transfer process to occur if the excitation wavelength is of sufficient energy as described in Sec. 2.3.1. With addition of AuNPs, we expect the interaction to be principally via electrostatic attraction of the negatively charged citrate capping molecule and the positively charged amine group. Little charge transfer would be expected from this as there is no covalent bond between the amine group and the gold. With AgNPs, the amine can bond directly to the silver surface. This can lead to additional charge transfer effects with this complex. The molecule now also acts like a bridge between the gold Klarite surface and the AgNP and charge transfer between the metals is now possible.

Our results indicate that the principal enhancement at $\lambda_{ex} = 785\,\text{nm}$ is EM in origin on addition of AuNPs. Since there appears to be no preferential enhancement of a particular group of modes (such as b_2) we believe any CT effects to be minimal here. The excitation wavelength is too low in energy for the Klarite-molecule CT process (as described in Sec. 2.3.1) to occur. For AgNPs at this wavelength, the relatively lower heights of the a_1 peaks suggest a smaller EM enhancement, which could be explained by a change in plasmonic behaviour moving from Au to Ag, with

any resonance tail of a dimer mode blue-shifted further away from the excitation wavelength. The b_2-modes, however, are relatively strongly enhanced, with the **9b** mode $8\times$ higher in intensity than in the AuNP case. This could indicate activation of CT effects due to bonding of the amine group to the AgNP. It could also mean bonding to the AgNP has catalysed the production of DMAB from pATP, causing a change in the relative peak heights as has been shown in other studies. [195]

At $\lambda_{ex} = 633\,\text{nm}$ the case is somewhat different. After addition of AuNPs the spectrum is enhanced but this time we see preferential enhancement of the CT (b_2) modes. The original spectrum (Klarite-pATP) without AuNPs also showed evidence of b_2 modes not present at 785 nm. Uetsuki et al. [29, 192] showed that for pATP attached to a SERS active gold surface, CT resonance excitation was observed at 633 nm, this could explain the stronger presence of the b_2 modes in this case compared to $\lambda_{ex} = 785\,\text{nm}$. This could also explain the presence of the fluorescence-like background due to excitation of electronic modes via charge transfer from the metal, which may then decay through fluorescence. This CT resonance excitation seems to be still further preferentially enhanced on addition of NPs. For AgNPs, the enhancement is less for the a_1 modes than in the AuNP case, but the b_2 modes are further enhanced providing strong evidence for a further CT enhancement of formation of DMAB, above that seen for the ATP/ATP-AuNP cases.

At $\lambda_{ex} = 532\,\text{nm}$ the ATP on Klarite provides a very weak signal since we are far away from any Klarite plasmonic resonance. The addition of AuNPs provides minimal enhancement to a_1 modes suggesting no CT and minimal EM enhancement. AgNPs produced enhancement to both a_1 and b_2 modes. This suggests some EM enhancement, which would be expected at lower wavelengths for silver coupled systems. The relative peak height change, with strong b_2 peaks, strongly supports again a charge transfer effect, or perhaps more likely the formation of DMAB. The lack of increase in SERS enhancement at any wavelength of AuNPs on flat gold, supports the hypothesis that addition of AuNPs causes an increase in SERS signal via assisting coupling into the existing plasmonic modes of Klarite, which do not exist on flat gold. For AgNPs on flat gold all excitation wavelengths showed the appearance of a_1 and b_2 pATP modes with dominance of the latter. Interestingly, comparing peak intensities here with those in the Klarite-pATP-AgNP structure, we see that a and b peaks are further enhanced in the Klarite pit, but by similar amounts for all wavelengths. The fact that the a_1 peaks are as strong here as the b_2 peaks suggests that the enhancement of b_2 peaks may indeed be due to formation of DMAB rather

than CT effects. If it was purely a CT effect we would not expect the a_1 peaks to be nearly as strong as the b_2 ones on addition of AgNPs, in the case here, where there was an absence of any peaks before colloid addition (see Fig. 8.7).

In the case of silver nitrate we hope to attach a silver ion to the amine group of the pATP. By doing this we reduce any possibility of further EM/plasmonic enhancement caused by the addition of NPs, whilst hopefully still observing a chemical enhancement. It is probable that we form complexes with more than one silver ion per amine group. Earlier studies have shown small clusters of silver ions (< 8 ions) attached to molecules can give strong SERS enhancements, [196] whilst time-dependent density functional theory calculations on a pyrazine molecule between two Ag_{20} clusters predicted huge charge transfer Raman enhancements of 10^5. [197] On Klarite, we see almost the same enhancement with $AgNO_3$ as with AgNPs. This suggests a large CT enhancement due to the silver ions, however, on flat gold the enhancement with $AgNO_3$ is not observed (perhaps minimally at $\lambda_{ex} = 532$ nm). If the mechanism here were purely CT, we would also expect enhancement on flat gold, as we saw with AgNPs. This confirms that there is no significant electromagnetic enhancement from the silver ions, suggesting they form clusters too small for plasmonic resonances. A plausible theory requires both the EM enhancement from the Klarite structure and a further enhancement from the silver ions or more likely the silver ions could be driving the photo-induced change of pATP into DMAB. It is unclear why enhancement of the silver ions is almost identical to AgNPs in Klarite but not on the surface. It could suggest that formation of DMAB is stronger with silver ions than with AgNPs. Careful experiments are needed to determine what state the silver nitrate is in on the surface to fully understand these results.

8.4. Conclusions

The chemical enhancement effect can be strong and significantly alter observed SERS spectra. The subtleties of CT enhancement or photo-induced catalytic change are frequently overlooked in studies focusing on the EM enhancement.

Here we have shown that addition of 20 nm AuNPs to a Klarite-analyte system can increase the SERS signal observed by 3000 %. Given careful consideration of the analyte, we have shown that at 785 nm the enhancement is principally electromag-

netic in origin, enhancing coupling into the existing Klarite plasmon modes. This is similar to that shown by Scholes et al. [185]

We have also shown that using 30 nm AgNPs leads to enhancement of the SERS signal on Klarite, but in this case was principally caused by either charge transfer or conversion of pATP into DMAB, leading to a huge change in the relative mode intensities between the a_1 and b_2 symmetry modes. Comparisons with AgNPs-pATP-flatgold and $AgNO_3$-pATP-flatgold provided evidence for the conversion of pATP to DMAB, but it was not possible to identify the exact enhancement origins or to rule out charge transfer completely.

Further work is needed to fully understand the pATP sandwich structures seen here. Isolating the molecule from the metals using silica or a polymer coating on the NPs and Klarite surface such as PVP [29] could help distinguish between chemical and EM effects, since removing the contact between the molecule and the metal should remove the enhancement of CT modes. This could prove difficult to form uniform nm-sized, pin-hole free coatings. Comparisons with other para-substituted molecules [192, 193] which do not have the amine group but instead have a methyl group, for example, could also allow us to remove the extra CT activity.

A study with systematic variation in NP size could provide useful tracking of the EM modes and the different roles of single particle, dimer and enhanced coupling into Klarite modes. It would be desirable to use EM simulations and optical measurements to track the wavelength dependence of the plasmonic modes. It is unlikely that CT modes would be affected by NP size, whereas the EM modes should be highly size-dependent.

9. Conclusions and future work

This thesis has investigated the nature of surface-enhanced Raman scattering on plasmonic nanostructures, focussing on the commercially-available Klarite nanostructure. I used and developed microscopic and angularly-resolved spectroscopic techniques as well as boundary element method modelling to aid understanding of the optical modes found on the Klarite nanostructure. I established appropriate techniques to measure the Raman scattering from both organic and inorganic-based systems and studied their temperature and time evolution after perturbation. This chapter briefly summarises the main findings and presents possible future directions of study.

9.1. Summary

In Chapter 5, for the first-time, I observed surface-enhanced Raman scattering of a sub-monolayer of CdSe core-only and CdSe/ZnS (core/shell) semiconducting quantum dots. [1] Varying the wavelength highlighted the differences between resonant and non-resonant SERS as well as the importance of the plasmonic cavity modes. This extends SERS to nanostructured spatially well-defined inorganic systems, paving the way for their use as robust SERS markers.

Using micron-sized CO_2 crystals fired (snow jet) at SERS substrates in Chapter 6 I have shown order of magnitude enhancements of the SERS peak signal on the gold Klarite surface. [2] Via development of a novel measurement technique (MTVE), I have been able to distinguish between effects affecting the SERS peak from those affecting the SERS background continuum. The results support the hypothesis that molecules are pushed into plasmonic hotspots located in surface-roughness features, causing the enhancement, whilst changes to surface roughness appear to affect the SERS background continuum. The different origins of the SERS background and peak signals open the possibility for further control over the SERS spectra to reduce

the SERS background and increase the peak intensity. This approach can be used to further increase the sensitivity of SERS substrates.

Chapter 7 examined the temperature dependence (from room temperature to 10 K) of SERS and resonant SERS in organic-molecular and inorganic-quantum dot systems. Intensity of SERS peaks and the SERS background continuum were observed to increase with decreasing temperature. This was shown to be linked to the decrease in damping in the metal as the temperature decreases. In the case of resonant SERS more complicated temperature dependence was observed and the SERS background was dominated by quantum dot fluorescence. At low temperatures (< 50 K) and pumping near the QD emission ($\lambda_{ex} = 633$ nm) I observed QD fluorescence line-narrowing and a reduction in PL-phonon replica broadening resulting in significant shape changes to the observed SERS spectra. Lowering the temperature provides another route to increase the sensitivity of SERS as well as providing an interesting platform to study inorganic QD systems.

Lastly in Chapter 8, coupling gold and silver nanoparticles using p-aminothiophenol molecular junctions on the Klarite nanostructure, I observed EM enhancements to the SERS signal of approximately $100\times$. In the case of silver nanoparticles, significant changes to the relative peak heights further suggested either charge-transfer enhancement of specific SERS peaks or the formation of 4,4'-dimercaptoaminobenzene due to photo-induced catalytic change was observed in addition to EM enhancement. This result highlights the importance of both chemical and EM factors to the SERS signal and thus the complexity necessary to obtain a full understanding of observed SERS spectra on nanostructured plasmonic surfaces.

In the appendix (see Appendix A) can be found a new template-stripping fabrication technique [3] I developed to produce near atomically flat gold using liquid glass and mica. This technique is useful to a wide-range of applications including SERS where it can be used to study the effect of surface roughness on novel SERS structures. It was also used in Chapter 5 to allow a dispersed layer of sub-10 nm quantum dots to be imaged using atomic force microscopy.

9.2. Future experiments

As SERS research progresses the understanding of its origins is developing and it will remain a strong area of interest for many years to come. Applications using SERS for

medical diagnostics have emerged, such as the RenDx® (Renishaw Diagnostics) [198] multiplex assay system currently undergoing medical trials. In the next decades, we should look forward to expanded use of SERS in medical settings. The study has added to the knowledge of SERS on plasmonic nanostructures, but many questions still remain. In this chapter I outline some of the directions this research could take heading forward.

9.2.1. The SERS background

Chapter 6 examined the SERS background and how it can be perturbed, although, further investigation is needed to determine the full origin of this background. In Chapter 5 we saw that in resonance systems the fluorescence signal can add to and dominate the normal SERS background. Even in non-resonant systems, the SERS background is strongly dependent on the excitation wavelength. Changing the substrate temperature (Chapter 7) and firing carbon dioxide crystals at its surface (Chapter 6) provide possible approaches to control the background and suggest the background has different origin than SERS peak signals. Developing further control of the SERS background is necessary and will result from further experiments to pinpoint the different processes contributing to the background signal. Possible routes are:

1. Tracking different lifetimes of the SERS background features could reveal the origin of the different processes. Fluorescence effects (such as two-photon metal luminescence) would have longer lifetimes compared to the much faster SERS signals. Using a gated SERS technique it may be possible to reduce the SERS background by only collecting the short lifetime SERS light.
2. Using a tunable SERS system where the excitation wavelength can be tuned through continuous wavelengths, it would be possible to clearly track the background continuum shape on and off plasmonic resonances of the system. This may yield insight into the plasmonic nature of the background.

9.2.2. Plasmons on Klarite

The precise nature of the localised plasmons on the Klarite mesostructure remain uncertain. As Klarite has both λ and sub-λ-scale structures, near-field diffraction

and/or plasmonic standing waves could impact the plasmonic properties. The roughness of the structure also plays a significant role potentially creating tightly localised ($\sim$ nm) hot spots within the larger pit resonances. Possible future directions include:

1. Experiments to see where the SERS enhancements originate from within the pit: Where are the localised hot spots? These hot spots are difficult to see optically as they are below the diffraction limit. Using tip-enhanced Raman scattering (TERS) to locally increase SERS intensity whilst scanning the Klarite nanostructure could yield high spatial resolution, although given the geometry may be difficult to perform.

2. Mapping the near-field optical response using photo-active polymers: The various models in the literature for the Klarite plasmon mode location (see Chapter 4) do not agree and experimentally mapping the near-field mode distribution would do much to resolve the discrepancies. Such mapping could perhaps be done using a photographic-like process to expose a photo-active polymer. Electron microscopy of the developed polymer could reveal, in great detail, the plasmonic near-field.

3. SERS marker placement: By placing SERS markers (such as QDs) into specific positions on the pit, perhaps by nanoimprint lithography or nanopipetting, it may be possible to track the SERS enhancement at different locations in the pit. From this, it might be possible to construct an image of the electric field intensity in the pit, shedding light on the nature of hot spots in the surface roughness of the pit. However, this experiment would be very time-consuming, and again, the geometry of the pit could pose an access problem.

9.2.3. Chemical effects

There remains a debate about the strength of the contribution to SERS from chemical effects caused by the molecule interacting with the metallic SERS surfaces. Hence:

1. Coating Klarite and nanoparticles with a silica or polymer film to selectively eliminate charge transfer effects could allow tracking of the purely electromagnetic enhancement. This approach could be combined with use of a variety of non-charge-transfer-active molecules. The difficulty then comes in controlling

the attachment and nanoparticle-Klarite separation and the background SERS signal may also be significantly affected in this case.

2. Using the temperature-controlled SERS measurements developed in this thesis, it may be possible to confirm the charge transfer origin of the pATP modes. Since the Fermi energy of the metals varies with temperature due to thermal occupation of states, so should the CT resonance condition. Combining this with a tunable SERS system could provide convincing evidence for CT versus EM enhancement of specific modes.

Out of the many possible experiments which could proceed out of this thesis, I have highlighted a few possible routes to take forward. These routes would yield a wealth of interesting results and help reveal some of the subtleties of the SERS effect on plasmonic nanostructures.

Appendix A.

Template-stripped gold

Templating against atomically flat materials allows creation of smooth metallic surfaces. The process of adding the backing (superstrate) to the deposited metals has proved to be the most difficult part in producing reliable, large-area, solvent resistant substrates and has been subject of recent research. In this appendix we describe a simple and inexpensive liquid glass template-stripping (lgTS) method for the fabrication of large area ultra-flat gold surfaces. [3] Using our lgTS method ultra-flat gold surfaces with normals aligned along the $\langle 111 \rangle$ crystal plane and with a root-mean square roughness of 0.275 nm (measured over 1 μm^2) were created. The surfaces are fabricated on silica-based substrates which are highly solvent resistant and electrically insulating using silicate precursor solution (commonly known as 'liquid glass') and concomitant mild heat treatment. We demonstrate the capabilities of such ultra-flat gold surfaces by imaging nanoscale objects on top and fabricating microelectrodes as an example application. Due to the simplicity and versatility of the fabrication process, lgTS will have wide-ranging application in imaging, catalysis, electrochemistry and surface science.

Metallic surfaces with near atomic roughness are increasingly essential to a plethora of applications in surface and interface sciences. These surfaces have found many applications in biology, electrochemistry and electronics. [45, 199] Such surfaces used in conjunction with scanning probe microscopies can facilitate imaging of biomolecules such as lipids and proteins, and organic and inorganic colloids, such as quantum dots. Gold is a highly inert metal with a high oxidation potential and therefore the material of choice in many electrochemical applications. Crystalline surfaces enable mechanistic studies at interfaces using electrochemistry and other surface science techniques. Gold is also easily and robustly functionalized with thiol (-SH) termi-

nated molecules. Such self-assembled monolayers of thiols on gold are one of the prevalent tools in nanoscience where ultra-flat surfaces are extremely valuable.

Furthermore, gold is an important material at visible wavelengths in the increasingly popular field of plasmonics. [200] Plasmonics has a wide range of applications including surface-enhanced Raman scattering (SERS), where surface roughness plays a key role in the million or more-fold signal enhancements commonly observed.

Ultraflat gold substrates have found use in confirming the effect of roughness [77] and to quantify enhancement factors. In short, a simple, low cost route to ultraflat gold which is compatible with commonly used solvents is enormously valuable to a large range of disciplines.

Traditionally, deposition methods such as sputtering and evaporation are used to obtain metal surfaces. However, these result in island formation leading to rough surface finishes. A solution has been found by combining these techniques with cleaved single crystals which reveal atomically flat planes. Metal deposition is carried out directly on top, producing near-atomically flat gold surfaces at the interface. After deposition and further processing to add a backing layer to the deposited metal, the crystalline template is removed, revealing the ultraflat gold surface. This is known as template-stripped gold (TSG).

A variety of TSG methods have been developed to add a backing layer to the ultraflat metal. Hegner et al.[201] use a mica film as the template and epoxy glue to attach the gold to a silicon wafer superstrate. Whilst providing a simple and robust method of TSG formation, the weakness of this method is the use of epoxy glue which is sensitive to organic solvents, in which swelling causes distortion of the gold surface. This system also suffers from trapped air bubbles and outgassing, which are problems under vacuum. [202] The epoxy method has been improved by introducing ceramic glues, which are not as severely plagued by organic solvent problems. [203] These epoxies are still not entirely solvent resistant. [202]

A novel non-epoxy approach involves nickel superstrates formed by electroplating onto the conductive gold surface. Nickel is conductive and not completely inert limiting the application of such prepared surfaces in electronics. Gold often prematurely delaminates from the mica surface during nickel electroplating. [204] Most recently, solid-state bonding techniques have been developed which rely on gold diffusion. [204, 199, 202] Two surfaces, a substrate (gold on mica) and a superstrate (gold on glass), are bonded under pressure and/or heat. Gold ions diffuse between

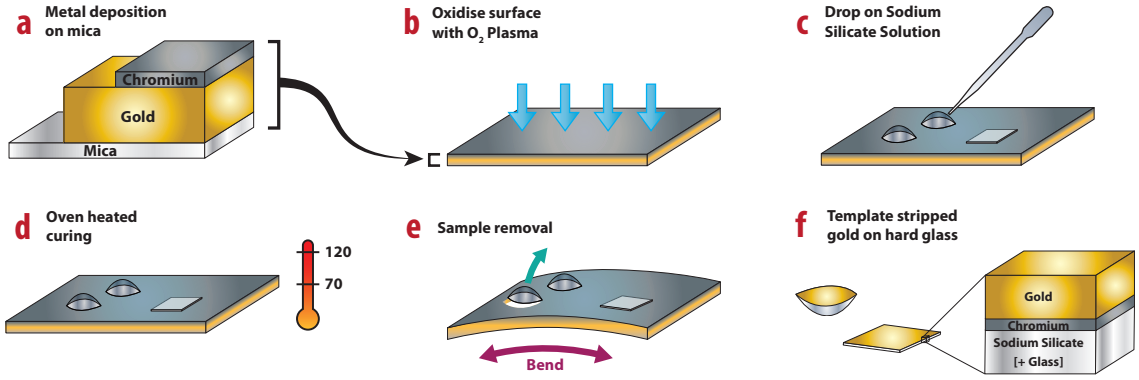

Figure A.1.: lgTSG fabrication schema **(a)** Gold (150 nm) and chromium (5 nm) layers are thermally evaporated onto a freshly cleaved mica substrate. **(b)** Chromium is hydrophillically functionalized by oxygen plasma. **(c)** Sodium silicate solution (liquid glass) is drop cast onto the chromium surface. Plasma cleaned glass slides can be placed on top of these droplets to form a sturdier backing. **(d)** Heating in a two stage process balances water evaporation and transformation to silica. **(e)** lgTSG can easily be removed by gently bending the mica. **(f)** The process results in ultraflat gold backed onto a glass slide or a thin (300 µm) silica sheet.

the two metal interfaces, fusing them together. As there is no glue, this method is not affected by solvent induced swelling, but it suffers from several technical drawbacks. Cold-welding [202] is highly sensitive to surface contamination, and is generally not reliable over large areas. This is overcome by heating the gold surfaces during bonding [204] which increases ion mobility, requiring temperatures above 300°C and pressures up to 4000 psi. The increased mobility leads to significant gold re-organization, which can cause delamination. The only solution is to deposit gold at a high temperature, a capability not available in most evaporators. Although centimetre sized films have been produced using solid-state bonding by distributing the load using aluminium foil, [204] this advance requires significant optimization. Moreover patterned designs, such as electrodes, are not possible with solid-state bonding methods due to the difficulty in alignment of masks used to generate them. A final variation on TSG to avoid substrate deformation by solvent swelling has been to use solder as the bonding agent. Conventional solders melt around 200°C, which damages the thin gold film, so low-melting (m.p.$\sim$ 70°C) solders are used. However, these are highly toxic, limiting the ease of creation. [205]

The rest of this appendix will show a novel silica-based approach for fabricating ultra-flat gold, called the liquid glass TS (lgTS) method. [2] This process has several

advantages over those described above. (1) It is solvent resistant and (2) consists of very few simple steps which are highly reproducible. (3) It is compatible with glass substrates, providing an insulating substrate. (4) It is able to create large-area ($>1\,\mathrm{cm}^2$) substrates as well as (5) patterns with 100 µm-sized features. (6) Many samples can be made in parallel and (7) the process requires only low cost materials and no specialized evaporation or high pressure systems. Furthermore, the silica-formed superstrate is transparent at visible wavelengths, and is therefore compatible with systems requiring optical access to the back of the gold film. In our process we deposit gold on freshly cleaved mica and then use a liquid silica precursor as both the glue and superstrate. A simple hydrophilic chromium functionalization of the gold surface, and gentle heating, allows this precursor to bond, and harden, respectively. The resulting ultraflat gold is easy to remove from its mica substrate. These procedures are not highly time-sensitive or intensive and do not require a clean-room atmosphere.

A.1. Materials and methods

High grade ruby muscovite $20\,\mathrm{cm}^2$ mica sheets (Agar Scientific), 99.99 % pure gold pellets (Birmingham Metal Company), chromium plated tungsten rods (Agar Scientific) and sodium silicate solution (Sigma-Aldrich 338443), also known as liquid glass, were used as received. Evaporation was performed on a BOC Edwards Auto 306 resistance evaporator at 10^{-6} mbar. Oxygen plasma treatment was performed using a Diener Electronic Femto plasma system. The samples were dried in a Binder FP programable oven at 2°C/min.

Cadmium Selenide QDs (Nanoco Technologies Ltd./Sigma-Aldrich Lumidots 662461) were used to show the imaging potential of the lgTSG substrates. The solutions were diluted further with toluene before use. Two varying density quantum dot layers were produced: (1) A small drop of low concentration (5 µg /ml) solution was drop cast onto the lgTSG, giving rise to a low QD density. (2) A higher density but still sub-monolayer coverage of QDs was created via SAM functionalization and QD adsorption [1] as seen in Chapter 5.

AFM was performed using a Veeco Nanoscope IV, with an ultra-sharp tapping mode tip (Nanosensors PPP-NCHR).

Thermogravimetric analysis (TGA) was performed on a TA Instruments Q500, from 20°C to 200°C at a rate of 1°C/min under air.

Wide-angle x-ray diffraction was carried out using a Bruker D8 diffractometer with a K_α beam of λ=1.5406 Å. Spectra were taken with angular increments of 0.00914° and a dwell time of 0.5 s.

A.2. Fabrication

Facile fabrication of solvent resistant ultraflat gold is outlined in Fig. A.1. Gold of 150 nm was thermally evaporated onto freshly cleaved mica. Under continued vacuum, 5 nm of chromium was deposited on top of the gold surface. The use of chromium as an adhesion layer is common between gold and silica surfaces and this principle was successfully applied in our inverse geometry. All evaporation was done at a rate of 0.2 $Å s^{-1}$. Evaporation masks were used to pattern electrodes.

The chromium layer was exposed to an oxygen plasma for 5 minutes to increase the thickness of the native surface oxide layer and thus increase hydrophilicity with average water contact angle decreasing from 65° to <3°. This allows the silica solution to wet the surface, which ensures uniform drying, and prevents the trapping of air bubbles during this process which can destroy the sample. The oxidized surface also promotes adhesion of the silicate network through Si-O bonding. Two types of samples were created, with and without an additional glass slide backing. In the first case, glass slides (1 cm^2) were cleaned and oxidized by oxygen plasma, to enhance wetting. The slides were drop-coated with 20 µl of sodium silicate solution and immediately inverted and placed onto the oxidized chromium surface. In the second case, for samples without the backing, the sodium silicate solution was drop cast directly onto the oxidized chromium surface.

Drying and conversion of liquid sodium silicate to a solid silicate network was then achieved by controlled heating to ensure bubble-free and low solubility lgTSG. Samples were heated in a two-stage process, first to 70°C and then 120°C, for 12 h each. The lower temperature annealing removes the water from solution but does not provide enough energy to remove water locked into the silicate structure. The higher temperature annealing frees this water, which lowers the hydration state and decreases the solubility of the solid sodium silicate network. The higher the fraction

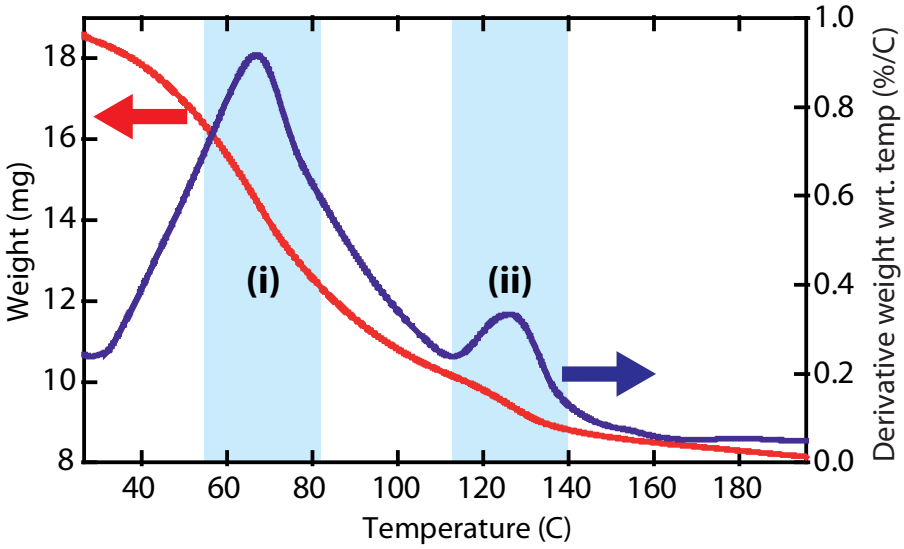

Figure A.2.: Thermogravimetric analysis (TGA) for sodium metasilicate. Two key regions are identified (i) and (ii), corresponding to water loss from the crystal structure at different temperatures. Heating to higher than 120 C is necessary to ensure sufficient water is removed from the structure.

of removed water, the less soluble the silica network. [206, 207, 208] Using thermogravimetric analysis (TGA) we obtained the drying profile shown in Fig. A.2 showing two distinct drying regions. Region (i) corresponds to the area where water is fully evaporated from the solution. Further water is released in region (ii), corresponding to a change in the silica hydration state. It is necessary to perform the annealing in two stages as direct heating to high temperatures leads to water boiling and the formation of bubbles. The resulting samples can be stored indefinitely in anhydrous conditions. lgTSG samples are easily and quickly removed from the mica substrate when needed by gently flexing the mica sheet.

A.3. Discussion

TSG roughness was characterized using tapping-mode AFM. We repeatably measured an average root-mean-squared (RMS) roughness to be 0.275 nm over an area of a square micron, confirming the near atomic flatness of the samples. This RMS value is equivalent to or better than values quoted in the literature. [204, 209, 210, 205, 211, 212, 201] Due to the ultra-smooth nature of lgTSG surfaces, it was possible to clearly image individual QDs, as shown in Fig. A.3. Ul-

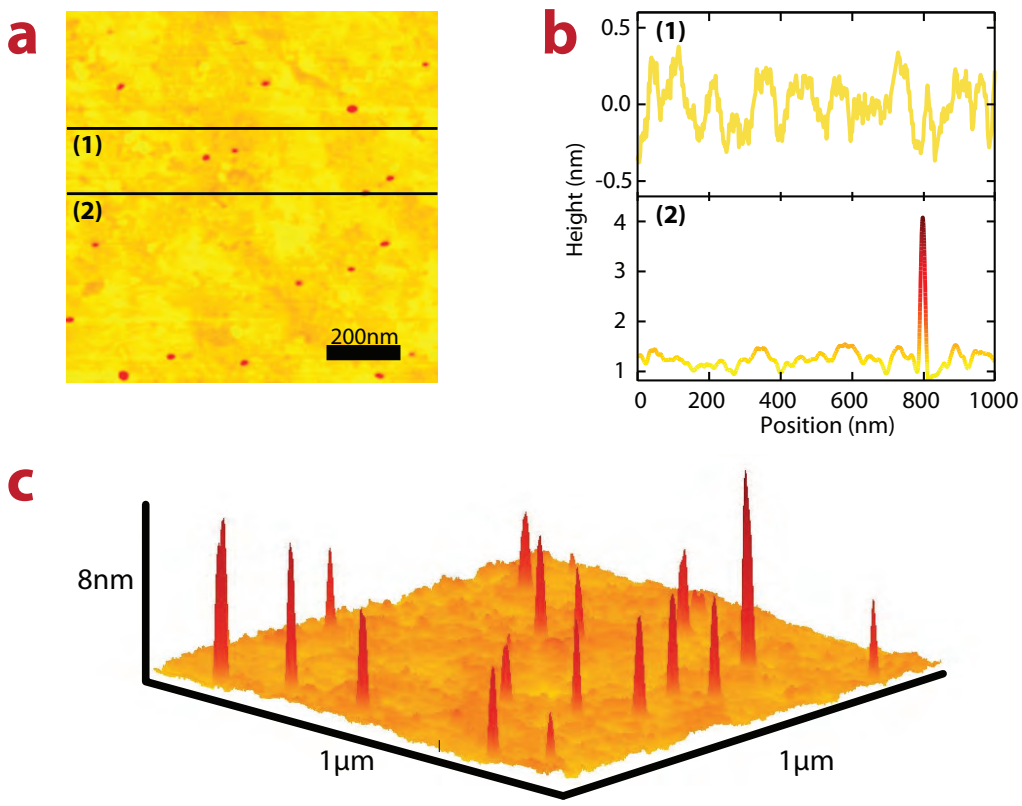

Figure A.3.: (a) AFM image of 6 nm CdSe quantum dots on a flat lgTSG surface. (b) cross-sections showing line height profiles across AFM image of a flat area (1) and over a quantum dot(2). (c) Three-dimensional AFM image of quantum dots on a lgTSG.

traflat gold is essential for such measurements because of the small (6 nm) diameter of the QDs. When measured on standard evaporated gold, they are lost in the surface roughness. The employed sample preparation procedure demonstrates one of the advantages of lgTSG, since standard TSG would swell and be destroyed by the deposition of the QDs from toluene.

Oriented crystallinity at the interface is important for catalytic, electrochemical and surface science studies as surface interactions are dependent on the crystal plane. Hence x-ray diffraction (XRD) tests were performed (by Dr. Alex Finnemore) to determine the crystallographic properties of the lgTSG thin films. The spectrum in Fig. A.4 is dominated by the gold $\langle 111 \rangle$ reflection peak. Contrary to that from polycrystalline gold, the peaks corresponding to other gold planes are missing. [210] Thus, the lgTSG films consists of $\langle 111 \rangle$ co-aligned crystals.

Since crystalline surfaces are important in electrochemistry we demonstrate the ease

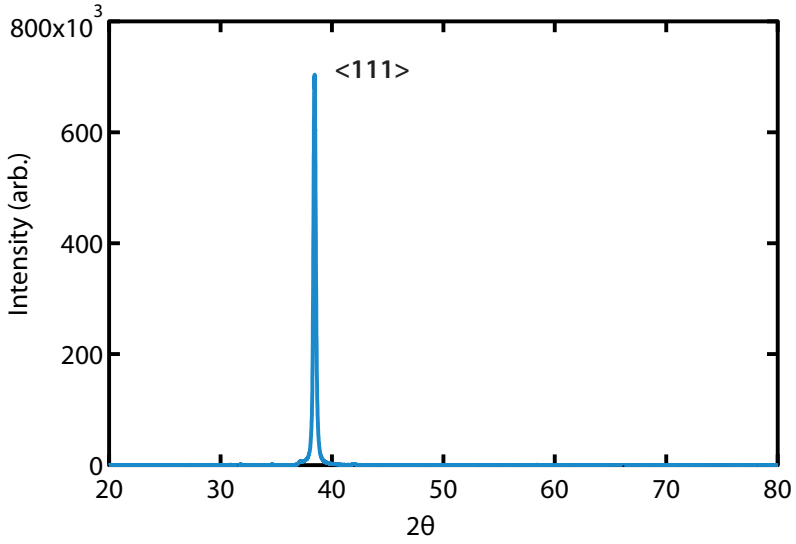

Figure A.4.: 2θ x-ray diffraction spectrum of TSG films showing the dominance of the $\langle 111 \rangle$ crystallographic plane.

of patterning using the lgTS process by fabricating micron-sized electrodes. An lgTSG interdigitated electrode fabricated using an evaporation mask and the lgTS procedure is shown in Fig. A.5, illustrating the versatility of the lgTS technique.

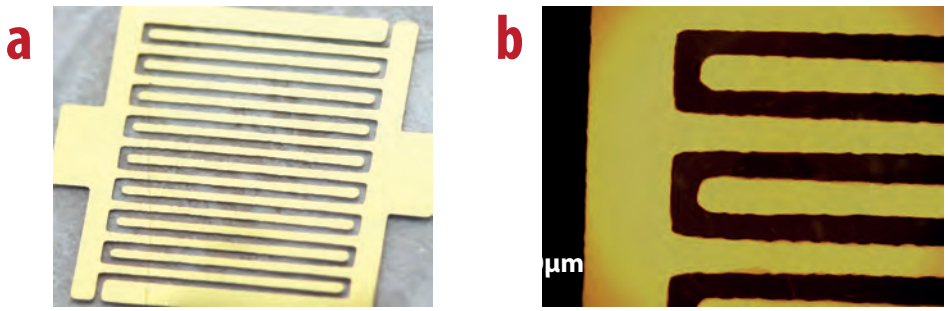

Figure A.5.: (a) Photograph of a 1 cm^2 gold electrode as prepared using the lgTS process. (b) 5 x Microscope image of the electrode, showing the 200 µm features.

Finally, we note that our lgTS technique represents a simple and cost-effective route to fabricate solvent resistant TSG. Sodium silicate solution is widely available and inexpensive. Competing methods such as those requiring solid-state bonding require specialized equipment and extensive calibration to achieve repeatable samples. The lgTS method is able to repeatably produce reproducible surfaces and many samples in parallel.

A.4. Conclusions

A simple and inexpensive way of fabricating TSG has been developed, resulting in metal surfaces with 0.275 nm RMS surface roughness. The resulting substrate is ultra-smooth, optically transparent and stable in a wide-variety of organic solvents. The gold is crystallographically aligned in the ⟨111⟩ direction. This facilitates easy handling in a chemical environment, often required for working with SAMs and is therefore advantageous for widespread use in nanoscience. This technique improves over existing methods in terms of sample preparation complexity, cost and solvent instability, while retaining the same level of surface flatness. Furthermore, we have demonstrated the utility of lgTSG surfaces in imaging nanoscale objects such as quantum dots. We have also shown the ability to pattern ultra-flat µm-sized structures with the lgTS process which should find widespread use in catalytic, electrochemical and surface science studies.

Bibliography

[1] Hugall JT, Baumberg JJ and Mahajan S. 'Surface-enhanced Raman spectroscopy of CdSe quantum dots on nanostructured plasmonic surfaces'. *Applied Physics Letters*, **95** 141111 (2009) DOI: 10.1063/1.3243982.

[2] Hugall JT, Baumberg JJ and Mahajan S. 'Disentangling the Peak and Background Signals in Surface-Enhanced Raman Scattering'. *The Journal of Physical Chemistry C*, **116** 6184 (2012) DOI: 10.1021/jp3002977.

[3] Hugall JT, Finnemore AS, Baumberg JJ, Steiner U and Mahajan S. 'Solvent-resistant ultraflat gold using liquid glass.' *Langmuir*, **28** 1347 (2012) DOI: 10.1021/la204299h.

[4] Mahajan S, Lee TC, Biedermann F, Hugall JT, Baumberg JJ and Scherman O. 'Raman and SERS spectroscopy of cucurbit[n]urils'. *Physical Chemistry Chemical Physics*, **12** 10429 (2010) DOI: 10.1039/c0cp00071j.

[5] Speed JD, Johnson RP, Hugall JT, Lal NN, Bartlett PN, Baumberg JJ and Russell AE. 'SERS from molecules bridging the gap of particle-in-cavity structures.' *Chemical Communications (Cambridge, England)*, **47** 6335 (2011) DOI: 10.1039/c0cc05325b.

[6] Raman C. 'Why the sky is blue?' (1968). URL: http://www.arvindguptatoys.com/arvindgupta/raman.htm (1968).

[7] Kneipp K, Wang Y, Kneipp H, Perelman L, Itzkan I, Dasari R and Feld M. 'Single Molecule Detection Using Surface-Enhanced Raman Scattering (SERS)'. *Physical Review Letters*, **78** 1667 (1997) DOI: 10.1103/PhysRevLett.78.1667.

[8] Nie S and Emory SR. 'Probing Single Molecules and Single Nanoparticles by Surface-Enhanced Raman Scattering'. *Science*, **275** 1102 (1997) DOI: 10.1126/science.275.5303.1102.

[9] Lal NN, Soares BF, Sinha JK, Huang F, Mahajan S, Bartlett PN, Greenham NC and Baumberg JJ. 'Enhancing solar cells with localized plasmons in nanovoids'. *Optics Express*, **19** 11256 (2011) DOI: 10.1364/OE.19.011256.

[10] Atwater H and Polman A. 'Plasmonics for improved photovoltaic devices.' *Nature Materials*, **9** 205 (2010) DOI: 10.1038/nmat2629.

[11] Barnes WL, Dereux A and Ebbesen TW. 'Surface plasmon subwavelength optics'. *Nature*, **424** 824 (2003) DOI: 10.1038/nature01937.

[12] Ozbay E. 'Plasmonics: Merging photonics and electronics at nanoscale dimensions'. *Science*, **311** 189 (2006) DOI: 10.1126/science.1114849.

[13] Khurgin JB and Sun G. 'Scaling of losses with size and wavelength in nanoplasmonics and metamaterials'. *Applied Physics Letters*, **99** 211106 (2011) DOI: 10.1063/1.3664105.

[14] Kusar P, Gruber C, Hohenau A and Krenn JR. 'Measurement and reduction of damping in plasmonic nanowires.' *Nano Letters*, **12** 661 (2012) DOI: 10.1021/nl203452d.

[15] Raether H. *Surface Plasmons on Smooth and Rough Surfaces and on Gratings*. Berlin, Heidelberg, New York, London, Paris, Tokyo: Springer-Verlag (1988).

[16] Zayats AV, Smolyaninov II and Maradudin AA. 'Nano-optics of surface plasmon polaritons'. *Physics Reports*, **408** 131 (2005) DOI: 10.1016/j.physrep.2004.11.001.

[17] Maier SA. *Plasmonics: Fundamentals and Applications*. Boston, MA: Springer US (2007). ISBN 978-0-387-33150-8. DOI: 10.1007/0-387-37825-1.

[18] Feynman RP, Leighton RB and Sands M. *The Feynman Lectures on Physics*. New York: Basic Books, new millen edn. (2010).

[19] Maier SA and Atwater HA. 'Plasmonics: Localization and guiding of electromagnetic energy in metal/dielectric structures'. *Journal of Applied Physics*, **98** 10 (2005) DOI: 011101 10.1063/1.1951057.

[20] Johnson PB and Christy RW. 'Optical Constants of the Noble Metals'. *Physical Review B*, **6** 4370 (1972) DOI: 10.1103/PhysRevB.6.4370.

[21] Stockman MI. 'Nanoplasmonics: past, present, and glimpse into future'. *Optics Express*, **19** 22029 (2011) DOI: 10.1364/OE.19.022029.

[22] Raman CV and Krishnan KS. 'A New Type of Secondary Radiation'. *Nature*, **121** 501 (1928) DOI: 10.1038/121501c0.

[23] Hahn DW. 'Raman Scattering Theory Accessed June 2009' (2007). URL: http://plaza.ufl.edu/dwhahn/RamanScatteringTheory.pdf (2007).

[24] Etchegoin PG and Le Ru EC. *Principles of Surface-Enhanced Raman Spectroscopy and related Plasmonic effects*. Oxford: Elsevier, 1st edn. (2009).

[25] Kneipp K, Moskovits M and Kneipp H (eds.). *Surface-Enhanced Raman Scattering*. 103. Berlin, Heidelberg, New York: Springer (2006). ISBN 978-3-540-33566-5. DOI: 10.1007/11663898.

[26] Fleischmann M, Hendra P and McQuillan A. 'Raman spectra of pyridine adsorbed at a silver electrode'. *Chemical Physics Letters*, **26** 163 (1974) DOI: 10.1016/0009-2614(74)85388-1.

[27] Albrecht MG and Creighton JA. 'Anomalously intense Raman spectra of pyridine at a silver electrode'. *Journal of the American Chemical Society*, **99** 5215 (1977) DOI: 10.1021/ja00457a071.

[28] Jeanmaire DL and Van Duyne RP. 'Surface raman spectroelectrochemistry Part I. Heterocyclic, aromatic, and aliphatic amines adsorbed on the anodized silver electrode'. *Journal of Electroanalytical Chemistry and Interfacial Electrochemistry*, **84** 1 (1977) DOI: 10.1016/S0022-0728(77)80224-6.

[29] Uetsuki K, Verma P, Yano T, Saito Y, Ichimura T and Kawata S. 'Experimental Identification of Chemical Effects in Surface Enhanced Raman Scattering of 4-Aminothiophenol'. *The Journal of Physical Chemistry C*, **114** 7515 (2010) DOI: 10.1021/jp9114805.

[30] Lin XM, Cui Y, Xu YH, Ren B and Tian ZQ. 'Surface-enhanced Raman spectroscopy: substrate-related issues'. *Analytical and Bioanalytical Chemistry*, **394** 1729 (2009) DOI: 10.1007/s00216-009-2761-5.

[31] Otto A. 'The 'chemical' (electronic) contribution to surface-enhanced Raman scattering'. *Journal of Raman Spectroscopy*, **36** 497 (2005) DOI: 10.1002/jrs.1355.

[32] Campion A and Kambhampati P. 'Surface-enhanced Raman scattering'. *Chemical Society Reviews*, **27** 241 (1998) DOI: 10.1039/a827241z.

[33] Osawa M, Matsuda N, Yoshii K and Uchida I. 'Charge transfer resonance Raman process in surface-enhanced Raman scattering from p-aminothiophenol

adsorbed on silver: Herzberg-Teller contribution'. *The Journal of Physical Chemistry*, **98** 12702 (1994) DOI: 10.1021/j100099a038.

[34] Gersten J, Birke R and Lombardi J. 'Theory of Enhanced Light Scattering from Molecules Adsorbed at the Metal-Solution Interface'. *Physical Review Letters*, **43** 147 (1979) DOI: 10.1103/PhysRevLett.43.147.

[35] Lombardi JR, Birke RL, Lu T and Xu J. 'Charge-transfer theory of surface enhanced Raman spectroscopy: Herzberg–Teller contributions'. *The Journal of Chemical Physics*, **84** 4174 (1986) DOI: 10.1063/1.450037.

[36] Lombardi J and Birke R. 'A Unified Approach to Surface-Enhanced Raman Spectroscopy'. *The Journal of Physical Chemistry C*, **112** 5605 (2008) DOI: 10.1021/jp800167v.

[37] García de Abajo F and Howie A. 'Relativistic Electron Energy Loss and Electron-Induced Photon Emission in Inhomogeneous Dielectrics'. *Physical Review Letters*, **80** 5180 (1998) DOI: 10.1103/PhysRevLett.80.5180.

[38] García de Abajo F and Howie A. 'Retarded field calculation of electron energy loss in inhomogeneous dielectrics'. *Physical Review B*, **65** 1 (2002) DOI: 10.1103/PhysRevB.65.115418.

[39] Cole RM, Baumberg JJ, Garcia de Abajo FJ, Mahajan S, Abdelsalam M and Bartlett PN. 'Understanding Plasmons in Nanoscale Voids'. *Nano Letters*, **7** 2094 (2007) DOI: 10.1021/nl0710506.

[40] Nuzzo RG and Allara DL. 'Adsorption of bifunctional organic disulfides on gold surfaces'. *Journal of the American Chemical Society*, **105** 4481 (1983) DOI: 10.1021/ja00351a063.

[41] Strong L and Whitesides GM. 'Structures of self-assembled monolayer films of organosulfur compounds adsorbed on gold single crystals: electron diffraction studies'. *Langmuir*, **4** 546 (1988) DOI: 10.1021/la00081a009.

[42] Bain CD, Troughton EB, Tao YT, Evall J, Whitesides GM and Nuzzo RG. 'Formation of monolayer films by the spontaneous assembly of organic thiols from solution onto gold'. *Journal of the American Chemical Society*, **111** 321 (1989) DOI: 10.1021/ja00183a049.

[43] Dubois LH and Nuzzo RG. 'Synthesis, Structure, and Properties of Model Organic Surfaces'. *Annual Review of Physical Chemistry*, **43** 437 (1992) DOI: 10.1146/annurev.pc.43.100192.002253.

[44] Loudon GM. *Organic Chemistry*. Redwood City, CA: The Benjamin/Cummings Publishing Company, Inc., 3rd edn. (1995).

[45] Love JC, Estroff LA, Kriebel JK, Nuzzo RG and Whitesides GM. 'Self-assembled monolayers of thiolates on metals as a form of nanotechnology.' *Chemical Reviews*, **105** 1103 (2005) DOI: 10.1021/cr0300789.

[46] Sabatani E, Cohen-Boulakia J, Bruening M and Rubinstein I. 'Thioaromatic monolayers on gold: a new family of self-assembling monolayers'. *Langmuir*, **9** 2974 (1993) DOI: 10.1021/la00035a040.

[47] Tao Yt, Wu CC, Eu JY, Lin WL, Wu KC and Chen CH. 'Structure Evolution of Aromatic-Derivatized Thiol Monolayers on Evaporated Gold'. *Langmuir*, **13** 4018 (1997) DOI: 10.1021/la9700984.

[48] Wang H, Chen S, Li L and Jiang S. 'Improved method for the preparation of carboxylic acid and amine terminated self-assembled monolayers of alkanethiolates.' *Langmuir*, **21** 2633 (2005) DOI: 10.1021/la046810w.

[49] Gooding JJ, Mearns F, Yang W and Liu J. 'Self-Assembled Monolayers into the 21st Century: Recent Advances and Applications'. *Electroanalysis*, **15** 81 (2003) DOI: 10.1002/elan.200390017.

[50] Farah P, Gibbons N, Huang F and Baumberg JJ. 'Ultrafast nonlinearities of minibands in metallodielectric Bragg resonators'. *Physical Review B*, **84** 1 (2011) DOI: 10.1103/PhysRevB.84.125442.

[51] Moskovits M. 'Surface roughness and the enhanced intensity of Raman scattering by molecules adsorbed on metals'. *Journal of Chemical Physics*, **69** 4159 (1978) DOI: 10.1063/1.437095.

[52] Pettinger B, Wenning U and Wetzel H. 'Surface plasmon enhanced Raman scattering frequency and angular resonance of Raman scattered light from pyridine on Au, Ag and Cu electrodes'. *Surface Science*, **101** 409 (1980) DOI: 10.1016/0039-6028(80)90637-8.

[53] Pockrand I and Otto A. 'Surface enhanced Raman scattering (SERS): Annealing the silver substrate'. *Solid State Communications*, **38** 1159 (1981) DOI: 10.1016/0038-1098(81)90979-0.

[54] Wood TH and Klein MV. 'Studies of the mechanism of enhanced Raman scattering in ultrahigh vacuum'. *Solid State Communications*, **35** 263 (1980) DOI: 10.1016/0038-1098(80)90493-7.

[55] Freeman RG, Grabar KC, Allison KJ, Bright RM, Davis JA, Guthrie AP, Hommer MB, Jackson MA, Smith PC, Walter DG and Natan MJ. 'Self-Assembled Metal Colloid Monolayers: An Approach to SERS Substrates.' *Science*, **267** 1629 (1995) DOI: 10.1126/science.267.5204.1629.

[56] Schwartzberg AM and Zhang JZ. 'Novel Optical Properties and Emerging Applications of Metal Nanostructures'. *The Journal of Physical Chemistry C*, **112** 10323 (2008) DOI: 10.1021/jp801770w.

[57] Kahl M, Voges E, Kostrewa S, Viets C and Hill W. 'Periodically structured metallic substrates for SERS'. *Sensors and Actuators B: Chemical*, **51** 285 (1998) DOI: 10.1016/S0925-4005(98)00219-6.

[58] Brolo AG, Arctander E, Gordon R, Leathem B and Kavanagh KL. 'Nanohole-Enhanced Raman Scattering'. *Nano Letters*, **4** 2015 (2004) DOI: 10.1021/nl048818w.

[59] Liu SW and Xiao M. 'Electro-optic switch in ferroelectric thin films mediated by surface plasmons'. *Applied Physics Letters*, **88** 143512 (2006) DOI: 10.1063/1.2193968.

[60] Dickson W, Wurtz G, Evans P, O'Connor D, Atkinson R, Pollard R and Zayats A. 'Dielectric-loaded plasmonic nanoantenna arrays: A metamaterial with tuneable optical properties'. *Physical Review B*, **76** 6 (2007) DOI: 10.1103/PhysRevB.76.115411.

[61] Camden JP, Dieringer JA, Zhao J and Van Duyne RP. 'Controlled Plasmonic Nanostructures for Surface-Enhanced Spectroscopy and Sensing'. *Accounts of Chemical Research*, **41** 1653 (2008) DOI: 10.1021/ar800041s.

[62] Cui B, Clime L, Li K and Veres T. 'Fabrication of large area nanoprism arrays and their application for surface enhanced Raman spectroscopy.' *Nanotechnology*, **19** 145302 (2008) DOI: 10.1088/0957-4484/19/14/145302.

[63] Henzie J, Shuford KL, Kwak ES, Schatz GC and Odom TW. 'Manipulating the optical properties of pyramidal nanoparticle arrays'. *The Journal of Physical Chemistry B*, **110** 14028 (2006) DOI: 10.1021/jp063226i.

[64] Im H, Bantz KC, Lindquist NC, Haynes CL and Oh SH. 'Vertically oriented sub-10-nm plasmonic nanogap arrays.' *Nano Letters*, **10** 2231 (2010) DOI: 10.1021/nl1012085.

[65] Abdelsalam ME, Bartlett PN, Baumberg JJ, Cintra S, Kelf TA and Russell AE. 'Electrochemical SERS at a structured gold surface'. *Electrochemistry Communications*, **7** 740 (2005) DOI: 10.1016/j.elecom.2005.04.028.

[66] Haynes CL and Van Duyne RP. 'Nanosphere Lithography: A Versatile Nanofabrication Tool for Studies of Size-Dependent Nanoparticle Optics'. *The Journal of Physical Chemistry B*, **105** 5599 (2001) DOI: 10.1021/jp010657m.

[67] Kelf T, Sugawara Y, Baumberg JJ, Abdelsalam M and Bartlett P. 'Plasmonic Band Gaps and Trapped Plasmons on Nanostructured Metal Surfaces'. *Physical Review Letters*, **95** 1 (2005) DOI: 10.1103/PhysRevLett.95.116802.

[68] Kelf T, Sugawara Y, Cole R, Baumberg JJ, Abdelsalam M, Cintra S, Mahajan S, Russell A and Bartlett P. 'Localized and delocalized plasmons in metallic nanovoids'. *Physical Review B*, **74** 12 (2006) DOI: 10.1103/PhysRevB.74.245415.

[69] Dieringer JA, McFarland AD, Shah NC, Stuart DA, Whitney AV, Yonzon CR, Young MA, Zhang X and Van Duyne RP. 'Introductory Lecture : Surface enhanced Raman spectroscopy: new materials, concepts, characterization tools, and applications'. *Faraday Discussions*, **132** 9 (2006) DOI: 10.1039/b513431p.

[70] Liu Y, Fan J, Zhao YP, Shanmukh S and Dluhy RA. 'Angle dependent surface enhanced Raman scattering obtained from a Ag nanorod array substrate'. *Applied Physics Letters*, **89** 173134 (2006) DOI: 10.1063/1.2369644.

[71] Brown RJC and Milton MJT. 'Nanostructures and nanostructured substrates for surface-enhanced Raman scattering (SERS)'. *Journal of Raman Spectroscopy*, **39** 1313 (2008) DOI: 10.1002/jrs.2030.

[72] Stewart ME, Anderton CR, Thompson LB, Maria J, Gray SK, Rogers JA and Nuzzo RG. 'Nanostructured plasmonic sensors'. *Chemical Reviews*, **108** 494 (2008) DOI: 10.1021/cr068126n.

[73] Fan M, Andrade GFS and Brolo AG. 'A review on the fabrication of substrates for surface enhanced Raman spectroscopy and their applications in analytical chemistry.' *Analytica Chimica Acta*, **693** 7 (2011) DOI: 10.1016/j.aca.2011.03.002.

[74] Henzie J, Lee J, Lee MH, Hasan W and Odom TW. 'Nanofabrication of

plasmonic structures.' *Annual Review of Physical Chemistry*, **60** 147 (2009) DOI: 10.1146/annurev.physchem.040808.090352.

[75] Taylor RW, Lee TC, Scherman O, Esteban R, Aizpurua J, Huang FM, Baumberg JJ and Mahajan S. 'Precise subnanometer plasmonic junctions for SERS within gold nanoparticle assemblies using cucurbit[n]uril "glue".' *ACS Nano*, **5** 3878 (2011) DOI: 10.1021/nn200250v.

[76] Li JF, Huang YF, Ding Y, Yang ZL, Li SB, Zhou XS, Fan FR, Zhang W, Zhou ZY, Wu DY, Ren B, Wang ZL and Tian ZQ. 'Shell-isolated nanoparticle-enhanced Raman spectroscopy.' *Nature*, **464** 392 (2010) DOI: 10.1038/nature08907.

[77] Li L, Hutter T, Finnemore AS, Huang FM, Baumberg JJ, Elliott SR, Steiner U and Mahajan S. 'Metal oxide nanoparticle mediated enhanced Raman scattering and its use in direct monitoring of interfacial chemical reactions.' *Nano Letters*, **12** 4242 (2012) DOI: 10.1021/nl302029p.

[78] Quagliano LG. 'Observation of molecules adsorbed on III-V semiconductor quantum dots by surface-enhanced Raman scattering'. *Journal of the American Chemical Society*, **126** 7393 (2004) DOI: 10.1021/ja031640f.

[79] Wang YF, Zhang JH, Jia HY, Li MJ, Zeng JB, Yang B, Zhao B, Xu WQ and Lombardi JR. 'Mercaptopyridine surface-functionalized CdTe quantum dots with enhanced Raman scattering properties'. *The Journal of Physical Chemistry C*, **112** 996 (2008) DOI: 10.1021/jp077467h.

[80] Wang YF, Sun ZH, Wang YX, Hu HL, Zhao B, Xu WQ and Lombardi JR. 'Surface-enhanced Raman scattering on mercaptopyridine-capped US microclusters'. *Spectrochimica Acta Part A: Molecular Spectroscopy*, **66** 1199 (2007) DOI: 10.1016/j.saa.2006.06.008.

[81] Ling X and Zhang J. 'First-layer effect in graphene-enhanced Raman scattering.' *Small*, **6** 2020 (2010) DOI: 10.1002/smll.201000918.

[82] Goncalves G, Marques PAAP, Granadeiro CM, Nogueira HIS, Singh MK and Grácio J. 'Surface Modification of Graphene Nanosheets with Gold Nanoparticles: The Role of Oxygen Moieties at Graphene Surface on Gold Nucleation and Growth'. *Chemistry of Materials*, **21** 4796 (2009) DOI: 10.1021/cm901052s.

[83] Perney N, García de Abajo F, Baumberg JJ, Tang A, Netti M, Charlton M and Zoorob M. 'Tuning localized plasmon cavities for optimized

surface-enhanced Raman scattering'. *Physical Review B*, **76** 35425 (2007) DOI: 10.1103/PhysRevB.76.035426.

[84] Perney NM, Baumberg JJ, Zoorob ME, Charlton MDB, Mahnkopf S and Netti CM. 'Tuning localized plasmons in nanostructured substrates for surface-enhanced Raman scattering'. *Optics Express*, **14** 847 (2006) DOI: 10.1364/OPEX.14.000847.

[85] Alexander TA and Le DM. 'Characterization of a commercialized SERS-active substrate and its application to the identification of intact Bacillus endospores'. *Applied Optics*, **46** 3878 (2007) DOI: 10.1364/AO.46.003878.

[86] He L, Liu Y, Lin M, Mustapha A and Wang Y. 'Detecting single Bacillus spores by surface enhanced Raman spectroscopy'. *Sensing and Instrumentation for Food Quality and Safety*, **2** 247 (2008) DOI: 10.1007/s11694-008-9054-0.

[87] Graham D and Faulds K. 'Quantitative SERRS for DNA sequence analysis.' *Chemical Society reviews*, **37** 1042 (2008) DOI: 10.1039/b707941a.

[88] Stokes RJ, Macaskill A, Dougan JA, Hargreaves PG, Stanford HM, Smith WE, Faulds K and Graham D. 'Highly sensitive detection of dye-labelled DNA using nanostructured gold surfaces.' *Chemical Communications (Cambridge, England)*, **2007** 2811 (2007) DOI: 10.1039/b705873j.

[89] Stokes RJ, Ingram A, Gallagher J, Armstrong DR, Smith WE and Graham D. 'Squaraines as unique reporters for SERRS multiplexing.' *Chemical Communications (Cambridge, England)*, **2008** 567 (2008) DOI: 10.1039/b715388k.

[90] Stokes RJ, Dougan JA and Graham D. 'Dip-pen nanolithography and SERRS as synergic techniques.' *Chemical Communications (Cambridge, England)*, **2008** 5734 (2008) DOI: 10.1039/b813249f.

[91] He L, Liu Y, Lin M, Awika J, Ledoux DR, Li H and Mustapha A. 'A new approach to measure melamine, cyanuric acid, and melamine cyanurate using surface enhanced Raman spectroscopy coupled with gold nanosubstrates'. *Sensing and Instrumentation for Food Quality and Safety*, **2** 66 (2008) DOI: 10.1007/s11694-008-9038-0.

[92] Lin M, He L, Awika J, Yang L, Ledoux DR, Li H and Mustapha A. 'Detection of melamine in gluten, chicken feed, and processed foods using surface enhanced Raman spectroscopy and HPLC.' *Journal of Food Science*, **73** T129 (2008) DOI: 10.1111/j.1750-3841.2008.00901.x.

[93] Fan C, Hu Z, Riley LK, Purdy Ga, Mustapha A and Lin M. 'Detecting food- and waterborne viruses by surface-enhanced Raman spectroscopy.' *Journal of Food Science*, **75** M302 (2010) DOI: 10.1111/j.1750-3841.2010.01619.x.

[94] Holthoff EL, Stratis-Cullum DN and Hankus ME. 'A nanosensor for TNT detection based on molecularly imprinted polymers and surface enhanced Raman scattering.' *Sensors*, **11** 2700 (2011) DOI: 10.3390/s110302700.

[95] Botti S, Cantarini L and Palucci A. 'Surface-enhanced Raman spectroscopy for trace-level detection of explosives'. *Journal of Raman Spectroscopy*, **41** 866 (2010) DOI: 10.1002/jrs.2649.

[96] Kantarovich K, Tsarfati I, Gheber LA, Haupt K and Bar I. 'Writing droplets of molecularly imprinted polymers by nano fountain pen and detecting their molecular interactions by surface-enhanced Raman scattering.' *Analytical Chemistry*, **81** 5686 (2009) DOI: 10.1021/ac900418x.

[97] Kantarovich K, Tsarfati I, Gheber LA, Haupt K and Bar I. 'Reading microdots of a molecularly imprinted polymer by surface-enhanced Raman spectroscopy.' *Biosensors and Bioelectronics*, **26** 809 (2010) DOI: 10.1016/j.bios.2010.06.018.

[98] Corrigan DK, Salton Na, Preston C and Piletsky S. 'Towards the development of a rapid, portable, surface enhanced Raman spectroscopy based cleaning verification system for the drug nelarabine.' *The Journal of Pharmacy and Pharmacology*, **62** 1195 (2010) DOI: 10.1111/j.2042-7158.2010.01152.x.

[99] Steuwe C, Kaminski CF, Baumberg JJ and Mahajan S. 'Surface enhanced coherent anti-stokes Raman scattering on nanostructured gold surfaces.' *Nano Letters*, **11** 5339 (2011) DOI: 10.1021/nl202875w.

[100] Goldberg-Oppenheimer P, Mahajan S and Steiner U. 'Hierarchical electrohydrodynamic structures for surface-enhanced Raman scattering.' *Advanced Materials*, **24** OP175 (2012) DOI: 10.1002/adma.201104159.

[101] Wu HY, Choi CJ and Cunningham BT. 'Plasmonic nanogap-enhanced Raman scattering using a resonant nanodome array.' *Small*, **8** 2878 (2012) DOI: 10.1002/smll.201200712.

[102] Jiao Y, Ryckman JD, Ciesielski PN, Escobar CA, Jennings GK and Weiss SM. 'Patterned nanoporous gold as an effective SERS template.' *Nanotechnology*, **22** 295302 (2011) DOI: 10.1088/0957-4484/22/29/295302.

[103] Betz JF, Cheng Y and Rubloff GW. 'Direct SERS detection of contaminants in a complex mixture: rapid, single step screening for melamine in liquid infant formula.' *The Analyst*, **137** 826 (2012) DOI: 10.1039/c2an15846a.

[104] Sato K, Shikida M, Yamashiro T, Tsunekawa M and Ito S. 'Roughening of single-crystal silicon surface etched by KOH water solution'. *Sensors and Actuators A: Physical*, **73** 122 (1999) DOI: 10.1016/S0924-4247(98)00270-2.

[105] Trupke M, Ramirez-Martinez F, Curtis EA, Ashmore JP, Eriksson S, Hinds EA, Moktadir Z, Gollasch C, Kraft M, Vijaya Prakash G and Baumberg JJ. 'Pyramidal micromirrors for microsystems and atom chips'. *Applied Physics Letters*, **88** 071116 (2006) DOI: 10.1063/1.2172412.

[106] Vernon KC, Davis TJ, Scholes FH, Gómez DE and Lau D. 'Physical mechanisms behind the SERS enhancement of pyramidal pit substrates'. *Journal of Raman Spectroscopy*, **41** 1106 (2010) DOI: 10.1002/jrs.2557.

[107] Mechler M, Kukhlevsky SV, Mechler A and McNaughton D. 'Near-field diffraction in a two-dimensional V-groove and its role in SERS.' *Physical Chemistry Chemical Physics*, **13** 20772 (2011) DOI: 10.1039/c1cp21750j.

[108] Skaife JJ, Brake JM and Abbott NL. 'Influence of Nanometer-Scale Topography of Surfaces on the Orientational Response of Liquid Crystals to Proteins Specifically Bound to Surface-Immobilized Receptors'. *Langmuir*, **17** 5448 (2001) DOI: 10.1021/la0017678.

[109] Fang J, Du S, Lebedkin S, Li Z, Kruk R, Kappes M and Hahn H. 'Gold Mesostructures with Tailored Surface Topography and Their Self-Assembly Arrays for Surface-Enhanced Raman Spectroscopy.' *Nano Letters*, pp. 5006–5013 (2010) DOI: 10.1021/nl103161q.

[110] Alivisatos AP. 'Semiconductor Clusters, Nanocrystals, and Quantum Dots'. *Science*, **271** 933 (1996) DOI: 10.1126/science.271.5251.933.

[111] Michalet X, Pinaud FF, Bentolila LA, Tsay JM, Doose S, Li JJ, Sundaresan G, Wu AM, Gambhir SS and Weiss S. 'Quantum dots for live cells, in vivo imaging, and diagnostics.' *Science*, **307** 538 (2005) DOI: 10.1126/science.1104274.

[112] Medintz IL, Uyeda HT, Goldman ER and Mattoussi H. 'Quantum dot bioconjugates for imaging, labelling and sensing'. *Nature Materials*, **4** 435 (2005) DOI: 10.1038/nmat1390.

[113] Somers RC, Bawendi MG and Nocera DG. 'CdSe nanocrystal based chem-/bio-sensors'. *Chemical Society Reviews*, **36** 579 (2007) DOI: 10.1039/b517613c.

[114] Mahajan S, Baumberg JJ, Russell AE, Bartlett PN and Russell E. 'Reproducible SERRS from structured gold surfaces'. *Physical Chemistry Chemical Physics*, **9** 6016 (2007) DOI: 10.1039/b712144j.

[115] Faulds K, Barbagallo RP, Keer JT, Smith WE and Graham D. 'SERRS as a more sensitive technique for the detection of labelled oligonucleotides compared to fluorescence'. *Analyst*, **129** 567 (2004) DOI: 10.1039/b406423b.

[116] Moskovits M. 'Surface-enhanced spectroscopy'. *Reviews of Modern Physics*, **57** 783 (1985) DOI: 10.1103/RevModPhys.57.783.

[117] Nanoco Technologies, Nanoco Group PLC. Company website [accessed: Feb 2012]. URL: http://www.nanocotechnologies.com/.

[118] Mahajan S, Cole RM, Soares BF, Pelfrey SH, Russell AE, Baumberg JJ and Bartlett PN. 'Relating SERS Intensity to Specific Plasmon Modes on Sphere Segment Void Surfaces'. *The Journal of Physical Chemistry C*, **113** 9284 (2009) DOI: 10.1021/jp900661u.

[119] Castro JL, López-Ramírez MR, Arenas JF and Otero JC. 'Surface-enhanced Raman scattering of 3-mercaptopropionic acid adsorbed on a colloidal silver surface'. *Journal of Raman Spectroscopy*, **35** 997 (2004) DOI: 10.1002/jrs.1247.

[120] Klein M, Hache F, Ricard D and Flytzanis C. 'Size dependence of electron-phonon coupling in semiconductor nanospheres: The case of CdSe'. *Physical Review B*, **42** 11123 (1990) DOI: 10.1103/PhysRevB.42.11123.

[121] Hwang YN, Park SH and Kim D. 'Size-dependent surface phonon mode of CdSe quantum dots'. *Physical Review B*, **59** 7285 (1999) DOI: 10.1103/PhysRevB.59.7285.

[122] Baranov A, Rakovich Y, Donegan J, Perova T, Moore R, Talapin D, Rogach A, Masumoto Y and Nabiev I. 'Effect of ZnS shell thickness on the phonon spectra in CdSe quantum dots'. *Physical Review B*, **68** 165306 (2003) DOI: 10.1103/PhysRevB.68.165306.

[123] Comas F, Trallero-Giner C, Studart N and Marques G. 'Interface optical

phonons in spheroidal dots: Raman selection rules'. *Physical Review B*, **65** 2 (2002) DOI: 10.1103/PhysRevB.65.073303.

[124] Azhniuk YM, Hutych YI, Lopushansky VV, Milekhin AG, Gomonnai AV and Zahn DRT. 'Surface phonons in CdS_{1-x} Se_x nanoparticles embedded in a dielectric medium'. *Physica Status Solidi (C)*, **6** 2039 (2009) DOI: 10.1002/pssc.200881753.

[125] Ekimov AI, Hache F, Schanne-Klein MC, Ricard D, Flytzanis C, Kudryavtsev IA, Yazeva TV, Rodina AV and Efros AL. 'Absorption and intensity-dependent photoluminescence measurements on CdSe quantum dots: assignment of the first electronic transitions'. *Journal of the Optical Society of America B*, **10** 100 (1993) DOI: 10.1364/JOSAB.10.000100.

[126] Novotny L and Hecht B. *Principles of Nano-Optics*. New York: Cambridge University Press (2012).

[127] Woggon U. *Optical Properties of Semiconductor Quantum Dots*. Berlin, Heidelberg, New York: Springer-Verlag (1997).

[128] Dabbousi BO, Rodriguez-Viejo J, Mikulec FV, Heine JR, Mattoussi H, Ober R, Jensen KF and Bawendi MG. '(CdSe)ZnS Core-Shell Quantum Dots: Synthesis and Characterization of a Size Series of Highly Luminescent Nanocrystallites'. *The Journal of Physical Chemistry B*, **101** 9463 (1997) DOI: 10.1021/jp971091y.

[129] Lu L, Xu XL, Liang WT and Lu HF. 'Raman analysis of CdSe/CdS core-shell quantum dots with different CdS shell thickness.' *Journal of Physics: Condensed Matter*, **19** 406221 (2007) DOI: 10.1088/0953-8984/19/40/406221.

[130] Norikazu Hiramatsu (Nanoco Technologies, Nanoco Group PLC). Personal communication (email) July 2012 (2012).

[131] Cole RM, Baumberg JJ, Abajo FJGD, Mahajan S, Abdelsalam M and Bartlett PN. 'Understanding Plasmons in Nanoscale Voids'. *Nano Letters*, **7** 2094 (2007) DOI: 10.1021/nl0710506.

[132] Saito Y, Wang JJ, Smith DA and Batchelder DN. 'A Simple Chemical Method for the Preparation of Silver Surfaces for Efficient SERS'. *Langmuir*, **18** 2959 (2002) DOI: 10.1021/la011554y.

[133] Doering WE and Nie S. 'Single-Molecule and Single-Nanoparticle SERS: Ex-

amining the Roles of Surface Active Sites and Chemical Enhancement'. *The Journal of Physical Chemistry B*, **106** 311 (2002) DOI: 10.1021/jp011730b.

[134] Otto A, Mrozek I, Grabhorn H and Akemann W. 'Surface-enhanced Raman scattering'. *Journal of Physics: Condensed Matter*, **4** 1143 (1992) DOI: 10.1088/0953-8984/4/5/001.

[135] Moskovits M, DiLella DP and Maynard KJ. 'Surface Raman spectroscopy of a number of cyclic aromatic molecules adsorbed on silver: selection rules and molecular reorientation'. *Langmuir*, **4** 67 (1988) DOI: 10.1021/la00079a012.

[136] Otto A. 'Raman scattering from adsorbates on silver'. *Surface Science*, **92** 145 (1980) DOI: 10.1016/0039-6028(80)90249-6.

[137] Heritage J, Bergman J, Pinczuk A and Worlock J. 'Surface picosecond raman gain spectroscopy of a cyanide monolayer on silver'. *Chemical Physics Letters*, **67** 229 (1979) DOI: 10.1016/0009-2614(79)85152-0.

[138] Otto A, Timper J, Billmann J, Kovacs G and Pockrand I. 'Surface roughness induced electronic Raman scattering'. *Surface Science*, **92** L55 (1980) DOI: 10.1016/0039-6028(80)90237-X.

[139] Burstein E. '"Giant" Raman scattering by adsorbed molecules on metal surfaces'. *Solid State Communications*, **29** 567 (1979) DOI: 10.1016/0038-1098(79)90665-3.

[140] Furtak T and Reyes J. 'A critical analysis of theoretical models for the giant Raman effect from adsorbed molecules'. *Surface Science*, **93** 351 (1980) DOI: 10.1016/0039-6028(80)90270-8.

[141] Mahajan S, Cole RM, Speed JD, Pelfrey SH, Russell AE, Bartlett PN, Barnett SM and Baumberg JJ. 'Understanding the Surface-Enhanced Raman Spectroscopy "Background"'. *The Journal of Physical Chemistry C*, **114** 7242 (2010) DOI: 10.1021/jp907197b.

[142] Sherman R, Hirt D and Vane R. 'Surface cleaning with the carbon dioxide snow jet'. *Journal of Vacuum Science & Technology A: Vacuum, Surfaces, and Films*, **12** 1876 (1994) DOI: 10.1116/1.579021.

[143] Schoenfisch MH and Pemberton JE. 'Air Stability of Alkanethiol Self-Assembled Monolayers on Silver and Gold Surfaces'. *Journal of the American Chemical Society*, **120** 4502 (1998) DOI: 10.1021/ja974301t.

[144] Sherman R. 'The removal of hydrocarbons and silicone grease stains from silicon wafers'. *Journal of Vacuum Science & Technology B: Microelectronics and Nanometer Structures*, **8** 563 (1990) DOI: 10.1116/1.585010.

[145] Sherman R. 'Dry surface cleaning using CO_2 snow'. *Journal of Vacuum Science & Technology B: Microelectronics and Nanometer Structures*, **9** 1970 (1991) DOI: 10.1116/1.585390.

[146] Socrates G. *Infrared and Raman Characteristic Group Frequencies: Tables and Charts*, vol. 35. Chichester: Wiley, 3rd edn. (2004).

[147] Joo TH, Kim MS and Kim K. 'Surface-enhanced Raman scattering of benzenethiol in silver sol'. *Journal of Raman Spectroscopy*, **18** 57 (1987) DOI: 10.1002/jrs.1250180111.

[148] Sobnack M, Tan W, Wanstall N, Preist T and Sambles J. 'Stationary Surface Plasmons on a Zero-Order Metal Grating'. *Physical Review Letters*, **80** 5667 (1998) DOI: 10.1103/PhysRevLett.80.5667.

[149] García-Vidal F and Pendry J. 'Collective Theory for Surface Enhanced Raman Scattering'. *Physical Review Letters*, **77** 1163 (1996) DOI: 10.1103/PhysRevLett.77.1163.

[150] Litorja M, Haynes CL, Haes AJ, Jensen TR and Van Duyne RP. 'Surface-Enhanced Raman Scattering Detected Temperature Programmed Desorption: Optical Properties, Nanostructure, and Stability of Silver Film over SiO_2 Nanosphere Surfaces'. *The Journal of Physical Chemistry B*, **105** 6907 (2001) DOI: 10.1021/jp010333y.

[151] Dick LA, McFarland AD, Haynes CL and Van Duyne RP. 'Metal Film over Nanosphere (MFON) Electrodes for Surface-Enhanced Raman Spectroscopy (SERS): Improvements in Surface Nanostructure Stability and Suppression of Irreversible Loss'. *The Journal of Physical Chemistry B*, **106** 853 (2002) DOI: 10.1021/jp0136381.

[152] Barrena E, Ocal C and Salmeron M. 'Evolution of the structure and mechanical stability of self-assembled alkanethiol islands on Au(111) due to diffusion and ripening'. *The Journal of Chemical Physics*, **111** 9797 (1999) DOI: 10.1063/1.480316.

[153] McCarley RL, Dunaway DJ and Willicut RJ. 'Mobility of the alkanethiol-

gold (111) interface studied by scanning probe microscopy'. *Langmuir*, **9** 2775 (1993) DOI: 10.1021/la00035a007.

[154] Ionita P, Volkov A, Jeschke G and Chechik V. 'Lateral diffusion of thiol ligands on the surface of au nanoparticles: an electron paramagnetic resonance study.' *Analytical Chemistry*, **80** 95 (2008) DOI: 10.1021/ac071266s.

[155] Farcau C and Astilean S. 'Evidence of a surface plasmon-mediated mechanism in the generation of the SERS background.' *Chemical Communications (Cambridge, England)*, **47** 3861 (2011) DOI: 10.1039/c0cc05190j.

[156] Ashcroft NW and Mermin ND. *Solid state physics*. London: Harcourt Brace, reprint edn. (1976).

[157] McKay J and Rayne J. 'Temperature dependence of the infrared absorptivity of the noble metals'. *Physical Review B*, **13** 673 (1976) DOI: 10.1103/PhysRevB.13.673.

[158] Biondi M. 'Optical Absorption of Copper and Silver at 4.2°K'. *Physical Review*, **102** 964 (1956) DOI: 10.1103/PhysRev.102.964.

[159] Haynes WR and Lide DR (eds.). *The Handbook of Chemistry and Physics*. Boca Raton, FL: CRC Press/Taylor and Francis, 92nd edn. (2012).

[160] Sambles JR, Bradbery GW and Yang F. 'Optical excitation of surface plasmons: An introduction'. *Contemporary Physics*, **32** 173 (1991) DOI: 10.1080/00107519108211048.

[161] Sarid D and Challener W. *Modern Introduction to Surface Plasmons*. Cambridge: Cambridge University Press (2010).

[162] Pang YS, Hwang HJ and Kim MS. 'Reversible Temperature Dependence in Surface-Enhanced Raman Scattering of 1-Propanethiol Adsorbed on a Silver Island Film'. *The Journal of Physical Chemistry B*, **102** 7203 (1998) DOI: 10.1021/jp981820p.

[163] Hinde RJ, Sepaniak MJ, Compton RN, Nordling J and Lavrik N. 'Surface-enhanced resonance Raman scattering of adsorbates under liquid nitrogen'. *Chemical Physics Letters*, **339** 167 (2001) DOI: 10.1016/S0009-2614(01)00323-2.

[164] Luedtke WD and Landman U. 'Structure and Thermodynamics of Self-Assembled Monolayers on Gold Nanocrystallites'. *The Journal of Physical Chemistry B*, **102** 6566 (1998) DOI: 10.1021/jp981745i.

[165] Nuzzo RG, Korenic EM and Dubois LH. 'Studies of the temperature-dependent phase behavior of long chain n-alkyl thiol monolayers on gold'. *The Journal of Chemical Physics*, **93** 767 (1990) DOI: 10.1063/1.459528.

[166] Tanaka A, Onari S and Arai T. 'Raman scattering from CdSe microcrystals embedded in a germanate glass matrix'. *Physical Review B*, **45** 6587 (1992) DOI: 10.1103/PhysRevB.45.6587.

[167] Dzhagan V, Valakh M, Raevskaya a, Stroyuk a, Kuchmiy S and Zahn D. 'Characterization of semiconductor core–shell nanoparticles by resonant Raman scattering and photoluminescence spectroscopy'. *Applied Surface Science*, **255** 725 (2008) DOI: 10.1016/j.apsusc.2008.07.018.

[168] Kusch P, Lange H, Artemyev M and Thomsen C. 'Size-dependence of the anharmonicities in the vibrational potential of colloidal CdSe nanocrystals'. *Solid State Communications*, **151** 67 (2011) DOI: 10.1016/j.ssc.2010.10.023.

[169] Balkanski M, Wallis R and Haro E. 'Anharmonic effects in light scattering due to optical phonons in silicon'. *Physical Review B*, **28** 1928 (1983) DOI: 10.1103/PhysRevB.28.1928.

[170] Alivisatos AP, Harris TD, Carroll PJ, Steigerwald ML and Brus LE. 'Electron–vibration coupling in semiconductor clusters studied by resonance Raman spectroscopy'. *The Journal of Chemical Physics*, **90** 3463 (1989) DOI: 10.1063/1.455855.

[171] Empedocles SA, Neuhauser R, Shimizu K and Bawendi MG. 'Photoluminescence from Single Semiconductor Nanostructures'. *Advanced Materials*, **11** 1243 (1999) DOI: 10.1002/(SICI)1521-4095(199910)11:15<1243::AID-ADMA1243>3.0.CO;2-2.

[172] Nirmal M, Murray C and Bawendi M. 'Fluorescence-line narrowing in CdSe quantum dots: Surface localization of the photogenerated exciton'. *Physical Review B*, **50** 2293 (1994) DOI: 10.1103/PhysRevB.50.2293.

[173] Bawendi MG, Carroll PJ, Wilson WL and Brus LE. 'Luminescence properties of CdSe quantum crystallites: Resonance between interior and surface localized states'. *The Journal of Chemical Physics*, **96** 946 (1992) DOI: 10.1063/1.462114.

[174] Nirmal M, Murray CB, Norris DJ and Bawendi MG. 'Surface electronic prop-

erties of CdSe nanocrystallites'. *Zeitschrift für Physik D Atoms, Molecules and Clusters*, **26** 361 (1993) DOI: 10.1007/BF01429195.

[175] Aravind P, Nitzan A and Metiu H. 'The interaction between electromagnetic resonances and its role in spectroscopic studies of molecules adsorbed on colloidal particles or metal spheres'. *Surface Science*, **110** 189 (1981) DOI: 10.1016/0039-6028(81)90595-1.

[176] Kottmann JP and Martin OJF. 'Retardation-induced plasmon resonances in coupled nanoparticles'. *Optics Letters*, **26** 1096 (2001) DOI: 10.1364/OL.26.001096.

[177] Huang F and Baumberg JJ. 'Actively tuned plasmons on elastomerically driven Au nanoparticle dimers.' *Nano Letters*, **10** 1787 (2010) DOI: 10.1021/nl1004114.

[178] Reinhard BM, Siu M, Agarwal H, Alivisatos AP and Liphardt J. 'Calibration of dynamic molecular rulers based on plasmon coupling between gold nanoparticles.' *Nano Letters*, **5** 2246 (2005) DOI: 10.1021/nl051592s.

[179] Su KH, Wei QH, Zhang X, Mock JJ, Smith DR and Schultz S. 'Interparticle Coupling Effects on Plasmon Resonances of Nanogold Particles'. *Nano Letters*, **3** 1087 (2003) DOI: 10.1021/nl034197f.

[180] Xu H, Aizpurua J, Käll M and Apell P. 'Electromagnetic contributions to single-molecule sensitivity in surface-enhanced Raman scattering'. *Physical Review E*, **62** 4318 (2000) DOI: 10.1103/PhysRevE.62.4318.

[181] Mock JJ, Hill RT, Degiron A, Zauscher S, Chilkoti A and Smith DR. 'Distance-dependent plasmon resonant coupling between a gold nanoparticle and gold film.' *Nano Letters*, **8** 2245 (2008) DOI: 10.1021/nl080872f.

[182] Hill RT, Mock JJ, Urzhumov Y, Sebba DS, Oldenburg SJ, Chen SY, Lazarides Aa, Chilkoti A and Smith DR. 'Leveraging nanoscale plasmonic modes to achieve reproducible enhancement of light.' *Nano Letters*, **10** 4150 (2010) DOI: 10.1021/nl102443p.

[183] Grabar KC, Freeman RG, Hommer MB and Natan MJ. 'Preparation and Characterization of Au Colloid Monolayers'. *Analytical Chemistry*, **67** 735 (1995) DOI: 10.1021/ac00100a008.

[184] Lee PC and Meisel D. 'Adsorption and surface-enhanced Raman of dyes

on silver and gold sols'. *The Journal of Physical Chemistry*, **86** 3391 (1982) DOI: 10.1021/j100214a025.

[185] Scholes FH, Davis TJ, Vernon KC, Lau D, Furman SA and Glenn AM. 'A hybrid substrate for surface-enhanced Raman scattering spectroscopy: coupling metal nanoparticles to strong localised fields on a micro-structured surface'. *Journal of Raman Spectroscopy*, **43** 196 (2012) DOI: 10.1002/jrs.3034.

[186] Wilson E. 'The Normal Modes and Frequencies of Vibration of the Regular Plane Hexagon Model of the Benzene Molecule'. *Physical Review*, **45** 706 (1934) DOI: 10.1103/PhysRev.45.706.

[187] Zhou Q, Li X, Fan Q, Zhang X and Zheng J. 'Charge Transfer between Metal Nanoparticles Interconnected with a Functionalized Molecule Probed by Surface-Enhanced Raman Spectroscopy'. *Angewandte Chemie*, **118** 4074 (2006) DOI: 10.1002/ange.200504419.

[188] Wang Y, Chen H, Dong S and Wang E. 'Surface enhanced Raman scattering of p-aminothiophenol self-assembled monolayers in sandwich structure fabricated on glass.' *The Journal of Chemical Physics*, **124** 74709 (2006) DOI: 10.1063/1.2172591.

[189] Sun M, Huang Y, Xia L, Chen X and Xu H. 'The pH-Controlled Plasmon-Assisted Surface Photocatalysis Reaction of 4-Aminothiophenol to p, p'-Dimercaptoazobenzene on Au, Ag and Cu Colloids'. *The Journal of Physical Chemistry C*, **115** 9629 (2011) DOI: 10.1021/jp201002v.

[190] Zhou Q, Zhao G, Chao Y, Li Y, Wu Y and Zheng J. 'Charge-Transfer Induced Surface-Enhanced Raman Scattering in Silver Nanoparticle Assemblies'. *The Journal of Physical Chemistry C*, **111** 1951 (2007) DOI: 10.1021/jp067045s.

[191] Huang YF, Zhu HP, Liu GK, Wu DY, Ren B and Tian ZQ. 'When the signal is not from the original molecule to be detected: chemical transformation of para-aminothiophenol on Ag during the SERS measurement.' *Journal of the American Chemical Society*, **132** 9244 (2010) DOI: 10.1021/ja101107z.

[192] Park WH and Kim ZH. 'Charge Transfer Enhancement in the SERS of a Single Molecule.' *Nano Letters*, **10** 4040 (2010) DOI: 10.1021/nl102026p.

[193] Kim K, Shin D, Choi JY, Kim KL and Shin KS. 'Surface-Enhanced Raman Scattering Characteristics of 4-Aminobenzenethiol Derivatives Ad-

sorbed on Silver'. *The Journal of Physical Chemistry C*, **115** 24960 (2011) DOI: 10.1021/jp208945s.

[194] Kim K, Kim KL, Lee HB and Shin KS. 'Similarity and Dissimilarity in Surface-Enhanced Raman Scattering of 4-Aminobenzenethiol, 4,4'-Dimercaptoazobenzene, and 4,4'-Dimercaptohydrazobenzene on Ag'. *The Journal of Physical Chemistry C*, **116** 11635 (2012) DOI: 10.1021/jp303378p.

[195] Huang YF, Wu DY, Zhu HP, Zhao LB, Liu GK, Ren B and Tian ZQ. 'Surface-enhanced Raman spectroscopic study of p-aminothiophenol.' *Physical Chemistry Chemical Physics*, **14** 8485 (2012) DOI: 10.1039/c2cp40558j.

[196] Peyser-Capadona L, Zheng J, González J, Lee TH, Patel S and Dickson R. 'Nanoparticle-Free Single Molecule Anti-Stokes Raman Spectroscopy'. *Physical Review Letters*, **94** 8 (2005) DOI: 10.1103/PhysRevLett.94.058301.

[197] Zhao LL, Jensen L and Schatz GC. 'Surface-enhanced raman scattering of pyrazine at the junction between two Ag_{20} nanoclusters.' *Nano Letters*, **6** 1229 (2006) DOI: 10.1021/nl0607378.

[198] Renishaw Diagnostics Ltd. Company website [accessed: Sep 2012]. URL: http://www.renishawdiagnostics.com/.

[199] Blackstock JJ, Li Z, Freeman MR and Stewart DR. 'Ultra-flat platinum surfaces from template-stripping of sputter deposited films'. *Surface Science*, **546** 87 (2003) DOI: 10.1016/j.susc.2003.09.039.

[200] Nagpal P, Lindquist NC, Oh SH and Norris DJ. 'Ultrasmooth patterned metals for plasmonics and metamaterials.' *Science*, **325** 594 (2009) DOI: 10.1126/science.1174655.

[201] Hegner M, Wagner P and Semenza G. 'Ultralarge atomically flat template-stripped Au surfaces for scanning probe microscopy'. *Surface Science*, **291** 39 (1993) DOI: 10.1016/0039-6028(93)91474-4.

[202] Blackstock JJ, Li Z and Jung GY. 'Template stripping using cold welding'. *Journal of Vacuum Science & Technology A: Vacuum, Surfaces, and Films*, **22** 602 (2004) DOI: 10.1116/1.1710492.

[203] Wagner P, Hegner M, Guentherodt HJ and Semenza G. 'Formation and in Situ Modification of Monolayers Chemisorbed on Ultraflat Template-Stripped Gold Surfaces'. *Langmuir*, **11** 3867 (1995) DOI: 10.1021/la00010a043.

[204] Mosley DW, Chow BY and Jacobson JM. 'Solid-state bonding technique for template-stripped ultraflat gold substrates.' *Langmuir*, **22** 2437 (2006) DOI: 10.1021/la052650s.

[205] Weiss EA, Kaufman GK, Kriebel JK, Li Z, Schalek R and Whitesides GM. 'Si/SiO_2-templated formation of ultraflat metal surfaces on glass, polymer, and solder supports: their use as substrates for self-assembled monolayers.' *Langmuir*, **23** 9686 (2007) DOI: 10.1021/la701919r.

[206] Uchino T, Sakka T and Iwasaki M. 'Interpretation of Hydrated States of Sodium Silicate Glasses by Infrared and Raman Analysis'. *Journal of the American Ceramic Society*, **74** 306 (1991) DOI: 10.1111/j.1151-2916.1991.tb06880.x.

[207] Shelby J and McVay G. 'Influence of water on the viscosity and thermal expansion of sodium trisilicate glasses'. *Journal of Non-Crystalline Solids*, **20** 439 (1976) DOI: 10.1016/0022-3093(76)90124-1.

[208] Tomozawa M, Erwin CY, Takata M and Watson EB. 'Effect of Water Content on the Chemical Durability of $Na_2O{\cdot}3SiO_2$ Glass'. *Journal of the American Ceramic Society*, **65** 182 (1982) DOI: 10.1111/j.1151-2916.1982.tb10399.x.

[209] Jung B and Frey W. 'Large-scale ultraflat nanopatterned surfaces without template residues'. *Nanotechnology*, **19** 145303 (2008) DOI: 10.1088/0957-4484/19/14/145303.

[210] Chai L and Klein J. 'Large area, molecularly smooth (0.2 nm rms) gold films for surface forces and other studies.' *Langmuir*, **23** 7777 (2007) DOI: 10.1021/la063738o.

[211] Ederth T. 'Template-stripped gold surfaces with 0.4-nm rms roughness suitable for force measurements: Application to the Casimir force in the 20–100-nm range'. *Physical Review A*, **62** 1 (2000) DOI: 10.1103/PhysRevA.62.062104.

[212] Samorí P, Diebel J, Löwe H and Rabe JP. 'Template-Stripped Gold Supported on Ni as a Substrate for SAMs'. *Langmuir*, **15** 2592 (1999) DOI: 10.1021/la981414x.